Author:
Duchi, Marta

Title:
Exploring Excited State Charge Transfer and Vibrational Coherences with Ultrafast Spectroscopy

Exploring Excited State Charge Transfer and Vibrational Coherences with Ultrafast Spectroscopy

Marta Duchi

A dissertation submitted to the University of Bristol in accordance with the requirements for award of the degree of Doctor of Philosophy in the Faculty of Science.

School of Chemistry

May 2020

Words Count: 44184

Abstract:

The interaction between light and matter is a basic concept for the understanding of natural processes fundamental for all life on our planet. In the last three decades, femtochemistry has been developed to investigate the first steps of photoinduced reactions such as photochemistry or ultrafast DNA photoprotection mechanisms. In this thesis, the application of ultrafast techniques to three systems and the study of charge transfer mechanisms and vibrational coherences generated by ultrashort pulses is presented.

A combined experiment of transient absorption and time-resolved infrared spectroscopies is used to investigate a model DNA composed of guanine and thymine, d(GpT). This study univocally demonstrates the formation of delocalised Franck-Condon excited state upon photoirradiation, which mediate a charge transfer mechanism with $d(G^{+}pT^{-})$ exciplex formation.

In Chapter 5, the implementation of a state-of-the-art phase stable spectrometer which allows the acquisition of both broadband transient absorption and two-dimensional electronic spectroscopy data is presented. The setup is characterised by boxcar geometry and used to investigate the solvation dynamics of Oxazine 4 in different solvents. Data analysis reveals the generation of vibrational wave packets in both the ground and excited state of the dye in solution. Franck-Condon active modes are retrieved from the purely vibrational coherent spectra and assigned. From the comparison of frequency-frequency maps of Oxazine 4 in methanol and ionic liquid, a much slower recovery of the central line slope is observed when the ionic liquid surrounds the rigid dye.

The solvation dynamics of zinc chlorin e6 in solution and inside a protein scaffold is also studied with broadband transient absorption spectroscopy. The ultrafast analysis reveals vibrational wave packets generated in the ground and excited state and a less efficient ability to “solvate” of the protein compared to conventional solvents.

Acknowledgements

PhD is a long run, probably, even longer than a marathon, it is a sacrifice, a struggle, an ever-ending fight. It is about understanding that the “right” version, sometimes, does not even exist. It is about making progress, enjoying the climbing, giving your (small) contributions to the field, your tiny extra piece of knowledge to Science.

PhD taught me a lot, and not “just” about nonlinear optics and chemistry. Therefore, my first “thank you” goes to the experience of doing a PhD and to the people that, every day, are working to make it happen. To my supervisor, sometimes my best friend and some other times my worst nightmare, Tom (also known as Dr Oliver). Building the lab and starting this “new adventure” with you has been between the greatest and the hardest thing I have ever done. We are sharing good memories; I am sure our paths will cross again. Despite all (for unknown reasons), I genuinely believe in the future of multidimensional spectroscopy.

I am also taking this opportunity to thank Mike and Andrew for their example and for showing me that science goes beyond the single and individual knowledge. Thanks for teaching me that science is based on collaborations, sacrifices, and teamwork.

Last but not least, I would like to say THANK YOU to Flo and our morning teas, (bloody love our cuppa mate!), the people with whom I have collaborated and immediately established a great friendship (Mike and Tom), and all the people in the group (you know who you are!). I am really thankful to all of you.

Ovviamente, il mio grazie più grande è e sarà sempre rivolto alla mia Famiglia, il mio porto sicuro nel naufragare della vita, ai miei più grandi sostenitori ed incoraggiatori. Ai miei genitori. A mio fratello. Ai miei nonni. A Rocco e alla sua famiglia. Ai miei zii e cugini. Siamo in tanti ma io vi porto nel cuore ad ogni passo. Qualunque distanza ci separa o ci separerà non sarà mai abbastanza grande da farci sentire lontani. Tutto questo, tutto ciò che so e che sono lo devo a voi.

Ai miei più cari amici che nonostante mezza Europa di mezzo mi hanno incoraggiata e sostenuta nell’inseguire i miei sogni. Siete la mia forza viva.

Vi lascio con una frase di G. B. Elion che mi rappresenta profondamente. Finally, G. B. Elion's words which probably represent me better than any other I could ever write.

"Don't be afraid of hard work. Nothing worthwhile comes easily. Don't let others discourage you or tell you that you can't do it. In my day I was told women didn't go into chemistry. I saw no reason why we couldn't."

Gertrude B. Elion

GRAZIE DI CUORE.

Author’s declaration

I declare that the work in this dissertation was carried out in accordance with the requirements of the University's *Regulations and Code of Practice for Research Degree Programmes* and that it has not been submitted for any other academic award. Except where indicated by specific reference in the text, the work is the candidate's own work. Work done in collaboration with, or with the assistance of, others, is indicated as such. Any views expressed in the dissertation are those of the author.

SIGNED: ..... DATE:.....

Table of Contents

List of Tables

.

List of Figures

List of Abbreviations

[EMI]+[SCN]-	1-ethyl-3-methylimidazolium thiocyanate
$[Et]^{+}[NO_3]^{-}$	ethylammonium nitrate
2D	Two-dimensional
2DES	Two-dimensional electronic spectroscopy
A	Acceptor
ACN	Acetonitrile
AOPDF	Acousto-optic programmable dispersive filter
BBO	β-barium borate crystal
BBTA	Broadband transient absorption
BO	Born-Oppenheimer
BS	Beam splitter
C1/C2	Chopper
C153	Coumarin 153
CD	Circular dichroism
Chl	Chlorophyll
CLS	Central line slope
CM	Chirped mirrors
D	Donor
d(GpT)	2′-deoxyguanosine 3′-monophosphate 5′-thymidine
DFT	Density functional theorem
dGMP	Deoxyguanosine monophosphate
DMSO	Dimethyl sulphoxide
DS	Delay Stage
dTMP	Thymidine monophosphate
EADS	Evolution-associated difference spectra
EET	Electronic energy transfer
ESA	Excited state absorption
ET	Electron Transfer
FC	Franck-Condon
FFCF	Frequency-frequency correlation function
FID	Free-induction decay

FRET	Förster resonant energy transfer
FROG	Frequency-resolved optical gating
FT	Fourier transform
FTIR	Fourier transform infrared
FWHM	Full width half maximum
GDD	Group delay dispersion
GSB	Ground state bleach
HOMO	Highest occupied molecular orbital
HPLC	High-pressure liquid chromatography
IC	Internal conversion
IEFPCM	Integral equation formalism polarisable continuum solvent model
IL	Ionic liquid
IR	Infrared
ISC	Inter system crossing
IVR	Intramolecular vibrational relaxation
LO	Local oscillator
LR-TDDFT	Linear-response time-dependent density functional theory
LUMO	Lowest unoccupied molecular orbital
MD	Molecular dynamics
MEOH	Methanol
ND	Neutral density
NMR	Nuclear magnetic resonance
NOPA	Nonlinear optical parametric amplifier
NR	Non-rephasing
OPA	Optical parametric amplifier
Ox 4	Oxazine 4
PE	Photon echo
PES	Potential energy surface
PET	Photoinduced electron transfer
PZ	Piezo stage
R	Rephasing
RC	Reaction Centre
S/N	Signal to noise ratio

SE	Stimulated emission
SHG	Second-harmonic generation
TA	Transient absorption
TG	Transient gating
TL	Transform-limited
TOD	Third-order dispersion
TRIR	Time-resolved infrared
TWINS	Translating-wedge-based identical pulse eNcoding system
UV	Ultraviolet
VC	Vibrational cooling
VR	Vibrational relaxation
WL	White light
ZnCe6	Zinc chlorin e6

Chapter 1

Introduction

1.1 Photochemistry

Photochemistry is the branch of chemistry which studies the interaction between matter and light.[1–4] Molecules in their excited state are generated by the absorption of suitable radiation in the ultraviolet (UV, 100 - 400 nm), visible (400 – 760 nm) and infrared (IR, 760 nm – 1 mm). The primary source of this radiation incident on our planet is the Sun. With an effective temperature of ~ 6000 K, the radiation emitted from the Sun can be approximated to a black body radiation with maximum intensity in the green-yellow region of the visible spectrum.[5] Not all radiations emitted from the Sun reaches the surface of our planet. Much of it is reflected, absorbed and scattered by the atmosphere. Of the light that arrives at the Earth's surface, 49% is in the near-IR, 42% visible, and only 9% is UV light.[6] Therefore, there is an abundance of sunlight available to drive photochemical change in nature, playing a fundamental role in the world we live. In nature, photochemistry forms the basis of a great variety of processes such as photosynthesis,[3] vision,[7] formation of vitamin D,[8] and it can induce mutagenic effects in DNA.[9–12]

Prior to 1817, photochemistry was studied only qualitatively, and photochemical changes, such as photosynthesis in plants, and blackening of silver halides were known.[1–3] At the beginning of the 19th century, Grotthus and later Draper started to develop a quantitative approach to photochemistry with the formulation of the first law of photochemistry:[13]

"Only that light which is absorbed by a system can cause chemical changes."

Despite its simplicity, the first law of photochemistry remains a foundation for photochemical and photobiological phenomena.

A significant advance to our understanding of photochemical reactions was subsequently made by Einstein and Stark, who applied the concept of quantisation to the absorption process. They formulated the so-called second law of photochemistry, also known as photochemical equivalence, that states:[13]

"For each photon of light absorbed by a molecular system, only one molecule is activated."

Today, the importance of photochemistry lies in a great variety of applications both in science and technology.[3] For example, a broad range of chemicals are now produced through photoinitiated synthesis, and synthetic organic photochemistry is currently developing towards more efficient and selective methods.[14,15] Further examples of the application of photochemical processes in science and technology are the photoinitiated polymerisation used in photography, lithography,[16] or the implementation of photochromic materials used in sunglasses lens.[17] A further motivation to study photochemical processes is given by the possibility to convert and store solar energy. The energy crisis has promoted the study of photovoltaic materials where an understanding of the photophysical and photochemical processes is essential for the development of more efficient devices.[18]

In this thesis, the interaction between coherent light and molecular systems such as a dinucleotide composed of thymine and guanine DNA basis, a dye molecule (Oxazine 4) and chlorin e6 in a maquette protein are studied with ultrafast techniques to address open questions about some current topics in photochemistry. Before presenting the results, key tools used in photochemistry and physical chemistry are introduced, followed by a

discussion about experimental techniques implemented to offer additional insight into the dynamics of the light-absorbing systems.

1.2 Potential Energy Surface

1.2.1 Born Oppenheimer Approximation

The Schrödinger equation is a key result in quantum mechanics to describe the wave function or the state function of a quantum-mechanical system.[19] The general form of the equation, which is used to describe the system evolution in time, is the time-dependent Schrödinger equation (see Chapter 2 and equation 2.5). This description predicts that the wavefunction can form stationary states which are quantum states with time-independent observable and definite energy. These stationary states can be described by using the time-independent Schrödinger equation:

$$E\,\Psi = \hat{H}\,\Psi \qquad (1.1)$$

where Ψ is the wave function, E is the total energy of the system (potential energy + kinetic energy), and $\hat{H}$ is the Hamiltonian operator.

It is only possible to solve the Schrödinger equation for hydrogen-like atoms while some approximations need to be done in order to solve it for more complicated systems.[19] A typical way to simplify the Schrödinger equation (still not sufficient to solve the equation for polyatomic molecules) is to consider that the nuclei have a much larger mass compared to the electrons. Therefore, the motion of the nuclei is much slower compared to the motion of the electrons; this approximation is named after Max Born and J. Robert Oppenheimer who proposed it in 1917.[20]

More specifically, the Hamiltonian of equation 1.1 depends on the nuclear and electronic contributions, and the time-independent Schrödinger equation can be written as:

$$[\hat{T}_N + \hat{T}_e + \hat{V}_{ee}(r) + \hat{V}_{NN}(R) + \hat{V}_{eN}(r,R)]\ \Psi(r,R) = E\ \Psi(r,R) \qquad (1.2)$$

where r represents the electronic coordinates and R stands for the nuclear coordinates. The total kinetic energy operator ($\hat{T}$) is given by the nuclei ($\hat{T}_N$), and the electrons ($\hat{T}_e$) kinetic energy operators, while the total potential energy operator ($\hat{V}$) is the sum of the electron-electron ($\hat{V}_{ee}$), nucleus-nucleus ($\hat{V}_{NN}$), and electron-nucleus ($\hat{V}_{eN}$) contributions. It is not possible to solve this equation for anything other than hydrogen-like systems. Therefore, considered that the electrons are much lighter than the nuclei, the nuclear motion is much slower than the electron velocities. Under such conditions, it is possible to invoke the Born-Oppenheimer (BO) approximation which allows the total wavefunction to be partitioned, as follows:

$$\Psi(r, R) = \sum_i \phi_i\ (r, R)\ \chi_i(R) \qquad (1.3)$$

where $\phi_i\ (r, R)$ is the electronic wavefunction that depends on both the coordinates of nuclei and electrons. Furthermore, $\chi_i(R)$ is the nuclear wavefunction which is no longer dependent on the coordinates of the electrons. Therefore, the Born-Oppenheimer approximation allows the total wavefunction to be written as a product of the electronic and the nuclear wave functions and enables the separation of the Hamiltonian operator into electronic and nuclear terms. From the variation of the nuclear configuration in small steps followed by the calculations of the potential curves, one can obtain the potential energy surface (PES). The electronic wave function is re-calculated (recomputed) many times as a function of nuclear geometry to generate a potential energy surface for the studied system. Note that the PES is now a central concept in physical chemistry with its ability to relate the potential energy of the molecule with its geometry.[21]

1.2.3 Vibrational Energy Levels

Let us now consider the simplest case: a diatomic molecule where the PES can be represented using the Morse potential V(r):[22]

$$V(r) = D_e \left\{1-e^{-a\,(r-r_e)^2}\right\} \qquad (1.4)$$

where D_e is the bond dissociation energy which is equal to the well depth, "a" is a factor that describes the shape of the curve and depends on the force constant at the minimum of the well, r_e is the equilibrium internuclear distance and $r - r_e$ the extent of nuclear displacement compared to the equilibrium configuration. A graphical representation of equation 1.4 is given in Figure 1.1, which depicts the Morse potential and the associated vibrational energy levels (represented as horizontal lines across the potential curve). Note that the distance between the vibrational levels decreases as the energy approaches the dissociation limit due to anharmonicity.[51,52]

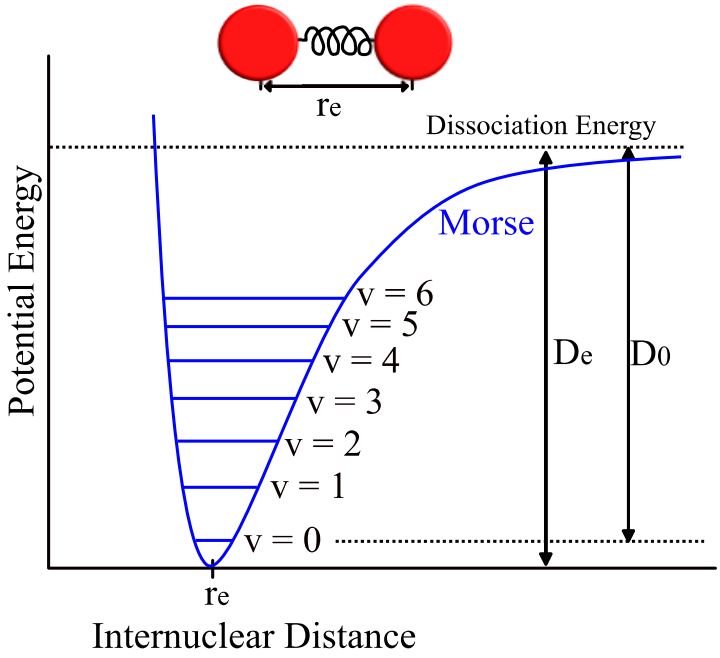

Figure 1.1 Morse potential for a diatomic molecule. The dissociation energy is indicated as D_e, and the first seven vibrational levels are indicated from v = 0 to v = 6.

The representation of the potential energy surface is simple for diatomic molecules, but it becomes more complicated for polyatomic species which are characterised by more than one degree of freedom. For such molecules, the total number of vibrational degrees of freedom is 3N – 6 (or 3N – 5 for linear species) where N corresponds to the number of atoms.[23] The representation of a system having many normal coordinates requires a hypersurface (quantum mechanically obtained from the Born Oppenheimer approximation, see the previous section) which is impossible to visualise in its entirety for polyatomic molecules. Therefore, the convention is to depict one or two vibrational modes at the same time, while treating the other modes as "frozen". Under such conditions, the simple representation shown in Figure 1.1 can also be used when studying polyatomic molecules.[23]

1.3 Photochemistry and Spectroscopy

1.3.1 Light-Matter Interactions

As stated by the two laws of photochemistry, the absorption of a photon by a molecule, generating an excited state, is the primary process of photochemistry. Considered that spectroscopy is the study of the interaction between light and matter, photochemistry and spectroscopy are, therefore, intimately related.[3]

To better understand the interaction between light and matter and the process of absorption and emission in molecules, let us assume that an electric field interacts with a molecule. In this representation, the electric field ($\underline{\mathcal{E}}$) is treated as a plane wave. Thus, it is expressed as: $\underline{\mathcal{E}}(r,t) = E\, e^{(\pm i\underline{k}\underline{r} - i\omega t)}$, where E is the amplitude of the field, "i" is the unit imaginary number, $\underline{r}$ is the position vector, t is time, ω is the angular frequency ($\omega = 2\,\pi\,\nu$, with ν frequency which is proportional to the wavelength of the radiation, λ), and $\underline{k}$ is the wave vector. Note

that the wave vector indicates the direction of propagation of the field, and the solution is characterised by either a positive $\underline{k}$ vector or negative. The positive vector manifests as waves propagating parallel to the direction of the wave vector; thus, the waves are said to be outgoing waves. On the contrary, a negative vector indicates that the waves are propagating against the direction of $\underline{k}$ and they are named incoming waves.

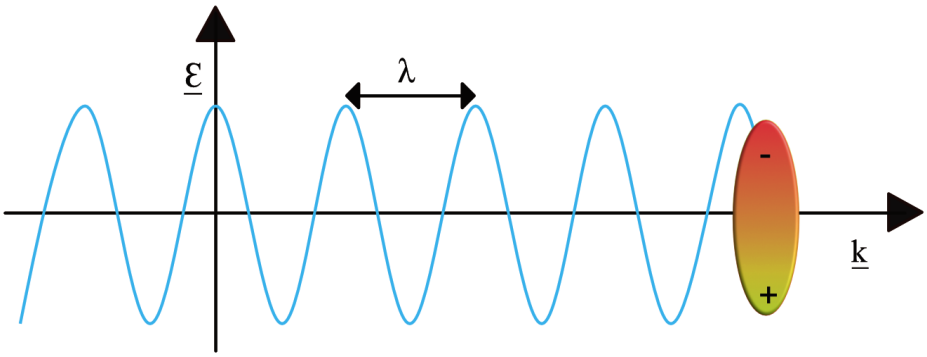

Figure 1.2 Generation of an induced molecular dipole through interaction with an oscillating electromagnetic radiation.

Upon light-matter interaction, the applied electric field induces an oscillatory dipole moment in molecules, causing the fluctuation of the free electron cloud with the frequency of the electromagnetic radiation.[3,24] Under such conditions, when the frequency of the incident light (ν_i) differs from the natural frequency of the molecule (ν_n) (as determined by the quantised energy states of the molecule), two phenomena can occur. The first phenomenon is known as scattering of radiation by a molecule. The second phenomenon is related to the radiation produced by the interference between the light and matter which is isotropic (equal value in different directions), and it can produce destructive interference in all direction except that of reflection and refraction.[3]

Nevertheless, when ν_i and ν_n are similar, the so-called resonant condition is established between the light (*e.g.*, photon)[25] and matter (atom or molecule), the oscillation is not bound anymore and, classically, it is defined as "free". In such a case, the photon can be absorbed by the atom or molecule which is subsequently promoted to an excited electronic state.[3]

Classically, a dipole moment (μ) is given by $\mu = \sum_j r_j q_j$, defined as the summation of the product of the position vector for all charged particles r_j, times the charge q_j.

The quantum mechanical representation of the oscillating dipole moment is given by the transition dipole moment. This quantity provides the strength of the interaction that leads to the transition between states. To define the transition dipole moment, let us assume that the transition occurs between two states, the initial (i) and final (f). These two states can be described by ψ_i and ψ_f wavefunctions which contain all the measurable information about the system studied. The transition dipole moment reads:[26]

$$\mu_{fi} = \langle \psi_f | \hat{\mu} | \psi_i \rangle = \int \psi_f^* \, \hat{\mu} \, \psi_i \, dr \tag{1.5}$$

where $\hat{\mu}$ is the transition dipole moment operator, the angle brackets indicate the bra/ket notation, and $\int dr$ means integrated over all coordinates. Equation 1.5 does not only describe the transition between two states, but $|\langle \psi_f | \hat{\mu} | \psi_i \rangle|^2$ gives the probability of it, and it is commonly used to establish whether or not transitions between electronic states are allowed.[27]

Note that the classical dipole moment and the quantum mechanical transition dipole moment are not the same, and the relationship established here is made for the sake of analogy.

1.3.2 Absorption and Emission

The phenomena of absorption and emission for quantised systems such as atoms and molecules were first treated in 1916 by Einstein who proposed the existence of three processes in light-matter interaction: absorption, spontaneous emission and stimulated emission.[28] With each event, Einstein associated a coefficient (known as the Einstein coefficient) which indicate the probability of each process.

For a two-level system characterised by two electronic excited states, E_1 and E_2, where $E_2 > E_1$, the absorption process occurs when the electronic transition is from the state at lower energy to the state at higher energy. This process is due to the absorption of a photon of energy $h\nu$, as shown in Figure 1.3 (a), and the Einstein coefficient associated with the absorption process is B_{12}.

Spontaneous emission is the process that involves the "spontaneous" (without the presence of an external field) decay of a photon from E_2 to E_1. The process is conventionally identified with the Einstein coefficient, A_{21}, which gives the probability that an electron in state E_2 spontaneously decays in E_1 (see Figure 1.3 (b)). The photon emitted is equal to the energy difference between the two states ($E_2 - E_1 = h\nu$).

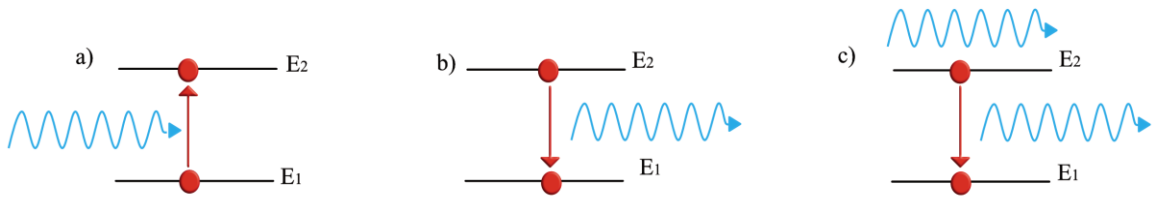

Figure 1.3 Electronic transition between two levels at energies E_1 and E_2 ($E_2 > E_1$) for (a) absorption, (b) spontaneous emission, and (c) stimulated emission in a two-level system.

Stimulated emission can be viewed as the inverse of the absorption process, as depicted in Figure 1.3 (c). This process is characterised by an electronic transition from E_2 to E_1 induced by the presence of an external field. Stimulated emission is described by the coefficient B_{21}, which corresponds to the probability that an electron decays from E_2 to E_1 emitting a photon with total energy $E_2 - E_1 = h\nu$.

1.3.3 Franck-Condon Principle

Molecular systems can be studied at room temperature where, typically, many molecules reside in the lowest vibrational level (v = 0) of the ground electronic state following the Boltzmann distribution.[29]

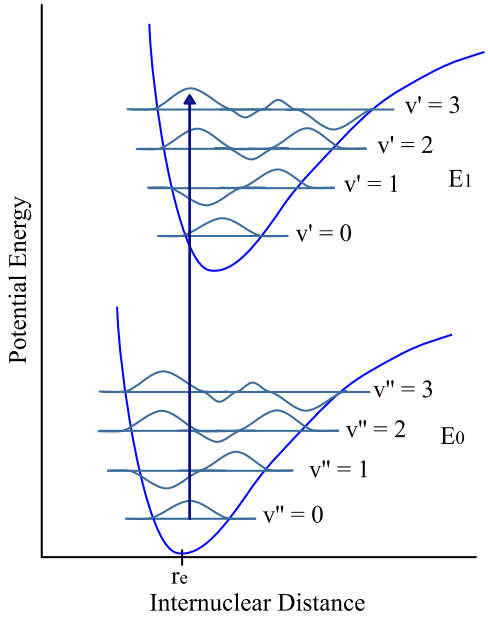

Figure 1.4 Energy diagram depicting the vibrational states and their wavefunctions to describe the Franck-Condon principle. The potential wells are shown such as the favoured transition in absorption (blue arrow) is the v'' = 0 to v' = 3.

In a specific case where the majority of the molecule resides in the lowest vibrational state, Figure 1.4 shows that the most probable transition is the one that originates from the centre

of the vibrational quantum level where the vibrational overlap integral has its maximum value.[19] Considered that an electronic transition occurs in < 10^{-15} s (sub fs), while a vibrational transition usually occurs in ~10^{-12} s (~ ps), the nuclei remain "frozen" during the electronic transition. The scientific community largely accepts this assumption which is known as the Franck-Condon (FC) principle. This principle states:[30–32]

"Electronic transitions are so fast in comparison to nuclear motions that immediately after the transition, the nuclei have nearly the same relative position and momentum as they did just before the transition."

Classically, this principle is depicted as a vertical arrow parallel to the potential energy axis, and it implies that the most probable transitions are the ones that occur with a small change of the momentum and position of the nuclei. Moreover, the state resulting from this transition is identified as FC state.[33]

1.4 Excited states

After presenting the key aspects of absorption and emission, which lead to the formation and deactivation of the excited states, the concept of excited state lifetime is introduced alongside with the photophysical processes that can occur in the excited state.

1.4.1 Excited state Lifetime and Photophysical Processes in Electronically Excited Molecules

An excited molecule can be a completely different chemical species compared to the species in the ground state, with far more internal potential energy. Many physical properties, such as dipole moment, pKa values, and redox potentials, differ between the

ground and the metastable excited state.[34] Thus, excited states are generally characterised by a change in the structure (*i.e.*, different minimum energy bond length or dihedral angles) which gives rise to different geometries and bonding properties compared to the ground state species.[33,35]

Upon photoirradiation, in a two-level system (see section 1.4.2), a molecule in the ground state can be promoted to the higher-energy state which is characterised by a certain lifetime, known as the radiative lifetime. For a molecule, in free space, the radiative lifetime must have a unique value, and for times longer than the radiative lifetime, the system reverts to its original state. Considering I and I_0 as the intensity of the emission at time zero (when the radiation start interacting with the system) and any time t such as $t >> t_0$, for a system comprises a large ensemble of molecules, the rate of the decay has an exponential form given in the following equation:[34]

$$I = I_0 \, e^{-t/\tau} \qquad (1.6)$$

where $\tau = 1/k$ with k the rate constant of the emission process. The lifetime (τ) is defined as the time taken for the radiation intensity to decay to 1/e th of the original value (occurring when $t = \tau$).[3,4,34] Moreover, in the case where the highest energy level (E_2) can decay only with radiative (emission of photon) emission to the lower energy state (E_1) the Einstein coefficient for the spontaneous emission (A_{21}) is related to the radiative lifetime, as follows: $A_{21} = 1/\tau$. However, in systems that cannot be described by a simple two-state model in the condensed phase, other phenomena such as molecular collisions can occur. These processes compete with the spontaneous emission and can reduce the lifetime of the excited state.[36]

In condensed phase systems, the pathways available for a molecule to return to the ground state are grouped under photophysical process some of which are an intrinsic characteristic

of the system and are unimolecular, while some others are a function of external perturbations and may be bimolecular processes. All these processes have to occur in a period shorter than the natural radiative lifetime in order to be competitive.[33]

The unimolecular processes are illustrated in the Jablonski diagram shown in Figure 1.5. This diagram can be read as follows: the first process that occurs is the absorption of a photon which may promote the molecule from the ground (S_0) to the excited state S_1, S_2 or higher energy levels. As illustrated, there are many possible routes for the deactivation of excited electronic states including, radiative (straight arrows) and non-radiative (undulated arrows) processes, Figure 1.5.

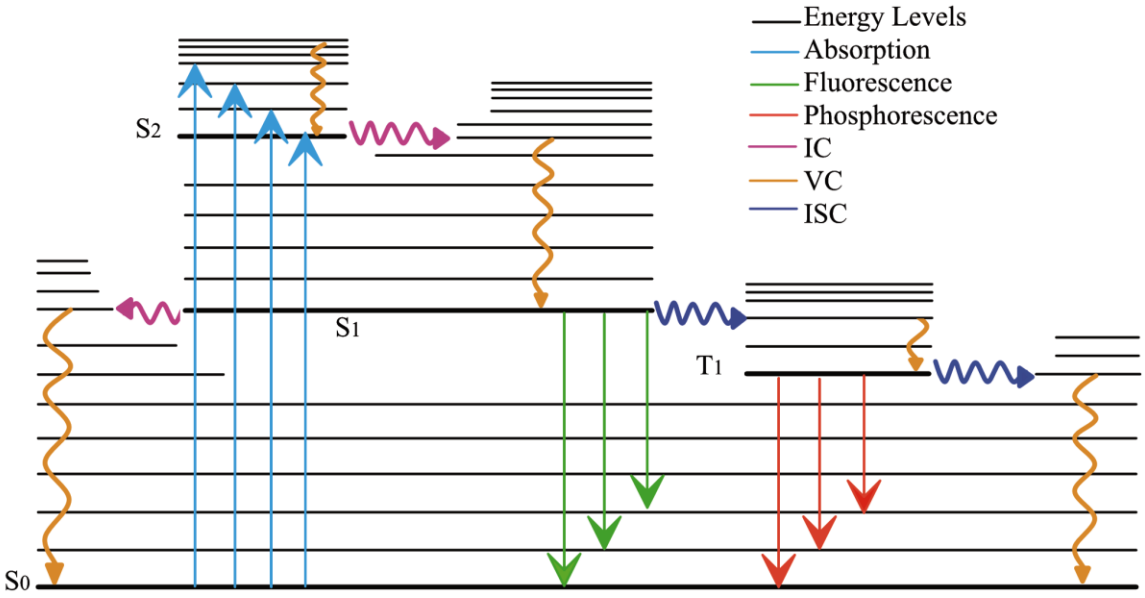

Figure 1.5 Jablonski diagram for unimolecular processes where, IC = internal conversion, ICS = intersystem crossing, VC = vibrational cooling. S_n denotes singlet electronic states, while T_n stands for triplet states. Straight arrows represent radiative processes, while undulated arrows are non-radiative processes.

The first radiative processes that might take place is the vibrational relaxation (VR). This process generally comprises two phenomena: intramolecular vibrational relaxation (IVR)

where the energy is redistributed within different quantum states of the same molecule, and vibrational cooling (VC) where the energy can be exchanged with the surrounding molecules until the lowest vibrational level of the electronic excited state is reached.[64]

A molecule excited to high singlet energy states such as S_2, S_3,..S_n may dissipate the energy through a non-radiative transition between two states with the same multiplicity; this process is the so-called internal conversion (IC). In general, VC immediately follows internal conversion to the lowest vibrational states of the electronic excited state. The rate of IC is inversely proportional to the energy gap between the two singlet electronic states involved in the process. Therefore, IC for closely-spaced states such as $S_3 \rightarrow S_2$ or $S_2 \rightarrow S_1$ is very rapid while the $S_1 \rightarrow S_0$ transition generally occurs in a slower time scale due to the more significant energy gap between the two states, and it might compete with processes such as fluorescence and intersystem crossing (ISC) characterised by a longer time scale.[37] However, note that this is a general rule that does not hold in the case of the conical intersections (molecular funnels) that, for example, contribute to the stability of DNA (see Chapter 4).

Upon photoirradiation, and as a consequence of IC and VC, the system may lose the energy through a radiative transition ($S_1 \rightarrow S_0$) in a process known as fluorescence.[3] The energy loss prior to fluorescence is the physical origin of Kasha's Rule known for stating that photon emission (fluorescence or phosphorescence) occurs with an appreciable yield from the lowest excited state of a given multiplicity.[33,38] Another phenomenon associated with fluorescence is the Stokes-shift defined as the energy gap between the maxima of the absorption and emission spectra of the same electronic state. Fluorescence occurs at longer wavelengths compared to the absorption.

A competitive deactivation path to IC and fluorescence is the non-radiative transition between two isoenergetic vibrational levels belonging to the electronically excited states characterised by different multiplicity, known as ISC.[33] The transition is usually from S_1 to T_1 or for reverse ISC from T_1 to S_1. In principle, this process should be a forbidden transition due to the conservation of spin angular momentum selection rule ($\Delta S = 0$). However, the spin-orbit coupling between the orbital angular moment and the spin angular momentum can make this transition weakly allowed. Since it is a partially forbidden transition, it typically occurs on timescales much longer than the other two competitive pathways.[3,35] However, the incorporation of heavy atoms into the molecule increases the spin-orbit coupling and makes this transition more probable.[3,35]

After ISC the molecule immediately undergoes VC to the ground vibrational state of the triplet state. Furthermore, emission of a photon from T_1 to S_1 might occur; this radiative transition between two electronic states of different spin multiplicity is known as phosphorescence. As seen for ISC this a spin forbidden transition, but again it is weakly allowed through spin-orbit coupling. The transition rate is prolonged compared to the other processes.[3,35]

1.5 Femtosecond Spectroscopy

To infer the atomic motions and the non-radiative processes described in the previous section is one of the primary goals of the femtochemistry field. The advent of this new discipline was a fundamental contribution to the study of vibrational motions and ultrafast processes that are the source of chemical reactions passing through the transition state.[39,40] With the fast time resolution, it is possible to observe molecular structures far from the equilibrium prior rotational and vibrational motions. In other words, femtochemistry and

femtosecond laser pulses can offer insight into the collective motion of atoms comprising molecules.[39,40]

Femtosecond experiments were characterised by three standard features reported by Zewail in its review paper titled "femtochemistry: past, present and future".[39,40] The first condition is the definition of a time zero (*"to clock the motion"*) given by the interference between an ultrashort pulse (called the pump) and a time-delayed second pulse known as the probe. The second condition is provided by the synchronisation of the molecular motion of the ensemble in solution. The third condition, which is a crucial concept in femtochemistry is to take advantage of the coherence created to probe the nuclear motion as a function of time. These three requirements are the basis of what it is called pump-probe spectroscopy.[40] Moreover, the concept of state coherence which, in this context, is an index of how long the system maintains the superposition of states,[41] can be identified as the core of femtosecond spectroscopy for being the cause of many observed effects, such as vibrational wave packets.[40] Experimentally, the preparation of the coherence and its detection requires very short pump and probe pulses and detection techniques such as pump-probe spectroscopy and two-dimensional electronic spectroscopy, detailed in Chapters 3 and 5, respectively.

Currently, femtochemistry is applied to study physical, chemical and biological reactions and gain insight into transition states or reaction intermediates. Therefore, femtosecond spectroscopy is mostly used to investigate different types of chemical changes and to study complex molecular systems such as proteins and DNA. Femtosecond studies have also been applied for the observation of matter in different phases such as gas and molecular beams, solids, nanoparticles, condensed phase. Pump-probe spectroscopy and femtosecond

studies are also applied to various chemical fields, for example, in organic chemistry where multiple transition states and reaction intermediates can be observed in chemical reactions such as isomerisation. This kind of spectroscopy is also applied in inorganic chemistry to study complex organometallic reactions and metal-metal and metal-ligand bonds, moreover it has been used in femtobiology where femtochemistry is applied to study elementary steps of vision, photosynthetic reaction, protein dynamics and electron and proton transfer mechanisms in DNA. The current femtosecond studies and pump-probe applications are related to many other fields; however, a review of them goes beyond the scope of this thesis.[40,42–50]

1.6 Electronic Interactions

Femtochemistry and experiments concerning femtoseconds pulses can be used to observe processes that occur in a short and relatively short time scale such as electron and energy transfer. These processes are described here through two different theories, known as Marcus theory and Förster resonant energy transfer. These processes occur between two species identified as a donor (D) and acceptor (A) and arise from weak electronic coupling. Therefore, the electronic states involved in electron and energy transfer can be treated as localised states while for medium or strong electronic coupling, the resulting state would have been described as delocalised.

1.6.1 Marcus Theory

Marcus theory was first developed by Rudolph A. Marcus in 1956, to explain the electron transfer between a donor and acceptor.[51–53] According to Marcus theory, the electron transfer reaction between the weakly coupled donor and acceptor progresses along a solvent rearrangement coordinate for the following reaction:

$$D + A \rightarrow D^{+} + A^{-} \qquad (1.7)$$

The rearrangement occurs upon electron transfer when the solvent changes (reorganises) its configuration in such a manner that the negative charge on A is stabilised as well as the positive charge on the donor; a representation is shown in Figure 1.6.

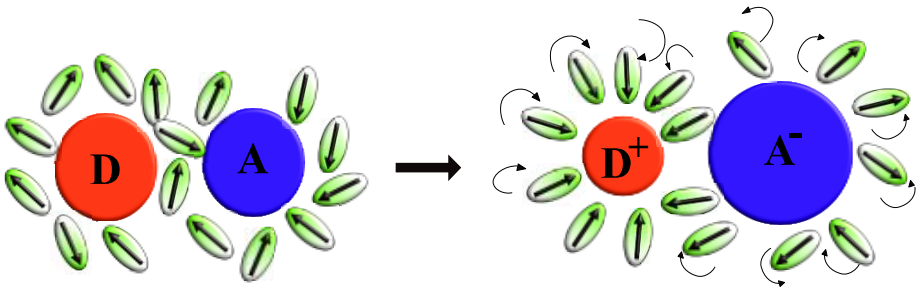

Figure 1.6 Donor acceptor representation before and after charge transfer.

The figure also shows the so-called outer shell, which is the external response of the medium while the inner shell refers to an internal vibrational mode that promotes the electron transfer reaction. Moreover, the electron is represented as localised either in D or in A^{-}. Therefore, the system represents the non-adiabatic (or diabatic) case where the electronic coupling of donor and acceptor is weak.

With the development of this theory, Marcus demonstrated that the rate of electron transfer could be classically derived from the Arrhenius rate constant,[54] and the electron transfer rate constant is:[51–53,55]

$$k_{ET} = A \exp\left[\frac{-(\Delta G^{\circ} + \lambda)^2}{4\lambda kT}\right] \qquad (1.8)$$

where A is the preexponential factor, and according to the semi-classical theory, it conveys information about the electronic coupling between the neutral reagents A and D. The exponential term contains information about the effect of the nuclear motion that occurs while the electron transfer takes place. It is usually referred to as the nuclear factor.[29] The

factor contains the Boltzmann constant (k), T the temperature, and the so-called reorganisation energy (λ) which is the energy needed to "reorganise" the system structure from reagent to product. Moreover, k_{ET} is also a function of ΔG°, which is the total Gibbs free energy change for the reaction. This state function is defined through thermodynamic properties as $\Delta G^{\circ} = \Delta H^{\circ} - T\Delta S^{\circ}$, where the change in enthalpy is ΔH°, and ΔS° represents the change in entropy under standard conditions.

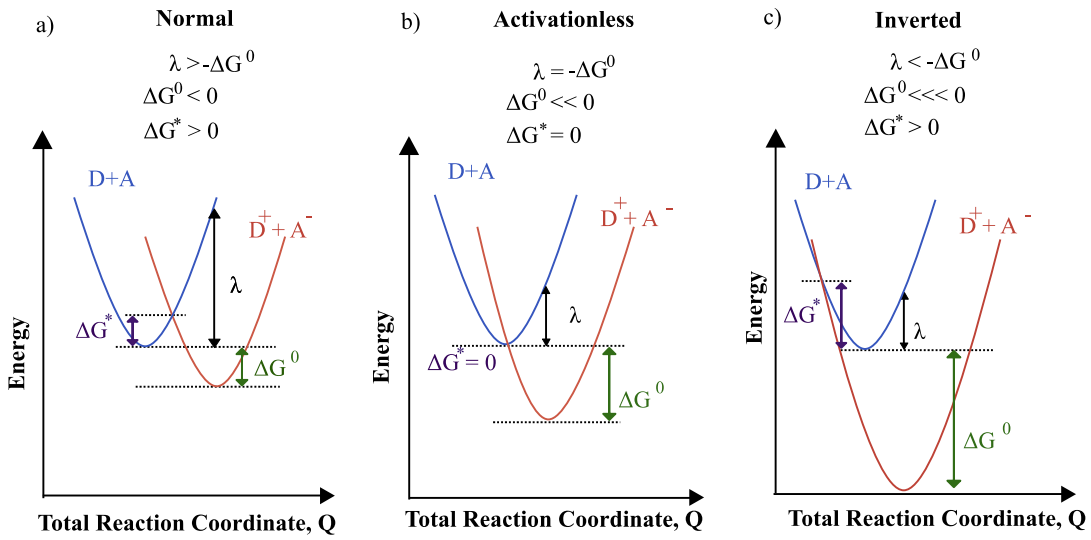

Figure 1.7 Reactant (D + A) and product ($D^+ + A^-$) potential energy curves for electron transfer showing the three different regimes, (a) normal, (b) activationless, and (c) inverted.

Also, note that for completeness, Figure 1.7 shows the Gibbs energy of activation (ΔG*), which is defined as the difference between the transition state of a reaction and the ground state of the reactant.

From the relationship between the reorganisation energy and the Gibbs free energy established in equation 1.8, three possible scenarios can occur during the electron transfer, as depicted in Figure 1.7. The first scenario analysed is the so-called normal regime (Figure 1,7 (a)), where the reorganisation energy is greater than the Gibbs free energy and ΔG* > 0. Under these conditions, an increment of the driving force (more negative ΔG^0) leads to

an increase of k_{ET} due to a smaller activation barrier between the reactant and product potential energy wells. As also predicted by the Arrhenius model, the rate of electron transfer has its maximum when $-\Delta G^0 = \lambda$ and the reaction is said to be activationless or barrierless with $\Delta G^* = 0$, as shown in Figure 1.7 (b).

The third scenario corresponds to a further increase of the driving force leading to the re-appearance of an activation barrier. This region is the novelty introduced by Marcus in describing the electron transfer reaction, and it is not contemplated by the classical description of a barrier activated electron transfer reaction (Figure 1.7 (c)). From a chemical perspective, the inverted behaviour indicates that additional vibrational excitation is required to reach the curve-crossing point.[56-58]

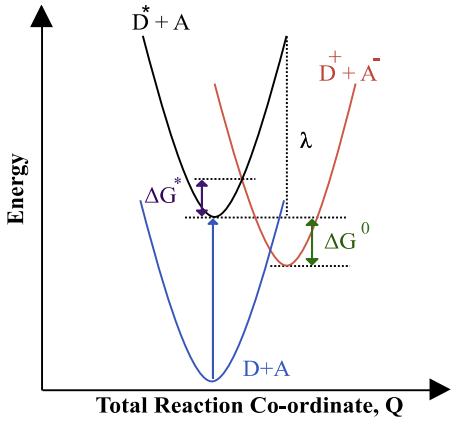

Figure 1.8 Schematic representation of the photoinduced electron transfer mechanism.

Marcus theory is usually used for the description of a number of important processes in biology and chemistry, including corrosion, photosynthesis, and charge separation in certain type of solar cells. In this thesis, Marcus theory sees its application in the study of a dinucleotide of guanine and thymine moieties. This theory gives the kinetics and thermodynamics explanations for the so-called photoinduced electron transfer (PET) from D to A. This charge transfer mechanism yields a charge-separated state constituted by the

acceptor radical anion and donor radical cation. Figure 1.8 depicts the photoinduced electron transfer mechanism, where the system is initially found in its ground state (D + A). Under such conditions, the electron transfer from D to A is not thermodynamically favoured. However, this scenario can change upon photon absorption when the light-absorbing donor can be promoted to its excited state (D* + A). This new scenario facilitates the PET that becomes a thermodynamically favourited mechanisms with $\Delta G^0 < 0$. Therefore, a charge transfer state, $D^+ + A^-$, can be generated.[59,60] This mechanism is of crucial importance in a variety of chemical and biological reactions and an example of PET between guanine (donor) and thymine (acceptor) will be given in Chapter 4.

1.6.2 Förster Resonant Energy Transfer

The electronic excitation transfer between two resonant states, belonging to the donor and the acceptor, was first described by Förster,[61,62] and it is now known as Förster resonant energy transfer (FRET). This process is due to a dipole-dipole interaction between D and A, where the electronic energy transfer (EET) is driven by an oscillatory transition dipole moment of the donor, which is resonant with the acceptor. It is important to note that FRET processes do not involve the emission and reabsorption of photons. Therefore, the resonance interaction can occur at a large intermolecular distance and does not require molecular collisions.[61,62]

The non-radiative transfer of electronic excitation from an electronically excited molecule, the donor, and a species on the ground state, the acceptor, leads to a reduction of the donor and increase of acceptor fluorescence intensities due to the following equation:

$$D^* + A \rightarrow D + A^* \qquad (1.9)$$

where D* is the electronically excited donor and A* the electronically excited acceptor. Therefore, both the ground and the excited state of the donor and acceptor play a fundamental role. Photoexcitation promotes the donor into its excited state (see Figure 1.9 (a), D → D*). Subsequently, a rapid vibrational cooling takes place, and the donor relaxes into its minimum energy geometry described by its reorganisation energy (λ_{D*}) in a few picoseconds. This process leaves the donor in the lowest vibrational level of the excited state, which requires a resonant condition to transfer the energy from D^* to A^*. When the resonant condition is fulfilled, and the oscillation of the excited donor coherence is equal to the difference in energy between the ground, and excited state of the acceptor FRET can take place. After energy transfer to the acceptor, vibrational cooling occurs, and the fluorescence of the species A is observed. The efficiency of the electronic energy transfer is experimentally followed by comparing the emitted fluorescence of D with A, which are often spectrally distinct.

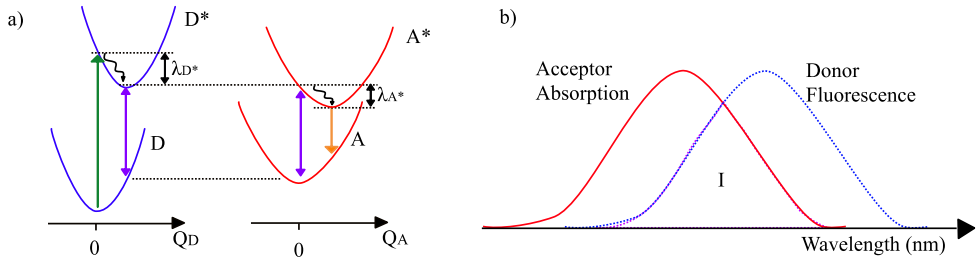

Figure 1.9 (a) Donor and acceptor potential energy curves and (b) graphical representation of the overlap integral (I) between the absorption spectrum of A and the fluorescence of D.

According to Förster theory, the rate constant of energy transfer (k_{EET}) from the donor to the acceptor is a function of the emission rate constant (k_D), the lifetime of the excited donor in the absence of energy transfer (τ_D), the distance between donor and acceptor (r) and the so-called critical-quenching radius also known as the Förster radius (R_0):[61,62]

$$k_{EET} = k_D \left(\frac{R_0}{r}\right)^6 = \frac{1}{\tau_D}\left(\frac{R_0}{r}\right)^6 \quad (1.10)$$

thus, the interaction strength is proportional to $1/r^6$, and the FRET rate can be used to characterise the D-A distance when R_0 and τ_D are known.

Another critical aspect of FRET is the definition of the Förster radius which is:[61,62]

$$R_0 = \text{const}\left(\frac{\kappa^2 \phi_D \, I}{n^4}\right)^{1/6} \quad (1.11)$$

where κ is the orientation factor, ϕ_D the fluorescence quantum yield (defined as the ratio between the rate of the process and the rate of absorption), n is the refractive index of the medium and "I" is the so-called spectral overlap integral defined as:

$$I = \int \varepsilon_A(\lambda) \, \lambda^4 \, F_D(\lambda) \, d\lambda \quad (1.12)$$

where ε_A is the extinction coefficient of the acceptor, λ is the wavelength, and F_D is the wavelength-dependent donor emission spectrum, see Figure 1.9 (b). The overlap integral is the mathematical description of the resonance between donor and acceptor transitions.

Moreover, FRET sees its application mainly in biological experiments such as molecular structure investigations. The theory is often referred to as "spectroscopic ruler" where the distance between two fluorophores (nanometre scale) is calculated as the ratio of fluorescence intensities. For example, FRET is used for detecting DNA mutations, biological membrane mapping and in protein studies.[61]

In conclusion, the FRET theory states that the energy transfer rate scales as r^{-6} (equation 1.10) and requires the resonance condition between donor fluorescence and acceptor absorption, graphically shown as the overlap between the two spectra (I).[61,62]

1.7 Solvation Dynamics and Vibrational Wave packets

To conclude, two concepts that will be useful for a full understanding of the data shown in this thesis are introduced in this section: solvation dynamics and vibrational wave packets.

1.7.1 Solvation Dynamics

Solvation dynamics is the study of the changes in the solvent structure obtained upon photoexcitation of the solute molecule.[11]

At the beginning of the field the attention was mainly focused on common solvents[11] while today, after the development of ultrafast lasers, the goal is to understand more complex systems or solvation in non-conventional solvents such as ionic liquids.[63–66] Experimentally, the time-dependent changes are usually followed by Stokes-shift observed in the emission spectrum of the solute.

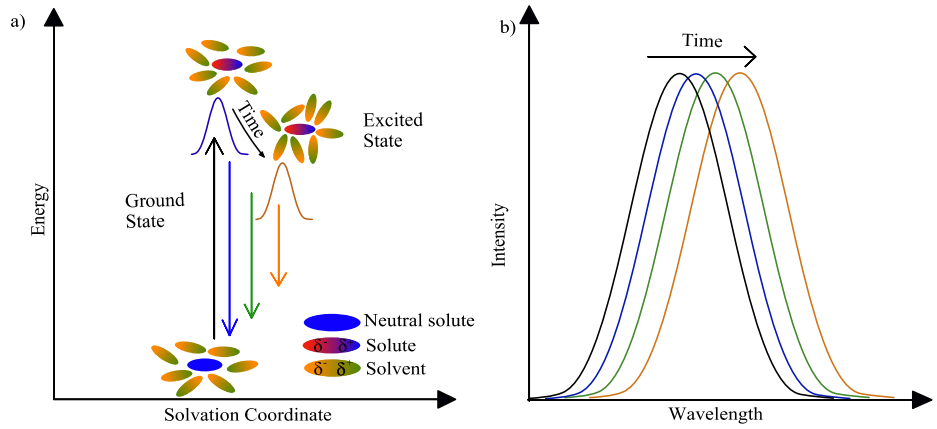

Figure 1.10 Schematic diagram representing (a) photophysical process in solvation dynamics, (b) red shift in solute emission spectra due to solvent reorganisation.

Figure 1.10 (a) schematically illustrates the solvation process, and it can be explained as follows. The molecular system is initially in the ground electronic state in equilibrium with the surrounding environment. Upon photon absorption, the permanent dipole moment of

the solute changes (typically it increases). The electronic transition is so fast that the solvent initially does not have enough time to reorient to the changed charge density of the solute, and the system is initially far from the excited state equilibrium. Subsequently, the solvent molecules reorient themselves in a way that can stabilise the new charge distribution of the solute. To better understand this process, the comparison with the time-resolved emission spectroscopy can be quite useful (Figure 1.10 (b)). The time-resolved technique shows that the frequency-shift of the spectrum monitors the time-dependent emission after excitation, and the time dependence of the solute emission on the solvent reorientation (solvation) leads to a red shift of the emission spectrum.[63–65]

1.7.2 Vibrational Wave Packets

Schrödinger first introduced the concept of wave packets in 1926 as a connection between the classical and quantum mechanical description of natural phenomena.[12] For almost sixty years, the concept of a wave packet had no practical use because the generation of such superpositions of states seemed impossible. However, with the development of femtosecond pulses, the generation and observation of wave packets became possible.[13,14] Now, it is well known that ultrashort pulses can generate vibrational (and/or rotational) wave packets because the pulse has sufficient bandwidth to form a coherent superposition of states. Ultrashort pulses can produce a coherence of vibrational states and subsequently take a snapshot of the systems which have been moved far from the equilibrium.[67] Under these circumstances the molecular dynamics can be represented through quantum mechanical wave packets which can be described as superpositions of vibrational states and in analogy with classical optics, the wave packets can be visualised as superpositions of plane waves.[67]

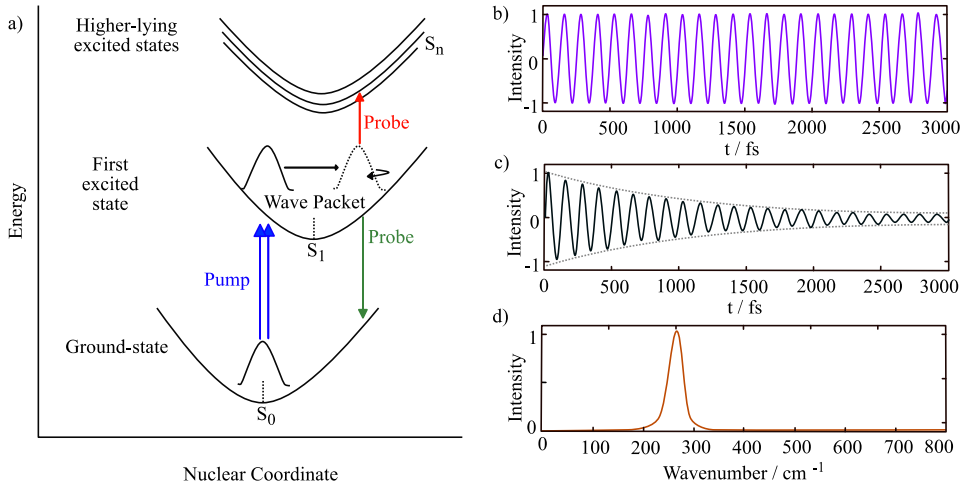

Figure 1.11 Wave packet transition. (a) The two light-matter interactions of the broadband pump excite a vibrational wave packet from the ground to the first excited state. The wave packet oscillates on the excited PES until a third light-matter interaction with the probe pulse occurs. The probe pulse is able to stimulate the transition of the wave packet, whether to a higher-lying potential or the ground state. (b) Signal undamped wave packet (ideal system), (c) damped oscillation via dephasing, and (d) the Fourier transform of the oscillatory signal.

Even though vibrational wave packets are quantum mechanical objects and show characteristic such as decoherence and interference, their motion can be often described with Newtonian dynamics. A typical example of wave packet generation is given by a molecule initially found in the vibrational ground state of the electronic ground state, after a certain time, the electronic state interacts with a short pulse (the quantum mechanics description assumes this pulse to be a delta function in time which can be approximated to a femtosecond pulse in real experiments), which promotes the initially equilibrated system into an excited state. In other words, the system starts from an incoherent superposition of states, the equilibrium is then altered by a broadband pulse (short pulse) and the system can be now described by a coherent superposition of states where the excitation carried out by

the short pulse is called FC excitation. The result of the coherent superposition is a wave packet in the excited state.

For a spatially localised wave packet an initial position can be roughly identified (roughly because of the uncertainty principle), the wave packet moves according to the gradient of the potential, and it can be described as a classical particle. After the generation of the wave packet in the first excited potential energy surface, it can interact with a probe pulse that interrogates the systems at specific time-delays which interferes constructively or destructively with the wave packet depending on the position of the wave packet in the PES. From this interaction the wave packet can be either promoted to higher-lying potential energy surfaces or the ground state as shown in Figure 1.11 (a) and in broadband transient absorption spectra it can be observed either on the excited state absorption (ESA) or stimulated emission regions (see Chapters 6 and 7).[68]

It is also worth noting that a short laser pulse can, in general, generate both the excited state and ground state wave packets. The formation of the ground state wave packet depends on a resonant Raman process, known as "resonant impulsive stimulated Raman scattering", and the resulting vibrational spectrum is identical to the molecular Raman spectrum.[69]

In an ideal system comprising of one normal mode the wave packet can last for an indefinite time (Figure 1.11 (b)), while in polyatomic condensed systems the coherent nuclear motions observed at early times are gradually damped, and they dephase due to processes such as coupling with the bath (Figure 1.11 (c)).[70] Through the Fourier transform of the damped oscillation excited state vibrational modes can be extracted since the vibrational

coherence detected preserves all spectral information of the excited state where the wave packet is generated and propagates (see Chapter 6 and 7).[70,71]

1.8 Conclusions

The sunlight incident on the Earth's surface initiates photochemical reactions that support and generate life on our planet. Therefore, the study of photochemistry and the characterisation of transitions states formed during photochemical reactions is significant for a better understanding of natural reactions such as photosynthesis, production of vitamin D and cis-trans isomerisation which drives primary events in vision.[3,4,13] Characterisation of the reaction intermediates can also be very useful while studying negative effects arising from sunlight absorption such as the formation of thymine dimers associated with skin cancer.[10] In the last three decades, a new chemistry field known as femtochemistry has been developed allowing the observation of transitions states and intermediates in real time which have encouraged the study of photochemical reaction offering additional insight into the dynamics of the system. Moreover, ultrafast experiments have revealed the formation of a coherent superposition of state associated to quantum beating signals in light harvesting complexes revealing the excited-state dynamics of biophysical and chemical systems.[64] In this thesis, the concept of femtosecond and the principles of femtochemistry will be used to characterise a dinucleotide formed by guanine and thymine to investigate the nature of the charge transfer state create upon photoexcitation. The solvation dynamics of a dye molecule in different solvents are also explored to compare the solute-solvent interactions in conventional and non-conventional solvents such as methanol and ionic liquids. The quantum coherence known as vibrational wave packet is also explored in a protein bound to chlorin e6 molecule and compared to "free" chlorin e6 to analyse the strength of this interaction.

References

1. Bowen, E. J. The Chemical Aspects of Light. *Oxford: Clarendon Press* (1946).

2. Cox E. A. & Kemp, T. J. Introductory photochemistry. *London: Chapman & Hall* (1972).

3. Rohatgi-Mukherjee, K. K. Fundamentals of Photochemistry *New Age International* (1978).

4. Wayne, R. P. Photochemistry London: Butterworth (1970).

5. Goody, R. M. & Yung, Y. L. Atmospheric radiation: Theoretical basis *Oxford University Press* (1964).

6. Frontier, S., Pichod-Viale, D., Lepretre, A., Davout, D. & Luczak, C. Écosystèmes : Structure, fonctionnement, evolution *Dunod* (1998).

7. Rosenfeld, T., Honig, B., Ottolenghi, M., Hurley, J. & Ebrey, T. G. Cis-trans isomerization in the photochemistry of vision. *Pure Appl. Chem.* **49**, 341–351 (1977).

8. Holick, M. F., MacLaughlin, J. A., Parrish, J. A. & Anderson, R. R. The Photochemistry and Photobiology of Vitamin D_3 *Plenum. Press, New York* 195–218 (1982)

9. Varghese, A. J. & Wang, S. Y. *cis-syn* Thymine Homodimer from Ultraviolet Irradiated Calf Thymus DNA *Nature* **213**, 909–910 (1967).

10. Varghese, A. J. & Wang, S. Y. Ultraviolet irradiation of DNA in vitro and in vivo produces a 3d thymine-derived product. *Science* **156**, 955–7 (1967).

11. Wang, S. Y.& Varghese, A. J. Cytosine-thymine addition product from DNA irradiated with ultraviolet light. *Biochem. Biophys. Res. Commun.* **29**, 543–549 (1967).

12. Wang, S. Y., Patrick, M. H., Varghese, A. J. & Rupert, S. C. Concerning the mechanism of formation of UV-induced thymine photoproduct in DNA. *Proc. Natl. Acad. Sci. USA* **57**, 465–472 (1967).

13. Albini, A. Photochemistry. *Springer* (2015).

14. Horspool, W. M. Synthetic Organic Photochemistry. *Springer* (1984).

15. Politano, F. & Oksdath-Mansilla, G. Light on the Horizon: Current Research and Future Perspective in Flow Photochemistry. Org. Process. Res. Dev., **22**, 1045-1062 (2018).

16. Yagci, Y., Jockusch, S. & Turro, N. J. Photoinitiated Polymerization: Advances, Challenges, and Opportunities. *Macromolecules* **43**, 6245–6260 (2010).

17. Smith, G. P. Chameleon in the sun: photochromic glass. *IEEE Spectrum* **3**, 39–47 (1966).

18. Ameta, S. C. & Ameta, R. Solar energy conversion and storage: photochemical modes. *CRC Press* (2016).

19. Schrödinger, E. An Undulatory Theory of the Mechanics of Atoms and Molecules. *Phys. Rev.* **28**, 1049–1070 (1926).

20. Born, M. & Oppenheimer, R. Zur Quantentheorie der Molekeln. *Ann. Phys. (Berl.)* **389**, 457–484 (1927).

21. Lewars, E. G. Computational Chemistry. *Springer* (2016).

22. Morse, P. M. Diatomic Molecules According to the Wave Mechanics. II. Vibrational Levels. *Phys. Rev.* **34**, 57–64 (1929).

23. Landau, L. D. & Lifshitz, E. M. Quantum Mechanics: non-relativistic theory. *Addidon-Wesley Pub. Co.* (1958).

24. 24. Maxwell, J. C. The Scientific Papers of James Clerk Maxwell (Vol. 1). *Dover Publication Inc.*(2013).

25. Einstein, A. & Infeld, L. The Evolution of Physics: The Growth of Ideas from the Early Concepts to Relativity and Quanta. *Cambridge University Press,* (1938).

26. Pauling, L. & Wilson, E. B. Introduction to quantum mechanics, with applications to chemistry. *London: McGraw-Hill publishing Co.*, (1935).

27. Heisenberg, W. Uber den anschaulichen Inhalt der quantentheoretischen Kinematik und Mechanik. *Z. Phys.* **43**, 172–198 (1927).

28. Stachel, J. J. The Collected Papers of Albert Einstein, *Princeton University Press* (1987).

29. Kuss-Petermann, M. & Wenger, O. S. Unusual distance dependences of electron transfer rates. *Phys. Chem. Chem. Phys.* **18**, 18657–64 (2016).

30. Condon, E. A Theory of Intensity Distribution in Band Systems. *Phys. Rev.* **28**, 1182–1201 (1926).

31. Franck, J. & Dymond, E. Elementary processes of photochemical reactions. *J Chem Soc. Faraday. Trans.* **21**, 536-542 (1926).

32. Condon, E. U. Nuclear Motions Associated with Electron Transitions in Diatomic Molecules. *Phys. Rev.* **32**, 858–872 (1928).

33. Alan D. McNaught & Andrew Wilkinson. IUPAC. Compendium of Chemical Terminology, (the "Gold Book"). *Blackwell Scientific Publication, Oxford* (1997).

34. Schlag, E. W., Schneider, S. & Fischer, S. F. Lifetimes in Excited state. *Annu Rev Phys. Chem.* **22**, 465–526 (1971).

35. Atkins, P & de Paula. J. Atkins' Physical Chemistry (Fourth edition) *Oxford University Press* (2005).

36. Förster, T., Fluoreszenz organischer Verbindungen. *Vendenhoeck Ruprecht* (1951).

37. Bixon, M. & Jortner, J. Intramolecular Radiationless Transitions. *J. Chem. Phys.* **48**, 715–726 (1968).

38. Kasha, M. Characterization of electronic transitions in complex molecules. *Discuss Faraday. Soc.* **9**, 14 -19 (1950).

39. Zewail, A. H. Femtochemistry. *Wiley-VCH* (2001).

40. Zewail, A. H. Femtochemistry. Past, present, and future. *Pure Appl. Chem.* **72**, 2219–2231 (2000).

41. Chenu, A. & Scholes, G. D. Coherence in energy transfer and photosynthesis. *Annu. Rev. Phys. Chem.* **66**, 69–96 (2014).

42. Zewail, A. H. Femtochemistry – Ultrafast Dynamics of the Chemical Bond (Vols. I and II) *World Scientific, New Jersey, Singapore* (1994).

43. Zewail, A. H. Laser selective chemistry: Is it possible? *Phys. Today* **33**, 2-8 (1980).

44. Zewail, A. H. Femtochemistry: Atomic-Scale Dynamics of the Chemical Bond Using Ultrafast Lasers (Nobel Lecture). *Angew. Chem. Int. Ed.* **39**, 2586–2631 (2000).

45. Zewail, A. H. Laser femtochemistry. *Science* **242,** 1645-1653 (1988).

47. El-Sayed, M. A., Tanaka, I. & Molin, Y. N. Ultrafast Processes in Chemistry and Biology – Chemistry for the 21st Century, *IUPAC, Blackwell Scientific, Oxford* (1994).

48. Manz, J. & Woste, L. Femtosecond Chemistry. *Wiley-VCH* (1995).

49. Chergui, M. Femtochemistry: Ultrafast chemical and physical processes in molecular systems. *World Scientific, Singapore* (1996).

50. Gaspard, P. & Burghardt, I. Chemical Reactions and Their Control on the Femtosecond Time Scale. *Wiley, New York* (1997).

51. Marcus, R. On the Theory of Oxidation-Reduction Reactions Involving Electron Transfer. I. *J. Chem. Phys.* **24**, 966–978 (1956).

52. Marcus, R. Electrostatic Free Energy and Other Properties of States Having Nonequilibrium Polarization. I. *J. Chem. Phys.* **24**, 979–989 (1956).

53. Marcus, R. On the Theory of Oxidation-Reduction Reactions Involving Electron Transfer. II. Applications to Data on the Rates of Isotopic Exchange Reactions. *J. Chem. Phys.* **26**, 867–871 (1957).

54. Arrhenius, S. Über die Dissociationswärme und den Einfluss der Temperatur auf den Dissociationsgrad der Elektrolyte. *Z. Phys. Chem.*, **1,** 96–116 (1889).

55. Marcus, R. A. & Sutin, N. Electron transfers in chemistry and biology. *Biochim. Biophys. Acta* **811**, 265–322 (1985).

56. Closs, G. L. & Miller, J. R. Intramolecular Long-Distance Electron Transfer in Organic Molecules. *Science* **240**, 440–447 (1988).

57. Fox, L. S., Kozik, M., Winkler, J. R. & Gray, H. B. Gaussian Free-Energy Dependence of Electron-Transfer Rates in Iridium Complexes. *Science* **247**, 1069–1071 (1990).

58. Rehm, D. & Weller, A. Kinetics of Fluorescence Quenching by Electron and H-Atom Transfer. *Isr. J. Chem.* **8**, 259–271 (1970).

59. Miller, J. R., Calcaterra, L. T, & Closs, G. L., Intramolecular long-distance electron transfer in radical anions. The effects of free energy and solvent on the reaction rates. *J. Am. Chem. Soc.***106**, 3047-3049 (1984).

60. Marcus, R. A. Electron transfer reactions in chemistry. Theory and experiment. *Rev. Mod. Phys.* **65**, 599–610 (1993).

61. Főrster, T. 10th Spiers Memorial Lecture. Transfer mechanisms of electronic excitation. *Discuss. Faraday Soc.* **27**, 7–17 (1959).

62. Förster, T. Zwischenmolekulare Energiewanderung und Fluoreszenz. *Ann. Phys. (Berl)* **437**, 55–75 (1948).

63. Bagchi, B. & Jana, B. Solvation dynamics in dipolar liquids. *Chem. Soc. Rev.* **39**, 1936-1954 (2010).

64. Fleming, G. R. & Cho, M. Chromophore-Solvent Dynamics. *Annu. Rev. Phys. Chem.* **47**, 109–134 (1996).

65. Chandra, A. & Bagchi, B. Molecular theory of solvation and solvation dynamics in a binary dipolar liquid. *J. Chem. Phys.* **94**, 8367–8377 (1991).

66. Arzhantsev, S., Ito, N., Heitz, M. & Maroncelli, M. Solvation dynamics of coumarin 153 in several classes of ionic liquids: cation dependence of the ultrafast component. *Chem. Phys. Lett.* **381**, 278–286 (2003).

67. Garraway, B. M. & Suominen, K. A. Wave packet dynamics in molecules. *Contemp. Phys.* **43**, 97–114 (2002).

68. McClure, S. D., Turner, D. B., Arpin, P. C., Mirkovic, T. & Scholes, G. D. Coherent Oscillations in the PC577 Cryptophyte Antenna Occur in the Excited Electronic State. *J. Phys. Chem. B* **118**, 1296–1308 (2014).

69. Pollard, W. T., Dexheimer, S. L., Wang, Q., Peteanu, L. A., Shank, C. V. & Methies, R. A. Theory of dynamic absorption spectroscopy of nonstationary states. 4. Application to 12-fs resonant impulsive Raman spectroscopy of bacteriorhodopsin. *The J. Phys. Chem.* **96**, 6147–6158 (1992).

70. Rafiq, S. & Scholes, G. D. Slow Intramolecular Vibrational Relaxation Leads to Long-Lived Excited state Wave packets. *J. Phys. Chem. A* **120**, 6792–6799 (2016).

71. Dean, J. C. Rafiq, S., Oblinsky, D. G., Cassette, E., Jumper, C. C.& Scholes G. D. Broadband Transient Absorption and Two-Dimensional Electronic Spectroscopy of Methylene Blue. *J. Phys. Chem. A* **119**, 9098–9108 (2015).

Chapter 2

Theoretical Framework for Nonlinear Spectroscopy

2.1 Introduction

When one or more input fields interact with the dipoles of the matter (the sample), a macroscopic response, the so-called polarization (P), is generated.[1] The polarization is a microscopic collective dipole moment and acts as a source to new frequency components. Therefore, it is a source to radiate a new electromagnetic field that, in coherent spectroscopy, is detected along a well-defined direction. Understanding the relationship between the light-induced polarization and the microscopic properties of a quantum mechanical system is the main aim of non-linear spectroscopies. In this field, ultrafast techniques are established tools to study condensed-phase systems and their dynamics.[2] Theoretical discussions about the interaction between the electric field and the polarization have been studied classically and quantum mechanically, and Mukamel has given the principles of nonlinear optical spectroscopy.[2] Moreover, theoretical discussion about multidimensional femtosecond spectroscopy, photon echo spectroscopy, and heterodyne detection have been reported by the groups of Fleming,[3–9] Mukamel,[2,10–12] Tokmakoff,[1,13] and Joffre[14,15] while two-dimensional electronic spectroscopy (2DES) was first theoretically explained by Jonas.[16] Therefore, the aim of this chapter is not to report the complete development of the theory of time-dependent quantum mechanics and multidimensional electronic spectroscopy, but to present the key points of the well-established theory relevant for this thesis.

2.2 Principles of Time-Dependent Quantum Mechanics

2.2.1 The Density Matrix

In quantum mechanics, when describing a quantum system, a state vector $|\psi(t)\rangle$ (ket) can be used to indicate the so-called pure state or wavefunction. However, a real system could also be found in an ensemble of different state vectors where, for example, the system has X% probability to be found in $|\psi_1(t)\rangle$ and Y% probability to be found in $|\psi_2(t)\rangle$. Under such conditions, the system is said to be in a mixed state, and the wavefunction representation can be substituted with the density matrix or density operator. The density matrix is particularly useful in treating mixed states, considered that both quantum states, pure and mixed, can be described by a single density operator[17,18] which is defined as the outer product of the wavefunction (ψ) with its conjugate:

$$\rho(t) = |\psi(t)\rangle\langle\psi(t)|. \tag{2.1}$$

Note that in quantum mechanics, the ket $|\psi(t)\rangle$ and bra $\langle\psi(t)|$ (complex conjugate) notation (or Dirac notation) is a common notation to describe quantum states.[19] Equation 2.1 implies that the density matrix represents the probability density, which in classical physics is expressed as a probability distribution. In other words, given a classical observable Z, the density matrix plays the role of its probability distribution and, in the quantum case, the expectation value of the measurement can be expressed as:

$$\langle Z\rangle = \langle\psi(t)|\,\hat{Z}\,|\psi(t)\rangle = \mathrm{Tr}\,[\hat{Z}\,\hat{\rho}]. \tag{2.2}$$

where $\hat{Z}$ is the linear operator (the operators are usually indicated by a "hat"), $\langle Z\rangle$ is the expectation value that corresponds to the mean value calculated as the average measurement of an observable (the angle brackets ($\langle\ \rangle$) are used to indicate the mean value). The bra/ket notation is used to give the $\langle\psi(t)|\,\hat{Z}\,|\psi(t)\rangle$ expression, which stands for the expectation values of the observable. The term "Tr" that denotes the trace of the matrix is

given by the two operators, $\hat{Z}$, and $\hat{\rho}$, where the square brackets are used to denote the commutator*. Therefore, equation 2.2 is the expectation value (or mean) of the observable represented by operator $\hat{Z}$ for the system in state $|\psi\ (t)\rangle$.[1]

2.2.2 Information in the Density Matrix

Pure and mixed states can be described using the density matrix, and the primary information obtained from this operator is given by the diagonal and off-diagonal elements.[2,20]

The diagonal elements (n = m) are the so-called population terms and, they represent the probability of occupying a pure quantum state:

$$\rho_{nn} = c_n\, c_n^* = p_n \geq 0 \tag{2.3}$$

while the complex off-diagonal elements are known as coherence terms, and they are characterised by an oscillatory factor, as shown in the following equation:

$$\rho_{nm} = c_n(t)\, c_m^*(t) = c_n\, c_m^*\, e^{-i\omega_{nm}t} \tag{2.4}$$

Therefore, the density matrix provides information about the purity of a quantum state, *e.g.*, for pure state Tr (ρ^2) =1 or <1 for mixed states.

2.2.3 Time-Evolution of the Density Matrix

In quantum mechanics the time evolution of a quantum state is described by the time-dependent Schrödinger equation (TDSE):

$$i\hbar\, \frac{\partial}{\partial t}|\Psi\ (t)\rangle = \hat{H}\, |\Psi\ (t)\rangle \tag{2.5}$$

*A commutator for two general elements p and q is defined as: [p, q] = pq -qp, and p and q only commute if the result is zero.

where “i” is the imaginary unit, ħ is h/2π (h is Planck’s constant), $\hat{H}$ is the Hamiltonian operator (operator of the energies of the system), Ψ is the state vector of the quantum system, and “t” is time.

The combination of the TDSE (equation 2.5) and the definition of ρ (equation 2.1) yields the equation of motion of the density matrix (see the appendix 2.1 for the derivation):

$$\frac{\partial \rho}{\partial t} = -\frac{i}{\hbar}[\hat{H}, \hat{\rho}] \tag{2.6}$$

where the terms in the equation have already been defined, and the brackets indicate the commutator, as seen for equation 2.2. Equation 2.6 is the Liouville-Von Neumann equation, and it is a basic tool used to treat the transition between a pure and a mixed state. This equation describes the time evolution of the density operator as the time-dependent Schrödinger equation (equation 2.5) represents the time evolution of pure quantum states.[21]

2.2.4 Liouville-von Neumann Equation

The mathematical description of experiments carried out in spectroscopy, and the calculation of the parameter that contains the dynamics information (polarization) of the system can be given by the solution of the Liouville-von Neumann equation.[2,20,21]

For a system initially found in thermal equilibrium that weakly interacts with an external agent A(t) that drives the system far from the equilibrium, the solution of equation 2.6 (note that this is a general case where the Hamiltonian is replaced by the operator A) can be obtained by integrating equation 2.6. Subsequently, a perturbation series can be found by substituting the density matrix calculated at a certain time t into itself (see appendix 2.2 for the equations) and, compactly, the density matrix reads:

$$\rho_I(t) = \rho^{(0)} + \rho^{(1)} + \rho^{(2)} + ... + \rho^{(n)} + ... \qquad (2.7)$$

which states that the time-dependent density matrix is equal to the sum of the density matrices obtained from time zero ($\rho^{(0)} = \rho(t_0)$) to its nth-order expansion $\rho^{(n)}$.

Furthermore, the n-th order term of the equation is proportional to the polarization observed in an nth order spectroscopy, *i.e.*, third-order spectroscopies depend on $\rho^{(3)}$. This description of the density matrix is only valid if the problem is solved using the interaction picture. The picture mentioned above is a hybrid description of the system that consists of an intermediate representation between the so-called Schrödinger and Heisenberg pictures. In the Schrödinger picture, the state vector evolves in time, and the operators are constant, on the contrary, the Heisenberg description incorporates time-dependent operators, but the state vectors are time-independent. In the interaction picture, both the operator and the state vector partially describe the time dependence of the observable. Generally speaking, the interaction picture is particularly useful when describing changes in the wavefunction and observables resulting from interactions (for example a quantum state that interacts with an external electric field).[19,22,23]

The extended way of calculating equation 2.7 can be simplified by using a super operator $\hat{\hat{\hat{G}}}$ (or Green's operator). It can be introduced to describe the perturbation series and the n-th order term of Equation 2.7 as follows:

$$\rho_I^{(n)}(t) = \left(-\frac{i}{\hbar}\right)^n \int_{t_0}^{t} dt_n \int_{t_0}^{t_n} dt_{n-1} \ldots \qquad (2.8)$$

$$\ldots \int_{t_0}^{t_2} \hat{\hat{\hat{G}}}(t-t_n)\, \hat{A}(t_n)\, \hat{\hat{\hat{G}}}(t_n-t_{n-1})\, \hat{A}(t_{n-1}) \ldots \hat{\hat{\hat{G}}}(t_2-t_1)\, \hat{A}(t_1) \rho_0\, dt_1$$

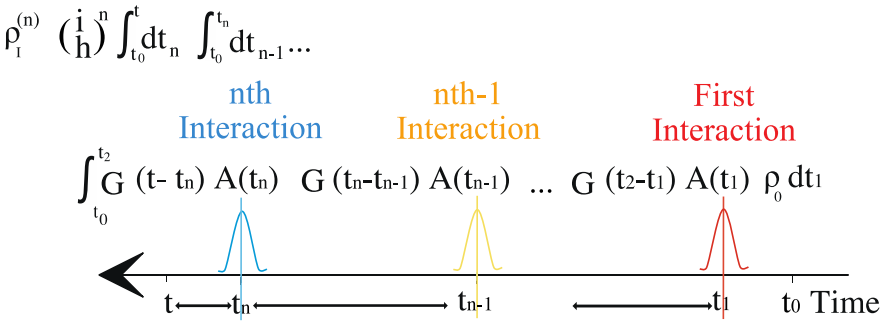

Figure 2.1 Physical representation of equation 2.8. The equation is more clearly understood if reading it from right to left.

Figure 2.1 shows a graphical representation of equation 2.8 and should be read from right to left, as follows: the system is initially in thermal equilibrium (ρ_0) until $t = t_1$ where $A(t_1)$ perturbs the system (the first interaction takes place); subsequently, the system evolves until the next interaction that occurs at $t = t_2$ when $A(t_2)$ introduces a second perturbation. The sequence proceeds until the n-th interaction, and that causes the system to evolve until the observation at time, t.[1]

2.2.5 Response Function

The response function formalism creates a link between the classically treated electric field ($\underline{\mathcal{E}}(t)$) and the system's dynamics (and properties) that are described through quantum mechanics. It is important to incorporate into the density matrix formalism the dependence on the external electric field explicitly, where the general external agent A can be identified as the interaction between the quantum system and the electromagnetic field with $A(t) = \mathcal{E}(t)\ \hat{\mu}\ (t)$ (note that the vectoral nature of the electric field is omitted to simplify the following formalism).[25,26] Therefore, the external agent is the product between the external electric field and the dipole operator ($\hat{\mu}(t)$) of the species that absorbs the radiation. This operator is time-dependent in the interaction picture, and it is a function of the electronic

transition dipole moment as reported by Mukamel.[24,25] Under such assumption, equation 2.8 can be re-written as:

$$\rho_I^{(n)}=\left(-\frac{i}{\hbar}\right)^n \int_0^\infty dt_n \int_0^\infty dt_{n-1}.. \int_0^\infty \hat{\hat{G}}(t_n,t_{n-1},...,t_1) \tag{2.9}$$

$$\times \hat{\mu}(t_{n-1}+\ldots+t_1)\ldots\hat{\mu}(t_1)\,\hat{\mu}(0)\,\rho(-\infty)$$

$$\times \mathcal{E}(t-t_n)\,\mathcal{E}(t-t_n-t_{n-1})...\mathcal{E}(t-t_n-t_{n-1}-\ldots-t_1)\,dt_1$$

where the observation time is taken as $t\rightarrow\infty$, and the n-th term of the density matrix is expressed as a function of the super operator $\hat{\hat{G}}$ (this approach is usually referred to as super operator of nonequilibrium system).[27]

To obtain the response function from equation 2.9, it is helpful to calculate the polarization at a given time t which has been demonstrated[25] to be given by the expectation value of the dipole operator $\hat{\mu}$ and (recalling equation 2.2) it reads:

$$\langle P(t)\rangle=\mathrm{Tr}\,[\hat{\mu}\,\hat{\rho}] \tag{2.10}$$

Thus, the n-th order polarization can be written as follows:[25]

$$P^{(n)}(t) = \int_0^\infty dt_1 \int_0^\infty dt_2 \ldots \int_0^\infty R^n(t_n,t_{n-1},...,t_1) \tag{2.11}$$

$$\times \mathcal{E}(t-t_n)\,\mathcal{E}(t-t_n-t_{n-1})...\mathcal{E}(t-t_n-t_{n-1}-...-t_1)\,dt_n$$

where $R^n(t_n,t_{n-1},...,t_1)$[5,8] is the n-th order nonlinear response function, which is directly proportional to the polarization and includes all relevant microscopic information about the system studied. More specifically, the n-th order response function can be expressed as:

$$R^n(t_n,t_{n-1},...,t_1) = \left(-\frac{i}{\hbar}\right)^n \langle\mu|\hat{\hat{G}}(t_n,t_{n-1},...,t_1)\hat{\mu}(t_{n-1},\ldots,t_1)\ldots\hat{\mu}(t_1)\,\hat{\mu}(0)|\rho(-\infty)\rangle \tag{2.12}$$

Where equation 2.12 shows that the response function is a real quantity,[2,9] and it describes how the matter responds to the applied field containing all the microscopic information of the studied system. Equations 2.9, 2.11 and 2.12 show that the nonequilibrium behaviour

is strongly related to the evolution of the system and depends on its full history, from the application of the electric field to the final observation.[2] Moreover, when studying the response function, one needs to take into account its three properties: causality, stationary properties and impulse response.[2]

Causality states that the system cannot respond before the application of the external agent, while the stationary principle is related to the observed response of the object studied. This response to the applied agent is a convolution of the time-development of the external field and the response of the surrounding environment. The stationary principle also states that the time dependence of the systems is only related to the time intervals between the applied external agents. Therefore, it is possible to define a time-interval $\tau = t\text{-}t_0$ where t and t_0 are the times when the system is observed and when the field is applied, respectively. The time-interval τ, also known as interaction time, is commonly used when deriving the response function in multidimensional spectroscopy.[9,25] However, the full and exact derivation of the response function goes beyond the scope of this thesis, and it has already been extensively reviewed before by Mukamel,[2,25] Tomakoff,[1] and Cho.[3]

The last property is known as the impulsive response, and it is related to the shape of the response function. When a perturbation interacts with the medium, it generates an impulsive response from the system that is driven away from the equilibrium. The shape of the response function will then start from zero, evolve, and then return to zero. From the evolution of the response function is clear that it can be treated as a combination of sine functions and it can be described through a Fourier analysis that includes the complete microscopic information which is indispensable to calculate the signal arising from nonlinear polarizations such as pump-probe signals.[25]

2.3 Time-Resolved Experiments

2.3.1 Third Order Polarization and Response Function

The relationship between the response function and the polarization (see equation 2.11) is a key aspect to understand and interpret results obtained using nonlinear spectroscopies, such as two-dimensional electronic spectroscopy. It is well established, even-order polarizations vanish in isotropic media,[2,28] and for a system of dilute and non-interacting molecules, the radiated field can be described using the third-order nonlinear polarization, $P^{(3)}(t)$.[2,5,28] Thus, equation 2.11 can be shown through the real quantities, the third-order response function, R^3, and the external electric field $\mathcal{E}(t)$ interacting with the system multiple times at specific time-delays:

$$P^{(3)}(t)= \int_0^\infty dt_3 \int_0^\infty dt_2 \int_0^\infty dt_1 \, R^3(t_3, t_2, t_1) \qquad (2.13)$$

$$\times \mathcal{E}(t - t_3)\, \mathcal{E}(t - t_3 - t_2)\, \mathcal{E}(t - t_3 - t_2 - t_1)$$

where the relationship between the third-order nonlinear polarization and the response function is well established. For different combinations of pulses, some of the terms in the third-order polarization will contain sums and differences of electronic transitions frequencies. Moreover, the sums of electronic transitions are highly oscillatory, and after time integration, they reveal a minimal contribution to the total signal; therefore, they can be neglected. This approximation is known as rotating wave approximation (RWA), and it is commonly used to calculate the individual terms of the response function.[2,9]

$R^3(t_1, t_2, t_3)$ can be calculated from the Liouville equation (equation 2.6) by expanding the density matrix (equation 2.12). This expansion, in combination with the RWA, reveals eight basic terms of the response function corresponding to the so-called Liouville space pathways and from where the dynamical contribution to the signal or molecular nonlinear

response functions can be derived.[2,9] As first reported by Mukamel *et al.*[24,25] and later by Cho *et al.*,[5] in a system which is initially in thermal equilibrium with a ground state density matrix expressed by ρ_{gg}, the nonlinear response function is composed of eight terms four of which give a contribution to the molecular nonlinear response function and the other four are their complex conjugate. The relevant four terms can be written as the trace (Tr) over all degrees of freedom considering both the solvent and the solute, and they read:

$$R_1(t_3, t_2, t_1)=Tr\,[\hat{\hat{G}}_{eg}(t_3)\,\hat{\hat{G}}_{gg}(t_2)\,\hat{\hat{G}}_{eg}(t_1)\,\rho_{gg}], \tag{2.14}$$

$$R_2(t_3, t_2, t_1)=Tr\,[\hat{\hat{G}}_{eg}(t_3)\,\hat{\hat{G}}_{ee}(t_2)\,\hat{\hat{G}}_{ge}(t_1)\,\rho_{gg}],$$

$$R_3(t_3, t_2, t_1)=Tr\,[\hat{\hat{G}}_{eg}(t_3)\,\hat{\hat{G}}_{gg}(t_2)\,\hat{\hat{G}}_{ge}(t_1)\,\rho_{gg}],$$

$$R_4(t_3, t_2, t_1)=Tr\,[\hat{\hat{G}}_{eg}(t_3)\,\hat{\hat{G}}_{ee}(t_2)\,\hat{\hat{G}}_{eg}(t_1)\,\rho_{gg}].$$

where $\hat{\hat{G}}_{mn}(t)$ is the aforementioned super operator (or Liouville-space Green's function) that describes the nuclear degrees of freedom of the all system (solute + solvent) both for the ground (g) and excited (e) electronic states. From this derivation one can deduce that information about multi-level molecular processes and solvation dynamics are contained with the nonlinear polarization and they can be studied with multidimensional spectroscopies.[5,9]

An electric field can be expressed in terms of its amplitude (E_0), carrier frequency (ω) and wave vector ($\underline{k}$), such as $\mathcal{E}(\underline{r}, t) = E_0 \exp(i\underline{k}\underline{r} - i\omega t)$. Hence, the third-order nonlinear polarization signal can be written as:[5,9]

$$P^{(3)}(t) = \sum_S P(\underline{k}_s, t)\, e^{(i\underline{k}_s\underline{r} - i\omega_s t)} + c.c \tag{2.15}$$

where the frequency (ω_s) and the wavevector ($\underline{k}_s$) of the polarization (signal, see subscript s) depend on the incident fields in such a way that $\omega_s = \pm\omega_1 \pm \omega_2 \pm \omega_3$ and $\underline{k}_s = \pm \underline{k}_1 \pm \underline{k}_2 \pm$

$\underline{k}_3$. These two relationships enforce the energy (frequency) and momentum (wave vector) conservation. In essence, the oscillatory polarization shown in equation 2.15 generates a coherent signal field in a direction given by $\underline{k}_s$ at the emitted signal frequency equal to ω_s. Thus, the various experimental techniques depending on the third-order polarization, such as photon echo (PE), transient-grating pump-probe spectroscopies and multidimensional spectroscopies arise from the different combination of the wave vectors and the precise timing of the driving pulses.[2,5,6,8,16,29]

2.3.2 Photon Echo and Two-Dimensional Electronic Spectroscopy

Two pulses photon echo studies were first reported in 1964 by Kurint *et. al*.[30] It was observed that two crossed-beams, time-delayed, and incident upon a sample could generate an optical signal in a well-defined spatial direction compared to the input pulses with an intensity proportional to the time delay between the two beams. This signal was called photon echo in analogy with the well-known spin echo. Subsequently, more advanced experiments were implemented, such as the 3-pulse photon echo, which became a commonly applied technique.[6] Thus, a typical photon echo experiment consists of three pulses characterised by three different wave vectors and frequencies.[5,6,31] These pulses are separated by time-delays t_1, t_2, and t_3 where t_1 is the time delay between the first and second pulse, t_2 between the second and third while t_3 between the third and the echo signal, (as shown in Figure 2.2 (a)). Note that the aforementioned delay times are also reported in the literature as τ, T, and t, which correspond to t_1, t_2, and t_3, respectively. In a photon echo experiment, the detected fourth field has a wave vector: $\underline{k}_s = -\underline{k}_1 + \underline{k}_2 + \underline{k}_3$ (rephasing) and $\underline{k}_s = \underline{k}_1 - \underline{k}_2 + \underline{k}_3$ (non-rephasing) generated at time t_3.[5]

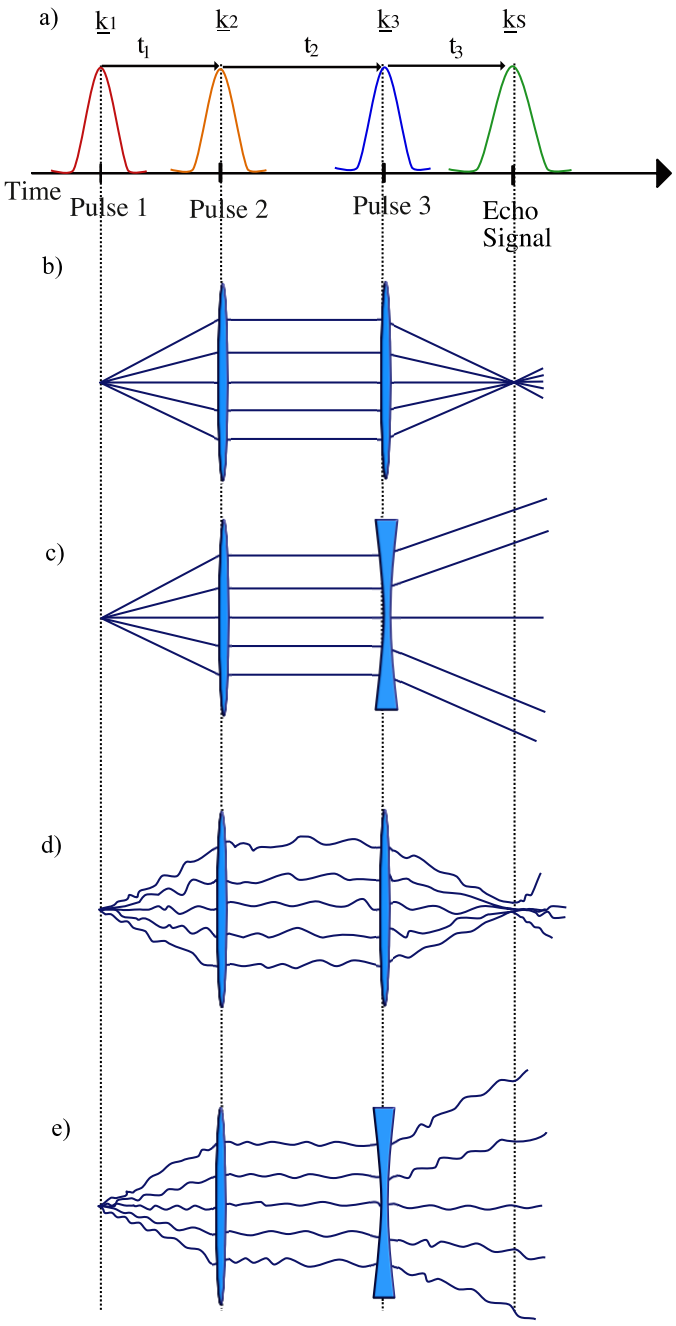

Figure 2.2 (a) Pulse sequence used in photon echo experiments. Three pulses photon echo ray optics analogy for a system not interacting with the bath, in the case of (b) rephasing and (c) non-rephasing signals. (d) Rephasing and (e) non-rephasing signals for a system interacting with the environment.

The critical aspects of a three-pulses photon echo experiment can be elucidated through an analogy to ray optics as reported by Fleming[6] (see Figure 2.2 (b), (c), (d) and d(e)). When

the first pulse interacts with the system, it generates a superposition between two electronic states. This superposition is known as coherence and t_1 as coherence time. Thus, the coherence evolves depending on its oscillatory component (see equation 2.4), which is a function of the energy difference between the ground and excited quantum states involved in the transition. Over the coherence time, the electronic phase factor associated with the systems evolves linearly, and the inhomogeneity of the system determines the slope. For a system comprising n molecules, there will be n-lines, and each of them will be characterised by different slopes starting from a common value, which is the one created by the first pulse (Figure 2.2 (b) and (c)). The interaction between the system and the second pulse generates a population given by the diagonal elements of the density matrix (equation 2.3) and because of the energy difference between the quantum level involved in this step is zero, the phase does not change during t_2 (the waiting time). The third pulse generates a second coherence (off-diagonal elements of the density matrix), which has the opposite sign compared to the first coherence generated. The final interaction either focuses the rays at time t_3 (echo time), which in photon echo is equal to the duration of the first-time interaction ($t_1 = t_3$ or $\tau = t$) and, the refocused beams are detected as a photon echo signal as shown in Figure 2.2 (b) or acts as a concave lens diverging the rays as depicted in Figure 2.2 (c). In this case (no-spectral diffusion) the rephasing signal will always be more intense than the non-rephasing at the detector.

The description above of a photon echo generation is valid for ideal systems, systems where the interaction with the bath is not considered (no spectral diffusion). Figure 2.2 (d) and (e) refer to the situation where the interactions between the solute and the solvent can alter the transition frequencies of the molecule. Processes in solution known as dephasing modify the slope of the electronic phase factor during t_1 and t_3, while fluctuation in the

inhomogeneous distribution known as spectral diffusion mainly manifests during the waiting time t_2. Thus, the disruption of the smooth electronic phase observed for the ideal system during t_2, t_1 and t_3 generates a loss of refocusing ability that leads to a decrease of the echo signal intensity but also to the ability to detect the spectral diffusion, Figure 2.2 (c). Therefore, when the spectral diffusion is strong the two signals, rephasing and non-rephasing will start to look the same at the detector. From the analogy with the optical rays, the photon echo experiment is a measure of the memory of the system depending on the transition frequency that is involved when the system is first excited.

Generally speaking, in photon echo experiments, the so-called rephasing signals can be selected and studied to investigate the line broadening mechanisms and the spectral diffusion of the system. This rephasing signal arises from the R_2 and R_3 (equation 2.14) terms that have the property of time-reversal, where the phase acquired during t_1 is reversed in t_3, as demonstrated by Mukamel[2,25] and reported in detail by Tokmakoff.[1] At this point, it is also worth noting that the other two Liouville pathways shown in equation 2.14 (R_1 and R_4) are known as non-rephasing contributions, and they differ from the rephasing terms because the phase during t_3 does not reverse the phase acquisition in t_1. The non-rephasing terms correspond to the free induction decay (FID) signal.

Moreover, it has been demonstrated [2,25] that the four Liouville pathways can be expressed in terms of momentum conservation where (in a two-level system) the two rephasing terms R_2 and R_3 have the signal vector, $\underline{k}_s$ ($\underline{k}_s = -\underline{k}_1 + \underline{k}_2 + \underline{k}_3$) therefore, they propagate along the same direction. However, these two terms evolve in different states during the waiting time (t_2), with R_2 propagating in the excited state and R_3 in the ground state. Comparably, the other two terms R_1 and R_4 (non-rephasing), are generated with the same wave vector and

propagate along the direction defined by $\underline{k}_s$ =+ $\underline{k}_1$ - $\underline{k}_2$ + $\underline{k}_3$. However, they are related to different states during t_2, with R_1 evolving in the ground and R_4 in the excited state.[1] A diagram showing the spatially separated rephasing and non-rephasing signals generated in a photon echo experiment is given in Figure 2.3.

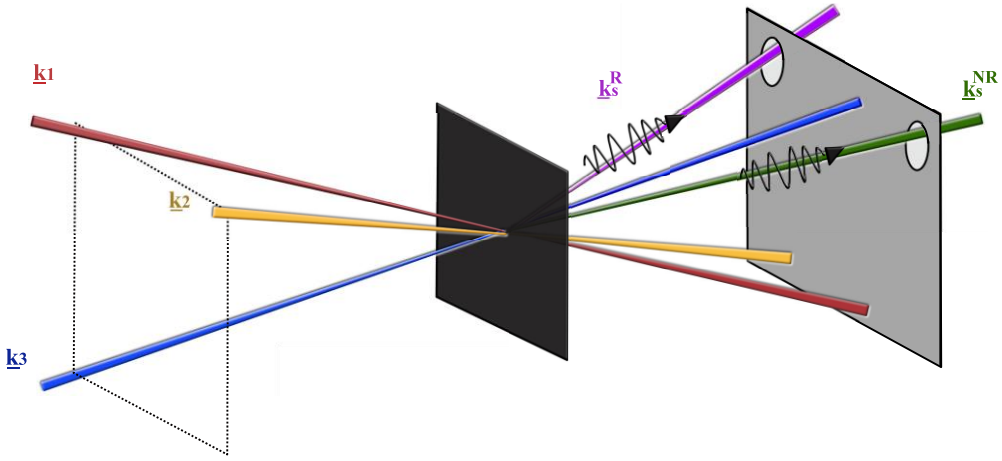

Figure 2.3 Diagram showing the spatially separated rephasing (R) and non-rephasing (NR) signals arising from a 3 pulse photon echo experiment.

The rephasing (photon echo) and non-rephasing (FID) signals are fundamental concepts when describing a two-dimensional (2D) experiment considering that the sum over these two signals corresponds to the total two-dimensional frequency-resolved photon echo signal which can be visualised as a frequency-frequency correlation map of the absorption and final emission of the system.[16] Two-dimensional electronic spectroscopy has been proven to be a powerful tool that allows the observation of several properties of the system, such as population transfer, coherent superposition of electronic states and electronic coupling.[32]

Like photon echo experiments, the excitation fields used in a 2DES experiment are three time-delayed identical pulses propagating along different directions.[9] 2DES experiments can be implemented using different geometries (see Chapter 5) for example, the

noncollinear "boxcar" geometry.[9] The noncollinear geometry does not only increase the signal-to-noise ratio compared to other 2DES configurations,[33] but it also allows to select the signal radiation which is produced into a specific spatial direction. Under such conditions, the third-order polarization can be written as a sum of response functions known as S_R and S_{NR}, which correspond to the total signal of the two-dimensional experiment.[9] However, the rephasing and non-rephasing signals are generated along two separate directions (see Figure 2.3), and experimentally, the detection of two signals spatially separated could be challenging to implement, requiring either a continuous motion of the detector or two matched array detectors (as usually implemented in photon echo spectroscopy). To overcome this issue, it has been demonstrated that in 2DES, the time ordering of the pulses can be set in such a way that means the rephasing and non-rephasing signals can be independently detected along the same direction[9,16,34] as it will be explained in Chapter 5.

2.3.3 Heterodyne Detection

To characterise the weak signal field emitted from samples in 2DES, a high sensitivity detection technique such as spectral interferometry is required.[9,15,16] In two-dimensional experiments, such as 2DES implemented as boxcar geometry, the enhancement of the weak signal field can be achieved through interference with a reference pulse, the so-called local oscillator (LO).[9,15,16] This enhancement is usually achieved by heterodyne detection, where the signal field $\mathcal{E}_s$ interacts with a well-characterised reference field, $\mathcal{E}_{LO}$, which is temporally separated (delayed) compared to the other three pulses, as shown in Figure 2.4. The LO used for heterodyne detection is attenuated compared to the other three incident fields ensuring that it does not interfere with the response of the system.[9]

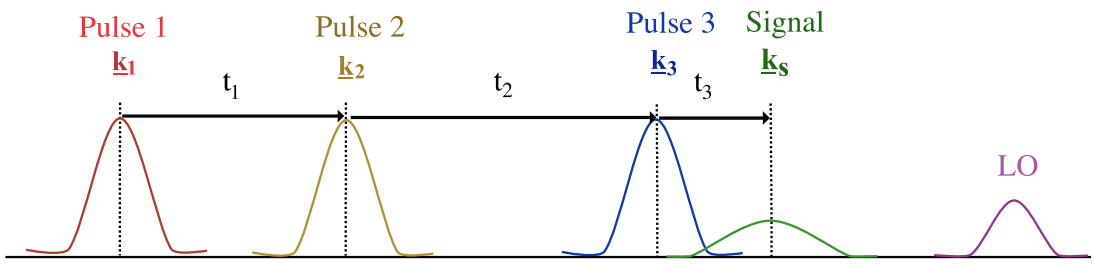

Figure 2.4 Pulse-sequence and time variables in the 2DES experiment implemented with heterodyned detection.

In a 2DES experiment, a spectrometer detects the interference between two pulses, which is collected as intensity, and the signal detected can be manipulated through Fourier transform (FT) analysis in the time domain (see appendix for the definition of FT) to obtain the signal amplitude and phase[7]. Note that while for 2DES is possible to retrieve the phase, in 3 pulse photon echo measurements, it was almost impossible. The heterodyned signal acquired in the two-dimensional electronic spectroscopy (S) is given by:

$$S = |\mathcal{E}_s + \mathcal{E}_{LO}|^2 \tag{2.16}$$

where equation 2.16 will be used in Chapter 5 to obtain the 2DES signal in the section "data analysis".

2.4 Frequency-Frequency Correlation Function and Lineshape

To understand the spectra obtained from 2D experiments, it is now necessary to introduce two new concepts, the correlation function and the relationship with the spectral lineshape. The correlation function is a powerful tool to describe the dynamics of an internal variable of a system in thermal equilibrium, and it is used to study randomly determined (stochastic) and irreversible processes in the condensed phase. These processes are not always completely and entirely random, but they depend on the time-dependent interaction between the molecules and the surrounding environment (the bath).[11]

The time-dependent correlation function provides information about how long a specific property can last before it vanishes, and it is defined as the average (shown by angled brackets) between a time-dependent quantity multiplied by the quantity at a particular time delay. The specific correlation function that relates the central frequency associated with an electronic transition is the so-called frequency-frequency correlation function (FFCF), and it is defined as follow:

$$C_{\delta\omega\delta\omega}(0, t)=\langle\delta\omega(t)\ \delta\omega(0)\rangle \propto e^{-\frac{t}{\tau_C}} \tag{2.17}$$

where $\delta\omega$ is the random fluctuation in frequency at time zero and time t, with $t > 0$, and τ_c is the so-called correlation time, which indicates the time scale associated with the random fluctuations. The FFCF gives information about the optical frequencies investigated and their evolution in time is influenced by changes in the molecular structure or interaction with the surrounding fluctuating environment (solvent or protein).[35,36]

Furthermore, the correlation time is also related to the lineshape g(t). This property conveys information about the interaction between the solute and solvent (solvation dynamics, just for excited state) and it can be expressed as:[1,2,35]

$$g(t) \propto \tau_C^2 \left(e^{-\frac{t}{\tau_C}} + \frac{t}{\tau_C} - 1 \right) \tag{2.18}$$

therefore, from the relationship between t and the correlation time, two opposite scenarios can be defined.[1]

For a short correlation time ($t >> \tau_c$), the lineshape is dynamical, and the line width depends on the rapid frequency or phase variation of both dipoles. The result of this homogeneous broadening is a dynamically broadened lineshape characterised by a narrower linewidth

compared to the distribution of frequencies available. The total lineshape is a Lorentzian function (Figure 2.5 (a)).

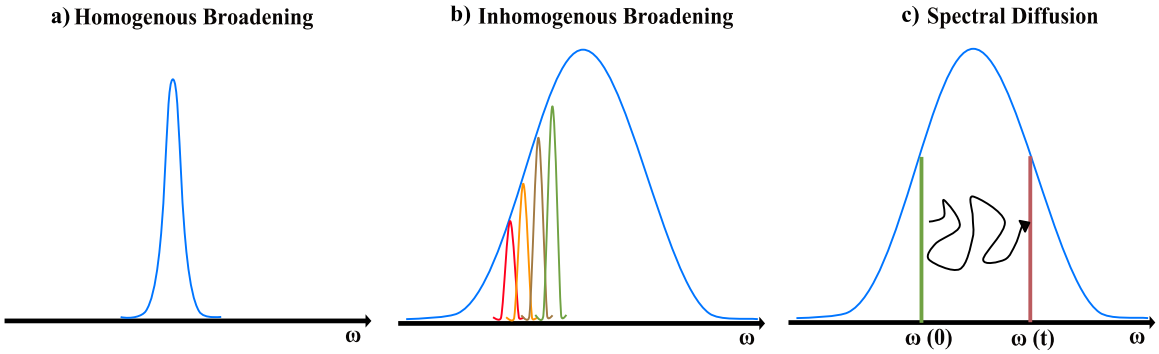

Figure 2.5 Illustration of (a) homogenous broadening, (b) inhomogeneous broadening, and (c) spectral diffusion.

When the correlation time is long ($t << \tau_c$), the lineshape of the spectrum is determined by a static distribution of different resonant frequencies, and it is common to refer to this scenario as inhomogeneous case. The overall ensemble lineshape is Gaussian, and it represents a static distribution of frequencies which is given by the different environments available to the system (*i.e.*, interaction with the bath or protein), see Figure 2.5 (b).

Homogeneous and inhomogeneous broadening can be pictured as two extreme limits and, a real system usually lies between these two cases (Figure 2.5 (c)). Each molecule in solution has an instantaneous frequency that differs from any other molecule in solution. The instantaneous frequency of a real system evolves in time generating the phenomenon known as spectral diffusion, which can be quantified in 2D spectra with the study of the frequency-frequency correlation function.[10,35]

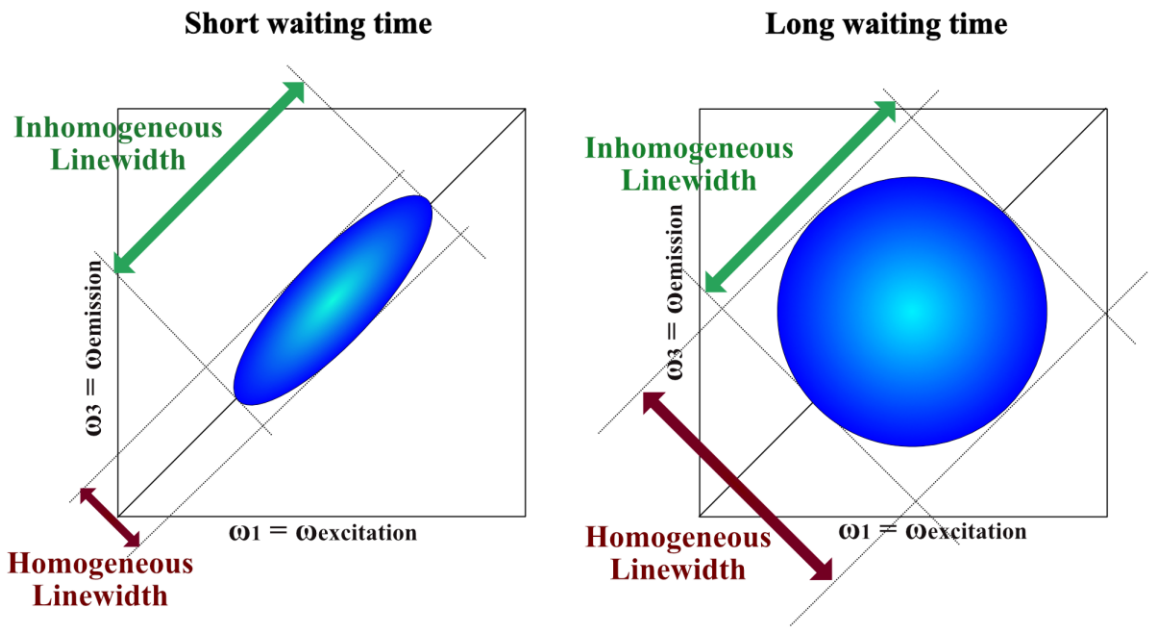

Figure 2.6 Model frequency-frequency correlation maps displaying the inhomogeneous and homogenous linewidth and their evolution (spectral diffusion).

Frequency-frequency maps are particularly useful when the homogenous and inhomogeneous broadening need to be separated.[36] Figure 2.6 gives illustrative 2DES spectra for a two-level system characterised by static inhomogeneous broadening. Under such conditions, each molecule in solution shows the same frequency in both ω_1 and ω_3 axis. The consequence is an elongated ensemble lineshape along the main diagonal ($\omega_1 = \omega_3$) where the inhomogeneous linewidth and homogenous linewidth can be isolated (as illustrated in the figure). In a system that is inhomogeneously broadened and spectral diffusion is significant, at long enough waiting times, the correlation between the $\omega_1 = \omega_3$ is lost, and the 2D spectrum will appear as symmetric, *i.e.*, if the initial spectrum is an elongated peak the spectrum at long waiting times will appear as a circular peak.[37]

2.5 From the Third Order Nonlinear Polarization to a Two-Dimensional Spectrum

A 2D spectrum can be retrieved from the third-order polarization simply using a two-dimension Fourier Transform along the time axes t_3 and t_1 of the third-order polarization $P^{(3)}(t_1,t_2,t_3)$ for a fixed waiting time t_2.[9] However, when running an experiment the intensity field is detected and not the third-order polarization. Moreover, in a 2D experiment, a spectrometer is used to measure the signal field, and $E_s(t_1,t_2,\omega_3)$ is detected (the detector automatically FT the time domain in the frequency domain, $t_3 \rightarrow \omega_3$) instead of $E_s(t_1,t_2,t_3)$. Thus, to analyse the signal acquired in a 2D experiment, it is necessary to know the relationship between the signal field and the polarization and then apply a Fourier Transform to the t_1 axis. The relationship between $P^{(3)}(t_1,t_2,\omega_3)$ and $E_s(t_1,t_2,\omega_3)$ is a function of the refractive index $n(\omega_3)$ as shown in the following equation:[2,5,9]

$$E_s(t_1,t_2,\omega_3) \propto \frac{i\omega_3}{n(\omega_3)} P^{(3)}(t_1,t_2,\omega_3) \tag{2.19}$$

Therefore, to obtain the 2D spectrum, it is necessary to FT only along t_1 to generate the 2D response function:

$$R_{2D}(\omega_1,t_2,\omega_3) = \int_{-\infty}^{\infty} i P^{(3)}(t_1,t_2,\omega_3) e^{i\omega_1 t_1} \, dt_1 \, . \tag{2.20}$$

Equation 2.20 shows that the 2D spectrum is a complex quantity; the real part is related to the absorptive features. At the same time, the imaginary part conveys information about the dispersive system properties, which is the two-dimensional equivalent of the refractive index (see also Chapter 5 in the section “data analysis” for experimental examples).

A consequence of this complex nature of the 2D spectra is that the real (“absorptive”) and the imaginary (“refractive”) contributions need to be plotted separately, alternatively, they

can be shown together as absolute value. It should also be noted that, experimentally, the laser bandwidth has a finite value; therefore, the spectra can be acquired only in a particular spectral "window" onto the response function and not over the entire electromagnetic spectrum. For this reason, the implementation of 2D spectroscopy is achieved with broadband laser pulses to cover the desired states of interest.[9]

2.6 Pump-Probe Spectroscopy

Pump-probe spectroscopy is briefly discussed for completeness, but a more detailed descriptions of transient electronic absorption (TA) and time-resolved infrared (TRIR) experiments are given in Chapter 3.

Pump-probe such as TA and TRIR are related to the multidimensional spectroscopies discussed in this chapter so far, and the signals from these pump-probe measurements can be viewed as the projection of the real part of the corresponding 2D spectrum onto the probe frequency axis, ω_3, where only one-time delay, the waiting time or t_2 is scanned during the experiment, and it is usually identified as pump-probe time-delay. Alternatively, 2D spectroscopy can be seen as a pump-probe experiment where the excitation (or pump) frequency axis is spectrally resolved.[2,16] Equation 2.21 shows the relationship between the response functions of a TA and 2D experiments.

$$S_{TA}(t_2,\omega_3) = \int_{-\infty}^{\infty} \mathrm{Re}[R_{2D}(\omega_1,t_2,\omega_3)]\ d\omega_1 \tag{2.21}$$

Considering the relationship between the pump-probe and 2D spectroscopies, it is intuitive to think about pump-probe spectroscopies as a part of the family of third-order spectroscopy where $P^{(3)}(t_1,t_2,t_3)$ contains the molecular information.[2,5,9]

In pump-probe experiments (see Chapter 3 for experimental details), the first two interactions occur simultaneously within the same pulse (pump pulse), while the third interaction (probe) is time delayed. The signal is generated collinear to the probe, and, thus, "self-heterodyned". For the momentum conservation the wave vector of the signal is given by $\underline{k}_s = \pm \underline{k}_{pu} \mp \underline{k}_{pu} + \underline{k}_{pr}$ where $\underline{k}_{pu}$ is the wave vector of the two pumps (pump propagation direction), and $\underline{k}_{pr}$ is the probe wave vector which determines the probe direction of propagation.[1,2]

2.7 Appendix:

Ap. 2.1 Time Evolution of the Density Matrix

Assuming that the wavefunction of a system is given by:

$$|\psi(t)\rangle = \sum_{n} c_n(t)\,|n\rangle \qquad \text{Ap. 2.1}$$

and the expectation value of a general operator Z is:

$$\langle \hat{Z} \rangle = \sum_{n,\,m} c_n(t) c_m^*(t)\,\langle m|\hat{Z}|n\rangle. \qquad \text{Ap. 2.2}$$

From the definition of the density matrix given in the main text (Equation 2.1), the elements of the density matrix are:

$$\rho(t) = \sum_{n,\,m} c_n(t) c_m^*(t)\,|n\rangle\langle m| = \sum_{n,\,m} \rho_{nm}\ (t)|n\rangle\langle m| \qquad \text{Ap 2.3}$$

it means that the density matrix elements, ρ_{nm}, are equal to the time-evolving expansion coefficients. The combination of the last two equations gives:

$$\langle \hat{Z} \rangle = \sum_{n,\,m} A_{nm}\ \rho_{nm}\ (t) = \mathrm{Tr}\,[\hat{Z}\,\hat{\rho}\,] \qquad \text{Ap. 2.4}$$

Ap. 2.2 Liouville-von Neumann Equation

Assuming that H_0 is the Hamiltonian of the system and it can be treated exactly under the influence of a time-dependent agent A(t), which is more difficult to treat. The total Hamiltonian that is partitioned in H_0 and A(t) is:

$$\hat{H}(t) = \hat{H}_0 + \hat{A}(t) \qquad \text{Ap. 2.5}$$

Let us assume that the system can be treated in the interaction picture. Under such a description, the Liouville-Von Neumann integrated equation can be expressed with the following equation:

$$\rho_I(t) = \rho_I(t_0) - \frac{i}{\hbar}\int_{t_0}^{t} [\hat{A}_I(t), \hat{\rho}_I(t)]\, dt \qquad \text{Ap. 2.6}$$

From equation 2.8, a perturbation series expansion can be found by substituting $\rho_I(t)$ into itself:

$$\rho_I(t) = \rho_0 - \frac{i}{\hbar}\int_{t_0}^{t} [\hat{A}_I(t_1), \hat{\rho}_0]dt_2 \qquad \text{Ap. 2.7}$$

$$+\left(-\frac{i}{\hbar}\right)\int_{t_0}^{t} dt_2 \int_{t_0}^{t_2} [\hat{A}_I(t_2), [\hat{A}_I(t_1), \hat{\rho}_0]]dt_1 + \ldots + \left(-\frac{i}{\hbar}\right)^n \int_{t_0}^{t} dt_n \int_{t_0}^{t_n} dt_{n-1} \ldots + \ldots.$$

It can be represented more compactly, as shown in equation 2.7. A super operator notation can be used to simplify the equations and the formalism, and the solution can be described by a super operator $\hat{\hat{G}}$, as:

$$\rho_I(t) = \hat{\hat{G}}(t)\rho_I(0). \qquad \text{Ap. 2.8}$$

The extended form of the time-dependent operator Ap 2.7 leads to the n-th order term (given in the simplified notation in equation 2.8) which can also be given as:

$$\rho_I^{(n)} = \left(-\frac{i}{\hbar}\right)^n \int_{t_0}^{t} dt_n \int_{t_0}^{t_n} dt_{n-1} \ldots \qquad \text{Ap. 2.9}$$

$$\ldots \int_{t_0}^{t_2} \hat{\hat{G}}(t-t_n)\hat{A}(t_n)\hat{\hat{G}}(t_n-t_{n-1})\hat{A}(t_{n-1})\ldots\hat{\hat{G}}(t_2-t_1)\hat{A}(t_1)\rho_0\, dt_1$$

Ap. 2.3 The Fourier Transform

The Fourier transform (FT) is a mathematical instrument that allows the analysis and manipulation in the time domain of data acquired in the frequency domain.

The FT is a liner integral that connects to different domains where one is the reciprocal of the other, such as momentum and space or time and frequency.[38]

The formal equation that describes an FT of the "conjugate variables" t and ω is given below:

$$f(\omega)=FT\ \{F(t)\}=\int_{-\infty}^{\infty}F(t)e^{-i\omega t}dt \qquad \text{Ap. 2.10}$$

Moreover, the inverse FT^{-1} is defined as:

$$F(t)=FT^{-1}\ \{f(\omega)\}=\int_{-\infty}^{\infty}f(\omega)e^{i\omega t}d\omega \qquad \text{Ap. 2.11}$$

FT definitions containing pre-factors can also be used, and they are commonly found in the literature. Note that for this thesis the different definitions are interchangeable, and the data analysis procedure is not affected by the presence of the pre-factors as long as the same definition of FT is used through the analysis.[38]

References

1. Tokmakoff, A. Lecture Notes: Time-Dependent Quantum Mechanics and Spectroscopy. *Massachusetts Institute of Technology: MIT OpenCouseWare, https://ocw.mit.edu/. License: Creative Commons BY-NC-SA.* (2011).

2. Mukamel, S. Principles of Nonlinear Optical Spectroscopy. *Oxford University Press* (1999) .

3. Cho, M. Coherent two-dimensional optical spectroscopy. *Chem. Rev.* **108**, 1331–1418 (2008).

4. Cho, M. Ultrafast vibrational spectroscopy in condensed phases. *Phys. Chem. Comm.* **5**, 40-58 (2002).

5. Cho, M., Scherer, N. F., Fleming, G. R. & Mukamel, S. Photon echoes and related four-wave-mixing spectroscopies using phase-locked pulses. *J. Chem. Phys.* **96**, 5618–5629 (1992).

6. Fleming, G. R. Protein dynamics and photon echoes. *Proc. Natl. Acad. Sci. USA* **95**, 15161–15162 (1998).

7. Brixner, T., Stenger, J., Vaswani, H. M., Cho, M., Blankenship, R. E. & Fleming, G. R. Two-dimensional spectroscopy of electronic couplings in photosynthesis. *Nature* **434**, 625–628 (2005).

8. Brixner, T., Stiopkin, I. V. & Fleming, G. R. Tunable two-dimensional femtosecond spectroscopy. *Opt. Lett.* **29**, 884–886 (2004).

9. Brixner, T., Mančal, T., Stiopkin, I. V. & Fleming, G. R. Phase-stabilized two-dimensional electronic spectroscopy. *J. Chem. Phys.* **121**, 4221–4236 (2004).

10. Mukamel, S. Multidimensional femtosecond correlation spectroscopies of electronic and vibrational excitations. *Annu. Rev. Phys. Chem.* **51**, 691–729 (2000).

11. Yan, Y. J. & Mukamel, S. Femtosecond pump-probe spectroscopy of polyatomic molecules in condensed phases. *Phys. Rev. A* **41**, 6485–6504 (1990).

12. Scheurer, C. & Mukamel, S. Infrared analogs of heteronuclear nuclear magnetic resonance coherence transfer experiments in peptides. *J. Chem. Phys.* **116**, 6803–6816 (2002).

13. Golonzka, O., Khalil, M., Demirdöven, N. & Tokmakoff, A. Vibrational anharmonicities revealed by coherent two-dimensional infrared spectroscopy. *Phys. Rev. Lett.* **86**, 2154–2157 (2001).

14. Dorrer, C., Belabas, N., Likforman, J. P. & Joffre, M. Spectral resolution and sampling issues in Fourier-transform spectral interferometry. *J. Opt. Soc. Am. B* **17**, 1795-1802 (2000).

15. Lepetit, L., Chériaux, G. & Joffre, M. Linear techniques of phase measurement by femtosecond spectral interferometry for applications in spectroscopy. *J. Opt. Soc. Am. B* **12**, 2467–2474 (1995).

16. Jonas, D. M. Two-dimensional femtosecond spectroscopy. *Annu. Rev. Phys. Chem.* **54**, 425–463 (2003).

17. Brown, L. M. & Rechenberg, H. Landmark Writings in Western Mathematics 1640-1940 (Chapter 69), *Elsevier Science* (2005).

18. Landau, L. Das Dampfungsproblem in der Wellenmechanik. *Z. Phys.* **45**, 430–441 (1927).

19. Dirac, P. A. M. A new notation for quantum mechanics. *Math. Proc. Camb. Philos. Soc.* **35**, 416-418 (1939).

20. Cohen-Tannoudji, C., Diu, B. & Laloe, F. Quantum mechanics. *Wiley- VCH.* (1977).

21. Berman, M. & Kosloff, R. Time-dependent solution of the Liouville-von Neumann equation: non-dissipative evolution. *Comput. Phys. Commun.* **63**, 1–20 (1991).

22. Messiah, A. Quantum Mechanics (Vol. I). *North-Holland, Publishing Co. Amsterdam.* (1961).

23. Negele, J. W. Quantum Many-Particle Systems. *Perseus Book* (1998).

24. Yan, Y. J. & Mukamel, S. Semiclassical dynamics in Liouville space: Application to molecular electronic spectroscopy. *J. Chem. Phys.* **88**, 5735–5748 (1988).

25. Mukamel, S. & Loring, R. F. Nonlinear response function for time-domain and frequency-domain four-wave mixing. *J. Opt. Soc. Am. B* **3**, 595 (1986).

26. Selig-Parthey, U., Brixner, T., Engel, B. & Wurthner, F. W. PhD Thesis: Methods of Nonlinear Femtosecond Spectroscopy in the Visible and Ultraviolet Regime and their Application to Coupled Multichromophore Systems. (2012).

27. Green, G. An Essay on the Application of mathematical Analysis to the theories of Electricity and Magnetism. *Nottingham* (1828).

28. Boyd, R. W. Nonlinear Optics (Third Edition). *Academic Press.* (2008).

29. Read, E. L., Lee, H. & Fleming, G. R. Photon echo studies of photosynthetic light harvesting. *Photosynth. Res.* **101**, 233–243 (2009).

30. Kurnit, N. A., Abella, I. D. & Hartmann, S. R. Observation of a Photon Echo. *Phys. Rev. Lett.* **13**, 567–568 (1964).

31. Lim, M., Hamm, P. & Hochstrasser, R. M. Protein fluctuations are sensed by stimulated infrared echoes of the vibrations of carbon monoxide and azide probes. *Proc. Natl. Acad. Sci. USA* **95**, 15315–15320 (1998).

32. Fuller, F. D. & Ogilvie, J. P. Experimental Implementations of Two-Dimensional Fourier Transform Electronic Spectroscopy. *Annu. Rev. Phys. Chem.* **66**, 1–24 (2015).

33. Fuller, F. D., Wilcox, D. E. & Ogilvie, J. P. Pulse shaping based two-dimensional electronic spectroscopy in a background free geometry. *Opt. Express* **22**, 1018–27 (2014).

34. Heisler, I. A., Moca, R., Camargo, F. V. A. & Meech, S. R. Two-dimensional electronic spectroscopy based on conventional optics and fast dual chopper data acquisition. *Rev. Sci. Instrum.* **85**, 063103 1-10 (2014).

35. Kwak, K., Park, S., Finkelstein, I. J. & Fayer. M. D. Frequency-frequency correlation functions and apodization in two-dimensional infrared vibrational echo spectroscopy: A new approach. *J. Chem. Phys.* **127**, 124503 1-17 (2007).

36. Oliver, T. A. A. Recent advances in multidimensional ultrafast spectroscopy. *R. Soc. Open. Sci.* **5**, 171425 (2018).

37. Cho, M., Brixner, T., Stiopkin, I., Vaswani, H. & Fleming, G. R. Two dimensional electronic spectroscopy of molecular complexes. *J. Chin. Chem. Soc.* **53**, 15–24 (2006).

38. James, J. F. Student's Guide to Fourier Transforms. *Cambridge University Press* (2002).

Chapter 3

Transient Absorption and Time-Resolved Infrared Spectroscopy

3.1 Introduction

The direct investigation of excited state molecular dynamics is crucial for the understanding of chemical reactions and natural processes such as photosynthesis.[1,2] It is well established that photophysical and photochemical processes are initiated by light absorption and play a fundamental role in the condensed phase.[3] Upon light irradiation, a molecule is excited to one or multiple excited states. Subsequently, the photogenerated excited state can undergo various ultrafast processes that lead to the dissipation of the excess energy.[4,5] Examples of ultrafast processes are not rare in natural events such as light absorption by a pigment that initiates photosynthesis,[6] the photodamage that can occur in DNA upon UV excitation,[7] and the excited state dynamics of a dye in solution.[8]

The direct observation of these processes required many advances in technology.[4,5,9,10] such as the development of laser technology and the ability to generate short pulses.[11–13] Thus, the advent of new technologies has opened up a fascinating area of research where pump-probe experiments have become commonplace.[4,14]

The generation of ultrashort laser pulses[15,16] has made the investigation of fast processes, *i.e.*, charge transfer (electron and/or proton transfer), excited state energy transfer and,

isomerisation more accessible, with pump-probe experiments now viewed as a work-horse tool in many laboratories around the world.

In Chapter 2, the fundamental theory of pump-probe spectroscopy was introduced, linking 2DES and pump-probe spectroscopies. In this chapter, the principles of the main pump-probe experiments, transient absorption, and time-resolved infrared spectroscopies will be given alongside a description of the experimental setup used to collect the data presented in Chapter 4. Details on data acquisition and the general approach to the data analysis will also be discussed.

3.2 Principles of Ultrafast Transient Absorption Spectroscopy

TA is an established technique used to follow the dynamics of the excited state directly and to observe the evolution of non-emissive and dark states in many chemical systems such as biological molecules.[2,17]

TA experiments consist of the generation of two pulses, the so-called: pump and probe. The first pulse to arrive at the sample is the pump that promotes a fraction of the molecule in the sample to an excited electronic state.[2] Subsequently, the evolution of the generated species is followed by a second pulse, the probe which arrives at the sample at a specific time delay compared to the pump. The probe pulse is generally weaker in intensity to avoid multiphoton absorption and multistep processes, and typically for TA experiments comprised of a white light supercontinuum probe.[2]

The two beams are focused into the sample and spatially overlapped to generate a response from the molecules that, in the pump-probe configuration according to phase matching (see

Chapter 2), is emitted collinear to the probe. After going through the sample, the probe and signal are collimated and then focused into a spectrograph that contains a grating. It frequency disperses the probe and signal which are then imaged onto a multi-element CCD array detector as depicted in Figure 3.1 (a). The signal is then digitalised and displayed as a difference in absorbance (ΔA) or transmittance (ΔT/T) with ΔA= -log (1 + ΔT/T).[18]

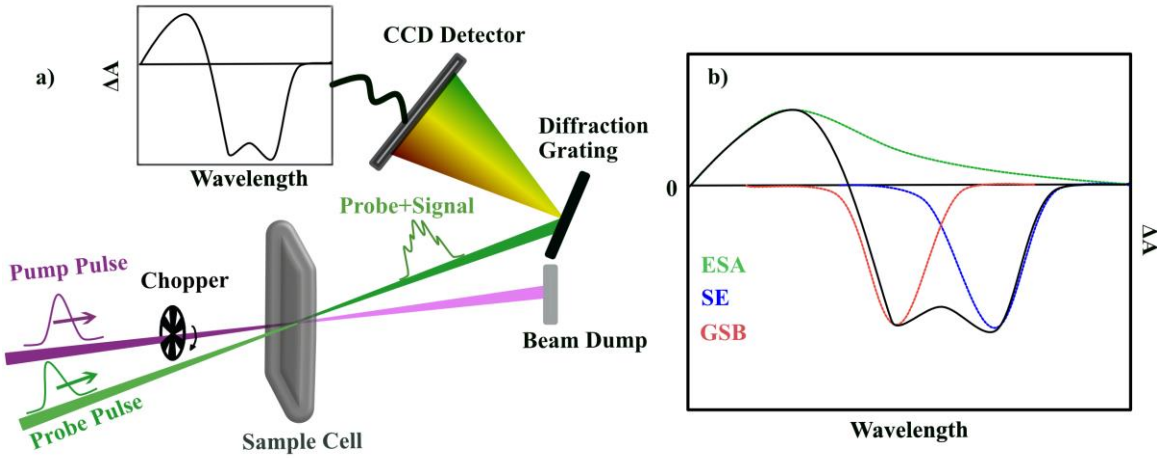

Figure 3.1 (a) Schematic representation of a pump-probe experiment. (b) TA overall spectrum and the signals contributing to it given in ΔA.

The difference in absorbance represents the difference between the absorption spectrum of the excited sample and the absorption spectrum of the molecule in the ground states, and is defined by the following expression[2]:

$$\Delta A\ (\lambda,t) = -\log \frac{I(\lambda,t)_{\text{pumped}}}{I(\lambda,t)_{\text{unpumped}}} \qquad (3.1)$$

where λ is the wavelength in nm, t is the time difference between pump and probe pulses (also t_2, see Chapter 2), and "I" is the detected intensity. Note that in equation 3.1, the condition of pumped and unpumped is generated by a mechanical wheel (chopper) placed in the pump pathway that blocks every other pump shot (see section 3.4 for further details).

The transient signal can also be given as the ratio between the difference in transmittance:

$$\frac{\Delta T\ (\lambda,t)}{T} = \frac{I(\lambda,t)_{\text{pumped}} - I(\lambda,t)_{\text{unpumped}}}{I(\lambda,t)_{\text{unpumped}}} \qquad (3.2)$$

Figure 3.1 (b) shows four possible signal contributions to the signal displayed in a ΔA spectrum, which can be both positive and negative. These multiple contributions to the final signal are classified as stimulated emission (SE), ground state bleach (GSB), excited state absorption (ESA), and absorption of the product(s).

1) Stimulated emission occurs when the weak probe beam passes through the sample and induces photoexcited molecules to emit another photon, causing molecules to return back to the ground state. This process can occur only for optically allowed transitions, and the signal is found at the same frequencies as the static fluorescence. The photon generated is emitted collinear to the probe, increasing the intensity of the I_{pumped} relative to $I_{unpumped}$, and in agreement with equation 3.1, the resulting signal is negative, as shown in Figure 3.1 (b). Note that in ΔT/T spectra, the stimulated emission is a positive signal.

2) Upon light irradiation, a small portion of molecules in the ground state are promoted to the excited state. Therefore, the number of molecules in the ground state decreases, producing the bleach signal (GSB). Hence, the ground state absorption in the excited sample is weaker compared with the not excited sample, and the signal appears as a negative contribution to the overall ΔA spectrum (positive signal in ΔT/T spectra). Moreover, it has been observed that for many chromophores with a small Stokes shift, the GSB + SE features will overlap in the transient spectrum

and merge into a single feature usually challenging to disentangle with pump-probe spectroscopy (see chapters 6 and 7).

3) The excited state absorption gives the third contribution. Once molecules are in their excited states, the probe can generate an optically allowed transitions from the excited states to excited states higher in energy. These transitions are observed at specific frequencies where the excited species may absorb the probe pulse and attenuates the probe beam yielding a positive ΔA (negative $\Delta T/T$).

4) Other photoproducts such as, triplet states, and charge-separated stated can also contribute to the ΔA spectrum. These species might be generated, and their absorption results in a positive signal in the transient absorption spectrum. Once the new transient is produced, it starts playing a role in the dynamics of the sample and its transient spectrum can overlap with the TA of the precursors, *i.e.*, a ground state bleach might appear at the wavelengths where the product ground state absorption resides.[19,20]

3.3 Principles of Time-Resolved Infrared Spectroscopy

The study of excited state dynamics is usually carried out with TA, which allows the direct investigation of excited state in solution. However, absorption bands of molecules such as DNA, its structural components,[21,22] and transient metal complexes[23] generally result in broad and somewhat featureless TA spectra. Thus, the extrapolation of structural and dynamical information from these features can be very challenging and not always entirely definitive. To overcome this issue, additional ultrafast techniques such as time-resolved infrared spectroscopy can be used. It has been proven that TRIR is a very powerful tool for

providing structural and dynamical information about the excited state of molecules by probing characteristic vibrational modes of these systems in solution.[23]

Generally speaking, TRIR is a pump-probe spectroscopy where a UV or visible pump beam initiates a photoinduced process, and a mid-IR probe interrogates the molecule at different time delays. As in the TA experiments, the data are acquired as a difference in absorption, and the final signal is given as a function of time delays and probe frequencies.

3.4 Transient Absorption and Time-Resolved Infrared Apparatus

The transient absorption and time-resolved infrared data presented in Chapter 4 were collected with an established setup, at the University of Bristol, which is schematically depicted in Figure 3.2. The established system, already reported,[24–26] is composed of a Coherent Vitara-S oscillator and Coherent Legend Elite HE+ regenerative amplifier, 1 kHz, 800 nm, and a total output of 5 W and 35 fs pulses. The fundamental 800 nm beam was split into three parts. The first two lines were used to seed two Coherent OperA Solo optical parametric amplifiers (OPAs). The first OPA is spectrally tunable from UV to IR (220-20000 nm), and it was used to generate the pump for TA experiments while the second OPA generated broadband tunable mid-IR pulses used as the probe for TRIR experiments. The third less intense beam was focused with a 15 cm lens into a rastered CaF_2 window moved perpendicular to the direction of propagation of the beam to generate the white light supercontinuum (WLC). A set of neutral density filters and irises attenuated the power of the 800 nm before the CaF_2 window, improving the white light spectral profile and stability.

The WL was used as probe for the transient absorption measurements, as shown in Figure 3.2.

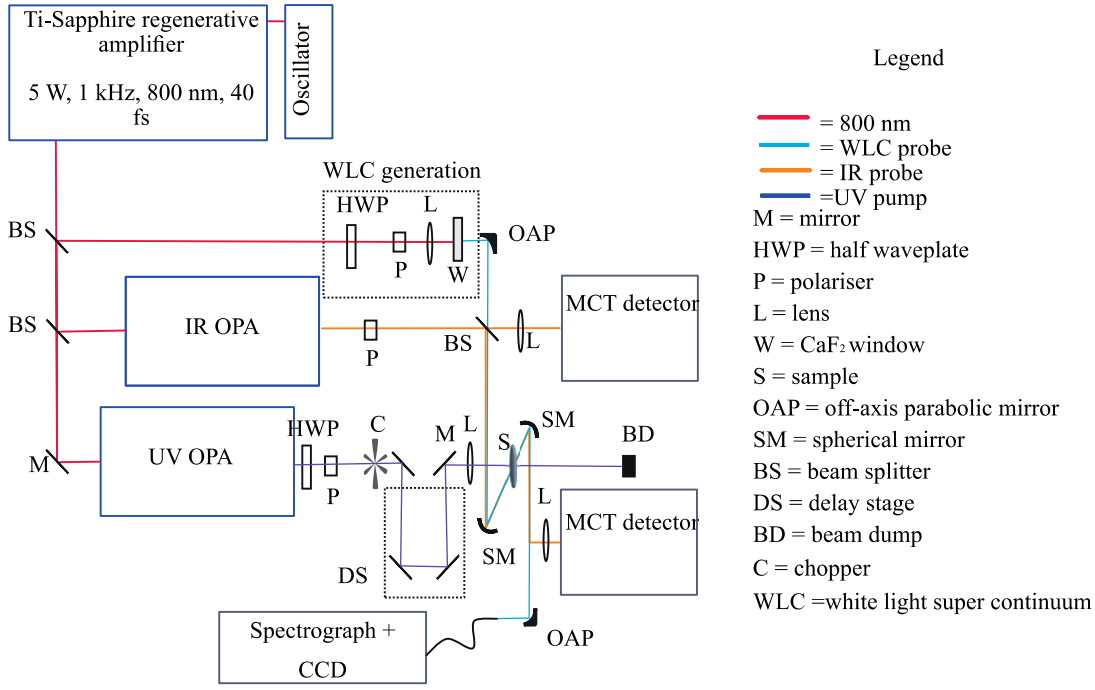

Figure 3.2 Schematic diagram of the setup used to acquire TA and TRIR data.

The pump excitation beam passes through a mechanical chopper that blocks every other shot. The repetition rate of the laser was 1 kHz, the chopper was set at 500 Hz, and the sample was excited 500 times per second. Therefore, the sample can be "excited" or "non-excited" the same amount of times per second. It allows the WLC to probe the "pumped" and "unpumped" state of the sample and the resulting signal was measured as intensity by the detector. From the $I(\lambda)_{pumped}$ and $I(\lambda)_{unpumped}$ the difference in absorbance was calculated using equations 3.1 or 3.2.

For the variation of the time delay between the pump and the probe beams, both in TRIR and TA experiments, the pump beam was sent along a longer beam path compared to the

probe beam. The length of this path is time-dependent, and it was controlled by an aluminium retroreflector (PLX) mirror mounted on a motorised 220 mm delay stage with a maximum delay achievable of 1.3 ns (see Chapter 4 for specific details about the power and spot sizes used during the experiment).

3.5 Spectra Collection

The TA and TRIR spectra presented in this thesis, in chapters 4, 6, and 7, have been collected as explained in this section using a LabView program to control the data acquisition.

For a fixed pump-probe time delay, the signal was measured for many numbers of shots and averaged to obtain a high signal-to-noise (S/N) ratio. In many cases, the number of shots was set between 700 to 1000, which, under our experimental conditions achieved a reasonable S/N. This routine was then repeated for many different pump-probe time delays, which were pre-programmed before the acquisition process.

A great advantage in our setup was the use of a multichannel detector that allows multiwavelength broadband detection in real time. Further, the data acquired were fitted in real time. For a fixed pump-probe time delay, a “rejection filter” was also applied. The filter could reject the data that deviate from the average signal (over 700-1000 shots) and

accept only the data within a specific standard deviation usually set between 0.4 and 0.6. The rejection filter significantly improves the S/N and the quality of the data.

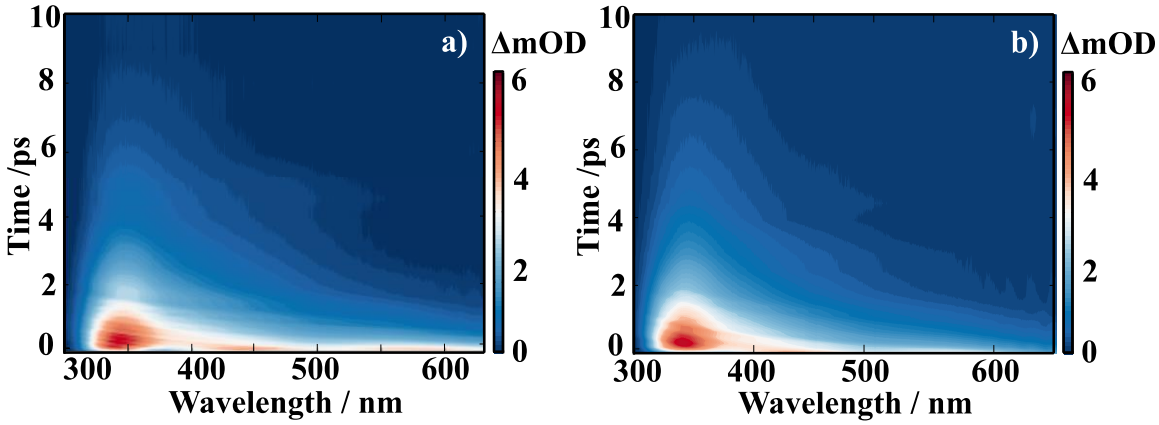

Figure 3.3 (a) TA spectrum of a mononucleotide (dGMP) in solution without rejection filter during cycle 1, (b) same data with rejection filter, and after averaging over 5 cycles. The data are given in ΔmOD.

Once the data at one time delay was recorded the delay stage was moved to another time delay. The total numbers of time delays for the experiment repeated in this thesis typically varied between 300 and 400, between 0 and 1.3 ns. Each dataset was then acquired for 7 or 10 times (number of cycles) and the resulting averaged data saved and analysed. Figure 3.3 (a) shows the TA spectrum of a dinucleotide (dGMP) taken without the rejection filter during cycle 1, while panel (b) is the same spectrum after 5 cycles and rejection filter applied.

3.6 Data Analysis

In TA as well as in TRIR spectroscopies, the large amount of data usually corresponds to thousands of points acquired in the frequency domain and hundreds to thousands of points in the time domain. Thus, the final data can be visualised as a data cube where the three dimensions are: pump-probe time delay, probe wavelength, and spectral intensity, which is usually given either in ΔA (sometimes given as optical density (ΔOD)) or $\Delta T/T$. To analyse such a large number of data points MatLab software is commonly used.

The first step in data analysis consists of examining the raw spectra, where slices of the data are selected. For example, by selecting one wavelength and plotting ΔOD or $\Delta T/T$ vs time, it is possible to extract information about the time evolution of the transient species (kinetics). Moreover, by looking at a single time point and displaying ΔOD or $\Delta T/T$ vs wavelength, the different features appearing in the spectrum can be associated with different physical processes, as shown in Figure 3.1(b). From their comparison with the static spectra (UV-vis or FTIR), information about the electronic states of vibrational modes can be retrieved.

In some cases, a different analysis using Global and Target Analysis is required to characterise multiple signals in the spectrum.[27] The time-resolved data contains a great variety of information, and it can be difficult to isolate the contribution of each species modelling the data with a relatively small number of components. Therefore, the ultrafast data are initially modelled with sequentially interconverting evolution-associated difference spectra (EADS), where the data are fitted with exponential functions and a lifetime is associated with each EADS. This process leads to an understanding of the excited state evolution. The final step of this analysis is the so-called target analysis. The goal of the analysis is to obtain the spectrum of a "pure" species, *i.e.*, spectra of the

intermediates and product/s, which are known as species associated spectra (SADS). The EADS differs from the SADS because the former represents a mixture of states and not the single species. To overcome this problem, a consecutive, parallel, or branched kinetic model, usually based on chemical intuition or previous information about the studied system, is applied during the target analysis, and the contribution of the single species is isolated to generate the SADS.[28]

3.7 Conclusions

In this chapter, an overview of the principal pump-probe techniques, TA and TRIR, is given. The direct investigation of the evolution of the excited state of a molecule is commonly carried out using TA.[2] It has been observed that certain molecules such as DNA and its constituent parts show a very broad and featureless TA spectra and the interpretation of the data is, in some instances, challenging. Further information about the structure of the molecule can be obtained with TRIR spectroscopy that conveys direct information on the vibrational features of the excited state. The data collection with specific references to the setup used to acquire the signals is shown in Chapter 4.

References

1. Sundström, V. Femtobiology. *Annu. Rev. Phys. Chem.* **59**, 53–77 (2008).

2. Berera, R., van Grondelle, R. & Kennis, J. T. M. Ultrafast transient absorption spectroscopy: principles and application to photosynthetic systems. *Photosynth. Res.* **101**, 105–118 (2009).

3. Glusac, K. What has light ever done for chemistry? *Nat. Chem.* **8**, 734–735 (2016).

4. Zewail, A. H. Femtochemistry. Past, present, and future. *Pure Appl. Chem.* **72**, 2219–2231 (2000).

5. Zewail, A. H. Femtochemistry-Ultrafast Dynamics of the chemical bond, Vols I and II. *World Scientific, New Jersey Singapore* (1994).

6. Breton, J., Martin, J.-L., Petrich, J., Migus, A. & Antonetti, A. The absence of a spectroscopically resolved intermediate state $P^{+}B^{-}$ in bacterial photosynthesis. *FEBS Lett.* **209**, 37–43 (1986).

7. Kwok, W. M., Ma, C. & Phillips, D. L. A doorway state leads to photostability or triplet photodamage in thymine DNA. *J. Am. Chem. Soc.* **130**, 5131–5139 (2008).

8. Mokhtari, A., Chebira, A. & Chesnoy, J. Subpicosecond fluorescence dynamics of dye molecules. *J. Opt. Soc. Am. B* **7**, 1551-1557 (1990).

9. Henriksen, N. E. & V Engel. Femtosecond pump-probe spectroscopy: A theoretical analysis of transient signals and their relation to nuclear wave-packet motion. *Annu. Rev. Phys. Chem.* **20**, 93–126 (2001).

10. Siegal, Y.,Glezer, E. N., Mazur, E., Manz, J. & Wöste, L. Femtosecond Chemistry. *Verlang Chemie, Berlin* (1994).

11. Spence, D. E., Kean, P. N. & Sibbett, W. 60-fsec pulse generation from a self-mode-locked Ti:sapphire laser. *Opt. Lett.* **16**, 42-44 (1991).

12. Shank, C. V. Ultrashort laser pulse and applications. *Springer Berlin* (1988).

13. Hecht, J. Short history of laser development. *Opt. Eng.* **49**, 091002 1-23 (2010).

14. Chergui, M. Femtochemistry and Femtobiology: The New Age. *Chemphyschem* **3**, 713-718 (2002).

15. Li, J. Ren, X., Yin, Y., Zhao, K., Chew, A., Cheng, Y., Cunningha,, E., Wang,Y., Hu, S., Wu, Y., Chini, M & Chang, Z. 53-attosecond X-ray pulses reach the carbon K-edge. *Nat. Commun.* **8**, 186 1-5 (2017).

16. Gaumnitz, T., Jain, A., Pertot, Y., Huppert, M., Jordan, I., Ardana-Lamas, F. & Worner, H. J. Streaking of 43-attosecond soft-X-ray pulses generated by a passively CEP-stable mid-infrared driver. *Opt. Express,* **25**, 27506–27518 (2017).

17. Walla, P. J., Linden, P. A., Hsu, C. P., Scholes, G. D. & Fleming, G. R. Femtosecond dynamics of the forbidden carotenoid S_1 state in light-harvesting complexes of purple bacteria observed after two-photon excitation. *Proc. Natl. Acad. Sci. USA* **97**, 10808–10813 (2000).

18. Hashimoto, S., Yabushita, A. & Iwakura, I. Transient process spectroscopy for the direct observation of inter-molecular photo-dissociation. *Struct. Dyn.* **4**, 054901 1-11 (2017).

19. Arlt, T., Schmidt, S., Kaiser, W., Lauterwasser, C., Meyer, M., Scheer, H. & Zinth, H. The accessory bacteriochlorophyll: a real electron carrier in primary photosynthesis. *Proc. Natl. Acad. Sci. USA* **90**, 11757–11761 (1993).

20. Vos, M. H., Breton, J. & Martin, J. L. Electronic Energy Transfer within the Hexamer Cofactor System of Bacterial Reaction Centers. *J. Phys. Chem. B* **101**, 9820–9832 (1997).

21. Kuimova, M. K. Dyer, J., George, M. W., Grills, D. C., Kelly, J. M., Matousek, P., Parker, A. W., Sun, X. Z., Towrie, M. & Whelan, A. M. Monitoring the effect of ultrafast deactivation of the electronic excited state of DNA bases and polynucleotides following 267 nm laser excitation using picosecond time-resolved infrared spectroscopy. *Chem. Comm.* **104**, 1182–1184 (2005).

22. Hare, P. M., Middleton, C. T., Mertel, K. I., Herbert, J. M. & Kohler, B. Time-resolved infrared spectroscopy of the lowest triplet state of thymine and thymidine. *Chem. Phys.* **347**, 383–392 (2008).

23. George, M. W. & Turner, J. J. Excited state of transition metal complexes studied by time-resolved infrared spectroscopy. *Coord. Chem. Rev.* **177**, 201–217 (1998).

24. Roberts, G. M., Marroux, H. J. B., Grubb, M. P., Ashfold, M. N. R. & Orr-Ewing, A. J. On the participation of photoinduced N-H bond fission in aqueous adenine at 266 and 220 nm: a combined ultrafast transient electronic and vibrational absorption spectroscopy study. *J. Phys. Chem. A* **118**, 11211–11225 (2014).

25. Rottger, K. Marroux H. J. B., Chemin, A. F. M., Elsdon, E., Oliver, T. A. A., Street, S. T. G., Henderson, A. S., Galan, M. C., Orr-Ewing, A. J. & Roberts, G. M. UV-induced

electron-driven proton transfer active in a chemically modified A·T DNA base pair? *J. Phys. Chem. B* **121**, 4448–4455 (2017).

26. Wynne, K. & Hochstrasser, R. M. The theory of ultrafast vibrational spectroscopy. *Chem. Phys.* **193**, 211–236 (1995).

27. Kennis, J. T. M. Larsen, D. S., van Stokkum, H. M., Vengris, M., von Thor, J. J. & van Grondelle, R. Uncovering the hidden ground state of green fluorescent protein. *Proc. Natl. Acad. Sci. USA* **101**, 17988–17993 (2004).

28. Snellenburg, J. J., Laptenok, S. P., Seger, R., Mullen, K. M. & van Stokkum, I. H. M. Glotaran: A Java-Based Graphical User Interface for the R Package TIMP. *J. Stat. Softw.* **49**, 1-22 (2012).

Chapter 4

Exploring Charge Transfer Dynamics in a Model Dinucleotide of Guanine and Thymine

The data and results presented in this chapter have been published: M. Duchi, M.P. O'Hagan, R. Kumar, S.J. Bennie, M.C. Galan, B.F.E. Curchod and T.A.A. Oliver, *Phys. Chem. Chem. Phys.*, **21**, 14407-14417 (2019). I performed all the static and transient absorption measurements and analysed these data. The dinucleotide samples were prepared and purified using a known synthesis by Michael O'Hagan in Prof. Carmen Galan's group. The theoretical calculations were performed in collaboration with Basile Curchod (Durham University) and Simon Bennie. Basile Curchod ran ground state molecular dynamics simulations. I performed the ground state geometry optimisations of various conformers. The time-dependent density functional theory calculations were performed by Basile Curchod, Simon Bennie and me.

4.1 Introduction

The ultraviolet component of solar radiation poses a threat to all life on Earth. If DNA absorbs UV light, deleterious photochemical reactions can be initiated, leading to genetic damage of the source code for life.[1,2] The mechanistic details of such processes have been the subject of intense study, with ultrafast spectroscopy playing a pivotal role in establishing the molecular mechanisms of DNA excited state deactivation or photoinduced reactions.[3–11] It is apparent that as the complexity of the DNA structure is increased from a bare nucleobase to a polynucleotide, the associated non-radiative relaxation dynamics

become increasingly complicated; the amplitude associated with the tens-to-hundreds of picoseconds excited state lifetime component becomes more significant,[4,7,8,12] and additional non-radiative pathways such as excited state charge transfer[7,13] or proton-coupled electron transfer become accessible.[9]

Intermolecular electrostatic interactions become increasingly influential when the structure is further extended to include multiple nucleic acids, *e.g.* di-, tri-, or oligo- nucleotides. In these single (or double) strands of DNA, π-stacking becomes an important structural motif, and due to the short distances between adjacent nucleobases, significant electronic coupling is anticipated.[3,14] Resultantly, theoretical studies have suggested the Franck-Condon electronic states are no longer localised to specific nucleobases,[15–17] and could be delocalised over up to 4 moieties.[18] Static circular dichroism[19] and ultrafast spectroscopic investigations[5,8,13,18,20] have established a picture where the photoexcited state of DNA structures are initially delocalised over multiple nucleobases. However, while these experimental studies are pioneering, they either represent a time-averaged picture of DNA systems,[19,21] or concentrate on sufficiently large systems where precise molecular details are difficult to ascertain,[5,8] deliberately incorporated unnatural nucleobases into structures to shift absorptions and thereby reducing inter-nucleobase dipole coupling compared to natural sequences,[7,13] or are unable to assign the transient products formed definitely.[20,22] Therefore, despite a consensus being reached, irrefutable experimental evidence supporting the hypothesis of delocalised Franck-Condon excited state in natural DNA sequences with a high level of molecular precision is missing.

Ultrafast transient absorption (TA), time-resolved infrared spectroscopy (TRIR) and theoretical calculations to study the non-radiative relaxation dynamics of 2'-

deoxyguanosine 3'-monophosphate 5'-thymidine, d(GpT), a dinucleotide that contains the naturally occurring nucleic acids thymine and guanine were used. Experimentally I demonstrated that (i) the Franck-Condon excited state of d(GpT) are significantly delocalised over both guanine and thymine and (ii) the Franck-Condon states rapidly decay into an ion-pair exciplex state forming $d(G^{+}pT^{-})$ products. (iii) At least 51% of photoexcited dinucleotides follow this non-radiative pathway, but efficiently reform neutral ground state molecules on a ~10 ps timescale, and thereby minimise the probability of deleterious excited state photochemical reactions.

4.2 Experimental Methods

4.2.1 Sample Preparation

2'-deoxyguanosine-5'-monophosphate disodium salt (>98%) and thymidine-5'-monophosphate disodium salt (>99%) were purchased from Carbosynth and used without further purification. 2'-deoxyguanosine 3'-monophosphate 5'-thymidine was synthesised using standard phosphoramidite coupling and deprotection procedures.[23,24] The final compound was purified by preparative high-pressure liquid chromatography (HPLC), and the nuclear magnetic resonance (NMR) spectra of the pure sample are shown in the appendix (section 4.6). For all reported spectroscopic studies, the mono- and di- nucleotide were prepared in phosphate-buffered solutions (pD 7) in D_2O at 10 mM concentrations. Samples have flowed continuously throughout experiments in a customised flow cell, 200 μm and 50 μm path lengths for transient absorption and time-resolved infrared experiments, respectively.

4.2.2 Ultrafast Spectroscopy

Details of the laser system and experimental apparatus are given in Chapter 3. Specific information about the pump and probe powers, spot size and pulse durations are given in this section.

In TA and TRIR experiments the 500 nJ UV pump (273 or 257 nm) was focused to a ~ 200 μm spot size at the sample and then overlapped with the white light continuum (WLC, 300-650 nm) or mid-IR (1500-1750 cm^{-1}) probe beams. After the sample, the collinear probe pulse and signal were collimated and focused into a spectrograph coupled to multi-element mid-infrared mercury cadmium telluride (MCT) or charge-coupled device (CCD) detectors for TRIR and TA, respectively. The instrument response function was determined via a 2-photon absorption in D_2O and calculated to be ~150 fs for TA and ~350 fs for TRIR experiments.

4.2.3 Computational Methods

To characterise the electronic structure of the first few singlet excited states of d(GpT), linear-response time-dependent density functional theory (LR-TDDFT) calculations with the exchange-correlation functional ωB97X-D and a cc-pVTZ basis set using an integral equation formalism variant polarisable continuum solvent model (IEFPCM) were performed.[25–30]

Classical molecular dynamics (MD) simulations of solvated d(GpT) were also performed using the Amber 14 software, utilising standard Amber force field parameters for d(GpT). The simulation was composed of a single d(GpT) molecule (initially in an open

conformation), surrounded by 2356 TIP3P water molecules and a sodium cation in an orthorhombic box. The energy of the initial configuration was first minimized for 2500 cycles. The temperature was set to 300 K for 25 ps in an NVT ensemble, followed by 20 ns of equilibration in an NpT ensemble. A production run was performed for 40 ns (NpT ensemble), from which representative geometries were selected. Each selected geometry was re-optimised at the DFT/ωB97X-D/6- 31G*/IEFPCM (water) level of theory.

4.3 Results and Discussion

4.3.1 Electronic and Vibrational Absorption Spectroscopy

The molecular structures of 2'-deoxyguanosine 5'-monophosphate (dGMP), thymidine-5'-monophosphate (dTMP) and d(GpT) are displayed in Figure 4.1 (a) alongside their associated UV absorption spectra of 10 mM buffered (pD 7) aqueous solutions Figure 4.1 (b). Two local maxima dominate the dGMP absorption spectrum at 276, and 252 nm which are assigned to the two lowest energy $^1\pi\pi^*$ states, S_1 and S_2, which have the associated ^1L_a and ^1L_b labels in Platt's notation.[31] dTMP has a maximum at 270 nm assigned to a $^1\pi\pi^*$ state (S_2), and the $^1n\pi^*$ (S_1) state lies at lower excitation energies, but it is optically dark to one-photon absorption.[12] The absorption spectrum of d(GpT) displays two local maxima at 273 and 257 nm. The two pump wavelengths used in TA and TRIR experiments were chosen to coincide with these two maxima.

Static Fourier-transform infrared (FTIR) spectra were acquired for the same solutions of the three molecules between 1540–1750 cm^{-1} and are displayed in Figure 4.1 (c). The vibrational spectrum of the dinucleotide in this range contains five main vibrational absorption bands centred at 1566, 1578, 1632, 1661, and 1682 cm^{-1}. The vibrational

frequencies were assigned based on prior investigations of the isolated nucleotides[32,33] to a pyrimidine ring breathing mode coupled to an amino stretch of the guanine moiety at 1566 cm^{-1}, C–N ring breathing stretch on guanine at 1578 cm^{-1}, carbon-carbon double bond of the thymine ring (1632 cm^{-1}), carbonyl stretches on either guanine or thymine (1661 wavenumber) and the C=O stretch adjacent to N–D and N–sugar groups on thymine (1690 cm^{-1}). The two peaks at 1578 and 1632 cm^{-1} (labelled with arrows in Figure 4.1(c)) are unique to guanine or thymine nucleobases and exploited as localised probes for the time-dependent population of the two nucleobases.

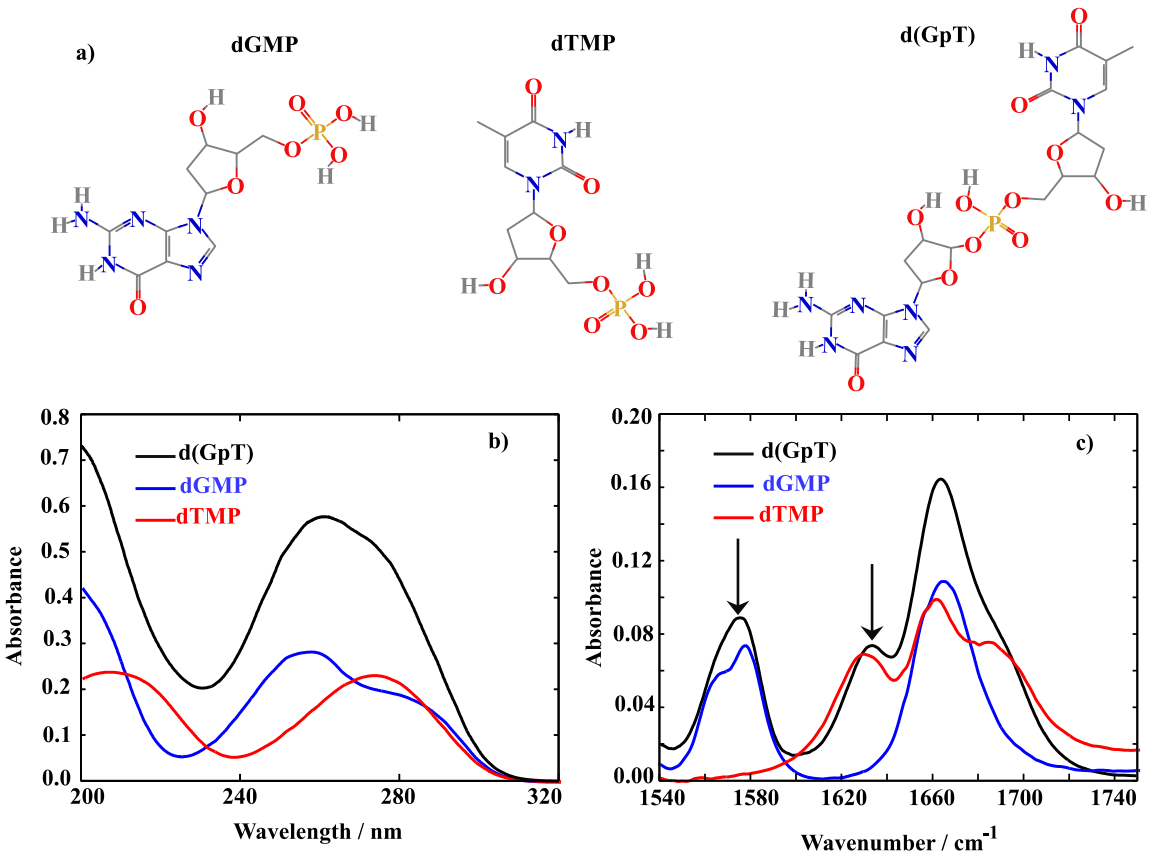

Figure 4.1 (a) Molecular structure of dTMP, dGMP and d(GpT). (b) Ultraviolet and solvent-subtracted (c) mid-infrared linear absorption spectra for 10 mM solutions of dGMP, dTMP and d(GpT). The arrows in panel (c) indicate two of the main vibrational features of interest (1578 and 1632 cm^{-1}) in the TRIR investigations.

4.3.2 Ground State Molecular Structure and Calculated Absorption and Emission Spectra

Dinucleotides are inherently conformationally very flexible molecules due to a large number of internal degrees of freedom. It is, therefore, reasonable to conclude that they will have associated complex conformational free energy landscapes which will support many different local minima structures. If the barriers to interconversion are sufficiently low, then multiple conformers will be present in a room temperature solution. Two dominant effects determine the balance of structures present in aqueous solution; (i) the hydrophobicity experienced by the hydrocarbon nucleobase rings which favour π-stacked conformations as illustrated in Figure 4.2 (a), and entropically favoured conformers where the energetic stabilisation of π-stacking is outweighed by conformational flexibility (*e.g.* Figure 4.2 (b)).

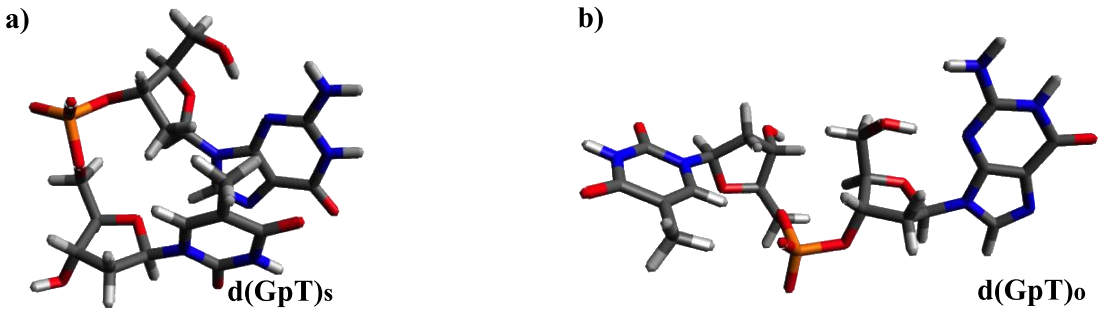

Figure 4.2 Calculated representative (a) π-stacked and (b) open structures of d(GpT) optimised at the ωB97X-D/6-31G*/IEFPCM level of theory.

The conformational structure has ramifications for the electronic structure of photoexcited d(GpT); in π-stacked configurations the inter-nucleobase distance is short (typically < 3 Å) and dipole-dipole coupling is anticipated to be the strongest. For structures that are not π-stacked, the inter-nuclear separation between rings is significant, and to a low-order approximation, excitation can be described as localised to individual nucleobases. To date,

quantification of the conformational equilibrium using molecular dynamics simulations has proved very challenging for di-, tri- or oligo-nucleotides as the MD force-fields have been optimised for double-stranded DNA (B-form),[34] and thus over-emphasise the percentage of π-stacked conformers. A recent study of d(TpT) exemplified this issue: MD simulations could not reproduce experimentally determined equilibrium constants extracted from NOSY and COSY NMR measurements.[35]

In this work, MD simulations were used to generate a variety of possible d(GpT) ground state conformations, from which several "representative" molecular structures were extracted. These MD geometries were then re-optimised using density functional theory (DFT) and used to inform the analysis of the time-resolved infrared measurements. It is important to emphasise that the MD simulations were not used to obtain the absolute global minimum energy structures or to predict the percentage of stacked d(GpT) molecules in solution due to the problem mentioned above with MD force fields. Throughout this chapter, I focus on two types of conformational structures: the π-stacked (denoted with subscript s) and open conformations (subscript o) of d(GpT) and, the optimised geometries of these structures at the DFT/ωB97X-D/6-31G* level with the polarisable continuum model using the integral equation formalism are displayed in Figure 4.2.

Theoretical analyses were also carried out to simulate the absorption spectra for the isolated dGMP and dTMP (see Figure 4.3 (a)) which reproduce the observed experimental trends; dGMP has a blue-shifted absorption maximum with a higher oscillator strength compared to dTMP. The close resemblance of the dGMP + dTMP calculated spectrum to that of $d(GpT)_o$ highlights the very weak interaction between G and T moieties in conformations lacking π-stacking, particularly at $\lambda > 230$ nm. The calculated spectrum of d(GpT)s

deviates more significantly from the sum of dGMP + dTMP or $d(GpT)_o$ spectra but agrees with the overall experimentally observed trends for d(GpT).

Further insights were gained from the analysis of the lowest energy LR-TDDFT calculated electronic transitions. The transition density corresponding to each electronic state was decomposed into the location of the photogenerated hole (where the electron was in S_0) and electron (the location of the electron in the excited electronic state). The dinucleotide, d(GpT), was partitioned in three components: G or T nucleobases and the remaining sugar-phosphate backbone (r). The location of the hole/electron for each transition is given in the matrices shown in Figure 4.3 ((b) and (c)). Concentrating on $d(GpT)_o$ initially; the first singlet excited state is localised to the thymine moiety (electron and hole are both located on T), whereas the S_2 state is localised on the guanine nucleobase. The first two transitions $d(GpT)_o$ are almost degenerate, and the S_1 and S_2 states only contain minor contributions (<11%) from the other nucleobase. This decomposition explains the close resemblance between the dGMP + dTMP and $d(GpT)_o$ calculated transitions. π-stacking in $d(GpT)_s$ results in far less localisation of the electron and hole to the same nucleobase (see Figure 4.3 (c)) which significantly alters the character of the lowest energy singlet excited state: (i) diagonal elements for both G and T are returned for S_1, S_2 and S_4 states, which is characteristic of coupled excitation of the two nucleobases, *i.e.* the excitation is delocalised, and (ii) upper off-diagonal elements are observed for low oscillator strength S_1, S_3 and S_4 states, indicating a significant charge-transfer character from guanine to thymine. The presence of low-lying excited states with different electronic characters in d(GpT) agrees with prior theoretical calculations (CASPT2/MM methods) for d(ApU).[36]

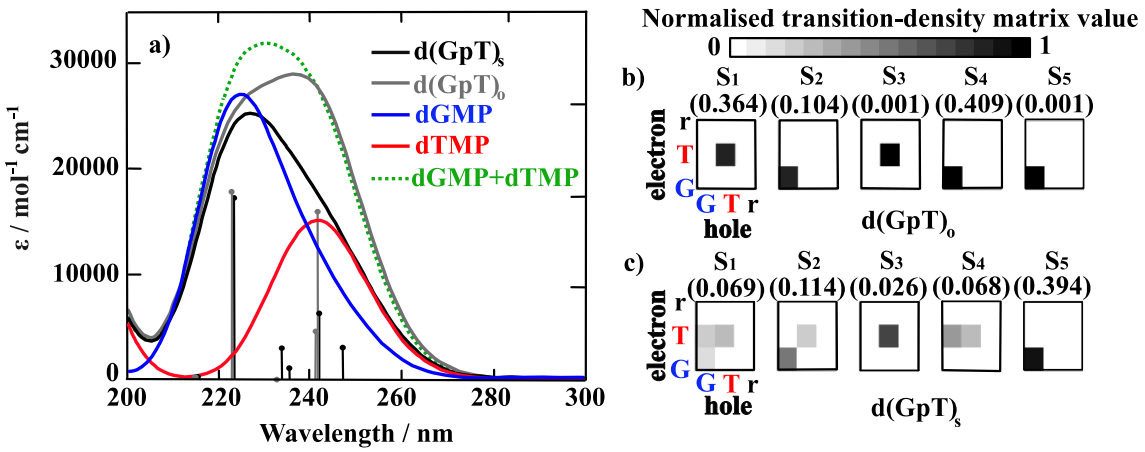

Figure 4.3 LR-TDDFT/ωB97X-D/cc-pVTZ/IEFPCM vertical transitions of dGMP, dTMP, $d(GpT)_o$ and $d(GpT)_s$. (a) Calculated absorption spectra showing the stick spectra for each electronic transition of $d(GpT)_{o/s}$ and convolved Gaussian spectra for all species. Analysis of the transition-density matrices for the first five excited state of (b) $d(GpT)_o$ and (c) $d(GpT)_s$. The oscillator strength and wavelength associated with each transition are given above the corresponding matrix. The hole location is given on the horizontal axis of each matrix, with the vertical axes giving the position of the electron. The greyscale intensity represents the normalised transition-density matrix values.

It is important to note that due to the close energetic proximity of these states, their ordering is expected to be very sensitive to the nuclear geometry; therefore, an additional π-stacked structure was selected from the classical molecular dynamics simulation, optimised with DFT, and the associated vertical electronic transitions calculated (see Figure 4.4). This structure, labelled $d(GpT)_{s2}$, is similar to $d(GpT)_s$ but the guanine nucleobase is rotated by 180° (compare inset of Figure 4.4 with Figure 4.2 (a)).

ωB97X-D/ccpVTZ/IEFPCM//ωB97X-D/6-31G*/IEFPCM calculations of $d(GpT)_s$ and $d(GpT)_{s2}$ revealed that the ground state energy of the $d(GpT)_s$ is more stable by 34.4 kJ/mol (0.36 eV). The vertical electronic transitions of the $d(GpT)_{s2}$ geometry have a higher

percentage of localised character compared to the respective transitions in d(GpT)$_s$. With reference to Figure 4.3 (c) and Figure 4.4 (b): the S_1 and S_2 states of d(GpT)$_{s2}$ show coupled excitation of both the guanine and thymine nucleobases, whereas S_3 is almost purely G $\rightarrow$T charge-transfer in character. This coupling results in the S_0–S_2 electronic transition having a larger associated oscillator strength and shifts the maximum of the theoretical spectra towards the red compared to d(GpT)$_s$.

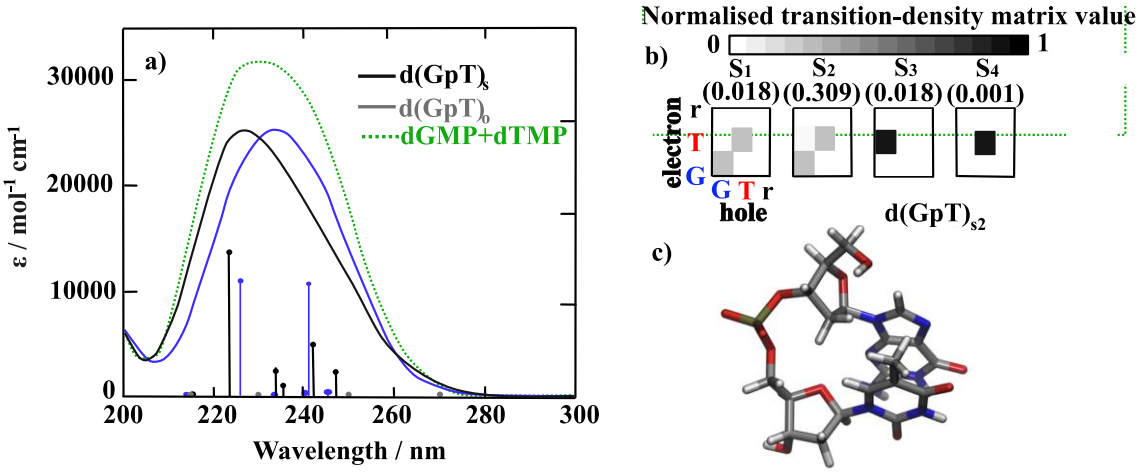

Figure 4.4 LR-TDDFT/ωB97X-D/cc-pVTZ/IEFPCM vertical transitions of d(GpT)$_{s2}$. (a) Calculated absorption spectra showing the stick spectra for each electronic transition of d(GpT)$_{s2}$ and convolved Gaussian spectra for all species. (b) Analysis of the transition-density matrices for the first four low-lying vertical excitation of d(GpT)$_{s2}$. The oscillator strength and the wavelength associated with each transition are given above the corresponding matrix. The horizontal axis defines the location of the hole, and the vertical axis gives the position of the electron. (c) Skeletal structure of d(GpT)$_{s2}$.

4.3.3 Temperature Dependent Circular Dichroism Spectroscopy

Circular dichroism (CD) is obtained from the different interaction between left and right-handed polarised light with chiral molecules.[37] CD is mostly used in empirical studies of

biomolecular samples, and it is a well-known probe of π-stacking in chiral structures such as DNA.[37] Although, CD spectroscopy is recognised as a complementary technique to NMR and X-ray to study molecular structures, DNA-conformational properties need to be deduced with caution as circular dichroism spectroscopy is sensitive to temperature, ionic strength and pH.[37]

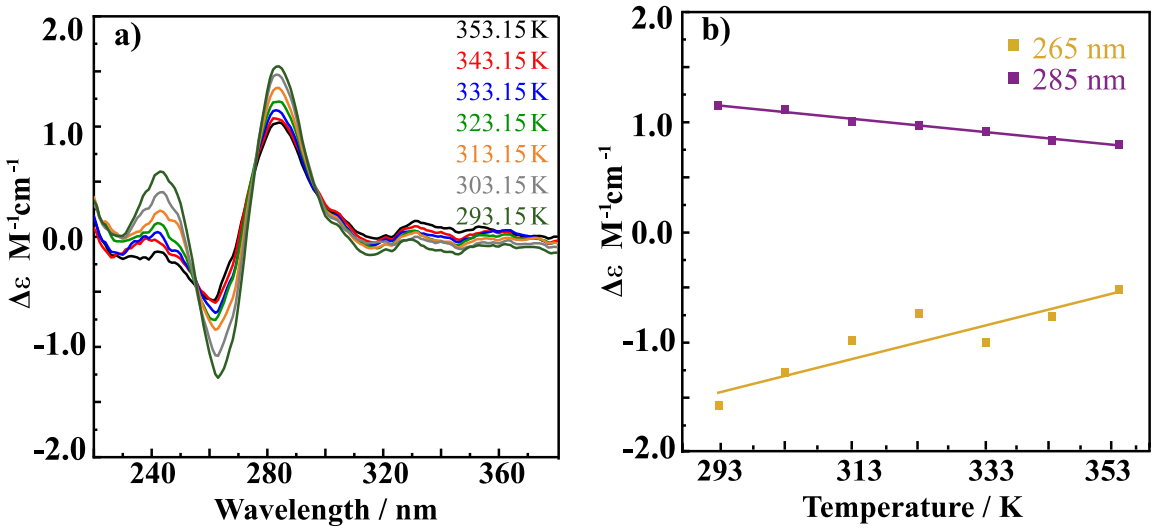

Figure 4.5 (a) d(GpT) CD spectra taken in the range 293 ≤ T ≤ 353 K, and (b) temperature dependence of maxima and minima observed in (a). Note that these data are given in units of molar ellipticity per residue.

Temperature dependent CD measurements were used to further investigate the stacking of d(GpT) in a 1 μM d(GpT) buffered D_2O solution. As the temperature was ramped from 293 to 353 K, CD spectra showed a decreased molar ellipticity associated with peaks at 265 and 285 nm (see Figure 4.5 (a) and (b)). A qualitative interpretation of the spectrum in Figure 4.5 (a) shows that the number of π-stacked molecules in solution is directly proportional to the change in temperature. At higher temperature, the additional thermal energy allows molecules to explore a broader range of the conformational free energy surface; therefore, it reduces the total number of π-stacked molecules in the ensemble.

4.3.4 Transient Absorption Spectroscopy

Ultrafast transient absorption spectroscopy was used to investigate the excited state dynamics of d(GpT), dGMP and dTMP using 273 and 257 nm photoexcitation. TA spectra obtained from 273 nm photoexcitation of three solutions at many different pump-probe time delays, *t*, are displayed in Figure 4.6 ((a) - (c)). Corresponding data for 257 nm excitation is shown in Figure 5 ((d) - (f)). The TA spectra for dGMP (Figure 4.6 (a) and (d)) are dominated by a positive ESA signal which has two local maxima centred at ~360 and ~550 nm. The frequency dispersed TA data are reminiscent of studies by Stuhldreier *et al.*, although the previous study used 260 nm excitation.[20]

The dTMP TA spectra (Figure 4.6 (b) and (e)) contain two main features; a negative peak centred at 357 nm and an ESA that spans the entire probe window with a maximum at 610 nm. The negative feature corresponds to stimulated emission (SE) from the short-lived $^1\pi\pi^*$ state, consistent with prior static and ultrafast spectroscopy studies.[38–40] The d(GpT) TA spectra, Figure 5 ((c) and (f)), are dominated by a broad ESA feature which bears little resemblance to the spectra of the constituent mononucleotides.

Kinetic traces for the peak of the ESA signals in the six datasets are displayed in Figure 4.7 (273 (a) and 257 (b)). These data were fitted to exponential decays convolved with a Gaussian instrument response function. As evident from both the frequency dispersed TA data (Figure 4.6) and the time constants returned from fitting these data (Table 4.1), almost all dTMP and dGMP molecules decay rapidly to the ground state within 1–2 ps at both excitation wavelengths, in accord with previous studies,[41–43] whereas the dinucleotide decays more slowly, and an additional 11 ± 2 ps exponential decay component was required to fit the data.

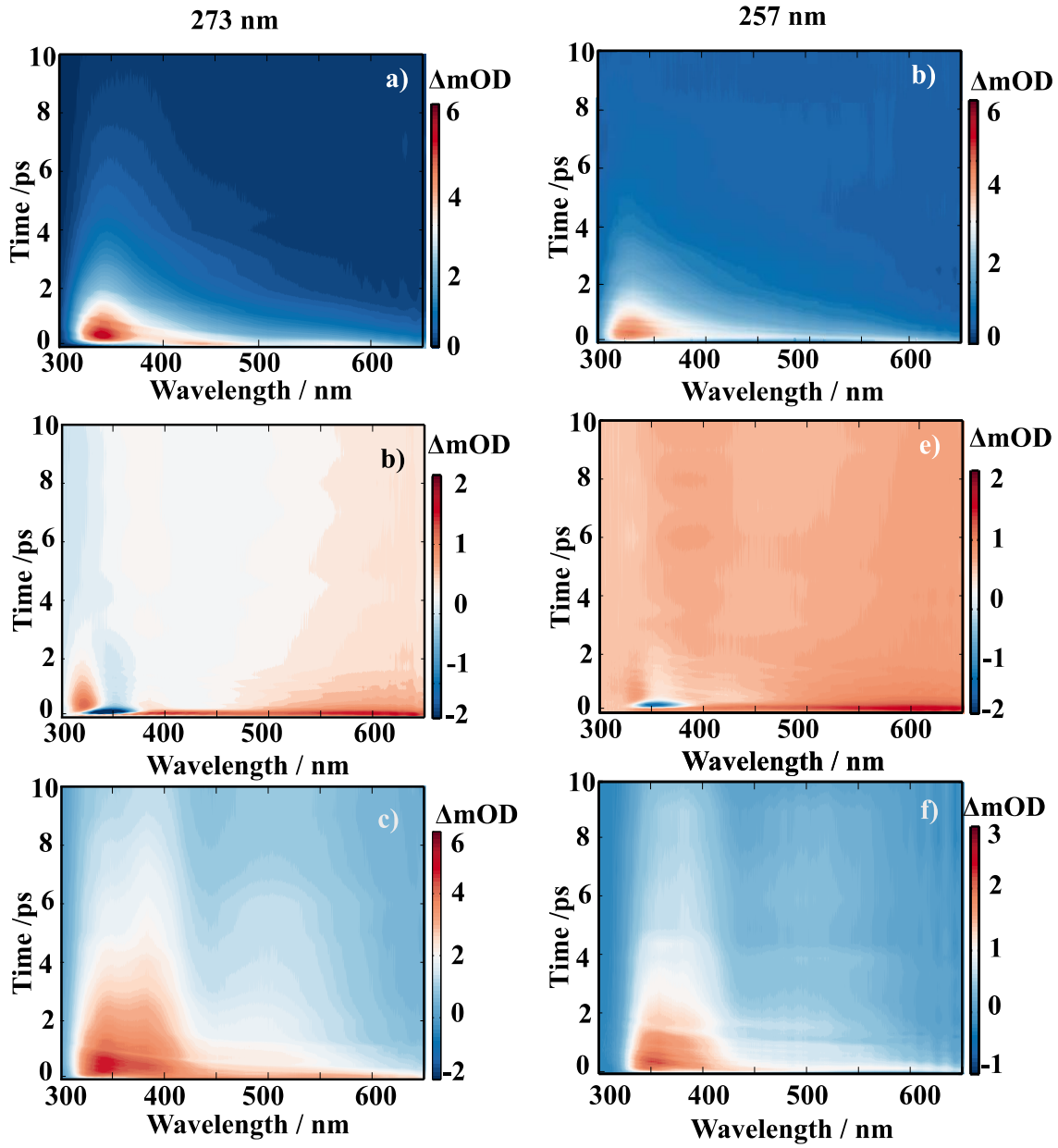

Figure 4.6 273 and 257 nm pump and white light supercontinuum probe TA spectra for (a, d) dGMP, (b, e) dTMP and (c, f) d(GpT) aqueous solutions (pD 7) for delay times up to $t \leq 10$ ps. Note the different intensity scales used for each panel.

What is not apparent from these data is any indication of the electronic structure of the photoexcited molecules from the diffuse excited state absorption signals. Due to the size of the d(GpT) molecule, conformational complexity, and the density of electronic states that fall within the 1.8–3.8 eV white light probe window, it would be complicated to calculate

all the $S_n \leftarrow S_m$ transition dipole moments at a high level of *ab initio* theory for multiple conformers, a range of excited state (S_m) and many possible product species. Such an approach has only been successful for modelling the S_1 ESA spectrum of smaller UV chromophores.[44] As many other groups have demonstrated, ultrafast mid-infrared probe experiments can yield additional information about the reaction dynamics of the system, such timescales for photoproduct formation.[7,10,17,45]

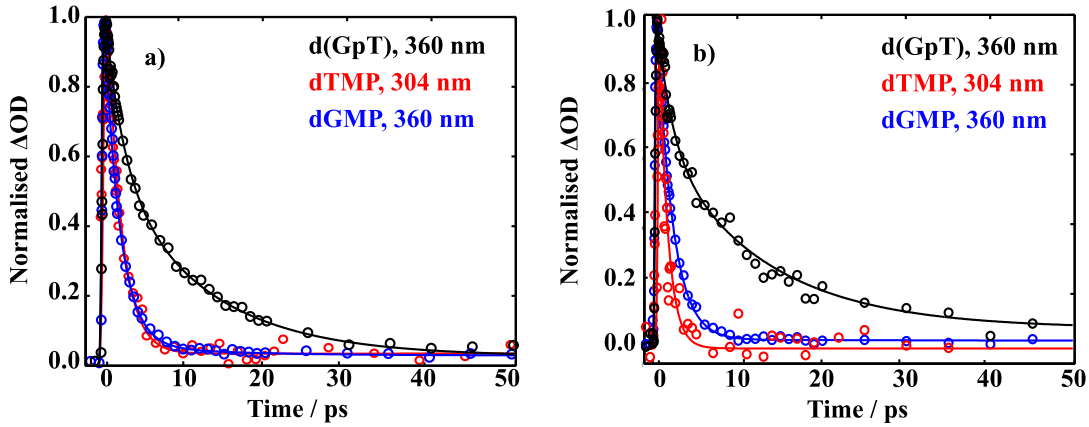

Figure 4.7 Normalised TA data (open circles) for the displayed probe wavelengths of dGMP, dTMP and d(GpT) under (a) 273 and (b) 257 nm photoexcitation. Solid lines display the fits to experimental data (see Table 4.1 for fit parameters).

Table 4.1 Kinetic fits to specific probe wavelengths of d(GpT), dGMP, and dTMP samples.

Sample	Pump / nm	Probe / nm	τ_1 / ps	A_1 (%)	τ_2 / ps	A_2 (%)	τ_3 / ns	A_3 (%)	R^2
d(GpT)	257	360	3 ± 2	43	9 ± 7	55	>1	2	0.99
	273	360	2.1± 0.7	45	11 ± 2	52	>1	3	0.99
dGMP	257	360	1.78 ± 0.07	90	> 1 ns	10	-	-	0.98
	273	360	2.1 ± 0.4	88	> 1 ns	12	-	-	0.99
dTMP	257	304	0.46 ± 0.04	93	> 1 ns	7	-	-	0.97
	273	304	1.4 ± 0.3	90	> 1 ns	10	-	-	0.94

4.3.5 Time-Resolved Infrared Spectroscopy

TRIR data collected using 273 nm photoexcitation is displayed in Figure 4.8 for (a) an equimolar mixture of dGMP, and dTMP, and (b) d(GpT) solutions, the corresponding TRIR data recorded with 257 nm pump pulses are displayed in Figure 4.8 ((c), (d)). The spectra are congested with overlapping positive and negative vibrational transient features.

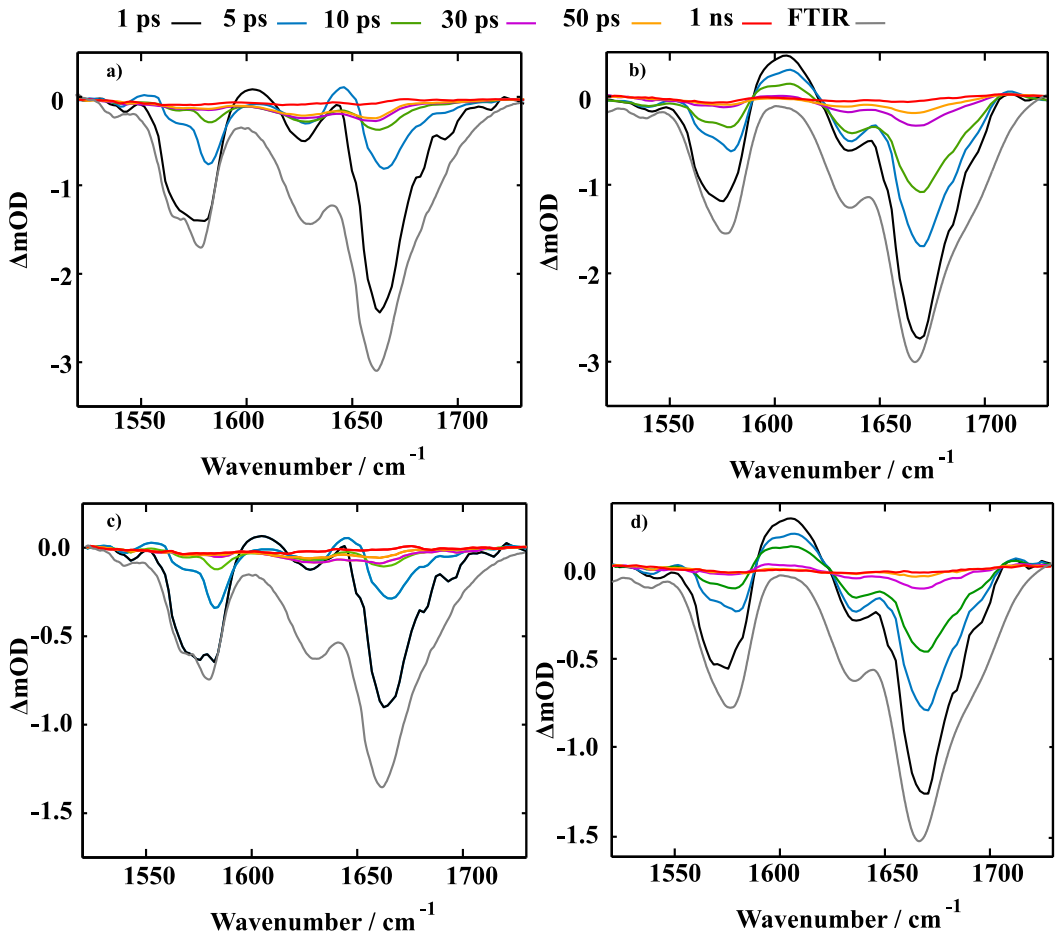

Figure 4.8 TRIR data for (a) equimolar mixture of dGMP + dTMP and (b) d(GpT) upon 273 nm photoirradiation. Data for 257 nm photoexcitation is given in panels (c) and (d). The grey line in each panel displays the respective inverted FTIR spectrum. The time delays are displayed on the top.

Both datasets are dominated by negative bands corresponding to transients that evolve on

the ground state during the pump-probe time delay and appear at the same, or very similar, frequencies as the main features present in the respective linear FTIR spectra. The analysis first focuses on the recovery of negative features centred at 1666, 1575 and 1635 cm^{-1}. The negative band centred at 1666 cm^{-1} corresponds to overlapping vibrational features associated with carbonyl stretching vibrations localised on guanine and thymine moieties. The associated kinetics of this feature for the mixture of mononucleotides and dinucleotide upon 273 nm photoirradiation are shown in Figure 4.9 (a), while panel (b) shows the kinetics for 257 nm photoexcitation.

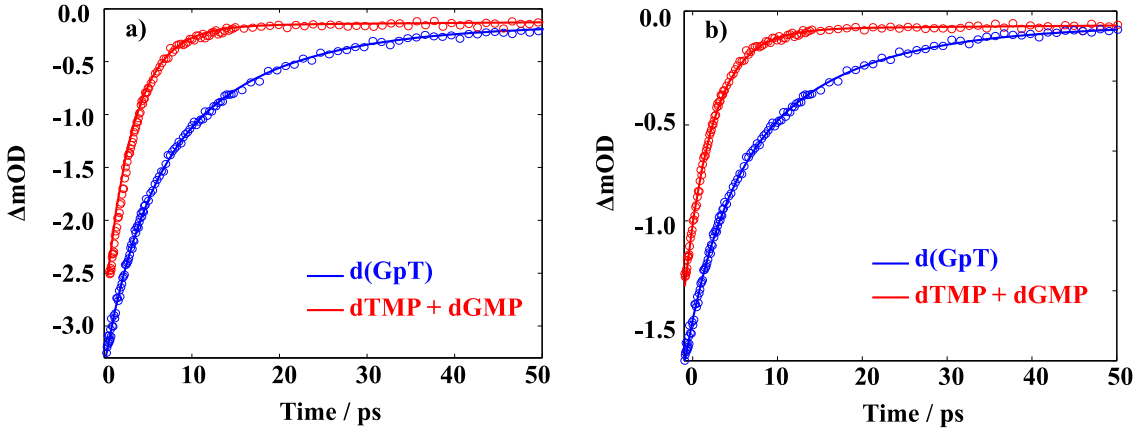

Figure 4.9 (a) Kinetics associated with 1666 cm^{-1} bleach feature for the mixture of mononucleotides (red open circles) and d(GpT) (blue open circles) upon 273 nm photoexcitation. Solid lines display the fits to experimental data (see Table 4.2 for fit parameters). Data for 257 nm excitation are given in panel (b).

The data were fitted to biexponential and triexponential functions, respectively, and the results summarised in Table 4.2. It is evident from the amplitudes and time constants returned from fitting, that a significant number of photoexcited d(GpT) molecules (54 and 51% for 273 and 257 nm excitation, respectively) have a longer excited state lifetime than the constituent mononucleotides.

Table 4.2 Amplitudes and time constants returned from fitting 273 and 257 nm pump, 1666 cm^{-1} probe TRIR data of d(GpT) and dGMP + dTMP solutions.

d(GpT) at 273 nm		**dGMP + dTMP at 273 nm**	
A_1 = 41 %	τ_1 = 4.1 ± 0.3 ps	A_1 = 94 %	τ_1 = 3.22 ± 0.02 ps
A_2 = 54 %	τ_2 = 13 ± 1 ps	A_2 = 6 %	τ_2 > 1 ns
A_3 = 5 %	τ_3 > 1 ns		R^2 = 0.99
	R^2 = 0.99		
d(GpT) at 257 nm		**dGMP + dTMP at 257 nm**	
A_1 = 47 %	τ_1 = 5.8 ± 0.4 ps	A_1 = 92 %	τ_1 = 3.47 ± 0.03 ps
A_2 = 42 %	τ_2 =19 ± 2 ps	A_2 = 8 %	τ_2 > 1 ns
A_3 = 11 %	τ_3 > 1 ns		R^2 = 0.99
	R^2 = 0.99		

The analysis of the negative features at 1575 (G band) and 1635 (T band) cm^{-1} which reports a return to ground state and vibrational cooling of S_0, are shown in Figure 4.10 and the lifetimes returned from the kinetic fits are given in Table 4.3. Fits to these data return similar time constants to the 1666 cm^{-1} feature; however, the kinetics associated with each of the vibrational bands are not identical. It might be due to contamination of overlapping adjacent features which have differing spectral shifts, and mode-dependent vibrational cooling timescales as observed in other DNA systems.[46,47] Like the TA data, the TRIR data contain a small-amplitude nanosecond component, which has been attributed to long-lived triplet species.[48,49]

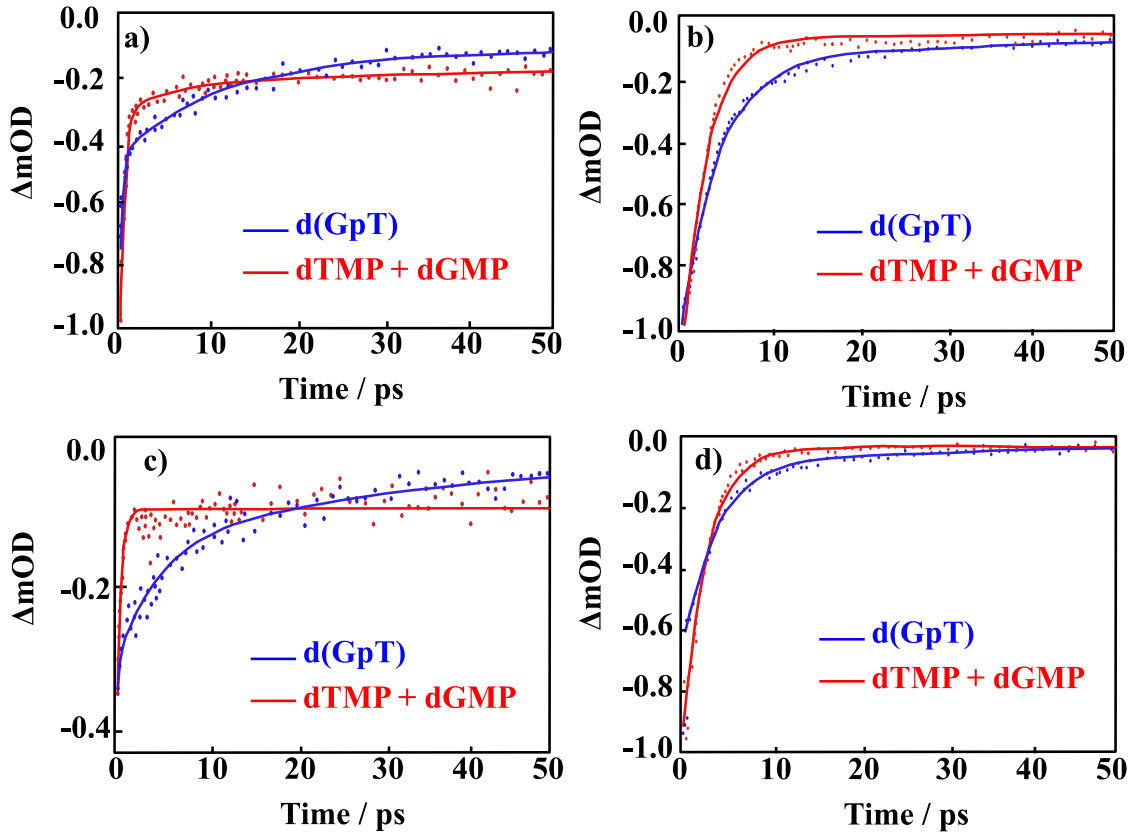

Figure 4.10 (a) Kinetics associated with 1635 cm^{-1} (T band) bleach feature for the mixture of mononucleotides (red circles) and d(GpT) (blue circles) upon 273 nm photoexcitation. (b) Kinetics for 1575 cm^{-1} (G band) upon 273 nm photoexcitation. Data for 257 nm excitation are given in panels (c) and (d) for 1635 and 1575 cm^{-1} probe frequency, respectively. The solid lines display the fits to experimental data.

Three positive features in the mixture of mononucleotides spectra are present at $t < 5$ ps (see Figure 4.8 (a) and (c)) and correspond to the vibrationally hot S_0 population that are formed promptly after ultrafast internal conversion to the ground state. The features at 1550, 1600 and 1655 cm^{-1} are red-shifted compared to the respective fundamental negative features due to the associated anharmonicity of the respective S_0 vibrational potentials. The dinucleotide data has significantly more amplitude associated with the 1580–1615 cm^{-1} feature compared to the mixture of mononucleotides spectra. Further, the d(GpT) TRIR spectra contain an additional isolated vibrational band centred at 1708 cm^{-1}, which is a

known signature of the guanine cation (G^+).[7,50–52] Based on prior studies[6,7,13,53] and the absence of any appreciable signature of solvated electron formation in TA spectra, it can be concluded that G^+ will be produced in conjunction with thymine anions (T^-) as part of an ion-pair exciplex. G^+ is only observed for irradiation of d(GpT) solutions and not the mixture of dGMP and dTMP. Therefore, it is apparent that changes in the electronic structure induced by π-stacking must be crucial to mediate exciplex formation.

Table 4.3 Kinetic fits associated with specific vibrational bands for 273 and 257 nm excitation of d(GpT) and the mixture of mononucleotide TRIR spectra.

Probe freq. / cm^{-1}	**d(GpT) (273 nm)**	**Amplitude**	**d(GpT) (257 nm)**	**Amplitude**
1575 cm^{-1} (G)	τ_1 = 4.1 ± 0.8 ps τ_2 = 33 ± 17 ps τ_3 > 1 ns R^2 = 0.99	A_1 = 75 % A_2 = 25 % A_3 = 3 %	τ_1 = 3.1 ± 0.8 ps τ_2 = 27 ± 7 ps τ_3 > 1 ns R^2 = 0.97	A_1 = 72 % A_2 = 26 % A_3 = 2 %
1635 cm^{-1} (T)	τ_1 = < 1 ps τ_2 = 11.4 ± 0.7 ps τ_3 > 1 ns R^2 = 0.98	A_1 = 67 % A_2 = 27 % A_3 = 6 %	τ_1 = 4.2 ± 0.8 ps τ_2 = 26 ±5 ps τ_3 > 1 ns R^2 = 0.95	A_1 = 65 % A_2 = 28 % A_3 = 7 %
Probe freq. / cm^{-1}	**Mixture (273 nm)**	**Amplitude**	**Mixture (257 nm)**	**Amplitude**
1575 cm^{-1} (G)	τ_1 = 2.9 ± 0.1 ps τ_2 > 1 ns R^2 =0.98	A_1 = 98 % A_2 = 2 %	τ_1 = 2.91 ± 0.07 ps τ_2 > 1 ns R^2 = 0.98	A_1 = 97 % A_2 = 3 %
1635 cm^{-1} (T)	τ_1 < 1 ps τ_2 > 1 ns R^2 = 0.98	A_1 = 98 % A_2 = 2 %	τ_1 < 1 ps τ_2 > 1 ns R^2 = 0.95	A_1 = 99 % A_2 = 1 %

Extracting the kinetics associated with the G^+ feature requires careful deconvolution with

an adjacent oppositely signed large amplitude feature which in principle does not have similar kinetics. The TRIR spectra at every pump-probe time delay were then fitted to the sum of Gaussian basis functions to model the vibrational dynamics as per ref[54]. Constraints were placed on negative features, enforcing the full width half maximum (FWHM) and central frequency were fixed to those of the (inverted) linear FTIR spectrum. This approach was preferred to a target analysis, which would struggle to capture the vibrational mode dependent cooling rates. The simulated spectra returned by the analysis are in excellent agreement with experimental TRIR.

More in details, the global target analysis of TRIR data used Gaussian fits to the 5 bands in the relevant probe region of the FTIR spectrum as functions for the 5 main negative bands in each spectrum. The central frequency and FWHMs were fixed to the fits to the linear spectra. An additional three positive Gaussians were chosen to correspond to hot S_0 transients at ~1550 and 1590 cm^{-1}. A third positive feature centred at 1708 cm^{-1} was used to model the G^+ cation formation. As no guide for these positive features (central frequency or peak width) is known, these parameters were allowed to float alongside the amplitudes of each of the 8 features. The vibrational ground state cooling has been determined to be mode dependent, the kinetics of the bleach features were independently fitted. These parameters were fitted for each pump-probe time delay. The resulting fits to each time delay are shown alongside the original data in Figure 4.11. Panels (a) and (b) are the TRIR and the corresponding target analysis upon 273 nm photoirradiation while (c) and (d) are for 257 nm photoirradiation and example fits to specific probe wavelengths are displayed in Figure 4.12 (a) for 273 nm excitation and (b) 257 nm.

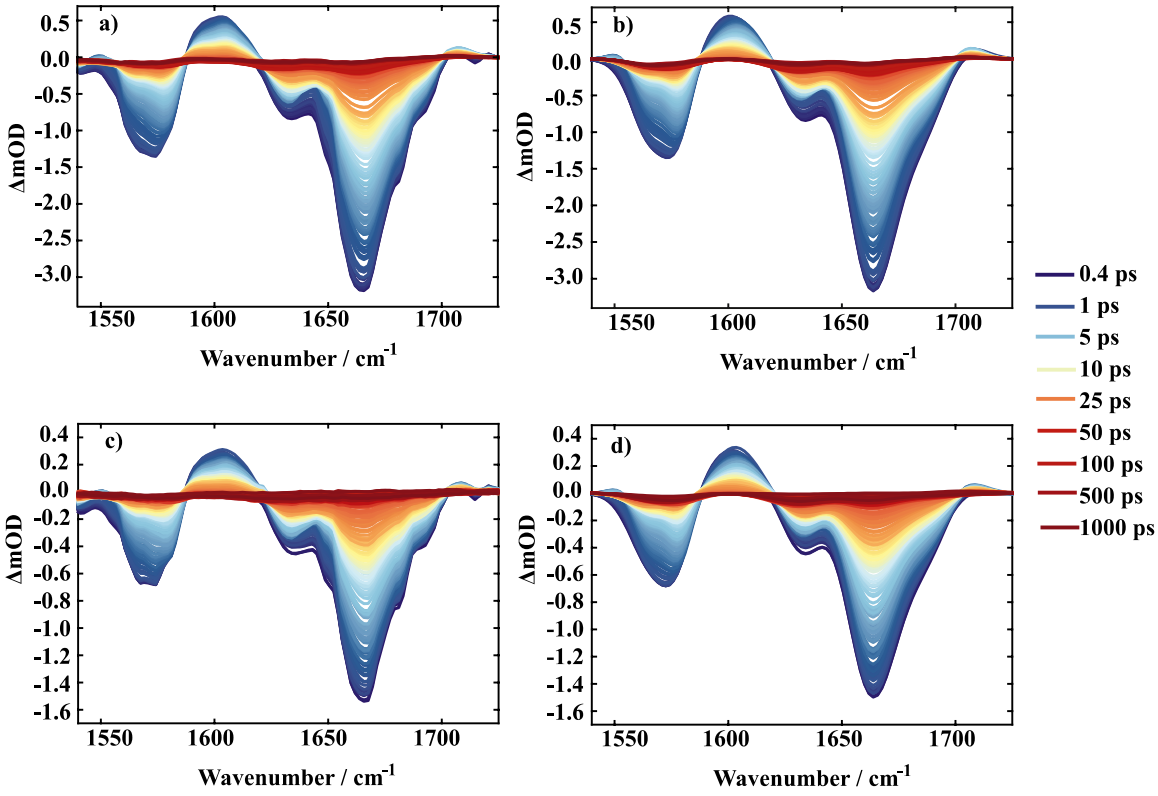

Figure 4.11 (a) 273 nm TRIR data and corresponding (b) target analysis. (c) 257 nm TRIR data and (d) corresponding target analysis.

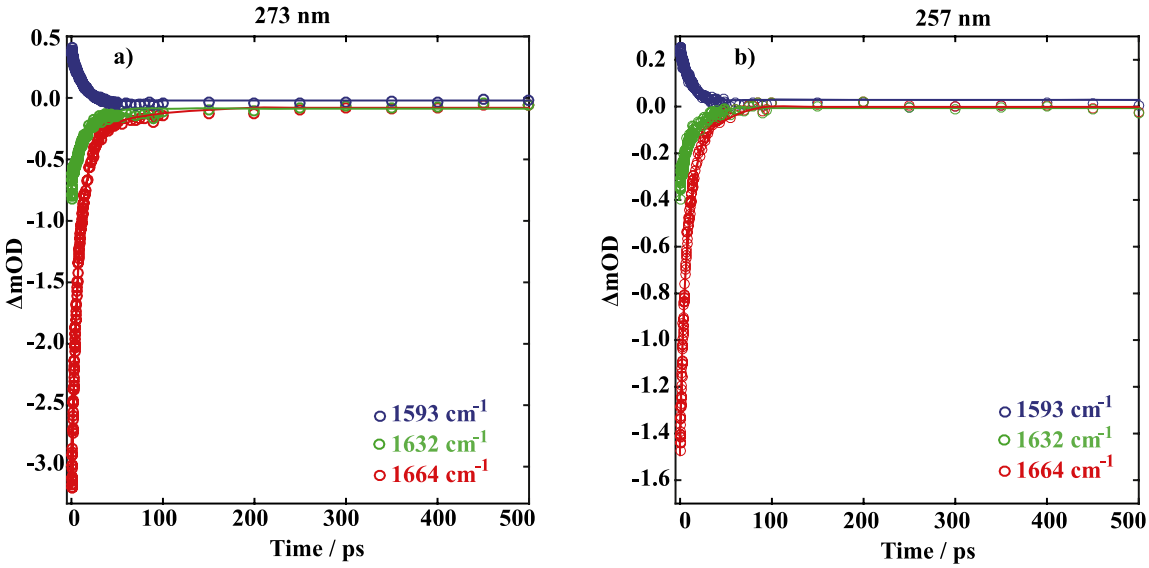

Figure 4.12 Examples of kinetic fits to specific wavelength probe regions for (a) 273 nm and (b) 257 nm irradiation.

The kinetics associated with the G^+ feature returned by Gaussian fitting for (a) 273 nm and (b) 257 nm excitation are given in Figure 4.13 and were fitted to an exponential decay with a 10.5 ± 0.2 ps and 11.1 ± 0.3 ps time constants, respectively. The guanine cation is formed so rapidly that it appears within the instrument response (~350 fs) and based on LR-TDDFT calculations it was possible to determine that this species can only be formed from π-stacked d(GpT) conformers. The experimentally determined oxidation and reduction potentials for the isolated DNA nucleobases[55] allows me to predict that d(G^+pT^-) is the most probable ion-pair product and ~1.3 eV more stable than d(G^-pT^+). This estimate is consistent with the observation of a G^+ vibrational signature at 1708 cm^{-1}. Despite observing a direct spectral signature associated with G^+, it was not possible to isolate the expected vibrational bands corresponding to T^-, which are expected between ~1650–1595 cm^{-1}.[53,56] Partially, it occurs because they will overlap with transients associated with the neutral molecule, but several other vibrational features associated with G^+ are also expected in this region.[7]

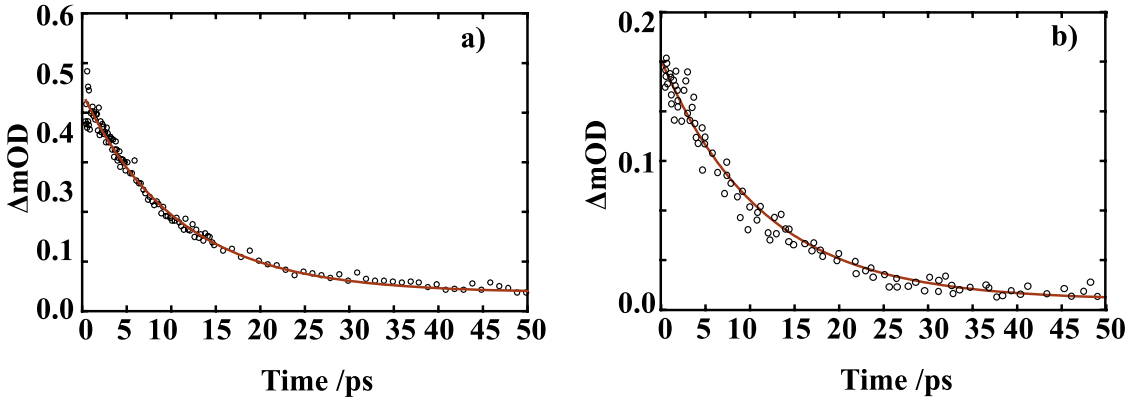

Figure 4.13 Kinetics associated with 1708 cm^{-1} feature from Gaussian fitting analysis of d(GpT) TRIR data upon (a) 273 and (b) 257 nm photoexcitation.

A comparison of TRIR data acquired at t = 350 fs with 273 and 257 nm excitation (see Figure 4.14 (a) and (b)) allows for the exploration of the nature of the initial vertical Franck-

Condon electronic states and the relative yield of $d(G^{+}pT^{-})$ product branching. From the different linear absorption cross-sections of the two mononucleotides at these two wavelengths, a preferential excitation of thymine is expected at 273 nm, and guanine at 257 nm (recall Figure 4.2 (a)). The TRIR data bear out this expectation; in the mixture of mononucleotides TRIR spectrum (Figure 4.14 (a)) more intense bleaching associated with vibrational bands unique to guanine is observed at 257 nm (1580 cm^{-1}), with thymine bands enhanced for 273 nm excitation (1630 cm^{-1}). If the electronically excited states of d(GpT) are localised to either chromophore then the relative ratio of bleaches at 1580 and 1630 wavenumber varying between pump excitation wavelengths in the dinucleotide TRIR data would be observed. As Figure 4.14 (b) illustrates the TRIR spectra at t = 350 fs are very similar, which implies a roughly equal number of guanine and thymine moieties are photoexcited at both excitation wavelengths. This observation is only possible if the vertical Franck-Condon states are significantly delocalised over both nucleobases. This comparative analysis has been performed for t = 350 fs data, as it is earliest time delay outside of the IRF window and before any excited state equilibration. Such processes may involve localisation of population to either nucleobase[16] and/or subsequent inter-nucleobase electronic energy transfer: either inevitably would lead to differential changes in the G/T bleach ratio. Such a hypothesis is consistent with the theoretical studies: the transition-density matrix analysis of LR-TDDFT calculations for $d(GpT)_s$ revealed the electron/hole distributions of the vertical singlet excited state are not exclusively localised to a single nucleobase, but depending on the specific dinucleotide geometry, contain $G \rightarrow T$ charge-transfer character and significant delocalisation across both guanine and thymine moieties. Notably, the lowest energy excited states with appreciable oscillator strengths, for either of the two stacked d(GpT) conformers are dominantly delocalised in character. Furthermore, prior theoretical calculations have estimated inter-nucleobase electronic

coupling constants between 50 and 775 cm^{-1} for several dinucleotides,[17,57] which is consistent with Franck-Condon delocalised adiabatic electronic states. What is more remarkable, however, is the relative intensity of the guanine cation feature appears to be very similar for the two excitation wavelengths compared to the shared G/T bleach feature at 1666 cm^{-1} and thus implies that the probability of $d(G^{+}pT^{-})$ formation is almost equal upon 273 and 257 nm excitation. What has not been determined is the absolute quantum yield for $d(G^{+}pT^{-})$ formation due to the uncertainty in the S_0 $d(GpT)_s$: $d(GpT)_o$ ratio. As such it is not possible to rule out competing monomer-like non-radiative pathways in photoexcited π-stacked species, wherein dynamics remain localised to either nucleobase and follow similar non-radiative decay pathways to either dGMP or dTMP.

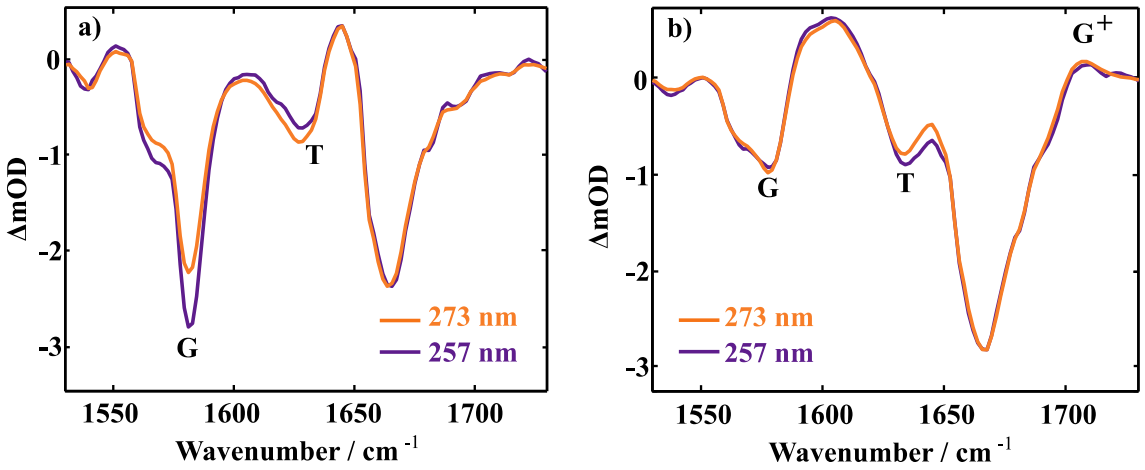

Figure 4.14 Overlaid TRIR data for *t* = 350 fs at 273 and 257 nm excitation for (a) dGMP + dTMP mixture and (b) d(GpT) solutions. Note that the 273 nm data is scaled to match the signal intensity of the 273 nm data at 1666 cm^{-1}.

4.4 General Discussion

Prior TRIR studies of di- or tri-nucleotides incorporated non-naturally abundant nucleic acids[7,13] to investigate excited state charge-transfer. The incorporation of non-abundant nucleobases in these two studies increases the energy gap between the decoupled

nucleobase excited state. It thus reduces inter-nucleobase dipole-dipole coupling, resulting in excited state with more localised electronic character. In the study of the dinucleotide comprised of 8-oxo-7,8-dihydroguanine (O) and adenine (d(OpA)), Zhang *et al.* observed a wavelength dependence to the charge-transfer product yield.[13] At the longest excitation wavelength, it was possible to selectively excite the O moiety in d(OpA), which initiated an inter-molecular excited state charge-transfer reaction with the adenine nucleobase yielding $d(O^{+}pA^{-})$ products. Using shorter wavelength to photoexcite d(OpA), the optically excited state was found to be delocalised across both O and A moieties, via the relative intensity of the O and A bleach features but reacted to produce a higher yield of $d(O^{+}pA^{-})$. The dynamics observed for the shorter wavelength excitation of d(OpA), are similar to those I have observed for d(GpT). However, the yield of $d(G^{+}pT^{-})$ products and the nature of the d(GpT) photoexcited state is seemingly independent of 273 or 257 nm excitation wavelength. The model dinucleotide d(GpT) contains naturally abundant nucleobases, and the decoupled excitation energies of the S_1 G and S_2 T states are very close in energy and thus significant electronic coupling (as evident in the transition-density matrix analyses) dramatically influences the nature of the Franck-Condon excited state. It can be expected that this will be true for di- or poly-nucleotide structures containing naturally abundant nucleobases, as the energy difference between the lowest energy excited state of all natural nucleobases is modest, and the dipole coupling predicted to be strong.

The combined experimental and theoretical study of a dinucleotide that contains naturally abundant occurring nucleobases supports a mechanism which is summarised by the schematic diagram given in Figure 4.15; the low-lying Franck-Condon excited state of $d(GpT)_s$ possess a mixture of charge-transfer and delocalised character that is very dependent on the precise molecular conformation. For π-stacked conformers, the lowest

energy transitions with high oscillator strengths are delocalised in nature. These states mediate ultrafast (< 350 fs) formation of d(G^+pT^-) exciplexes. In a diabatic picture, this suggests there will be a surface crossing between valence and ion-pair electronic states very close to the vertical Franck-Condon region and mediates rapid exciplex formation. The precise details of which states are involved is difficult to ascertain due to the density of near degenerate electronic states, with the energetic ordering inevitably very dependent on the precise nuclear geometry.

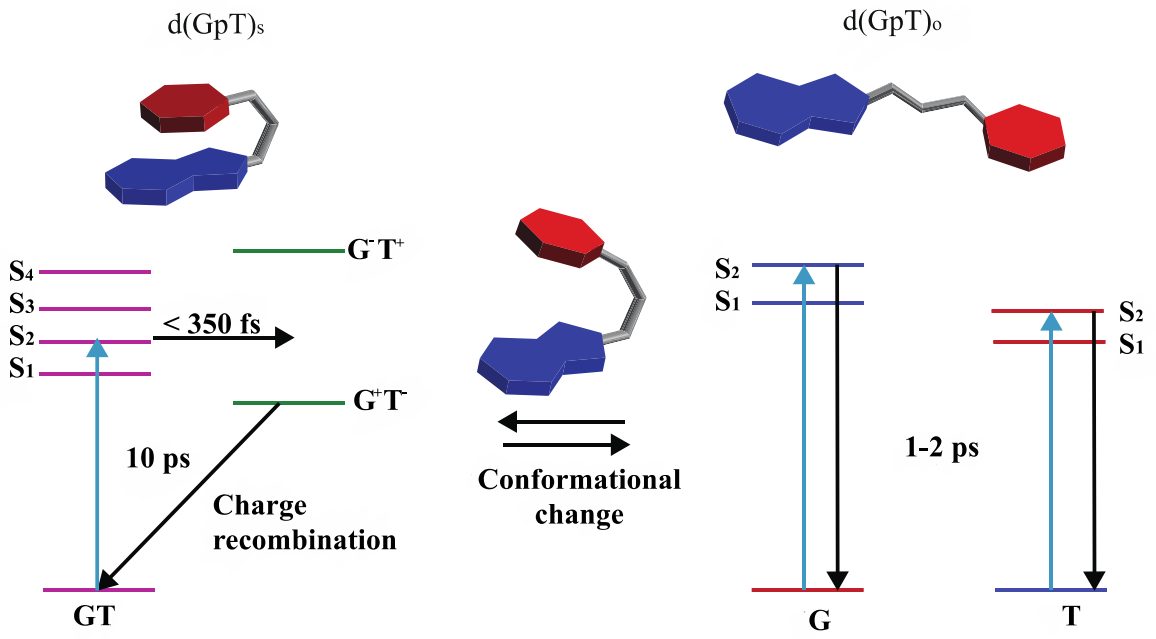

Figure 4.15 Schematic summary of photoinduced dynamics of d(GpT), where T is represented by red hexagons, G by fused blue hexagon and pentagons, and the phosphate-sugar backbone by a grey tube.

Either for dinucleotides that are unstacked in S_0 or rapidly undergo a conformational transformation into unstacked conformers, molecules will follow a non-radiative relaxation pathway similar to the respective mononucleotides, which includes passage through conical intersections facilitating the rapid funnelling of molecules back to the ground state on a ~1–2 ps timescale.

The studies of coupled excited state chromophores all hinge around the dynamical relationship between the so-called ‘exciton’ (adiabatic) and ‘site’ (diabatic) bases. Ideally, the time-dependent coupling between different diabatic states would be followed by on-the-fly dynamical calculations; however, at present, the computational cost for systems such as d(GpT) prohibit such simulations. From an experimental perspective, one possible route is via application of two-dimensional electronic-vibrational spectroscopy in the ultraviolet, to study time-dependent correlations between broadband (delocalised) UV electronic excitation and (localised) vibrational emission.[58–60]

4.5 Conclusions

Ultrafast transient absorption and time-resolved infrared spectroscopies, alongside theoretical calculations, were used to investigate the photoinduced exciton dissociation in thymine 2'-deoxyguanosine-3'-monophosphate-5'-thymidine, d(GpT) in buffered aqueous solution. Femtosecond transient absorption spectroscopy revealed the excited state lifetime of data of d(GpT) has an additional ~10 ps decay lifetime component of upon 273 and 257 nm photoexcitation compared to its constituent mononucleotides. Time-resolved infrared measurements (TRIR) revealed the molecular origin of this extended excited state lifetime via the presence of a vibrational signature which is univocally assigned to the guanine cation in the dinucleotide which is formed as part of d($G^{+}pT^{-}$) exciplexes.

A direct comparison of d(GpT) TRIR spectra for different excitation wavelengths indicates that the initial Franck-Condon photoexcited state of d(GpT) must be significantly delocalised across guanine and thymine moieties. Calculations show that the low-lying Franck-Condon states are comprised from a complex mixture of delocalised, charge-transfer and localised character depending on the specific nuclear configuration. These

states act as a precursor to d(G^+pT^-) exciplexes that are formed on a < 350 fs timescale, and I propose it occurs via a surface-crossing between diabatic valence and ion-pair potential energy surfaces. The study focuses on a dinucleotide structure that contains naturally abundant nucleobases, whereas prior TRIR studies,[7,13] have examined the dynamics of di- or tri-nucleotides and have incorporated non-naturally abundant nucleobases into structures, which detunes the intermolecular electronic coupling. Due to the very similar excitation energies of the lowest energy bright states of natural nucleobases, and the large electronic coupling dipole strengths associated between them,[17,57] the dynamics observed for d(GpT) is expected to be representative in natural DNA sequences. The photogenerated d(G^+pT^-) charge-transfer products are short-lived (~10 ps) and ground state neutral d(GpT) molecules are reformed with a high quantum yield and may guarantee the photostability of DNA avoiding deleterious reactions (*i.e.*, dimerisation and/or bond-cleavage) after photoexcitation.[1,2]

4.6 Appendix

Ap. 4.1 Nuclear Magnetic Resonance

The NMR spectra of d(GpT) are reported to show the purity of d(GpT).

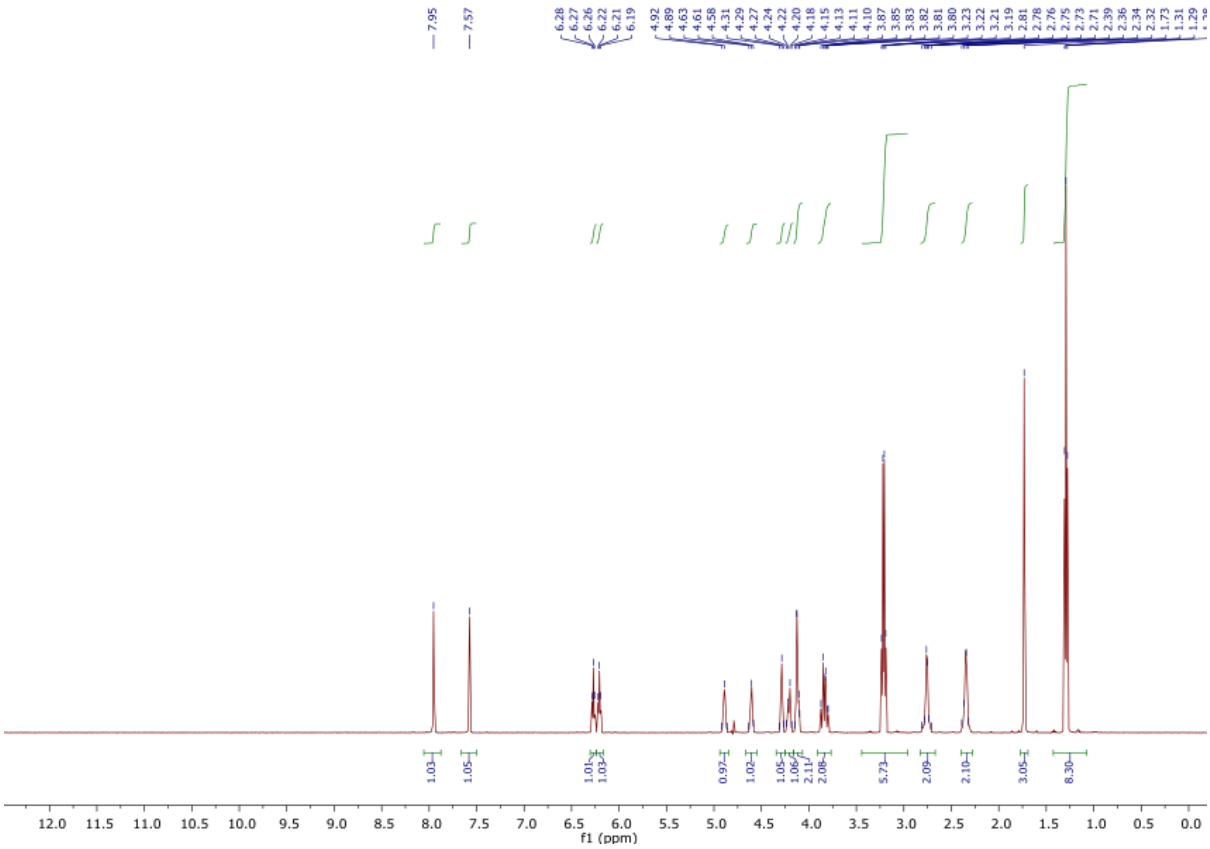

Figure Ap. 4.1 ^{1}H-NMR 500 MHz spectrum of d(GpT) in D_2O.

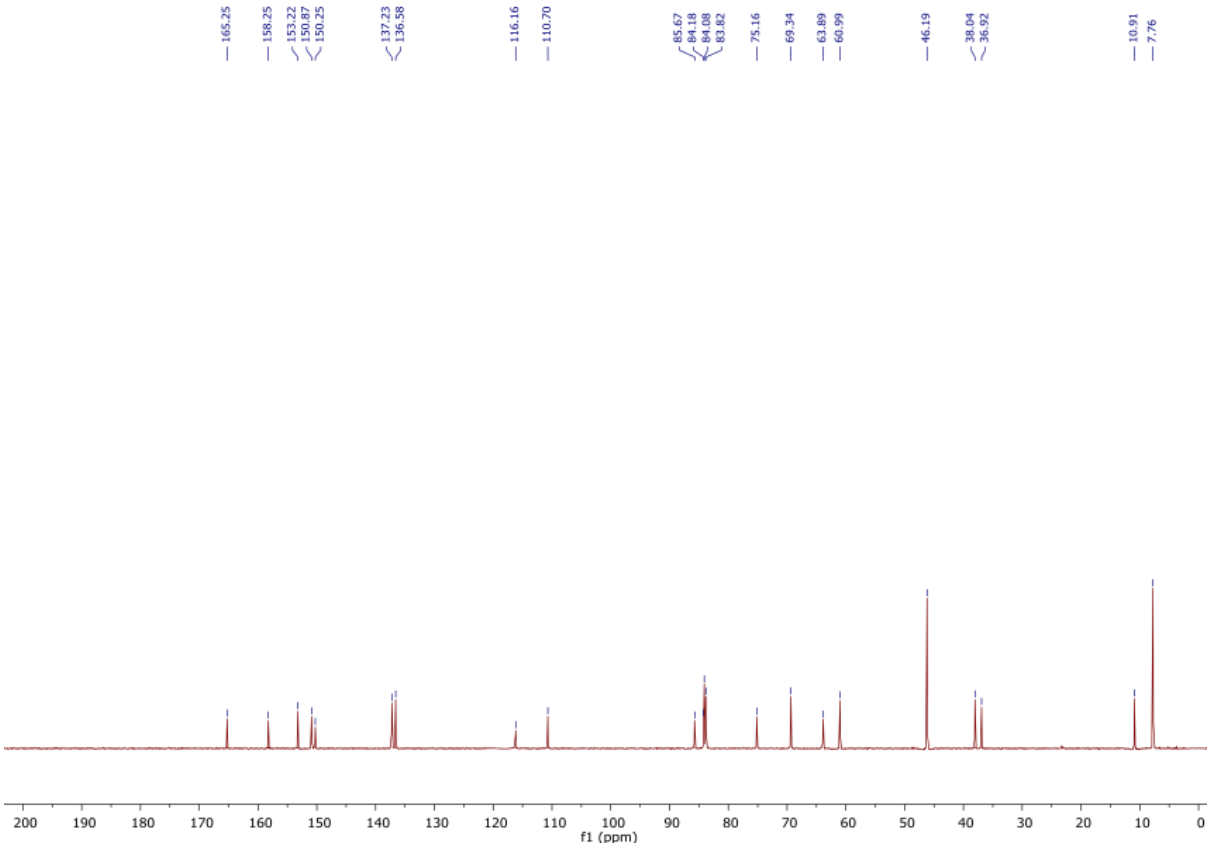

Figure Ap. 4.2 ^{13}C-NMR 126 MHz spectrum of d(GpT) in H_2O

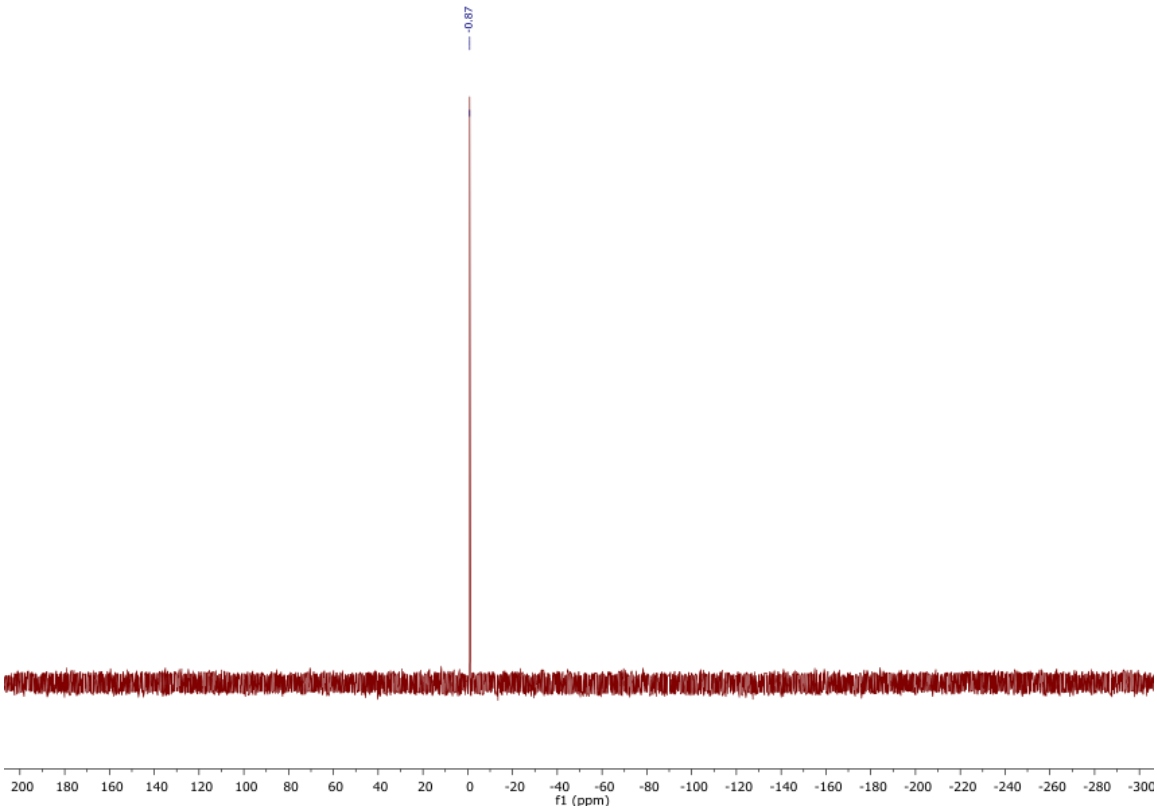

Figure Ap. 4.3 ^{31}P-NMR 400 MHz spectrum of d(GpT) in H_2O.

References

1. Taylor, J. Unraveling the Molecular Pathway from Sunlight to Skin Cancer. *Acc. Chem. Res.* **27**, 76–82 (1994).

2. Sinha, R. P. & Häder, D. P. UV-induced DNA damage and repair: a review. *Photochem. Photobiol. Sci.* **1**, 225–236 (2002).

3. Markovitsi, D., Gustavsson, T. & Banyasz, A. Absorption of UV radiation by DNA: spatial and temporal features. *Mutat. Res.* **704**, 21–28 (2010).

4. Middleton, C. T., de La Harpe, K., Su, C., Law, Y. K., Crespo-Hernandez, C. E. & Kohler B. DNA excited state dynamics: from single bases to the double helix. *Annu. Rev. Phys. Chem.* **60**, 217–239 (2009).

5. Buchvarov, I., Wang, Q., Raytchev, M., Trifonov, A. & Fiebig, T. Electronic energy delocalization and dissipation in single- and double-stranded DNA. *Proc. Natl. Acad. Sci.USA.* **104**, 4794–4797 (2007).

6. Takaya, T., Su, C., kimberly de Harpe, L., Crespo-Hernandez, C. E. & Kohler, B. UV excitation of single DNA and RNA strands produces high yields of exciplex states between two stacked bases. *Proc. Natl. Acad. Sci.USA.* **105**, 10285–10290 (2008).

7. Bucher, D. B., Pilles, B. M., Carell, T. & Zinth, W. Charge separation and charge delocalization identified in long-living states of photoexcited DNA. *Proc. Natl. Acad. Sci.USA.* **111**, 4369–4374 (2014).

8. Crespo-Hernandez, C. E., Cohen, B. & Kohler, B. Base stacking controls excited state dynamics in A·T DNA. *Nature* **436**, 1141–1144 (2005).

9. Zhang, Y., Li, X. B., Fleming, A. M., Dood, J., Beckstead, A. A., Orendt, A. M., Burrows, C. J. & Kohler, B. UV-Induced Proton-Coupled Electron Transfer in Cyclic DNA Miniduplexes. *J. Am. Chem. Soc.* **138**, 7395–7401 (2016).

10. Schreier, W. J., Schrader, T. E., Koller, F. O., Gilch, P., Crespo-Hernandez, C.E., Swaminathan, V. N., Carell, T., Zinth, W. & Kohler, B. Thymine dimerization in DNA is an ultrafast photoreaction. *Science* **315**, 625–629 (2007).

11. Schwalb, N. K. & Temps, F. Base sequence and higher-order structure induce the complex excited state dynamics in DNA. *Science* **322**, 243–245 (2008).

12. Hare, P. M., Crespo-Hernandez, C. E. & Kohler, B. Internal conversion to the electronic ground state occurs via two distinct pathways for pyrimidine bases in aqueous solution. *Proc. Natl. Acad. Sci. USA.* **104**, 435–440 (2007).

13. Zhang, Y. Dood, J., Beckstead, A. A., Li, X. B., Nguyen, K. V., Burrows, C. J., Improta, R. & Kohler, B. Efficient UV-induced charge separation and recombination in an 8-oxoguanine-containing dinucleotide. *Proc. Natl. Acad. Sci. USA.* **111**, 11612–11617 (2014).

14. Voityuk, A. A., Rosch, N., Bixon, M. & Jortner, J. Electronic Coupling for Charge

Transfer and Transport in DNA. *J. Phys. Chem. B.* **104**, 9740–9745 (2000).

15. Blancafort, L. & Voityuk, A. A. Exciton delocalization, charge transfer, and electronic coupling for singlet excitation energy transfer between stacked nucleobases in DNA: an MS-CASPT2 study. *J. Chem. Phys.* **140**, 095102 (2014).

16. Improta, R. & Barone, V. Interplay between "Neutral" and "Charge-Transfer" Excimers Rules the Excited State Decay in Adenine-Rich Polynucleotides. *Angew. Chem.* **123**, 12222–12225 (2011).

17. Bouvier, B., Gustavsson, T., Markovitsi, D. & Millie, P. Dipolar coupling between electronic transitions of the DNA bases and its relevance to exciton states in double helices. *Chem. Phys.* **275**, 75–92 (2002).

18. Markovitsi, D., Onidas, D., Gustavsson, T., Talbot, F. & Lazzarotto, E. Collective behavior of Franck-Condon excited state and energy transfer in DNA double helices. *J. Am. Chem. Soc.* **127**, 17130–17131 (2005).

19. Nielsen, L. M., Hoffmann, S. V. & Nielsen, S. Electronic coupling between photo-excited stacked bases in DNA and RNA strands with emphasis on the bright states initially populated. *Photochem. Photobiol. Sci.* **12**, 1273–1285 (2013).

20. Stuhldreier, M. C. & Temps, F. Ultrafast photo-initiated molecular quantum dynamics in the DNA dinucleotide d(ApG) revealed by broadband transient absorption spectroscopy. *Faraday Discuss.* **163**, 173-188 (2013).

21. Burin, A. L., Armbruster, M. E., Hariharan, M. & Lewis, F. D. Sum rules and determination of exciton coupling using absorption and circular dichroism spectra of biological polymers. *Proc. Natl. Acad. Sci. USA.* **106**, 989–994 (2009).

22. Stuhldreier, M. C., Rottger, K. & Temps, F. Distinctive Spectral Features of Exciton and Excimer States in the Ultrafast Electronic Deactivation of the Adenine Dinucleotide. *Ultrafast Phenomena XIX, Springer Proc. Phys.* 452–454 (2015).

23. Samanta, A., Krause, A. & Jaschke, A. A modified dinucleotide for site-specific RNA-labelling by transcription priming and click chemistry. *Chem. Commun.* **50**, 1313–1316 (2014).

24. Donga, R. A., Khaliq-Uz-Zaman, S. M., Chan, T.-H. & Damha, M. J. A novel approach to oligonucleotide synthesis using an imidazolium ion tag as a soluble support. *J. Org. Chem.* **71**, 7907–7910 (2006).

25. Santoro, F., Barone, V. & Improta, R. Can TD-DFT calculations accurately describe the excited state behavior of stacked nucleobases? The cytosine dimer as a test case. *J. Comput. Chem.* **29**, 957–964 (2008).

26. Santoro, F., Barone, V. & Improta, R. Influence of base stacking on excited state behavior of polyadenine in water, based on time-dependent density functional calculations. *Proc. Natl. Acad. Sci. USA.* **104**, 9931–9936 (2007).

27. Raeber, A. E. & Wong, B. M. The Importance of Short- and Long-Range Exchange on Various Excited State Properties of DNA Monomers, Stacked Complexes, and Watson-Crick Pairs. *J. Chem. Theory Comput.* **11**, 2199–2209 (2015).

28. Sun, H., Zhang, S., Zhong, C. & Sun, Z. Theoretical study of excited state of DNA base dimers and tetramers using optimally tuned range-separated density functional theory. *J. Comput. Chem.* **37**, 684–693 (2016).

29. Plasser, TheoDORE 1.4: a package for theoretical density, orbital relaxation, and exciton analysis, 2016, http://Theodore-qc. sourceforge.net.

30. Nogueira, J. J., Plasser, F. & González, L. Electronic delocalization, charge transfer and hypochromism in the UV absorption spectrum of polyadenine unravelled by multiscale computations and quantitative wavefunction analysis. *Chem. Sci*. **8**, 5682–5691 (2017).

31. Platt, J. R. Classification of Spectra of Cata-Condensed Hydrocarbons. *J. Chem. Phys.* **17**, 484–495 (1949).

32. Banyay, M., Sarkar, M. & Graslund, A. A library of IR bands of nucleic acids in solution. *Biophys. Chem.* **104**, 477–488 (2003).

33. Peng, C., Jones, K. C. & Tokmakoff, A. Anharmonic vibrational modes of nucleic acid bases revealed by 2D IR spectroscopy. *J. Am. Chem. Soc.* **133**, 15650–15660 (2011).

34. Brown, R. F., Andrews, C. T. & Elcock, A. H. Stacking Free Energies of All DNA and RNA Nucleoside Pairs and Dinucleoside-Monophosphates Computed Using Recently Revised AMBER Parameters and Compared with Experiment. *J. Chem. Theory Comput.* **11**, 2315–2328 (2015).

35. Nganou, C., Kennedy, S. D. & McCamant, D. W. Disagreement Between the Structure of the dTpT Thymine Pair Determined by NMR and Molecular Dynamics Simulations Using Amber 14 Force Fields. *J. Phys. Chem. B* **120**, 1250–1258 (2016).

36. Li, Q., Giussani, A., Segarra-Marti, J., Nenov, A., Rivalta, I., Voityuk, A. A., Mukamel, S., Roca-Sanjuan, D., Garavelli, M. & Blancofort L., Multiple Decay Mechanisms and 2D-UV Spectroscopic Fingerprints of Singlet Excited Solvated Adenine-Uracil Monophosphate. *Chem. Eur. J.* **22**, 7497–7507 (2016).

37. Kypr, J., Kejnovska, I., Renciuk, D. & Vorlícková, M. Circular dichroism and conformational polymorphism of DNA. *Nucleic Acid Res.*. **37**, 1713–1725 (2009).

38. Jailaubekov, A. Ultrafast electronic deactivation of DNA bases in aqueous solution. *PhD Thesis, University Southern California* (2007).

39. Udenfriend, S. & Zaltzman, P. Fluorescence characteristics of purines, pyrimidines, and their derivatives: measurement of guanine in nucleic acid hydrolyzates. *Anal. Biochem.* **3**, 49–59 (1962).

40. Gustavsson, T. Banyasz, A., Lazzarotto, E., Markovitsi, D., Scalmani, G., Frish, M.

J., Barone, V. & Improta, R. Singlet excited state behavior of uracil and thymine in aqueous solution: a combined experimental and computational study of 11 uracil derivatives. *J. Am. Chem. Soc.* **128**, 607–619 (2006).

41. Onidas, D., Markovitsi, D., Marguet, S., Sharonov, A. & Gustavsson, T. Fluorescence Properties of DNA Nucleosides and Nucleotides: A Refined Steady-State and Femtosecond Investigation. *J. Phys. Chem.B* **106**, 11367–11374 (2002).

42. Peon, J. & Zewail, A. H. DNA/RNA nucleotides and nucleosides: direct measurement of excited state lifetimes by femtosecond fluorescence up-conversion. *Chem. Phys .Letters* **348**, 255–262 (2001).

43. Pecourt, J., Peon, J. & Kohler, B. DNA excited state dynamics: ultrafast internal conversion and vibrational cooling in a series of nucleosides. *J. Am. Chem. Soc.* **123**, 10370–10378 (2001).

44. Zhang, Y., Oliver, T. A., Ashfold, M. N. & Bradforth, S. E. Contrasting the excited state reaction pathways of phenol and para-methylthiophenol in the gas and liquid phases. *Faraday Discuss.* **157**, 141-163 (2012).

45. Rottger, K. Marroux, J. B., Grubb,M. P., Coulter, P. M., Bohnke, H., Henderson, A. S., Galan, M. C., Temps, F., Orr-Ewing A. J. & Roberts, G. M. Ultraviolet Absorption Induces Hydrogen-Atom Transfer in G·C Watson-Crick DNA Base Pairs in Solution. *Angew. Chem.* **54**, 14719–14722 (2015).

46. Nielsen, J., Thøgersen, J., Jensen, S., Nielsen, S. & Keiding, S. Vibrational dynamics of deoxyguanosine 5'-monophosphate following UV excitation. *Phys. Chem. Chem. Phys.* **13**, 13821–13826 (2011).

47. Zhang, Y., Improta, R. & Kohler, B. Mode-specific vibrational relaxation of photoexcited guanosine 5'-monophosphate and its acid form: a femtosecond broadband mid-IR transient absorption and theoretical study. *Phys. Chem. Chem. Phys.* **16**, 1487–1499 (2014).

48. Hare, P. M., Crespo-Hernandez, C. E. & Kohler, B. Solvent-dependent photophysics of 1-cyclohexyluracil: ultrafast branching in the initial bright state leads nonradiatively to the electronic ground state and a long-lived $^{1}n\pi^{*}$ state. *J. Phys. Chem.B* **110**, 18641–18650 (2006).

49. Etinski, M., Fleig, T. & Marian, C. M. Intersystem crossing and characterization of dark states in the pyrimidine nucleobases uracil, thymine, and 1-methylthymine. *J. Phys. Chem. A* **113**, 11809–11816 (2009).

50. Kuimova, M. K. Cowan, A. J., Matousek, P., Parker, A. W., Sun, X. Z., Towrie, M. & George, M. W.Monitoring the direct and indirect damage of DNA bases and polynucleotides by using time-resolved infrared spectroscopy. *Proc. Natl. Acad. Sci. USA* **103**, 2150–2153 (2006).

51. Towrie, M. Doorley, G. W., George, M. W., Parker, A. W., Quinn, S. J. & Kelly, J. M. ps-TRIR covers all the bases--recent advances in the use of transient IR for the

detection of short-lived species in nucleic acids. *Analyst* **134**, 1265–1273 (2009).

52. Parker, A. W., Lin, C., George, M. W., Towrie, M. & Kuimova, M. K. Infrared characterization of the guanine radical cation: finger printing DNA damage. *J. Phys. Chem. B* **114**, 3660–3667 (2010).

53. Pilles, B. M. Bucher, D. B., Liu, L., Gilch, P., Zinth, W. & Schreier, W. S.. Identification of charge separated states in thymine single strands. *Chem. Commun.* **50**, 15623–15626 (2014).

54. Doorley, G. W., Wojdyla, M., Watson, G. W., Towrie, M., Parker, A. W., Kelly, J. M. & Quinn, S. J. Tracking DNA Excited state by Picosecond-Time-Resolved Infrared Spectroscopy: Signature Band for a Charge-Transfer Excited State in Stacked Adenine–Thymine Systems. *J. Phys. Chem. Lett.* **4**, 2739–2744 (2013).

55. Seidel, C. A., Schulz, A. & Sauer, M. H. Nucleobase-Specific Quenching of Fluorescent Dyes. 1. Nucleobase One-Electron Redox Potentials and Their Correlation with Static and Dynamic Quenching Efficiencies. *J. Phys. Chem.* **100**, 5541–5553 (1996).

56. Martinez-Fernandez, L,.Zhang, Y., de La Harpe, K., Beckstead,A. A., Kohler, B. & Improta, R. Photoinduced long-lived charge transfer excited state in AT-DNA strands. *Phys. Chem. Chem. Phys.* **18**, 21241–21245 (2016).

57. Voityuk, A. A. Fragment transition density method to calculate electronic coupling for excitation energy transfer. *J. Chem. Phys.* **140**, 244117 (2014).

58. Oliver, T. A. A. Recent advances in multidimensional ultrafast spectroscopy. *R. Soc. Open Sci* **5**, 171425 (2018).

59. Oliver, T. A. A., Lewis, N. H. & Fleming, G. R. Correlating the motion of electrons and nuclei with two-dimensional electronic-vibrational spectroscopy. *Proc. Natl. Acad. Sci. USA.* **111**, 10061–10066 (2014).

60. Lewis, N. H., Dong, H., Oliver, T. A. A. & Fleming, G. R. A method for the direct measurement of electronic site populations in a molecular aggregate using two-dimensional electronic-vibrational spectroscopy. *J. Chem. Phys.* **143**, 124203 (2015).

Chapter 5

Two-Dimensional Electronic Spectroscopy

5.1 Introduction

Chapter 2 provides an overview of the theoretical framework and vocabulary that is commonly used in non-linear optical spectroscopy. The principles of photon echo spectroscopy that underpin two-dimensional electronic spectroscopy were developed by Mukamel[1], whose "principles of nonlinear optical spectroscopy" are now considered as the lingua franca of the coherent experiments.[2]

Before the advent of 2D spectroscopy, the conventional spectroscopies such as time-resolved fluorescence or transient absorption could not always resolve the significant number of information given by molecular interactions, and a complete and unambiguous understanding of the microscopic behaviour of the systems studied was sometimes challenging to extrapolate.[3,4] New techniques were then developed taking inspiration from nuclear magnetic resonance. This technique became more advanced with NOESY (2D exchange spectroscopy), and COSY(correlation spectroscopy).[5] Subsequently, a similar path was followed by optical spectroscopies where the contribution of the "extra dimension" turned out to be very advantageous. A positive contribution brought by this new spectroscopy could be associated to the direct observation of the coupling between the states that are responsible for molecular dynamics processes.[2]

The first two-dimensional electronic spectroscopy (2DES) setup implementation was developed in the 1990s by the Jonas group[4,6–8] for the study of the third-order response of a dye molecule. 2DES is now more common thanks to the fast development of new technologies such as diffractive optics[9,10] and pulse shaping.[11,12] Two-dimensional electronic spectroscopy is primarily used to study a great variety of chemical samples such as atoms,[13] molecular aggregates,[14] biological and biomolecular pigment-protein complexes[15–20] and semiconductors.[21,22]

5.2 Pulse Shaper

Before introducing the standard geometries used for the implementation of 2DES, it might be helpful to provide an overview of a device that is extensively used and discussed in multidimensional spectroscopy: the pulse-shaper.

In 2DES experiments, pulse shapers can be used to generate the time-delay between two pulses with high time precision and refresh rate. In this way, the phase stability of the system is improved, and the detection of specific signals such as rephasing and non-rephasing can be controlled via phase-cycling. Pulse shapers are becoming commonplace in 2D spectroscopy not just for their ability to generate the time-delays between the beams, but also because they are an "in-line" device that can optimize the laser pulse compression when combined with specific pre-compression stages (see also chirped mirrors and pulse shaper section).[3]

Pulse shapers are tools for removing the scatter and separate 2D signals via phase cycling, they convey a zero-uncertainty in the pump delays, and they allow the spectra to be collected in fewer time steps compared to some other methods. However, pulse shapers are

usually lossy, and often have a maximum 40% throughput (for broadband operation this can be low as 20%). Furthermore, a second issue can be encountered when the pulse shaper is not coupled with a specific pre-compression stage: a reduction in laser bandwidth. This problem can lead to experimental difficulties when compressing the pulse to sub 30 fs.[3]

Despite the issues that can be faced with pulse shapers, they are commonly used by different groups. For example, the Nelson group developed a spatial-temporal 2D pulse shaper where four pulses used in a boxcar geometry (see section 5.3.3), are incident at different locations of a spatial light modulator pulse shaper which enables independent time control of each pulse.[23] More recently, also the Ogilvie group has implemented a hybrid 2DES setup where an acousto-optic programmable dispersive filter (AOPDF or Dazzler pulse shaper) is used with diffractive optics to collect a background-free signal.[24] Furthermore, a boxcar geometry setup that uses a pulse shaper to compress the pulses, but not to control the time-delay between the beams was developed by the Collini group.[25]

5.3 Experimental Implementation

Following the pioneering work of the Jonas group[4,7,8] for the detection of the third-order nonlinear response using the boxcar geometry, several approaches to 2DES spectroscopy have been developed in the last 20 years.[26] Three methods to experimentally realise 2D spectroscopy can be used: the fully collinear, pump-probe and boxcar geometries.[3,26]

5.3.1 Fully Collinear Geometry

The fully collinear geometry was first implemented by Warren *et al.*[13] to study a model system of Rubidium vapour. In this setup, an acousto-optic pulse shaper is used to generate

three collinear pulses. The 2D signal is generated with the linear and higher-order signals, and it propagates in the same direction of the incident beams. The main advantage of this collinear approach is that the difficulties of dealing with multiple pulses spatially separated is suppressed. However, the signal is generated on the top of a large background of the excitation pulses, and spurious pulses can be induced by the pulse shaper, which might interfere with the desired signal.[3,13] Moreover, because the spectral resolution is determined by the pulse shaper the maximum waiting time in a standard 2D experiment is limited, and the optical design of spatiotemporal pulse shapers may also cause some issue with the variable chirp at different frequencies and time-delays.[13]

5.3.2 Pump-probe Geometry

Jonas first proposed the pump-probe approach[4,7] and, to date, it has been the most widely used method for multidimensional spectroscopy. As in pump-probe spectroscopy, the pump-probe geometry is characterised by two collinear pump beams and a probe that overlaps with the other two pulses at the sample (see Figure 5.1 (a)). Under such conditions, considering that $\underline{k}_1 = \underline{k}_2$, the rephasing ($\underline{k}_s = -\underline{k}_1 + \underline{k}_2 + \underline{k}_3$) and non-rephasing ($\underline{k}_s = +\underline{k}_1 - \underline{k}_2 + \underline{k}_3$) signals are emitted collinear to the $\underline{k}_3$ probe and collected at the same time. The pump-probe geometry has two main advantages compared to the other implementations. First, the probe acts as a standard for the zero-phase relative to the signal and therefore does not require an additional measurement to determine the signal phase; second, the time errors that can arise from the separation of rephasing and non-rephasing signal are removed. However, because the signal is generated on the top of the probe beam, it is not background-free, and from a comparison between fully noncollinear geometry data and pulse-shaped partially collinear spectroscopy, it has been determined that the fully non-collinear 2DES measurements are characterised by a signal-to-noise that is 20 times higher than in pump-

probe measurements.[24] Another difficulty to face in pump-probe geometry is the generation of the coherence time, t_1, which is the time difference between the two pump-pulses. A common approach is to use a pulse shaper that automatically generates the time-delay between the two identical beams.[12,27] In this configuration, the pulse shaper has a second advantage, with its ability to act shot-to-shot, it can remove laser power fluctuations and reduce the noise during the data acquisition.[3]

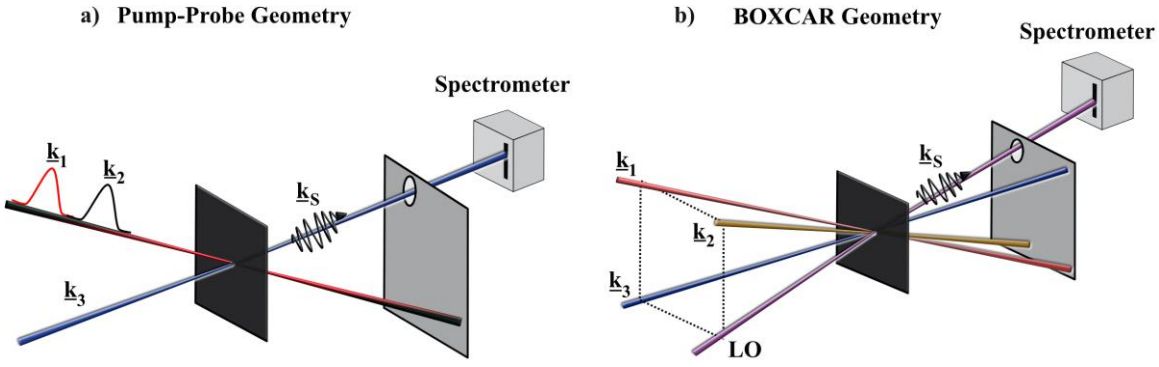

Figure 5.1 Comparison between (a) pump-probe and (b) boxcar geometries.

An alternative to the pulse shaper approach for the generation of phase-stable pump pairs is the TWINS (Translating-Wedge-Based Identical Pulse eNcoding System) developed by the Cerullo group.[28] Using this method, a pair of birefringent wedges generate the delay between two phase-stable pulses.[28] There are two positive aspects related to the TWINS: it is a far more economically viable option than a pulse shaper and can be used with broader bandwidth. However, the wedges have also some disadvantages, they do not allow the separation of rephasing and non-rephasing signals, or provide any means of scatter reduction, and because they are implemented in a pump-probe geometry the signal is not background-free.[3]

5.3.3 Boxcar Geometry

The boxcar was the first geometry to be implemented, and it consists of four spatially separated beams (the fourth beam is for heterodyne detection), as shown in Figure 5.1 (b). This implementation comes with advantages and disadvantages, as already noted for the other geometries. The main advantage is that the signal is generated background-free, while the downside of this implementation usually resides in its alignment, which can be quite challenging to achieve.[3,4] Theoretically, the phase-matched signal that is generated by the interference of three spatially separated pulses ($\underline{k}_1$, $\underline{k}_2$, $\underline{k}_3$) and the reference beam (local oscillator, LO) propagates along two different directions corresponding to the rephasing and non-rephasing signals (recall Figure 2.3). However, through careful manipulation of the separate beams it is possible to radiate the two time-separated signals in the same direction, parallel to the LO (see section 5.8 for further details).

In the boxcar geometry implementation, the generation of four identical beams, $\underline{k}_1$, $\underline{k}_2$, $\underline{k}_3$, and $\underline{k}_{LO}$, can be very challenging and four main methods have been developed to overcome this technical issue: use of a spatial filter with four holes arranged in boxcar geometry,[29] generation of the four beams with two interferometers,[30] diffractive optics,[9] and use of conventional beam splitters.[4]

The first method to generate four identical beams is by placing a mask with four holes in the input beam line. This passive method is straightforward to implement; however, it is characterised by power loss, increase of background signal and scatter, and does not work for spatially chirped lasers, such as the output of a non-linear optical parametric amplifier.[23,31]

The second method that has been used is the implementation of two interferometers, one to generate the pump pulses and the other one for the probe and local oscillator. In this apparatus, a third interferometer is used to control the phase between the other two interferometers actively.[22,30] This setup is useful in an experiment where a long coherence time needs to be scanned, however, it requires active stabilisation and the rephasing and non-rephasing signals cannot be acquired together.[26]

Diffractive optics are the most used technique and, depending on the characteristic of the light source they can be used as single two-dimension or two perpendicularly mounted diffractive optics to generate the four beams in a BOXCAR configuration. The use of this technique provides high phase stability and an easy alignment of the four beams for the heterodyne detection. However, the setup with diffractive optics has the limitation of the spectral bandwidth (the diffracted beams can overlap when the bandwidth is an octave of the wavelength).[9]

The latter method consists of using conventional beam splitters. This method is the most straightforward and, probably, the most intuitive. By splitting the input beam twice, four identical beams are created and arranged in the so-called boxcar geometry. Subsequently, the four beams are focused and overlapped into the sample, and the signals comprising both rephasing and non-rephasing contributions are collected background-free. This method was used to implement the Bristol setup even if, as every other method discussed so far, it has downside aspects that are still challenging to solve. First, a setup built with only beam splitters is not phase-stable.[4] However, to overcome this issue, the detection can be carried out in the rotating frame with the pair-wise method.[32] This implementation reduces the setup fluctuation and strict phase stability remains. The second issue is due to the alignment

of the four beams which is very difficult, and their perfect overlap at the sample position is challenging to achieve. If the overlap is not maximised the direction of propagation of the signal may be slightly different compared to the direction of propagation of the LO, leading to a decrease in intensity of the signal detected. However, with well-mounted optics and balanced glass-thickness in each of the four beam pathways and minimized airflow, the fluctuation and phase issue can be minimized.[3]

5.4 Development of a New Two-Dimensional Electronic Spectroscopy Apparatus

The setup developed in Bristol is a hybrid 2DES apparatus that combines the boxcar geometry realised only with conventional optics[17,32,33] and an acousto-optic programmable dispersive filter.[25] The time resolution, (~25 fs) is achieved by using the AOPDF, while the boxcar geometry allows the acquisition of background-free signal. Two choppers are also used to remove the scatter.[33]

5.4.1 Nonlinear Optical Parametric Amplifier

Cerullo *et al*. have already given a comprehensive guide for a basic understanding of the physical processes of light generation from a coherent source such as femtosecond optical parametric amplifiers (OPAs) and nonlinear OPAs (NOPA).[34] Such a thorough description of nonlinear processes that quantitively explain the operation of OPAs and NOPAs goes beyond the scope of this thesis; thus, the NOPA presented in this chapter is explained only qualitatively, and any details refer to the apparatus in Bristol.

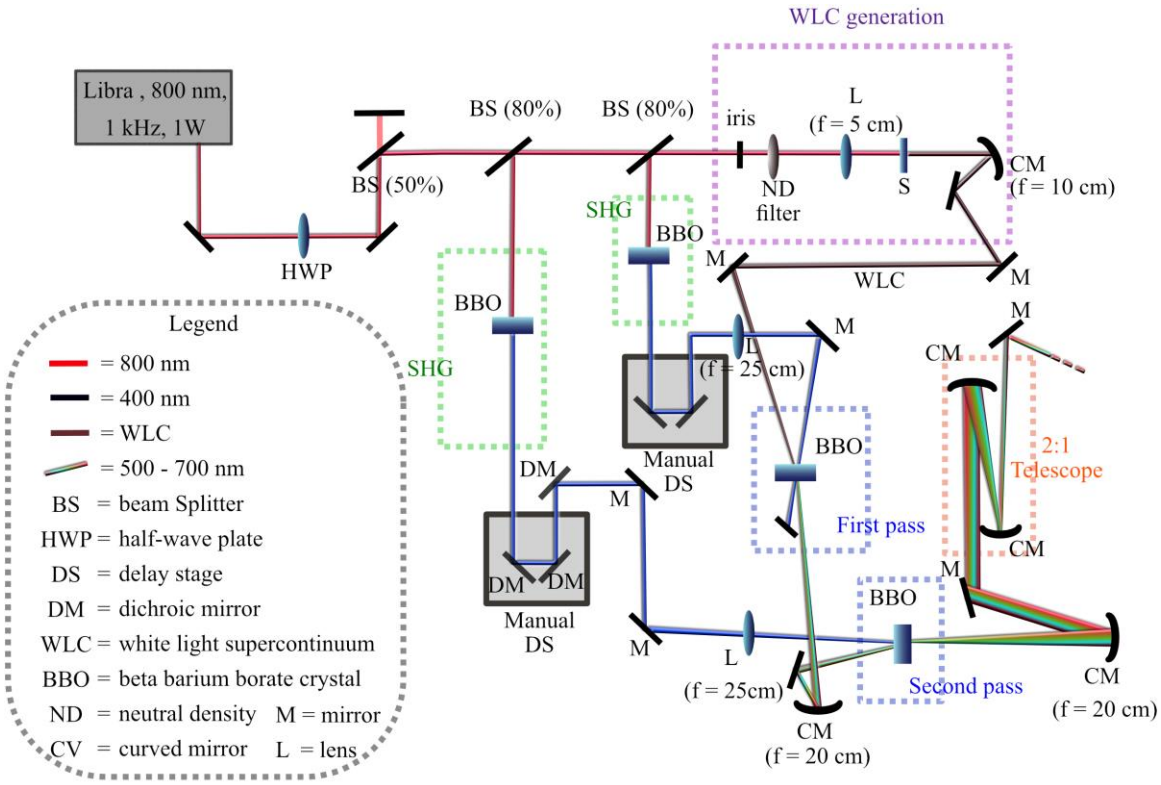

Figure 5.2 Diagram of the home-built NOPA.

A Coherent Libra laser (1 kHz, 1 W, 800 nm) provides the pump source for all the following experiments. At the beginning of the setup a periscope, placed at the output of the amplifier, lowered the output beam to 12 cm above the laser table. After the periscope, a half waveplate was used to rotate the unpolarized 800 nm light to p-polarised radiation. A 50 % beam splitter separates the fundamental into two beam lines, one of which is blocked, while the second line is used to generate the broadband visible light. Subsequently, an 80% beam splitter was set at the beginning of the double pass NOPA where the transmitted light (80 %, ~ 0.4 W) was used in the amplification stage, while the other 20% (~ 0.1 W) of the radiation was used in the first pass to generate the broadband visible light spectrum. In the first pass, the beam was subsequently split with an 80% beam splitter. The 20 % transmitted light (~ 0.08 W) is used to generate white light (WL) while 80 % of it was used in the 400 nm (blue light, 6.00 mW) pump generation in the first pass of the NOPA.

The WL was produced by focusing the 800 nm into a sapphire with a 5 cm focal lens. A neutral density (ND) filter and an iris were positioned just before the lens to attenuate the power and to select a spatially homogenous part of the 800 nm. The 400 nm was generated through second-harmonic generation (SHG, see Ap. 5.1 for definition) of the fundamental beam using a β-barium borate crystal (Eksma Optics 10 x 10 x 0.5 mm, $\theta = 29.2°$, $\varphi = 90°$). After generation of the 400 nm, dichroic mirrors were used to separate the residual 800 nm from the blue light. At this stage, two of the dichroic mirrors were mounted into a manual delay stage used to adjust the relative time delay with the WL beam path.

After the blue and the white light generation these two beams were focused into a second BBO crystal (Eksma Optics 6 x 6 x 2 mm, $\theta = 32°$, $\varphi = 90°$) with a 20 cm focal lens and 10 cm curved mirrors, respectively. The two incoming beams were directed towards the NOPA crystal, non-collinearly, but, focused on the same plane. The angle evaluated inside the BBO crystal between the signal (visible light) and the pump (400 nm), was kept at ~ 4° and the phase-matching angle at ~ 31° to maximise the broadband signal.[34] Under such conditions, it was possible to amplify a wide part of the white light seed, generating a ~ 120/150 full width half maximum (FWHM, from ~ 500 to 700 nm) output with a pulse energy of 1.31 mW.[34] To increase the power of the broadband spectrum generated, the visible light was then collimated and focused with a 20 cm curved mirror into a second BBO-crystal (Eksma Optics, size = 6 x 6 x 2 mm, $\theta = 32°$, $\varphi = 90°$) where it overlaps with another 400 nm beam (17.5 mW) focused into the crystal with a 20 cm focal lens. From the amplification stage, the power was observed to increase by a factor of five (to 6.20 mW). However, the second pass led to a slight reduction of the FWHM of the spectrum from ~120 to ~90 /100 nm.

Subsequently, the visible light generated by the NOPA was sent through an iris that spatially isolate the main beam from the halo produced around it. Subsequently, it was collimated with a curved mirror and with a 2:1 telescope to improve the beam mode further. After these steps, the mode of the beam was still slightly elliptical but remains collimated until the sample region (~ 2 m downstream). The broadband laser beam generated with the double pass NOPA (~ 100s of femtoseconds) was subsequently compressed, as explained in the following section.

5.4.2 Chirped mirrors and Pulse Shaper Compression

The broadband pulse generated by the NOPA is positively chirped by the material dispersion, *i.e.* the propagation of the beam(s) through transmissive elements, such as the sapphire, optical elements (lenses, beam splitters, filters, etc.) and by the BBO crystals.[34] Under such circumstances, pulse compression was necessary to achieve a transform-limited (TL) pulse duration. To obtain this short pulse in OPAs and NOPAs, it was usually sufficient to correct for the second-order dispersion, or group delay dispersion (GDD), while for transform-limited temporal resolution the third-order dispersion (TOD) needs to be taken into account.

This stage can be achieved using different arrangements (see appendix "Compression Stage" for further details) from which two techniques were implemented in the apparatus described in this chapter, and only one chosen for the final version of the setup.

The two techniques are the following: chirped mirrors (CMs) and Dazzler ultrafast pulse shaper. Figure 5.3 (a) shows the scheme used while implementing the compression with commercial chirped mirrors (Layertec) and glass wedges while panel (b) shows the diagram

in the case where the compression is achieved with the Dazzler ultrafast pulse shaper and a pair of SF11 glass prisms for the pre-compression stage.

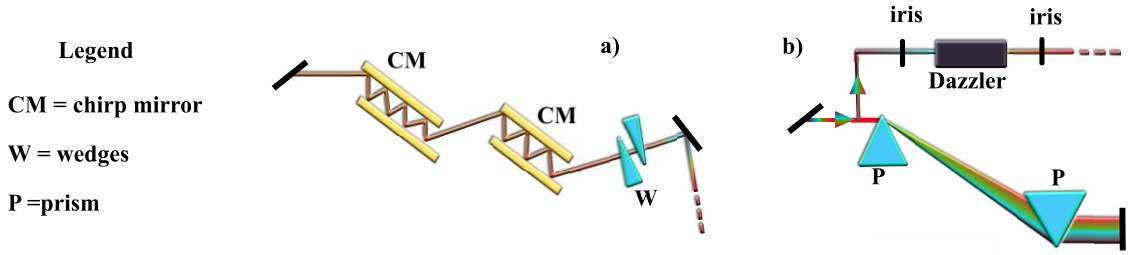

Figure 5.3 Diagram of the visible pulse compression achieved with (a) chirped mirrors and fused-silica wedges, and (b) prisms and Dazzler ultrafast pulse shaper.

The pulse duration achieved with the chirped mirrors was monitored with second-harmonic generation frequency-resolved optical gating[35] (SHG-FROG, the traces are shown in Chapter 6 and 7), and the pulse duration achieved was ~15 fs (for FWHM ~120 nm). CMs are used to compensate for the second order GVD, but they are not effective on higher-order chirp components. For this reason, a significant amount of third-order dispersion is observed when using commercial CMs. Furthermore, their compensation for the second-order nonlinear effects is observed to be nonlinear through the spectrum, it applies a non-linear phase through the spectrum, as shown for broadband pump-probe data in Figure 5.4 (a). This issue would lead to distorted line shapes in 2D data. Therefore, the commercial CMs were replaced with a more sophisticated method used to achieve a compression of ~ 25 fs with a FWHM ~ 60 nm (see transient gating-FROG traces in Chapter 6 and 7). In the presented apparatus, the AOPDF was used to correct for group velocity dispersion and third-order dispersion (see appendix), but there was no need to correct for higher-order dispersions, as shown in the data reported in Figure 5.4 (b).

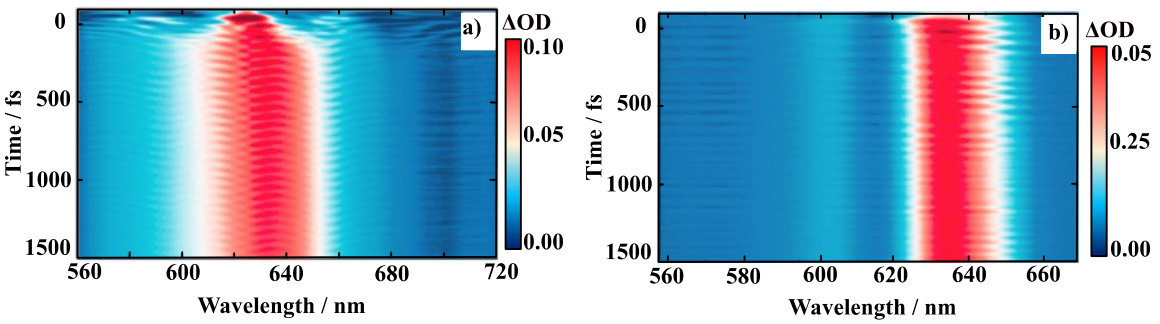

Figure 5.4 Broadband transient absorption data where the pump and probe pulses were compressed with (a) chirped mirrors and (b) AOPDF.

To provide a comparison between the compression achieved with commercial CMs and Dazzler ultrafast pulse shaper, I compare Fourier transform maps of broadband transient absorption data acquired for zinc chlorin e6 in a phosphate buffer solution. Figure 5.5 (a) reports the FT map obtained when the data are taken with pulses compressed by chirped mirrors where a shorter pulse duration and broader bandwidth achieved led to a more congested spectrum showing FT amplitudes up to 1500 cm^{-1}.

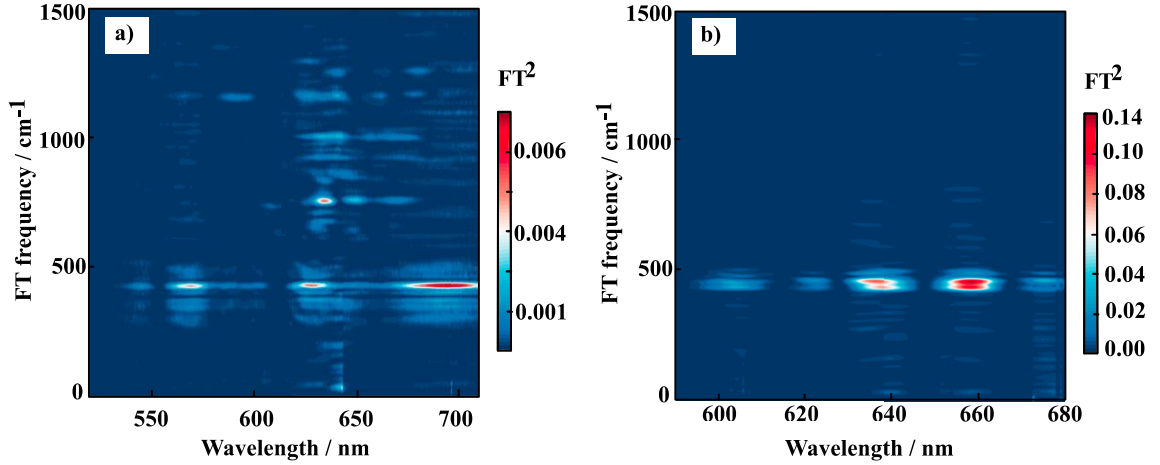

Figure 5.5 FT amplitude maps of chlorin e6 in buffer acquired with (a) chirped mirrors compression, (b) Dazzler ultrafast pulse shaper.

Panel (b) shows the data acquired with the Dazzler pulse shaper where the longer pulse duration and narrower spectrum do not allow the observation of FT frequencies higher than

600 cm^{-1}. Also, note that these two compression stages led to the observation of the same FT amplitudes (Figure 5.5 (a) and (b)), and for broadband transient absorption experiments both methods can be considered valid options when working with strongly chirped pulses, in agreement with prior studies.[36] Therefore, for what has been observed and reported in this paragraph, the broadband transient absorption data shown in Chapter 6 and 7 were acquired with CMs compression (broader probe spectrum and shorter pulse); while the 2DES data reported in Chapter 6 were taken with pulses compressed with Dazzler ultrafast pulse shaper.

5.4.3 Implementation of Boxcar Geometry

After the compression stage first achieved with CMs and wedges, and then substituted with a Dazzler ultrafast pulse shaper pre-compensated with two SF11 prisms, the boxcar geometry was implemented, as shown in Figure 5.6 (see also Figure Ap. 5.3 and Figure Ap. 5.4 for an overview of the entire setup).

The oscillator, NOPA and compression stage are located close to the Ti:Sapphire laser in a vibrationally isolated laser table, while the boxcar 2DES spectrometer was constructed in a second table. The two tables were connected via a heavy-weight connection yoke. Two irises positioned at the end and beginning of the joined tables are used to control the NOPA output alignment and monitor the day to day pointing.[32,33]

The boxcar geometry consisted of four identical parallel beams generated from the same source and arranged in a square configuration (each beam formed a vertex of the box) before being focused into the sample. Two beam splitters were used to generate the four beams and the time-delays were given by the synchronous movement of three mechanical

delay stages. Any vibration of the laser table may alter the pathlength of one beam without affecting the other three leading to a phase shift. In our case, we have faced this problem by phase-locking the four pulses, as previously reported by Heilser.[33]

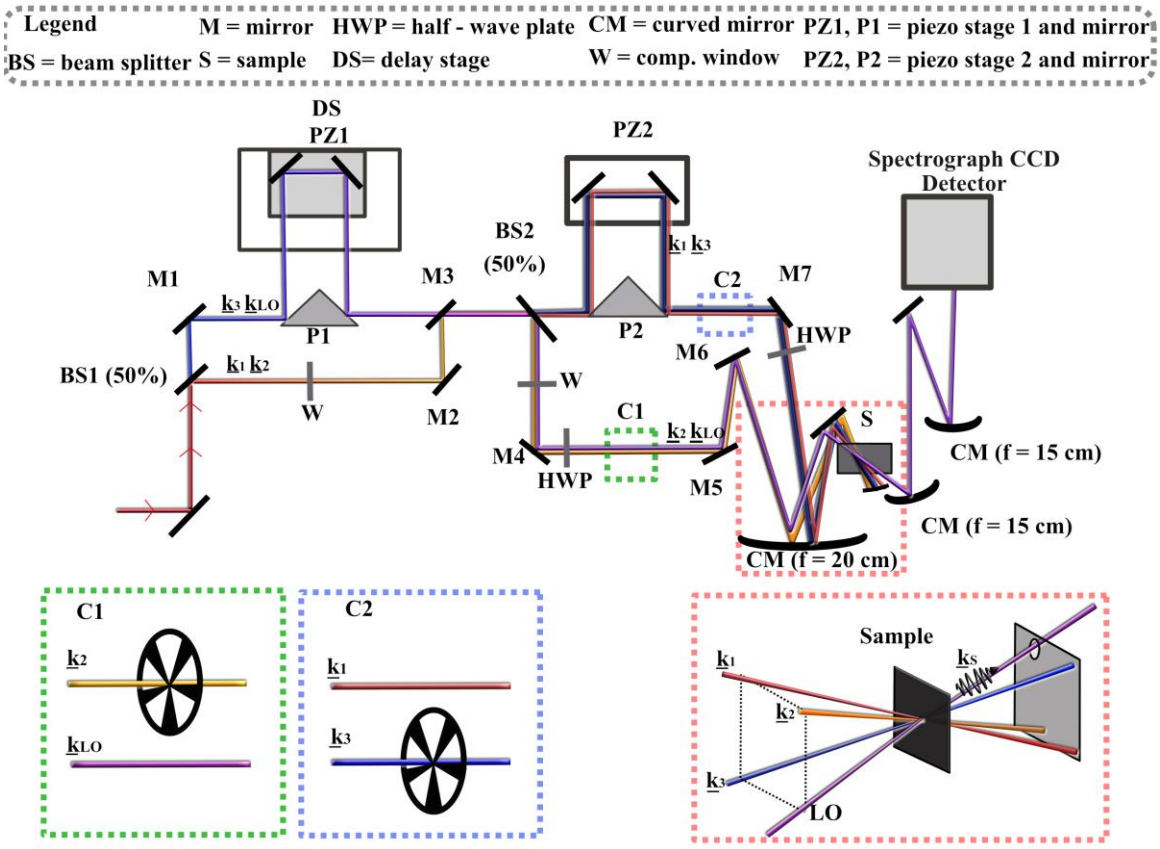

Figure 5.6 Diagram of the boxcar geometry implemented. Note that the green, blue and red squares correspond to labelled parts of the setup where the choppers reside.

The boxcar spectrometer was constructed, as follows: a broadband beam splitter (BS1) with approximately 50% transmittance for visible wavelengths was placed after the second iris used to align the beam after the Dazzler. BS1 generated two identical beams at 90° to each other. The first beam travelled through a pair of delay stages mounted one on top of the other. The lower delay stage, DS (PI, M-531 heavy-duty micro positioning stage) could move up to 300 mm (~ 2 ns), with a load capacity of 2 kg and high bidirectional femtosecond precision while the other stage was a piezoelectric stage (PI, P-622.ZCD),

PZ1, that can travel 250 μm (~ 1.5 ps), with closed-loop positioning and capable of attosecond precision. PZ1 was mounted on a solid block of stainless steel and bolted to DS. The stainless-steel block is ~ 1 kg, below the load capacity of the long-range stage. A silver roof-mirror was then mounted on PZ1 perpendicular to the laser table. The second beam followed a path of equal length compared to the first beam. The second beam, generated at 12 cm above the laser table, was then lowered to 10 cm. The lowering procedure allowed the two beams to travel at different heights (10 and 12 cm above the optic table) before encountering a second beam splitter (BS2). BS2 created four beams that travelled in pairs through two different paths; one was directed to a second piezoelectric stage, PZ2, (PI, P-622.ZCD) with a roof mirror mounted perpendicular to the optic table. The second pair of beams followed a path without any delay stage. From now on, I will refer to the two beams going through the third piezo stage as beam 1 and 3 and the other two beams as beam 2 and LO.

The polarization of each pair of beams (1/3 and 2/LO) was controlled by two half-wave plates placed before the sample. The four beams were focused into the sample with a large 3 inches spherical mirror (SM, 20 cm focal length) and a small square mirror was used to direct the four beams toward the sample with an incident angle of ~ 90°. The SM focuses all the beams to a single point, and the beam size at the focus (for each of the four beams) was measured to be ~ 90 μm visualised with a CCD beam profiling camera (WinCamD-UCD).

Two choppers, C1 and C2, were used to modulate beams 2 and 3, respectively, as previously implemented by Heilser *et al.*[33] The two rotating wheels were used to remove

the scatter contributions and to allow the acquisition of the pump-probe and 2DES data under the same experimental conditions (section 5.5).

The sample was positioned at the focal point of the four beams. After the sample, beams 1, 2 and 3 were blocked with an iris while the LO and the rephasing and non-rephasing signals generated along the same direction were collimated and focused into the detector (Andor, Shamrock 163 coupled to a 1024 pixel CCD camera Entwicklungsbüro Stresing). To avoid generation of competing non-linear signals from the interference with the LO, the reference beam was attenuated with a fused silica neutral density filter (ND). The CCD camera was triggered by a TTL (transistor-transistor logic) pulse at 1 kHz from the synchronization delay box of the Libra laser which was also capable of recording the TTL signal of each chopper state simultaneously. Therefore, for each shot acquired, the state of the two choppers was always reordered, for example, the "state" of beam 2 and 3, either they were both open (they are allowed to go through the choppers) or closed (the choppers block the beams). In our case, the chopper state was defined before each measurement and controlled by a home built LabView program.

5.5 Scatter and Background Signal Subtraction

One of the concerns when implementing a boxcar geometry setup is the observation of scatter arising from beams 1, 2 and 3.[3,10,33] This phenomenon is phase coherent with the LO (and 2D signal), and it depends on the interference between the reference and the pump beams at the detector.[10] Furthermore, there is the possibility that the delayed local oscillator can generate a separate pump-probe signal along the detection axes with any of the three other beams.[37]

To overcome this issue, two solutions have been previously proposed: double modulation and lock-in detection[38] or shutters.[10] Both implementations can improve the signal to noise ratio of the 2DES data, but they also have a downside, the lock-in detection needs a high repetition rate laser and a 1024 channel lock-in amplifier while the shutters reduce the acquisition duty cycle of the data. In 2011 and later in 2014, a third option to overcome the scatter issue was proposed by Augulis and Zigmantas[38] first, and then Heilser *et al.*[33]: the double chopper arrangement. This implementation represents an intermediate solution between the double modulation and slow shutters. For completeness and also for a better understanding of the setup that I have implemented, a brief description of the chopper sequence is given in this section. However, a detailed description has already been reviewed in ref.[33]

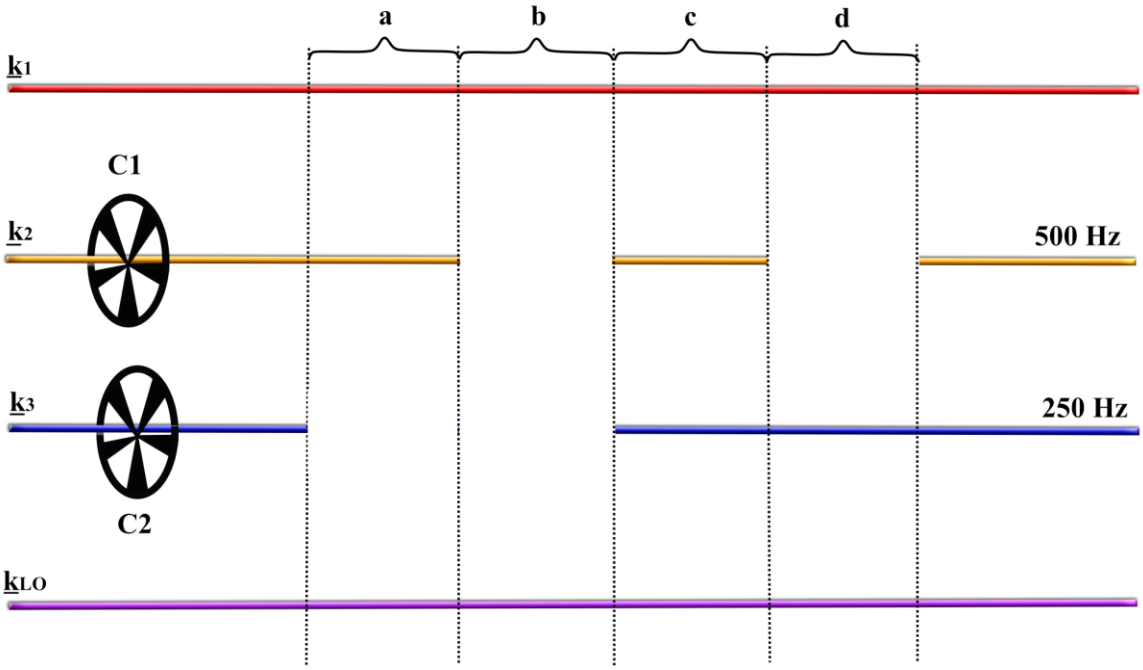

Figure 5.7 Choppers configuration used in 2DES.

Figure 5.7 shows the two choppers, C1 and C2 acting on beam 2 and 3, respectively. C1 is synchronised at ½ of the repetition rate of the laser (500 Hz) while C2 has a frequency of ¼ of the Libra laser (250 Hz). The two choppers are not covered during the experiments

because the slow rotational speed means the air turbulence induced was negligible, and the setup phase stability is maintained (as shown in the next section). The synchronisation of C1 and C2 at 500 and 250 Hz creates four different chopper states experienced by the sample. Henceforth, I will refer to these four configurations as a, b, c and d, see Figure 5.7.

Let us now recall the definitions of $\mathcal{E}_s$ and $\mathcal{E}_{LO}$ (signal and local oscillator fields) given in Chapter 2 and assume that T_n is the scatter arising from beams 1, 2 or 3. The combination of the four configurations mentioned above (a, b, c, and d) can generate two main signals shown here as α and β and defined in equations 5.1 and 5.2 and in ref:[33]

$$\alpha = a - b = |T_1 + T_2 + \mathcal{E}_{LO}|^2 - |T_1 + \mathcal{E}_{LO}|^2 \tag{5.1}$$

$$= | T_2 |^2 + 2 \text{ Re } \{T_1 T_2^*\} + 2 \text{ Re}\{T_2 \mathcal{E}_{LO}^*\}$$

$$\beta = c - d = |T_1 + T_2 + T_3 + \mathcal{E}_S + \mathcal{E}_{LO}|^2 - |T_1 + T_3 + \mathcal{E}_{LO}|^2 \tag{5.2}$$

$$= | \mathcal{E}_S |^2 + | T_2 |^2 + 2 \text{ Re } \{T_1 T_2^*\} + 2 \text{ Re}\{T_2 \mathcal{E}_{LO}^*\} + 2 \text{ Re } \{T_1 \mathcal{E}_S^*\}$$

$$+ 2 \text{ Re}\{T_2 \mathcal{E}_S^*\} + 2 \text{ Re}\{T_3 \mathcal{E}_S^*\} + 2 \text{ Re}\{T_2 T_3^*\} + 2 \text{ Re}\{T_S \mathcal{E}_{LO}^*\}$$

where a LabView program is written to acquire these two signals in real time and processed via the following relation:

$$\beta - \alpha = \tag{5.3}$$

$$| \mathcal{E}_S |^2 + 2 \text{ Re } \{T_1 \mathcal{E}_S^*\} + 2 \text{ Re}\{T_2 \mathcal{E}_S^*\} + 2 \text{ Re}\{T_3 \mathcal{E}_S^*\} + 2 \text{ Re}\{T_2 T_3^*\} + 2 \text{ Re}\{\mathcal{E}_S \mathcal{E}_{LO}^*\}.$$

The last term of equation 5.3 ($2 \text{ Re}\{\mathcal{E}_S \mathcal{E}_{LO}^*\}$) represents the heterodyne interference of the signal with the LO and corresponds to the 2D signal of interest. However, equation 5.3 also shows that other terms generated collinear to the signal may also be detected. However, the detection of these terms is not a real issue in a heterodyne detected experiment where the interference with the LO generally increases the signal response, and the term $2 \text{ Re } \{T_n \mathcal{E}_S^*\}$ can be considered negligible. Note that in situations where the scatter is very pronounced,

these terms can contribute to the final signal. Furthermore, the term $2\,\mathrm{Re}\{T_2 T_3^*\}$ is not a pump-probe signal; therefore, its contribution can also be ignored. These considerations lead to the following approximation:

$$\beta - \alpha \sim |\,\mathcal{E}_S\,|^2 + 2\,\mathrm{Re}\{\mathcal{E}_S \mathcal{E}_{LO}^*\} \tag{5.4}$$

This equation gives rise to three distinct signals in the time domain that can be manipulated to obtain the desired 2D spectrum as it will be further explained in the data analysis section (see equation 5.7).

The presence of a second chopper (C2) allows the direct subtraction (see $\beta - \alpha$) of the term $2\,\mathrm{Re}\{T_2 \mathcal{E}_{LO}^*\}$ which contains the so-called pump-probe contribution. This signal is generated when beam 2 acts as a pump, and the LO is the probe. This term cannot be isolated during the data manipulation, and its subtraction can be quite challenging if not implemented "in situ" particularly for samples that have strong TA signals.[33]

So far, the double chopper configuration is advantageous to record the heterodyne signal without the contribution of terms generated from scatter. Another advantage is the acquisition of the LO spectra for each t_2. This acquisition can be easily explained by carefully analysing Figure 5.7. When beam 2 and 3 are blocked the sample is only illuminated by beam 1 and LO and, omitting very small contaminations that can arise from the interference between the LO and beam 1, the detector acquires the reference beam spectrum. Note that for the specific case of Oxazine 4 (presented in Chapter 6) the LO spectrum is acquired only at the beginning and end of the experiment (and not at each t_2), where no differences are noticed between the two spectra. Thus, the data analysis is carried out using the same LO spectrum for each t_2 acquired (see data analysis section).

5.6 Time Ordering with Three Delay Stages

To acquire a full 2D spectrum, both the rephasing and non-rephasing signals need to be recorded. As already stated in Chapter 2 these two signals are in principle emitted along two spatially separated directions given by the linear combination of the wave vectors; therefore, in a simple picture, two matched spectrometers are required, or the spectrometer should be moved continuously to detect these two contributions (recall Figure 2.3). To overcome this problem and to acquire both rephasing and non-rephasing signals, in the same direction, I adopted a pairwise beam manipulation technique.[10]

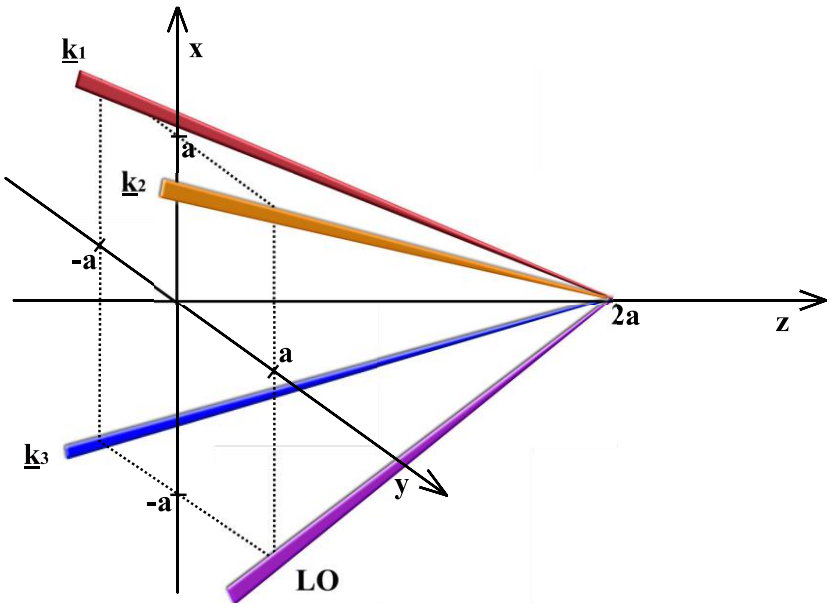

Figure 5.8 Diagram of the three-dimensional x, y, z system with the four beams displayed in the boxcar geometry.

To better understand this scenario, it is useful to visualise the geometrical representation of the four beams as shown in Figure 5.8 which is adapted from refs.[33,39] The diagram represents a generical situation where four vectors converge into a point that belongs to the z-axis. This point is arbitrarily chosen to be at 2a from the origin of the axis; thus, the vectors can be written as:

$$\underline{k}_1 = (a, -a, 2a), \quad (5.5)$$

$$\underline{k}_2 = (a, a, 2a),$$

$$\underline{k}_3 = (-a, -a, 2a),$$

$$\underline{k}_{LO} = (-a, a, 2a).$$

Considered that the rephasing (R) and the non-rephasing (NR) signals are generated along $-\underline{k}_1 + \underline{k}_2 + \underline{k}_3$ and $+\underline{k}_1 - \underline{k}_2 + \underline{k}_3$, respectively, in a vectorial form they can be expressed as:

$$\underline{k}_s\,(R) = (-a + a - a,\ a + a - a,\ -2a + 2a + 2a) = (-a, a, 2a) = k_{LO} \quad (5.6)$$

$$\underline{k}_s\,(NR) = (a - a - a,\ -a - a - a,\ 2a - 2a + 2a) = (-a, -3a, 2a) \neq k_{LO}$$

where the rephasing signal is emitted along the LO direction of propagation while $\underline{k}_S$ and $\underline{k}_{LO}$ are not coincident for the non-rephasing scenario. However, if it were possible to invert the time ordering of $\underline{k}_1$ and $\underline{k}_2$ during the experiment, $\underline{k}_s$ (NR) and (R) would be inverted compared to equation 5.6, with $\underline{k}_s$ (NR) = k_{LO} and $\underline{k}_s$ (R) ≠ $\underline{k}_{LO}$.

Experimentally, one would ideally move from one scenario where the $\underline{k}_s$ (R) propagates along the LO direction to the second scenario where $\underline{k}_s$ (NR) is generated and propagates along the LO direction under the same experimental conditions. The alternation of these two scenarios is experimentally achieved by controlling the pulses relative time delays; thus, both $\underline{k}_s$ (R) and $\underline{k}_s$ (NR) can be detected without changing the position of the detector.

To better understand this implementation, let us now consider the role of the three delay stages. In this setup, DS and PZ1 controls the delay between the pulses 1/2 and 3/LO, while the time delay between the pair of beams 3/1 and 2/LO depends on PZ2. The LO is always delayed with an additional glass (ND filter) by 1985 fs (measured with SHG-FROG) with respect to the other three pulses. Thus, the initial scenario of the data acquisition can be depicted as in Figure 5.9 (a) where both the coherence and waiting time are set at zero.

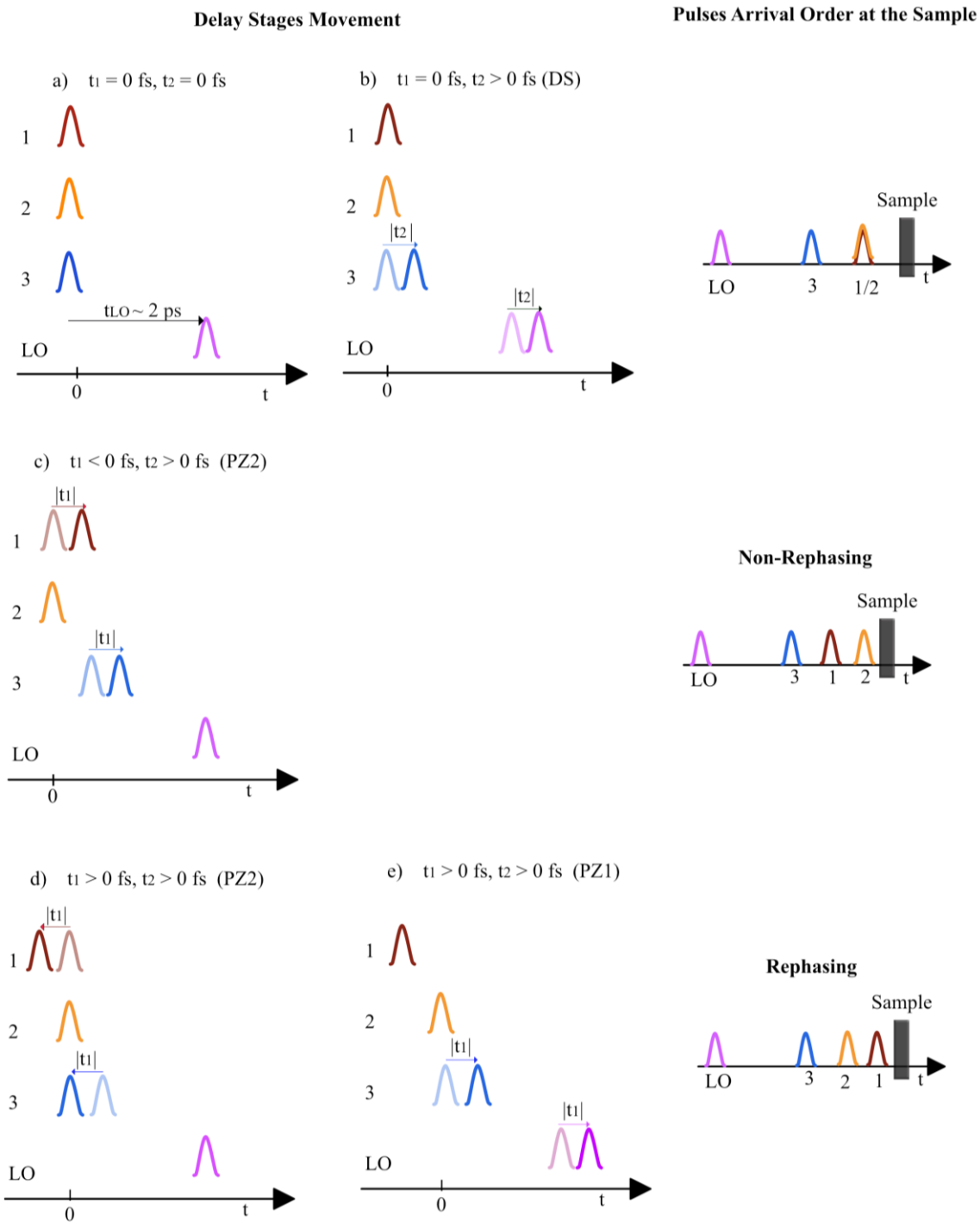

Figure 5.9 Delay stages movement and pulses arrival time at the sample.

Subsequently, the waiting time is moved to positive values ($t_2 > 0$), by changing the position of DS, as displayed in Figure 5.9 (b). The change in position of DS also modifies both the time delay of pulse 3 and LO while it leaves pulse 1 and 2 unchanged. Therefore, the pulses arrival time at the sample is 1/2, 3 and LO, as shown in Figure 5.9 (top right). At this point,

the acquisition of the non-rephasing signal is straight forward. The pulse arrival sequence, 2,1,3 and LO, gives the signal which can be achieved by moving PZ2 backwards (negative coherent times following the convention),[10,33,39] in such a way that the pathway followed by the beams 1 and 3 is longer than the initial path. Therefore, they are delayed compared to beam 2, as shown in Figure 5.9 (c and panel on the right).

For positive coherence times which correspond to the rephasing signal (pulse ordering 1, 2, 3 and LO), the picture is slightly more complicated because both piezoelectric stages need to move in the opposite direction to collect the correct signal. The issue now is that the forward movement of PZ2 causes pulses 1 and 3 to arrive at the sample before pulse 2 (see Figure 5.9 (d)), which would also modify the waiting time. To overcome this issue, and to allow pulse 2 to arrive at the correct time delay and to generate a rephasing signal, PZ1 needs to be moved backwards by exacting the same amount as PZ2 is moved forwards, as illustrated in Figure 5.9 (e).

It is now worth noting that the constant phase shift between the LO and the signal that is generated by the relative movement of the stages means the signal is acquired in the rotating frame.[40,41] The direct consequence of acquiring the 2D spectra under such conditions it that the signal (in the t_1 delay) does not oscillate close to the optical frequency; thus, the envelope of the response function is captured (which depends on the coherence time). Acquiring only the envelope of the response function can be advantageous because it significantly reduces the time steps in t_1 that must be sampled and reduces the phase stability requirements significantly.[32,33,40,41]

5.7 Phase-stable Setup

Considering a setup where a single light source generates the four pulses, and they experience the same optics as the reference beam (LO) the absolute phase difference turns out to be zero, and the setup is considered phase-stable.[10] In the presented case, the phase fluctuation of the setup was minimized and, as Heilser *et. at.*[33] have already proved, the configuration adopted with the beams travelling in pairs was very advantageous to reduce the fluctuations of the setup. The mathematical demonstration (taken from the Heilser's work[33] and given in the appendix for completeness) shows that even when the pulses are subjected to small shifts and fluctuations these can be cancelled out (as reported in equation Ap. 5.8), and the setup can be said to be phase-stable. Note that this analysis does not consider major fluctuations induced by the air current. For this reason, I built a setup that was enclosed by a box from the output of the Libra laser to the detection region. Moreover, the size of the 2D spectrometer was kept as small as possible.

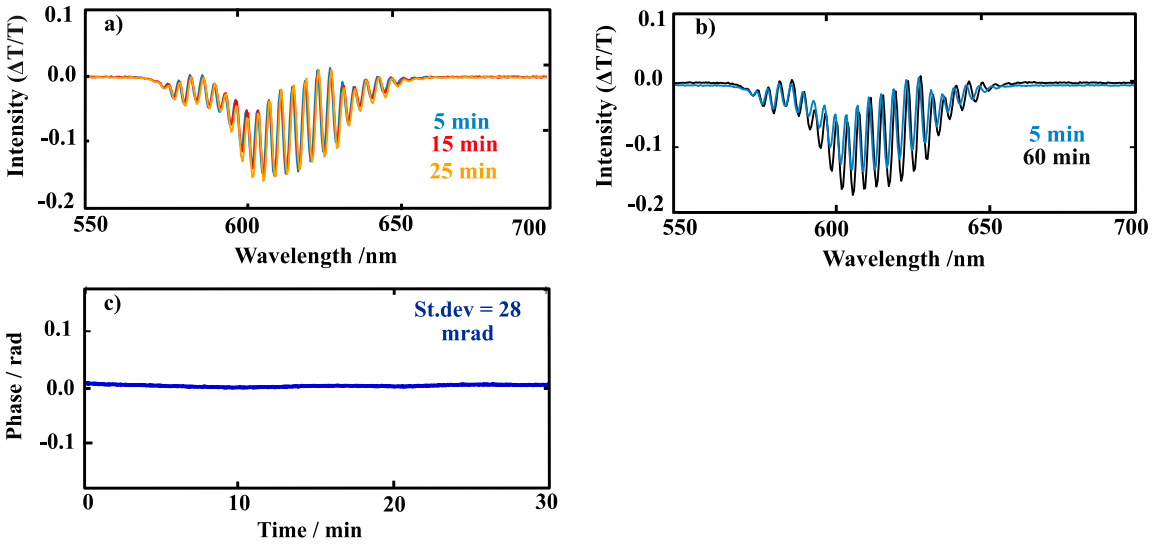

Figure 5.10 Interference paths acquired (a) at 5, 15 and 25 min, (b) 5 and 60 min, and (c) the standard deviation of the fluctuation for 30 minutes.

To further test the phase stability of my 2DES experiment, I measured the interference fringing pattern between beams 1 and 2 focused into a pinhole (with diameter = 100 μm). The interference pattern acquired every second for 60 minutes showed that the phase remained stable for the first 30 minutes (Figure 5.10 (a)); subsequently, a deviation from its initial value was observed, see example in Figure 5.10 (b). To evaluate the quality of the phase stability, the standard deviation in radians was also calculated for the first 30 minutes, and it returned 28 mrad. The value obtained is similar to other spectrometer(s) considered phase-stable as the one in ref.[28]

5.8 Data Acquisition

After generating the desired broadband spectrum with the double-pass NOPA and compression with the Dazzler ultrafast pulse-shaper, the beam was coupled to the 2D boxcar geometry spectrometer. The alignment was monitored with irises placed throughout the setup to monitor the day to day reproducibility. The spatial overlap of the four beams generated in the boxcar geometry was achieved with either a CCD camera or a pinhole. Because of the geometry configuration (boxcar), it was quite challenging to place the CCD camera at the sample position without blocking one of the four beams; therefore, my personal preference was to use the pinhole in order to avoid this issue. I had also observed that when the beam travels through the irises placed along the boxcar configuration the four beams focus and spatially overlap without any further adjustment, however, this was not the case when the frequencies produced by the NOPA were changed. This case is more complicated because the collimation might need to be adjusted (*i.e.* the telescope needs to be re-optimised) as well as the Dazzler pre-compensation stage (the distance between the two prisms) might be changed depending on the frequencies generated.

Before starting any 2D experiment the four pulses were characterised with TG-FROG,[35] and the traces obtained were analysed with a commercial software written in MatLab and developed by Trebino's group.[35] This software is commonly used by many groups and it allows the phase and the pulse duration to be retrieved. The TG-FROG measurement was done with beams 1, 2 and 3 and DMSO (non-linear Kerr medium) in 1 mm cuvette. The TG FROG traces, and the duration of the pulses are reported in Chapters 6 and 7.

Subsequently, the temporal overlap between 3 pulses was monitored with SHG-FROG or TG-FROG. The SHG-FROG measurement consisted of focusing the three pulses in a BBO-crystal placed at the sample region and detecting the second-harmonic generation of each beam pair. However, in the current configuration this measurement is not easy to implement because it is necessary to change the sample holder with the BBO-crystal mount and to completely realign the detection region (the collimation and focus before the Andor spectrometer). This procedure needs to be carried out for each signal given by a pair of pulses, and because the three signals generated are spatially separated the overall procedure is time-consuming. Alternatively, the time-zero between pulse 1, 2 and 3 can be monitored with TG-FROG by scanning DS, subsequently PZ2, and re-setting time zero after each scan. The signal that depends on DS is centred at 0 by adjusting the relative position of DS and PZ1 while the adjustment of the transient gating signal that depends on PZ2 is achieved by resetting the time-zero of the piezo stage. This iterative process was repeated until scanning of both PZ2 and DS converged on a common time zero.

When all the three pulses are centred at time zero, the sample is inserted into the setup, and the LO introduced and aligned into the spectrometer. The time delay between the stages is initially set at zero ($t_1 = t_2 = 0$, see also Figure 5.9) and the z-axis of the sample was moved

to maximize the spectral modulations of the detected LO spectrum. Because the beams are not perfectly perpendicularly to the sample, a small adjustment of the x-axis might be required to avoid beam block or scatter. To minimize any scatter, DS was then moved to a negative population time where the modulation of the LO should be zero. If the modulations at $t_2 < 0$ persisted, the sample was translated along the x-axis until the LO spectrum was free from the undesired signals. During this alignment process, it is good to block the beams now and then to ensure that the signal observed does not depend on some random interference between a pair of beams. All of these procedures are iterative, and they need to be executed until the signal is optimised.

Once the optimum signal was found, the measurement routine was started, and rephasing and nonrepeating signals were acquired for each interval of t_1 desired as well as for each t_2 needed. After the pump-probe spectrum for each waiting time was acquired, the DS is moved to the desired t_2, and the 2D spectrum acquisition starts by scanning the coherence time delay (t_1). The measurements shown in this thesis were usually collected for a total of 100/150 t_1 delays averaging 600 laser shots for each waiting time chosen. The total acquisition of each 2DES spectrum took around 3 minutes, including the collection of the local oscillator.

5.9 Data Analysis

In our experiment for each population time, t_2, two different signals were acquired. The first is the pump-probe signal where beam 2 acts as pump and LO as probe and the second signal was a spectral interferogram which corresponds to the frequency-resolved photon echo signal of the sample interfering with the delayed local oscillator (via heterodyne detection). Each spectral interferogram was recorded as function of the coherence time, t_1,

and spectrally dispersed along the emission axis ω_3. Figure 5.11 (a) shows the spectral interferogram containing the 2DES signal of a dye molecule at t_2 = 120 fs as a function of t_1 where both rephasing (positive t_1) and non-rephasing (negative t_1) components are shown. In Figure 5.11 (b) a section of the spectrum is taken at t_1= 0 fs.

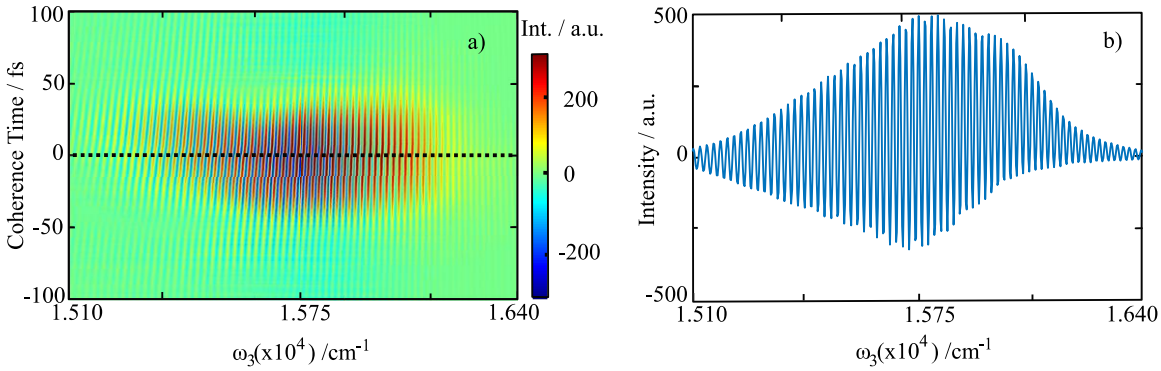

Figure 5.11 (a) Contour map of the spectral interferogram acquired at t_2 = 120 fs, (b) slice of the spectral interferogram at t_1= 0 fs corresponding to the dashed line.

The goal is to use these interferograms to obtain a complex 2DES spectrum at various population times as a function of excitation and emission frequencies (ω_1, ω_3). As first step to achieve the goal, the acquired spectrum that is not linearly spaced in frequency was interpolated to linearly space the frequencies. To show how to manipulate the spectral interferogram recorded I should recall that the heterodyne signal acquired is given by equation 2.16 ($S = |\mathcal{E}_s + \mathcal{E}_{LO}|^2$) where $\mathcal{E}_s(t_1,t_2,\omega_3) = E_s(t_1,t_2,\omega_3)e^{i\omega_3 t_s}$ and $\mathcal{E}_{LO}(\omega_3) = E_{LO}(\omega_3)e^{i\omega_3 t_{LO}}$ (E_n is a constant and complex vector of the electric fields which includes the phase term, ω_3 is the carrier frequency, and t_n is the relative time). By also considering equation 5.4, the acquired spectral interferogram can be written as:

$$S(t_1,t_2,\omega_3) = |E_S(t_1,t_2,\omega_3)|^2 \qquad (5.7)$$

$$+ E_S(t_1,t_2,\omega_3)E^*_{LO}(\omega_3)\, e^{i\omega_3(t_S-t_{LO})} + E_{LO}(\omega_3)E^*_S(t_1,t_2,\omega_3)\, e^{-i\omega_3(t_S-t_{LO})}$$

where $|E_{LO}(\omega_3)|^2$ has been omitted because the action of the two choppers subtracts it.[33] Thus, equation 5.7 shows that the signal acquired is a function of three terms, the first of which is not time-dependent and it corresponds to the homodyne signal, while the second and third terms appear to be at $\pm (t_s - t_{LO})$. To visualise the time separation of these three terms and isolate the complex signal field needed, the inverse FT along the ω_3 frequency domain was necessary. Figure 5.12 (a) shows a contour map of the three contributions to the signal at a given t_2 (t_2= 120 fs) as a function of the coherence time, while Figure 5.12 (b) displays the three contributions for the rephasing part of the signal at t_2 = 120 and t_1= 10 fs.

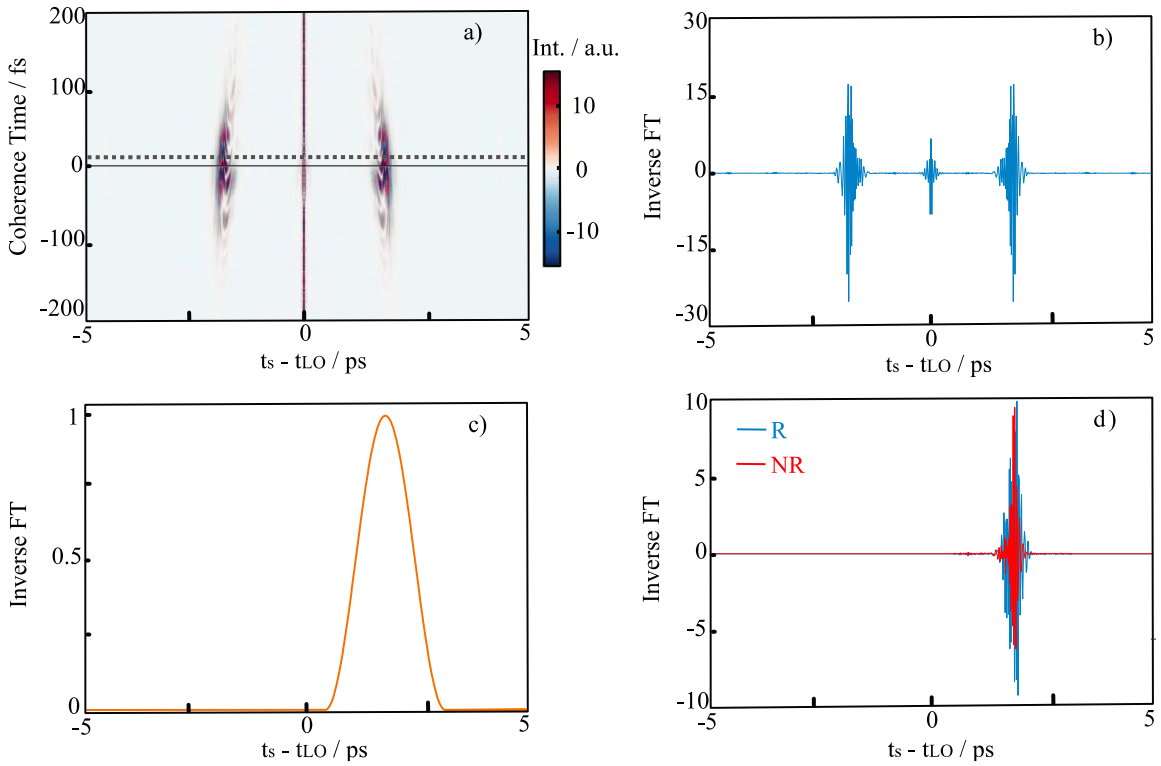

Figure 5.12 (a) Contour map of the three terms shown in equation 5.7 at t_2 = 120 fs comprising of both rephasing and non-rephasing signals, (b) a slice of the previous map taken at t_1= 10 fs corresponding to the dashed line in the first panel. (c) Window function applied to the data at each t_1 time-delay and (d) the rephasing and non-rephasing signal isolated after the windowing process.

To isolate the $E_S(t_1,t_2,\omega_3)E^*_{LO}(\omega_3)\, e^{i\omega_3(t_S-t_{LO})}$ contribution from the other two terms a window function, see Figure 5.12 (c), was applied along the t_1 axes for each coherence time. After the windowing procedure, both the rephasing and non-rephasing signals that contribute to the desired complex signal field of equation 5.7 were isolated from the others, as shown in Figure 5.12 (d).

The complex signal field was subsequently FT from t_3 to ω_3 ($S(t_1,t_2,t_3) \rightarrow S(t_1,t_2,\omega_3)$). Note that E_n is a complex vector, and it includes the phase factor (Φ_n) of the field; therefore, the term isolated after applying the window function can be written as:

$$E_S(t_1,t_2,\omega_3)E^*_{LO}(\omega_3)e^{i\omega_3(t_S-t_{LO})} = |E_S(t_1,t_2,\omega_3)||E_{LO}(\omega_3)|e^{i[\omega_3(t_S-t_{LO})+(\Phi_S-\Phi_{LO})]} \quad (5.8)$$

$$=\sqrt{I_S(t_1,t_2,\omega_3)I_{LO}(\omega_3)}e^{i[\omega_3(t_S-t_{LO})+(\Phi_S-\Phi_{LO})]}$$

where | | represents the absolute value of the field, the phase relative to the signal and local oscillator are explicitly written and the intensity term (I_n) is retrieved from its definition ($I = E^2$).

To obtain the desired signal and phase, equation 5.8 still needs to be divided by $\sqrt{I_{LO}(\omega_3)}$. In the implemented 2DES setup the LO spectrum is acquired at the beginning and end of every scan by blocking $\underline{k}_1$,$\underline{k}_2$, and $\underline{k}_3$. After removing the LO intensity contribution, equation 5.8 is also divided by $e^{i\omega_3\Delta t}$ where the Δt contribution was experimentally determined via SHG-FROG beforehand; thus, equation 5.8 can be written as:

$$|E_S(t_1,t_2,\omega_3)|e^{i(\Phi_S-\Phi_{LO})} = \sqrt{I_S(t_1,t_2,\omega_3)}e^{i(\Phi_S-\Phi_{LO})} \quad (5.9)$$

where the time-dependent oscillations are now removed from ω_3 axes. However, the spectral interferometry is still dependent on the so-called relative phase between the signal and the local oscillator ($\Phi_S-\Phi_{LO}$), which is the measured value. It is now worth recalling

that the total 2D spectrum is composed of a real (absorptive) and imaginary (dispersive parts) that depend on the so-called "global phase" which is an unknown parameter usually challenging to measure. The phase correction is commonly done by comparing the measured phased spectra to the pump-probe spectrum acquired at the corresponding t_2 time delay by using the projection slice theorem to retrieve the global phase of the spectrum.[3,8,43] After applying a test phase, the 2D spectrum was integrated over the ω_1 direction resulting in a one-dimensional signal which has the same shape as the pump-probe signal but a different phase. The two spectra are then normalised, and a least-squares difference fit is performed to obtain the global phase for a given t_2 delay. After phase correction, the complex 2D map is Fourier transformed along t_1 to obtain the 2DES maps which are given by the sum of the rephasing and non-rephasing signals for each waiting time. Figure 5.13 is an example of the 2DES spectra obtained for Oxazine 4 in methanol at t_2 = 30 (panel (a)), and 180 fs (panel (b)).

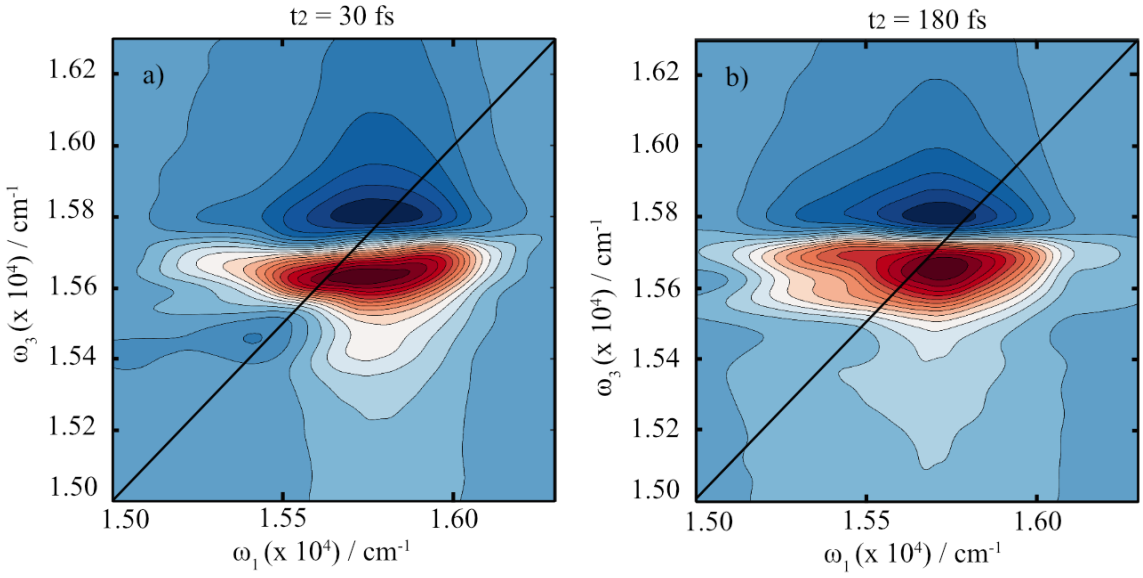

Figure 5.13 2DES spectra of Oxazine 4 in methanol at t_2 = (a) 30, and (b) 180. The black lines show the diagonals of the 2D spectra.

5.10 Appendix

Ap. 5.1 Second-harmonic Generation

Non-linear optical effects arise from the interaction of a high-intensity light source such as an ultrafast laser incident on a non-linear medium. In linear optics, the matter response scales linearly with the amplitude of the electric field, while, in non-linear optics, the material properties can change more rapidly due to the high-intensity of the field applied. From this interaction, non-linear effects are generated and used for study in spectroscopy and development of state-of-the-art apparatus.

Equation Ap 5.1 displays the relationship between the applied field E(t) and the polarization P(t) which are related as follows[1,5]:

$$P(t) = \varepsilon_0 \chi^{(1)} E(t) \qquad \text{Ap 5.1}$$

where ε_0 represents the permittivity of free space and χ is the linear susceptibility.

When an intense field is applied to a lossless and dispersionless medium, the optical response can be generalised as:

$$P(t) = \varepsilon_0 [\chi^{(1)} E^1(t) + \chi^{(2)} E^2(t) + \chi^{(3)} E^3(t) + ...] \qquad \text{Ap. 5.2}$$

$$= P^1(t) + P^2(t) + P^3(t) + ... = P^L(t) + P^{NL}(t)$$

where $P^2(t)=\chi^{(2)}E^2(t)$ and $P^3(t)= \chi^{(3)}E^3(t)$ are the so-called second-order nonlinear polarization and third-order nonlinear polarization. P^L is the linear response of the electric field and P^{NL} is the nonlinear response. Equation Ap. 5.2 is the mathematical representation of an intense field that, after interaction with the medium, generates new frequency components which are source of new frequency components in the electromagnetic field.

Second-harmonic generation (SHG), arises from the second-order non-linear polarization, and it is a non-linear phenomenon that allows the conversion of a generic frequency, ω, into its second-harmonic frequency, 2ω. This non-linear phenomenon can be described as a radiation (*i.e.*, a laser beam) at frequency ω incident upon a non-centrosymmetric crystal which generates the following second-order non-linear polarization[1]:

$$P^{(2)}(t)= \varepsilon_0\chi^{(2)}E^2(t) = 2\varepsilon_0\chi^{(2)}EE^{*}+\varepsilon_0\chi^{(2)}E^2e^{-i2\omega} + c.c \qquad \text{Ap. 5.3}$$

where the electric field of the beam is expressed through its oscillatory component $E(t)=Ee^{-i\omega t}+ E^{*}e^{i\omega t}$. Equation Ap. 5.3 shows that the second-order polarization has two contributions, one is at zero frequency ($2\varepsilon_0\chi^{(2)}EE^{*}$) while the second one has a contribution at 2ω ($\varepsilon_0\chi^{(2)}E^2e^{-i2\omega}$).

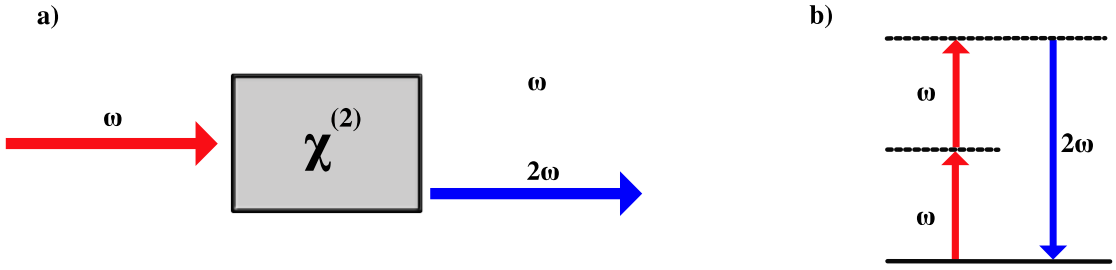

Figure Ap. 5.1(a) Representation of SHG occurring in a non-linear medium. (b) Energy level of SHG process showing two photons at frequency (ω) and one photon generated at frequency 2ω. The dashed lines represent virtual states.

Figure Ap. 5.1 (a) represents of the non-linear process (very efficient) where nearly all the power of the incident beam can be converted into its second-harmonic. Figure Ap. 5.1 (b) is a diagram of energy levels (dashed lines are virtual states) for SHG where two photons at the same frequency, ω, are destroyed to simultaneously generate a third photon at a frequency 2ω.

Ap. 5.2 Compression Stage

There are several methods to add negative second-order dispersion to the broadband pulses such as grating pairs, prisms pairs, deformable mirrors, chirped mirrors and acousto-optic modulators.[34]

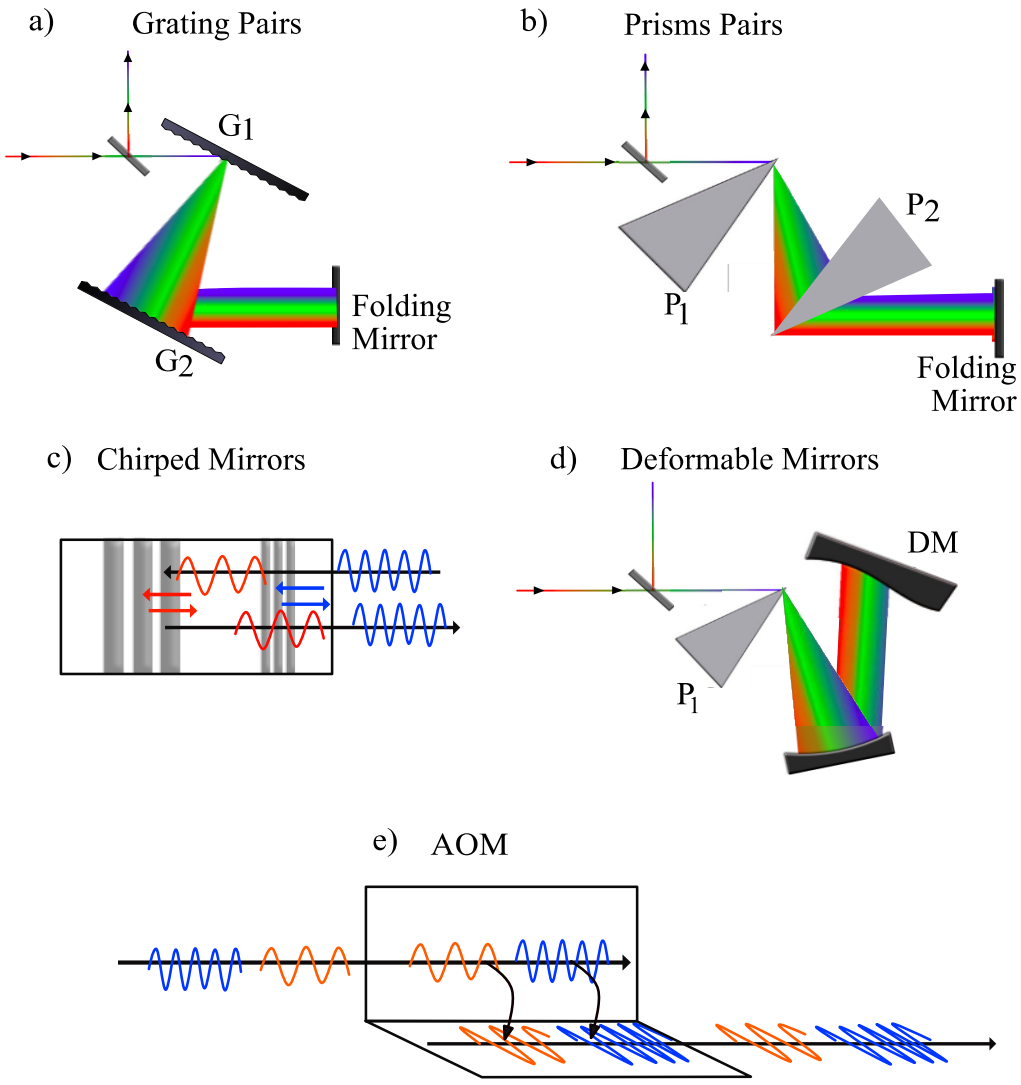

Figure Ap. 5.2 Methods for pulse compression (a) grating pairs, (b) prisms pairs, (c) chirped mirrors, (d) deformable mirrors and (e) acousto-optic modulator.

The first method, the grating pairs, is not commonly used in this sort of setup because of the large GDD and high losses values introduced by the gratings. A representation of

grating pairs is depicted in Figure Ap. 5.2 (a) while Figure Ap. 5.2 (b) represents a simple compressor made by two prisms and a folding mirror. The prism compressor adds negative GDD that depends on the glass insertion of the two prisms and a significant negative TOD. An interesting parameter to control when working with prisms is the ratio between TOD and GDD (TOD/GDD) that is strongly dependent on the prism material and frequency. The materials characterised by the smallest ratio are fused silica, magnesium fluoride (MgF_2), calcium fluoride (CaF_2) and SF11 and the prisms used in the compression stage are usually made by one of these materials. The main advantage of the prism compressor is that it can correct for GDD, but not for TOD; thus, it is suitable for compression down to ~ 20 fs, but not shorter. Furthermore, prisms compression has another disadvantage that needs to be considered. The GDD and TOD added are proportional to the distance between the two prisms and when the input beam is tuneable, *i.e.* NOPAs, the compressor needs to be re-aligned and re-adjusted as the NOPA wavelength is changed.

Another alternative that can be used for pulse compression consists of multiple bounces on chirped mirrors (CMs). Figure Ap. 5.2 (c) shows a basic scheme of CMs. The main advantage of these devices is that the GDD introduced does not depend on the alignment because it only depends on the number of bounces. The dispersion introduced can only vary in discrete steps. For this reason, the CMs are always implemented in combination with a pair of silica wedges used to adjust the amount of material on the beam path and compensate for the negative GDD introduced by the mirrors. The main disadvantage of the CMs is their relatively high cost and the need of specific design when working in the IR spectral region and/or when the pulse compression requires to compensate for the TOD.

Deformable mirrors (Figure Ap. 5.2 (d)) use a modern technology involving micron membrane to correct for the second and third-order dispersion. After a dispersive element, a grating or prism, the deformable mirror can perform a spatial FT and convert an angular dispersion into a spatial separation. A very similar process occurs when pulse-shapers are used to compress a pulse. A phase modulation occurs when the electromagnetic field interacts with an acoustic wave that propagates collinearly to the electromagnetic field (Figure Ap. 5.2 (e)). The acousto-optic programmable dispersive filter pulse shaper has the advantage that is easy to use and can precisely correct for any dispersion (*i.e.* GDD and TOD). The disadvantages are that the pulse shapers contain a thick nonlinear crystal and pre-compensation is needed. Moreover, these devices can be very lossy, with up to 80% of the power being lost, and they usually add complexity and cost to the final setup.[34,44,45]

Ap. 5.3 Setup Overview

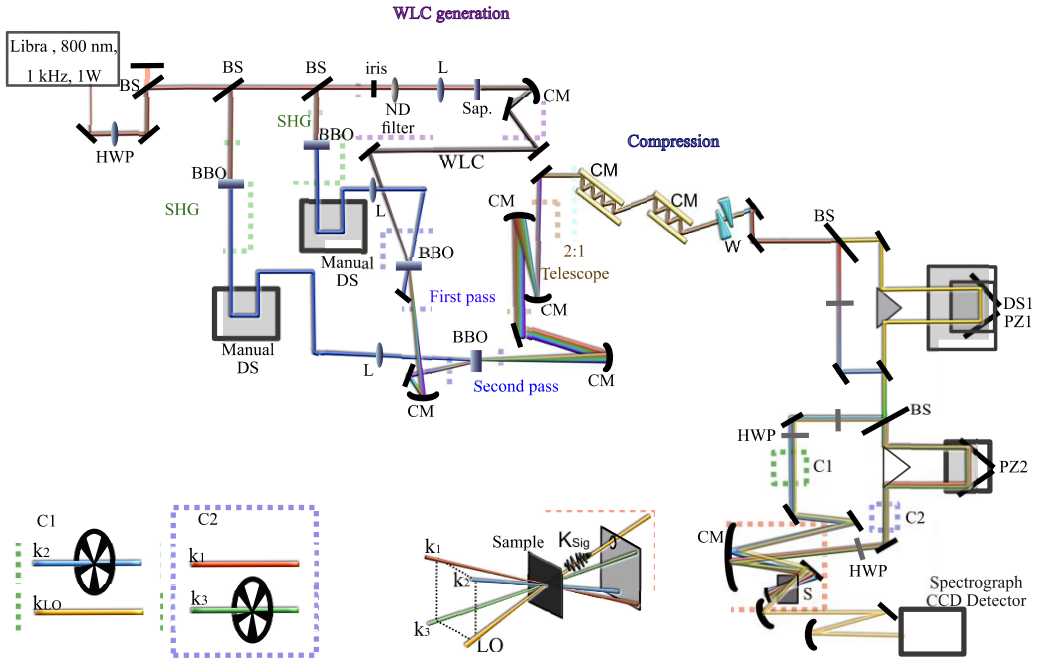

Figure Ap. 5.3 Overview of the setup implemented where the compression stage is achieved with CMs and wedges.

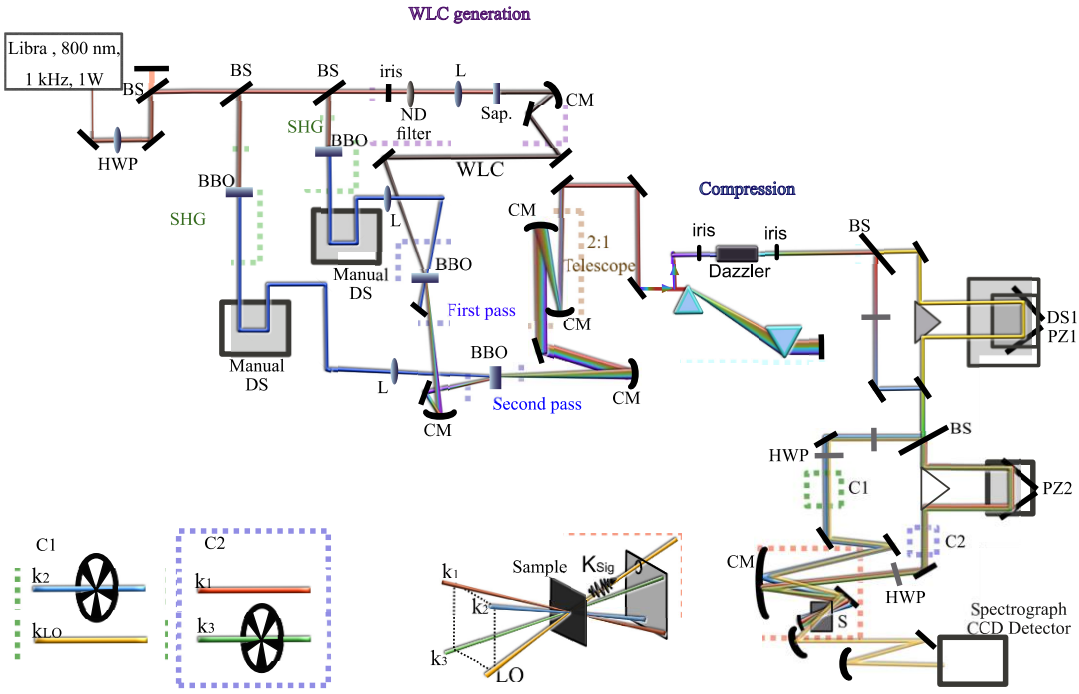

Figure Ap. 5.4 Overview of the setup implemented where the compression stage is achieved with the Dazzler pulse shaper, and the light is pre-compressed with fused silica prisms.

Ap. 5.4 Phase-stable Apparatus

The following demonstration has been adapted to the Bristol setup from ref.[33]

The phase of the (rephasing, $\underline{k}_s = -\underline{k}_1 + \underline{k}_2 + \underline{k}_3$) detected heterodyne ($\Delta\varphi_S$) signal acquired under our experimental conditions is:

$$\Delta\varphi_S = -\varphi_1 + \varphi_2 + \varphi_3 - \varphi_{LO} + \varphi_{SIG} \qquad \text{(Ap 5.4)}$$

where φ_{SIG} corresponds to the phase of the homodyne signal and φ_n is the phase of each laser beam that interact to generate the signal. The overall phase fluctuation depends on both the optics and the geometry used, and it is given by the following equation:

$$\delta(\Delta\varphi_S) = \delta(-\varphi_1 + \varphi_2) + \delta(\varphi_3 - \varphi_{LO}) \qquad \text{(Ap. 5.5)}$$

In our case, the phase fluctuations depend on the optics that each beam is experiencing from BS1 to the sample. For example, beam 1 phase fluctuation corresponds to (see Figure 5.5):

$$\delta(\varphi_1) = \delta\varphi_{BS1} + \delta\varphi_{M2,M3} + \delta\varphi_{BS2} + \delta\varphi_{PZ2+P2} + \delta\varphi_{M7} + \delta\varphi_{CM}\,. \qquad \text{(Ap. 5.6)}$$

Moreover, writing it for all the beams and substituting the terms into equation Ap. 5.5, the results are:

$$\varphi_2 - \varphi_1 = \delta\varphi_{M4} + \delta\varphi_{M5} + \delta\varphi_{M6} - \delta\varphi_{PZ2+P2} - \delta\varphi_{M7} \qquad \text{(Ap. 5.7)}$$

$$\varphi_3 - \varphi_{LO} = -\delta\varphi_{M4} - \delta\varphi_{M5} - \delta\varphi_{M6} + \delta\varphi_{PZ2+P2} + \delta\varphi_{M7}$$

Thus, the phase fluctuation is zero:

$$\delta(\Delta\varphi_S) = 0 \qquad \text{(Ap. 5.8)}$$

References

1. Mukamel, S. Principles of Nonlinear Optical Spectroscopy. *Oxford University Press* (1999)

2. Cho, M., Brixner, T., Stiopkin, I., Vaswani, H. & Fleming, G. R. Two Dimensional Electronic Spectroscopy of Molecular Complexes. *J. Chin. Chem. Soc.* **53**, 15–24 (2006).

3. Fuller, F. D. & Ogilvie, J. P. Experimental Implementations of Two-Dimensional Fourier Transform Electronic Spectroscopy. *Annu. Rev. Phys. Chem.* **66**, 667-690 (2015).

4. Jonas, D. M. Two-dimensional femtosecond spectroscopy. *Annu. Rev. Phys. Chem.* **54**, 425–463 (2003).

5. . Ernst, R. R., Bodenhausen, G., Wokaun, A. & Redfield, A. G. Principles of Nuclear Magnetic Resonance in One and Two Dimensions. *Phys. Today* **42**, 75–76 (1989).

6. Cho, M. Coherent two-dimensional optical spectroscopy. *Chem. Rev.* **108**, 1331–1418 (2008).

7. Hybl, J. D., Albrecht, A. W., Faeder, S. M. G. & Jonas, D. M. Two-dimensional electronic spectroscopy. *Chem. Phys. Lett.* **297**, 307-313 (1998).

8. Hybl, J. D., Albrecht Ferro, A. & Jonas, D. M. Two-dimensional Fourier transform electronic spectroscopy. *J. Chem. Phys.* **115**, 6606-6622 (2001).

9. Cowan, M. L., Ogilvie, J. P. & Miller, R. J. D. Two-dimensional spectroscopy using diffractive optics based phased-locked photon echoes. *Chem. Phys. Lett.* **386**, 184–189 (2004).

10. Brixner, T., Mančal, T., Stiopkin, I. V. & Fleming, G. R. Phase-stabilized two-dimensional electronic spectroscopy. *J.Chem. Phys.* **121**, 4221–4236 (2004).

11. Grumstrup, E. M., Shim, S.-H., Montgomery, M. A., Damrauer, N. H. & Zanni, M. T. Facile collection of two-dimensional electronic spectra using femtosecond pulse-shaping Technology. *Opt. Express* **15**, 16681-16689 (2007).

12. Myers, J. A., Lewis, K. L. M., Tekavec, P. F. & Ogilvie, J. P. Two-color two-dimensional Fourier transform electronic spectroscopy with a pulse-shaper. *Opt. Express* **16**, 17420-17428 (2008).

13. Tian, P., Keusters, D., Suzaki, Y. & Warren, W. S. Femtosecond Phase-Coherent Two-Dimensional Spectroscopy. *Science* **300**, 1553–1555 (2003).

14. Ginsberg, N. S., Cheng, Y.C. & Fleming, G. R. Two-dimensional electronic spectroscopy of molecular aggregates. *Acc. Chem. Res.* **42**, 1352–63 (2009).

15. Engel, G. S., Calhoun, T. R., Read, E. L., Ahn, T., Mancal, T., Cheng, Y. C., Blankenship, R. E. & Fleming, G. R. Evidence for wavelike energy transfer through quantum coherence in photosynthetic systems. *Nature* **446**, 782–786 (2007).

16. Collini, E., Wong, C. Y., Wilk, K. E., Curmi, P. M. G. & Brumer, P. Coherently wired light-harvesting in photosynthetic marine algae at ambient temperature. *Nature* **463**, 644–647 (2010).

17. Turner, D. B., Dinshaw, R., Lee, K. K., Belsley, M. S., Wilk, K. E., Curmi, P. M. & Scholes, G. D. Quantitative investigations of quantum coherence for a light-harvesting protein at conditions simulating photosynthesis. *Phys. Chem. Chem. Phys.* **14**, 4857–4874 (2012).

18. Lewis, K. L. M. & Ogilvie, J. P. Probing Photosynthetic Energy and Charge Transfer with Two-Dimensional Electronic Spectroscopy. *J. Phys. Chem. Lett.* **3**, 503–510 (2012).

19. Ginsberg, N. S., Davis, J. A., Ballottari, M., Cheng, Y. C. & Bassi, R. Solving structure in the CP29 light harvesting complex with polarization-phased 2D electronic spectroscopy. *Proc. Natl. Acad. Sci. U. S. A.* **108**, 3848–3853 (2011).

20. Ostroumov, E. E., Mulvaney, R. M., Cogdell, R. J. & Scholes, G. D. Broadband 2D Electronic Spectroscopy Reveals a Carotenoid Dark State in Purple Bacteria. *Science* **340**, 52–56 (2013).

21. Turner, D. B. & Nelson, K. A. Coherent measurements of high-order electronic correlations in quantum wells. *Nature* **466**, 1089–1092 (2010).

22. Singh, R., Moody, G., Siemens, M. E., Li, H. & Cundiff, S. T. Quantifying spectral diffusion by the direct measurement of the correlation function for excitons in semiconductor quantum wells. *J. Opt. Soc. Am. B.* **33**, C137-C143 (2016).

23. Vaughan, J. C., Hornung, T., Stone, K. W. & Nelson, K. A. Coherently Controlled Ultrafast Four-Wave Mixing Spectroscopy. *J. Phys. Chem.* **111**, 4873–4883 (2007).

24. Fuller, F. D., Wilcox, D. E. & Ogilvie, J. P. Pulse shaping based two-dimensional electronic spectroscopy in a background-free geometry. *Opt. Express* **22**, 1018–1027 (2014).

25. Bolzonello, L., Volpato, A., Meneghin, E. & Collini, E. Versatile setup for high-quality rephasing, non-rephasing, and double quantum 2D electronic spectroscopy. *J. Opt. Soc. Am. B.* **34**, 1223-1233 (2017).

26. Song, Y., Li, X. & Ogilvie, J. P. Two-dimensional electronic spectroscopy. *Encyclopedia of Modern Optics.* **2,** 184-196 (2018).

27. Shim, S. H., Strasfeld, D. B., Ling, Y. L. & Zanni, M. T. Automated 2D IR spectroscopy using a mid-IR pulse shaper and application of this technology to the human islet amyloid polypeptide. *Proc. Natl. Acad. Sci. U. S. A.* **104**, 14197–14202 (2007).

28. Brida, D., Manzoni, C. & Cerullo, G. Phase-locked pulse pair for two-dimensional spectroscopy by a birefringent delay line. *J. Opt. Soc. Am.* **15**, 3027-3029 (2012).

29. Huang, Z., Wang, P., Shen, X., Yan, T., Zhang, Y.& Liu, J. Compact design for two-dimensional electronic spectroscopy. *Laser Phys.* **26**, 035403 1-6 (2016).

30. Karaiskaj, D. Bristow, A. D., Yang, L., Dai, X., Mirin, R. P., Mukamel, S. & Cundiff, S. T. Two-Quantum Many-Body Coherences in Two-Dimensional Fourier-Transform Spectra of Exciton Resonances in Semiconductor Quantum Wells. *Phys. Rev. Lett.* **104**, 117401 1-4 (2010).

31. Zhang, Y., Meyer, K., Ott, C. & Pfeifer, T. Passively phase-stable, monolithic, all-reflective two-dimensional electronic spectroscopy based on a four-quadrant mirror. *Opt. Lett.* **38**, 356–8 (2013).

32. Selig, U., Langhojer, F., Dimler, F., Lohrig, T., Schwarz, C., Gieseking, B. & Brixner, T. Inherently phase-stable coherent two-dimensional spectroscopy using only conventional optics. *Opt. Lett.* **33**, 2851-2853 (2008).

33. Heisler, I. A., Moca, R., Camargo, F. V. A. & Meech, S. R. Two-dimensional electronic spectroscopy based on conventional optics and fast dual chopper data acquisition. *Rev. Sci. Instrum.* **85**, 063103 1-10 (2014).

34. Manzoni, C. & Cerullo, G. Design criteria for ultrafast optical parametric amplifiers. *J. Opt.* **18**, 103501 1-33 (2016).

35. Trebino, R. Frequency-Resolved Optical Gating: The Measurement of Ultrashort Laser Pulses. *Kluwer Academic, Norwell, MA* (2000).

36. Liebel, M., Schnedermann, C., Wende, T. & Kukura, P. Principles and applications of broadband impulsive vibrational spectroscopy. *J. Phys. Chem.* **119**, 9506–9517 (2015).

37. Tan, H.-S. Theory and phase-cycling scheme selection principles of collinear phase coherent multi-dimensional optical spectroscopy. *J. Chem. Phys.* **129**, 124501 1-13 (2008).

38. Augulis, R. & Zigmantas, D. Two-dimensional electronic spectroscopy with double modulation lock-in detection: enhancement of sensitivity and noise resistance. *Opt. Express* **19**, 13126–33 (2011).

39. de Almeida Camargo, F. V. PhD thesis: Unravelling Vibrational and Electronic Coherences via Two-Dimensional Electronic Spectroscopy of Zinc-Porphyrins.*University of East Anglia* (2017).

40. Hamm, P., Zanni, M., Concepts and Methods of 2D Infrared Spectroscopy. *Cambridge University Press* (2011).

41. Shim, S.-H. & Zanni, M. T. How to turn your pump–probe instrument into a multidimensional spectrometer: 2D IR and Vis spectroscopies via pulse shaping. *Phys. Chem. Chem. Phys.* **11**, 748–761 (2008).

42. Dorrer, C., Belabas, N., Likforman, J. P. & Joffre, M. Spectral resolution and sampling issues in Fourier-transform spectral interferometry. *J. Opt. Soc. Am. B* **17**, 1795-1802 (2000).

43. Myers, J. A. PhD Thesis:Two-Dimensional Electronic Spectroscopy of the Photosystem II D1D2-cyt. B559 Reaction Center Complex. *University of Michigan* (2010).

44. Szipöcs, R., Spielmann, C., Krausz, F. & Ferencz, K. Chirped multilayer coatings for broadband dispersion control in femtosecond lasers. *Opt. Lett.* **19**, 201-203 (1994).

45. Kärtner, F. X., Matuschek, N., Schibli, T. & Haus, H. A. Design and fabrication of double-chirped mirrors. *Opt. Lett.* **22**, 831-833 (1997).

Chapter 6

Investigating Ultrafast Solvation Dynamics of Oxazine 4

6.1 Introduction

Oxazine derivatives are widely used in organic synthesis as intermediates, and they exhibit a great variety of biological activity, meaning they are used as antitumor, antimalarial, antimicrobial and analgesic.[1] Recent studies have also suggested that due to their properties, oxazine derivatives might be employed for the development of new chemicals to combat various diseases.[1,2] Therefore, significant efforts have been directed to understand the chemical and physical properties of these molecules. For example, their solute-solvent interactions have been previously studied in conventional solvents with several techniques[3–6] such as holeburning,[7] and three pulse photon echo.[3,8,9] However, very little is reported about the oxazine derivatives dynamics in unconventional solvents such as ionic liquids (ILs).

Ionic liquids have been recently used as liquid-rocket propellent, high-temperature lubricants and biosensing.[10] In parallel with their developing application, the characterisation of the physical properties of these liquids and how they differ from conventional organic solvents has been the subject of many studies.[10,55–64] The considerable attention received thus far is due to their classification as “green” solvents and their potential to replace the volatile organic solvents.[11,12] A large number of studies have

explored fundamental aspects of solvation in ionic liquids and revealed that the solvation energies of the ILs are comparable to those found in highly polar organic solvents.[9,10,55–64] Moreover, it was established that polar solvation in conventional solvents shows a bimodal character given by a slow diffusive and an ultrafast components (100s fs).[10] The investigation of solvation dynamics in ionic liquids demonstrated that the mechanism is biphasic, as observed for conventional solvents, however, ionic interactions and ion monomer motions dictate a solvation "mechanism" different from conventional solvents.[10,11,13,14] For example, the fast component of Coumarin 153 in conventional solvents such as methanol, and acetonitrile is around 120 fs while in ILs is 278 ps.[10,13,15] To date, many techniques have been applied to characterise solvation dynamics in ionic liquids using both spectroscopic[10,11,14,16] and thermodynamic methods.[17–19] Despite numerous studies the primary process of solvation dynamics and its biphasic nature in ILs are unclear and the interaction between the solute and the first shell of ions constituting the solvent is still difficult to model.[8–10,36]

Here, Oxazine 4 (Ox 4) in conventional solvents and ionic liquids is studied to address the nature of the excited state involved in the molecular dynamics by employing broadband transient absorption spectroscopy (BBTA) and two-dimensional electronic spectroscopy (2DES). Both the dynamics and the vibronic information are contained in steady-state measurements. However, the featureless spectra obtained from molecules in solutions are usually congested and difficult to disentangle.[20,21] The characterisation of the chemical species is accomplished by using broadband pulses with a very high time resolution (fs). These broadband pulses can generate a coherent superposition of vibronic states, also known as vibrational wave packets.[20] The wave packet formed is detected in BBTA measurements in the time domain. Fourier transform into the frequency domain reveals the

Franck-Condon (FC) active modes. Their dephasing is determined pre-FT in the time domain providing an insight into the solute-solvent interaction.[20] The ground and excited-state displacements determine the FC activity that can be detected by the coherent spectroscopy which is a useful technique to observe the ground and excited-states vibrational modes.[22–30] It can be argued that other spectroscopies such as Raman and time-resolved infrared spectroscopy are very useful techniques to investigate the dynamics of molecules in solution considering that they have been proven to be highly sensitive probes for molecular structures.[31] However, information about the excited state vibrational dynamics is either not provided or very challenging to obtain from these techniques. Moreover, the combination of broadband spectroscopy with two-dimensional spectroscopy can lead to the understanding of the solvation process.[20]

In this chapter, BBTA was used to investigate Ox 4 in acetonitrile (ACN), dimethyl sulfoxide (DMSO), methanol (MeOH) and 1-ethyl-3-methylimidazolium thiocyanate $[EMI]^+[SCN]^-$ while the 2DES was carried out for the Ox 4 in MeOH, DMSO, and $[EMI]^+[SCN]$. The time-resolved data will be presented with density functional theory (DFT) calculations to assign the FC active modes.

6.2 Experimental and Computational Sections

6.2.1 Experimental Methods

N-ethyl-7-ethylimino-2,8-dimethylphenoxazin-3-amine also known as LD690 or Oxazine 4 was purchased from Exciton and solutions of ~5 x 10^{-5} M and extinction coefficient at the maximum is ε_{615}= 1.09 x 10^5 M^{-1} cm^{-1}were made in three conventional organic solvents, MeOH, ACN and DMSO, and two ionic liquids: $[EMI]^+[SCN]^-$ and ethylammonium nitrate $[Et]^+[NO_3]^-$. Figure 6.1 shows the molecular structures of the ionic liquids and Oxazine 4.

Table 6.1 summarises the physical properties of the solvents where $[Et]^+[NO_3]^-$ was only used in the static measurements.

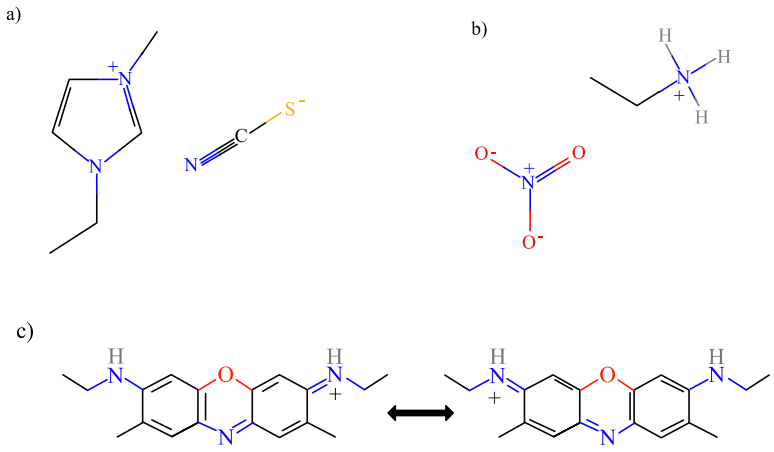

Figure 6.1 Molecular structures of (a) 1-ethyl-3-methylimidazolium thiocyanate $[EMI]^+[SCN]^-$, (b) ethylammonium nitrate $[Et]^+[NO_3]^-$, and (c) Oxazine 4.

Table 6.1 Density (d) in g/mL, refractive index (n) dielectric constant (ε), and viscosity (η) at 20° C of MeOH, ACN, DMSO, $[EMI]^+[SCN]^-$ and $[Et]^+[NO_3]^-$.

	d (g/mL)	n	ε	η (cP)	purchased from (purity)
MeOH	0.791	1.3284	32.7	0.594	Sigma-Aldrich (99.9 %)
ACN	0.782	1.3441	37.5	0.334	Sigma-Aldrich (99.8 %)
DMSO	1.096	1.4783	46.7	1.99	Sigma-Aldrich (99.8 %)
$[EMI]^+[SCN]^-$	1.12	1.537[31]	-	24.7	Iolitec (98%)
$[Et]^+[NO_3]^-$	1.21	1.45[32]	26.3 ± 0.5 [32]	36.5	Iolitec (97 %)

The absorption and emission static spectra of Ox 4 in MeOH, ACN, DMSO, $[EMI]^+[SCN]^-$ and $[Et]^+[NO_3]^-$ were collected with Genesys 10S UV-vis absorption (Thermo Scientific) and Cary Eclipse fluorescence spectrometers, respectively. The excitation wavelength chosen for each fluorescence analysis corresponded to the relative absorption maximum.

A full detailed description of the setup is given in Chapter 5. However, a summary is added here for completeness. A Libra (Coherent, 800 nm, 1 kHz) laser was used to seed a double pass nonlinear optical parametric amplifier to generate a visible broadband spectrum spanning from 540 to 720 nm. After visible light generation, the pulse was compressed with chirped mirrors (BBTA measurements) and with an acousto-optic dispersive filter (Dazzler) in the case of 2DES data. The chirped mirrors and Dazzler compressions were characterised with second harmonic generation frequency-resolved optical gating (SHG-FROG) and transient gating (TG-FROG). Analysis of these measurements returned 15 and 28 fs pulses, respectively (see Figure 6.2).

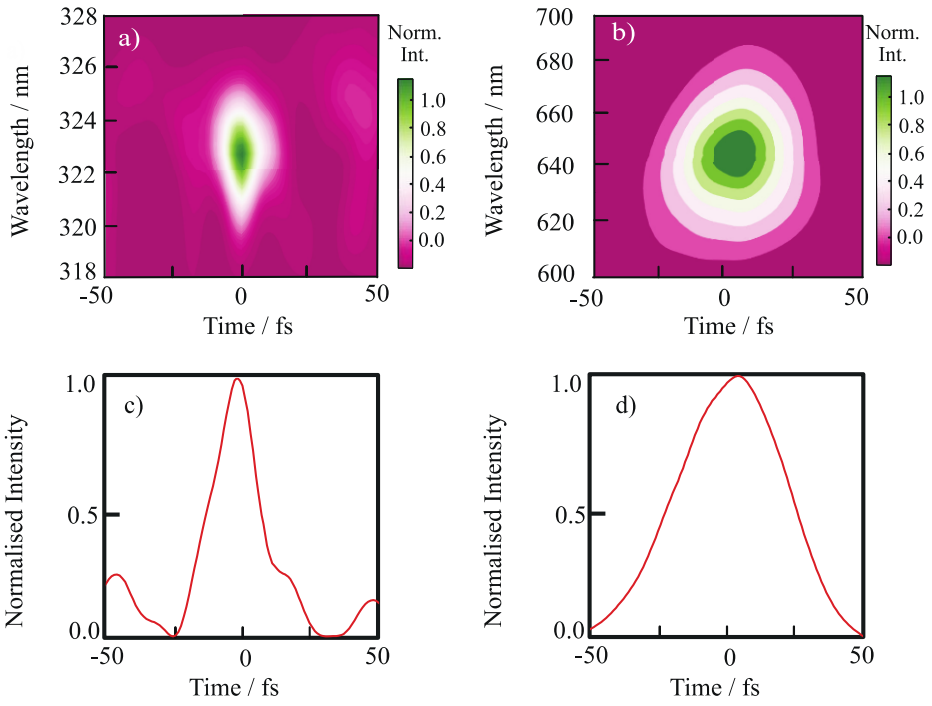

Figure 6.2 Contour map of (a) SHG-FROG, and (b) TG-FROG traces. (c) Time slices of the SHG-FROG at 323 nm, and (d) 650 nm.

Subsequently, the compressed NOPA beam was split into four equal beams by a pair of beam splitters, as explained in Chapter 5. In the BBTA experiment, two identical beams were blocked while the other two were used as pump and probe in the experiment. A mechanical chopper was placed in the pump line to block every other shot and generate the

transient spectra. A mechanical delay stage produced the time delay between the two pulses up to 2 ps. In this configuration, the data were acquired at the magic angle using a pulse energy of both the pump and probe at 6 nJ (per beam), with a spot size of 90 μm. The delay stage was scanned in 4 fs time steps from 0 to 1500 fs, and the signal to noise was improved by applying a noise rejection filter throughout the experiment.

For 2DES data collection, the four identical beams were used. The time delays between the four beams were controlled with three delay stages to acquire the rephasing and non-rephasing signal. Scatter was subtracted using two choppers to acquire the 2DES signals. The pulse energy of each beam used to generate the nonlinear signal was 2 nJ and the coherence time was scanned in 1 fs steps from -150 to +150 fs. To generate the 2D maps acquired in t_1, ω_3 the spectrum was inversed Fourier transformed to t_1, t_3, and a window function was applied along t_3 to remove the homogeneous signal at zero. Finally, the spectrum was Fourier transformed along t_1 to obtain the final (ω_1-ω_3) 2D spectrum. The spectrum was phased accordingly to the projection slice theorem, and only the total (real) spectra are shown in this chapter.[20,33,34]

6.2.2 Computational Methods

Density functional theory (DFT) and time dependent DFT (TDDFT) calculations were

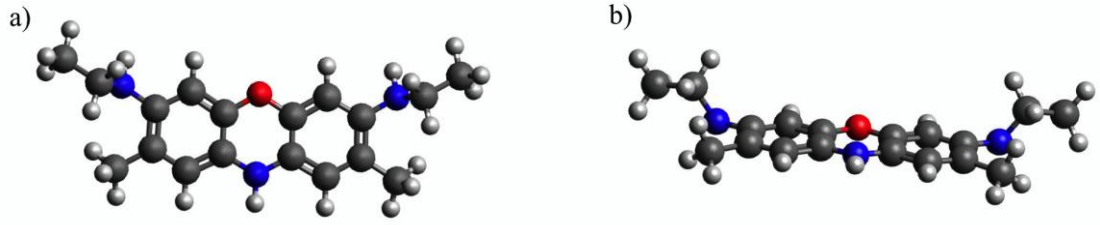

Figure 6.3 (a) Top down and (b) side on view of the optimised geometry for the ground state of Oxazine 4 (DFT, B3LYP/6-31+G).

performed using Gaussian09 to minimise the S_0 and S_1 geometries and recalculate the associated harmonic frequencies of Oxazine 4. The gas-phase calculations were performed using the B3LYP functional and the 6-31+G basis set. Figure 6.3 shows the optimised geometries for the ground state.

6.3 Results and Discussion

6.3.1 Steady-State Analysis

The absorption and fluorescence spectra of Ox 4 collected in methanol, acetonitrile, dimethyl sulfoxide and the two ionic liquids are shown in Figure 6.4.

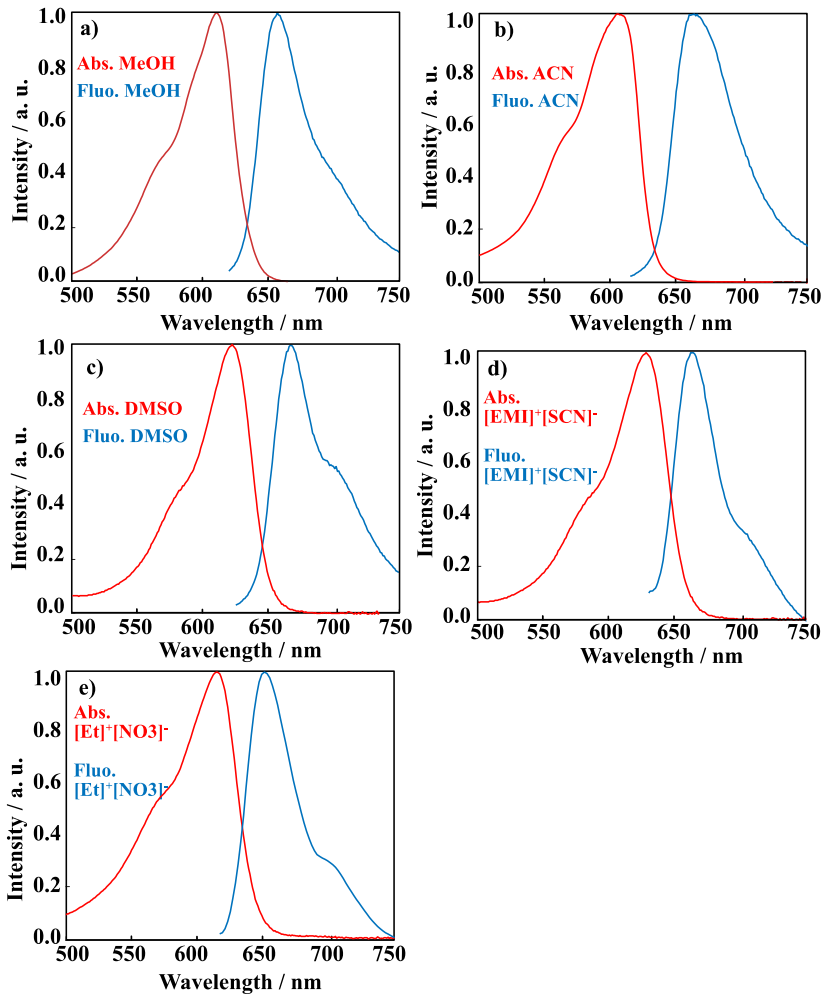

Figure 6.4 Normalised absorption (red) and emission (blue) spectra of Oxazine 4 in (a) MeOH, (b) ACN, (c) DMSO, (d) 1-ethyl-3-methylimidazolium thiocyanate, and (e) ethylammonium nitrate.

The maximum wavelengths of each spectrum studied are summarised in Table 6.2. Both the absorption and fluorescence spectra display a side band.[35] None of the solvents I studied shows a double peak in the fluorescence spectrum, as previously reported for Oxazine 4 in hydrogen-bonding solvents such as n-alcohols. Further, the shape of the emission spectra is always close to the mirror image of the absorption.[35] The comparison between the absorption and fluorescence spectra in Figure 6.4 shows that there is nothing distinctive about the spectra of the Ox 4 in conventional solvents or ILs, consistent with the behaviour already found for Coumarin 153 (C153) in ILs.[10,11] More precisely, the shifts of the spectra in the ionic liquids is indistinguishable from the other three polar solvents.

Table 6.2 Maximum of the absorption and emission spectra for the Oxazine 4 in four different solvent and the calculated Stokes-shift.

	Methanol	Acetonitrile	DMSO	$[EMI]^+[SCN]^-$	$[Et]^+[NO_3]^-$
Absorption λ_{max} /nm	611	606	623	628	616
Fluo. λ_{max} /nm	657	664	667	664	653
Stokes-shift /nm	46	59	44	36	37
cm^{-1}	1146	1468	1058	862	920

Table 6.2 also shows the Stokes shift that characterises the solvatochromic molecule. To relate the Stokes shift with an intrinsic property of the solvent, it is possible to describe the environmental sensitivity of the dye with the Lippert and Mataga theoretical model, already used for Ox 4 in conventional solvents (n-alcohols), as reported in ref.[35] The following formula is the simplest way to relate the Stokes-shift ($\delta\nu$) of a dipolar molecule to a solvent dielectric property (ε) and refractive index (n):[10]

$$\delta\nu = \frac{2(\mu_e-\mu_g)^2}{chR^2}\left[\frac{\varepsilon-1}{2\varepsilon+1} - \frac{n^2-1}{2n^2+1}\right] \quad (6.1)$$

The dipole moments of the ground (g) and excited (e) states are given by $\mu_{e,g}$, and the radius of the sphere containing the solute molecule also known as Onsager radius is R. Planck's constant is h, and c is the speed of light.

According to equation 6.1, by plotting the Stokes shift as a function of the solvent properties, such as ε and n, one can obtain the size of the solvent charge distribution upon light absorption. It has been reported, that equation 6.1 well describes the relationship between the Stokes shift found for Ox 4 in a set of n-alcohols and the solvent properties. On the contrary, the simple dielectric description of the Lippert-Mataga equation does not accurately describe the behaviour of Ox 4 for all conventional solvents. However, very little is known about its relationship with ILs.[35]

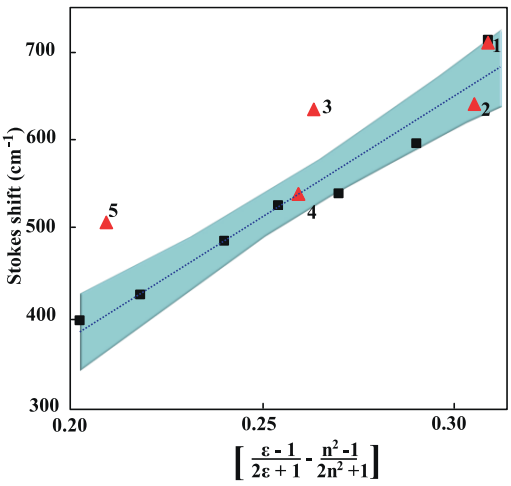

Figure 6.5 Plot of the Stokes shift of Ox 4 in n-alcohols (n = 1-6, 8, 10, from right to left from ref.[35]) given in black and measured as the distance between the absorption and fluorescence spectra, versus the strength of the solvent dielectric constant and the Ox 4 in the five solvents studied (1 = methanol, 2 = acetonitrile, 3 = DMSO, 4 = $[EMI]^+[SCN]^-$ and 5 = $[Et]^+[NO_3]^-$). The 95 % confidence interval of the data in ref.[35] is highlighted in blue.

Figure 6.5 is a comparison between the already published plot of the Stokes shift of Ox 4 in n-alcohols,[35] and the values obtained in the five solvents studied in this work. Note that the published value obtained for Ox 4 in methanol coincide with the value calculated here, as shown in Figure 6.5 in red and black. Moreover, the slope of the curve shown in the graph is 2700 ± 200 which coincides with the one reported by Bardeen *et al*. [35] When analysing this system, it is also worth noting that the dielectric constant of $[EMI]^+[SCN]^-$ is not known; however, a database that elucidates a trend given by the ILs anion and cation variation is available.[32] According to the published values for the dielectric constants, in the 1-alkyl-3-methylimidazolium bis(trifluoromethylsulfonyl)imide a minimal variation of ε (14 ± 1) from ethyl to pentyl is observed, suggesting that a small change in the alkyl group does not affect this solvent property. Therefore, in Figure 6.5, the ε value for $[EMI]^+[SCN]^-$ was chosen to be 13.7 ± 0.8, which is the published value for 1-butyl-3-methylimidazolium thiocyanate.[24] The data obtained in methanol, acetonitrile and $[EMI]^+[SCN]^-$ show a linear dependence on the Stokes shift, while DMSO and $[Et]^+[NO_3]^-$ data do not fit this trend.

The data shown in Figure 6.5 are in good agreement with the findings for Ox 4 in n-alcohols and conventional solvents where it has been shown that the dielectric continuum picture works well for some classes of solvents as alcohols.[35] Certainly, the simple picture of dielectric solvation given in equation 6.1 is insufficient to explain the steady-state spectroscopy of Ox 4 in an ionic liquid as shown from the deviation of point 5 from the trend in Figure 6.5.

For the dye Coumarin 153 (C153), it has also been demonstrated that the solvent permittivity of conventional solvents is related to the experimentally measured Stokes shift, while for ionic liquids the dipole solvation can be related to ion density or mean ion

separation.[10] In this work, a trend of the data acquired in the ionic liquid is quite difficult to establish because only two relatively viscous ILs were investigated. Certainly, the simple theory of dielectric continuum is not sufficient to explain the behaviour of Ox 4 in all solvents. Therefore, the same trend found for C153 in ionic liquids is unlikely for the molecule studied in this work. Note that the simple theoretical model for solvation, as treating the solvent as an uncharged sphere or dielectric continuum is not exhaustive to explain the behaviour of Oxazine 4 in solution which might be determined by discrete molecular interactions between the solute and the solvent molecules and not just the bulk solvent properties as per equation 6.1.[35]

6.3.2 Broadband Transient Absorption Spectroscopy

BBTA spectra (in ΔT/T) for the Ox 4 in methanol, acetonitrile, dimethyl sulfoxide and 1-ethyl-3-methylimidazolium thiocyanate are given in Figure 6.6 with the respective linear absorption, and emission spectra shown on the top of each panel. The positive transient signals span a broad region between 580 and 720 nm consistent with the previously reported TA data of Ox 4 in methanol.[36] At early time delays the positive feature is stronger where the absorption and emission spectra overlap suggesting a contribution from both the ground and the excited state; therefore the ground state bleach (GSB) and stimulated emission (SE) signals overlap in this region. Moreover, the positive signals spanning from 580 to ~670 nm are dominant in every solvent studied. The GSB/SE feature decreases in intensity on the red side of the transient spectra probably due to an overlap between positive (GSB/SE) and negative (excited state absorption, ESA) contributions.

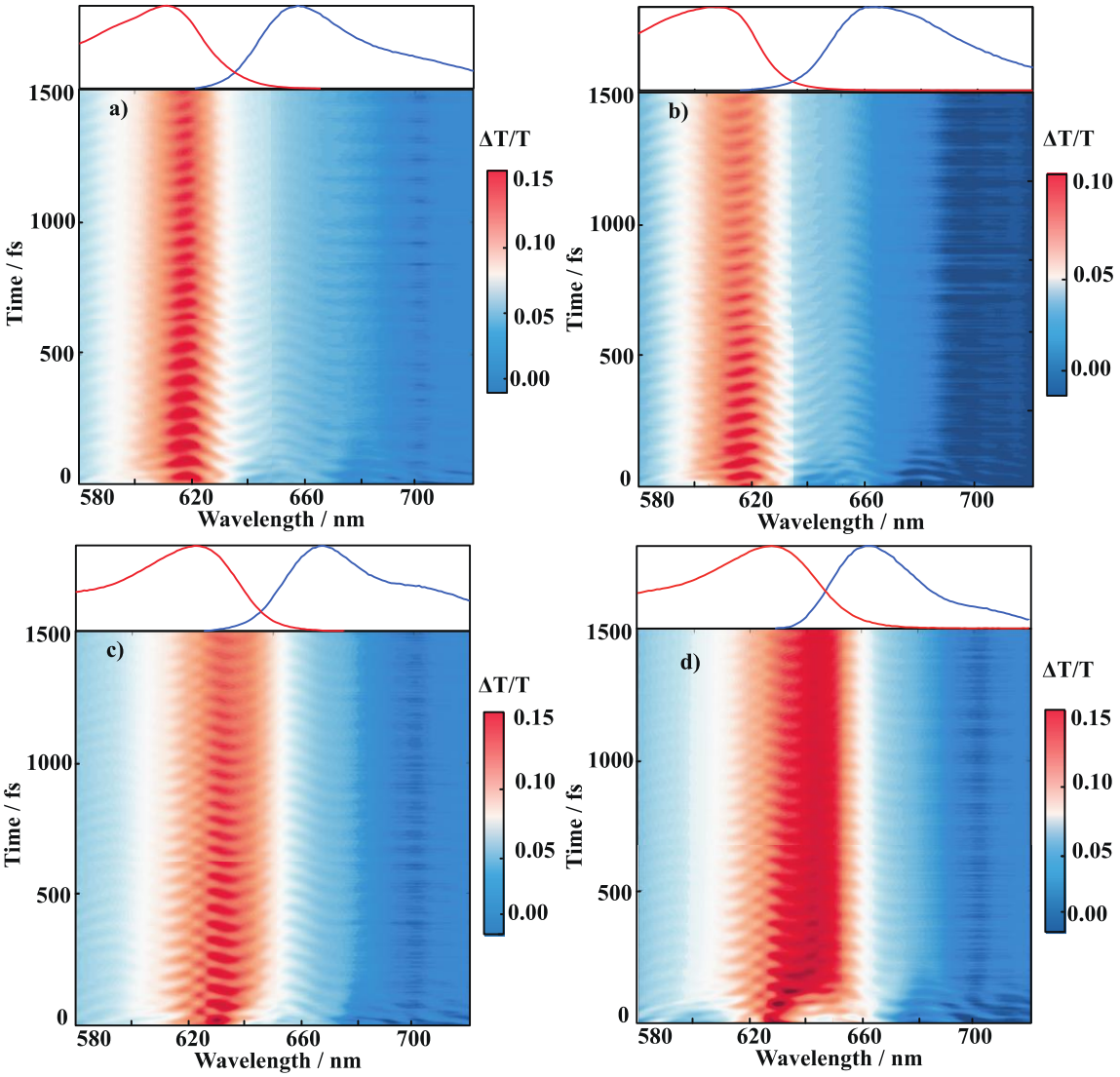

Figure 6.6 BBTA spectra and linear absorption (red) and fluorescence (blue) spectra for Ox 4 in (a) methanol, (b) acetonitrile, (c) dimethyl sulfoxide, and (d) 1-ethyl-3-methylimidazolium thiocyanate.

The BBTA signals are modulated by coherent oscillations, as previously reported for Ox 4 in methanol,[36] and persist in all spectra, up to 1.5 ps. In addition to the vibrational coherences observed, a small dynamic Stokes shift is also expected in the four solutions. This phenomenon depends on solvent re-organization and stabilization of S_1,[21,37,38] and its observation can be used to study the solute-solvent interaction (how the solute interacts with the surrounding bath) and the system reactivity.[37,39,40] Unfortunately, in the studied

cases, the dynamic Stokes shift found in the 1.5 ps window is too small to carry out these analyses.

All the BBTA spectra obtained were fitted with a biexponential function at each probe wavelength and the population dynamics removed to achieve the purely vibrational coherent BBTA spectra.[20,28,41]

Figure 6.7 (a) shows the BBTA spectrum of the Ox 4 in $[EMI]^+[SCN]^-$. Figure 6.7 (b) shows the kinetics at 620 nm of the BBTA spectrum in blue and the same feature after subtracting the population dynamics contribution, in orange. Figure 6.7 (c) is the contour map of the purely vibrational coherent spectrum obtained after removing the population dynamics at each probe wavelegth.

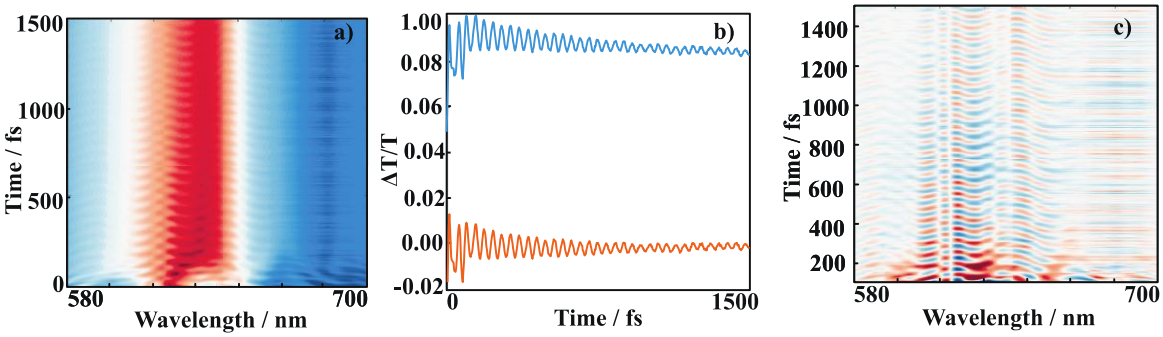

Figure 6.7 (a) BBTA spectrum of Ox 4 in $[EMI]^+[SCN]^-$. Blue trace in panel (b) represents the kinetics at 620 nm while the orange is the same trace after subtracting the population dynamics. Applying the subtraction to each probe wavelength yields the (c) purely vibrational coherent BBTA spectrum.

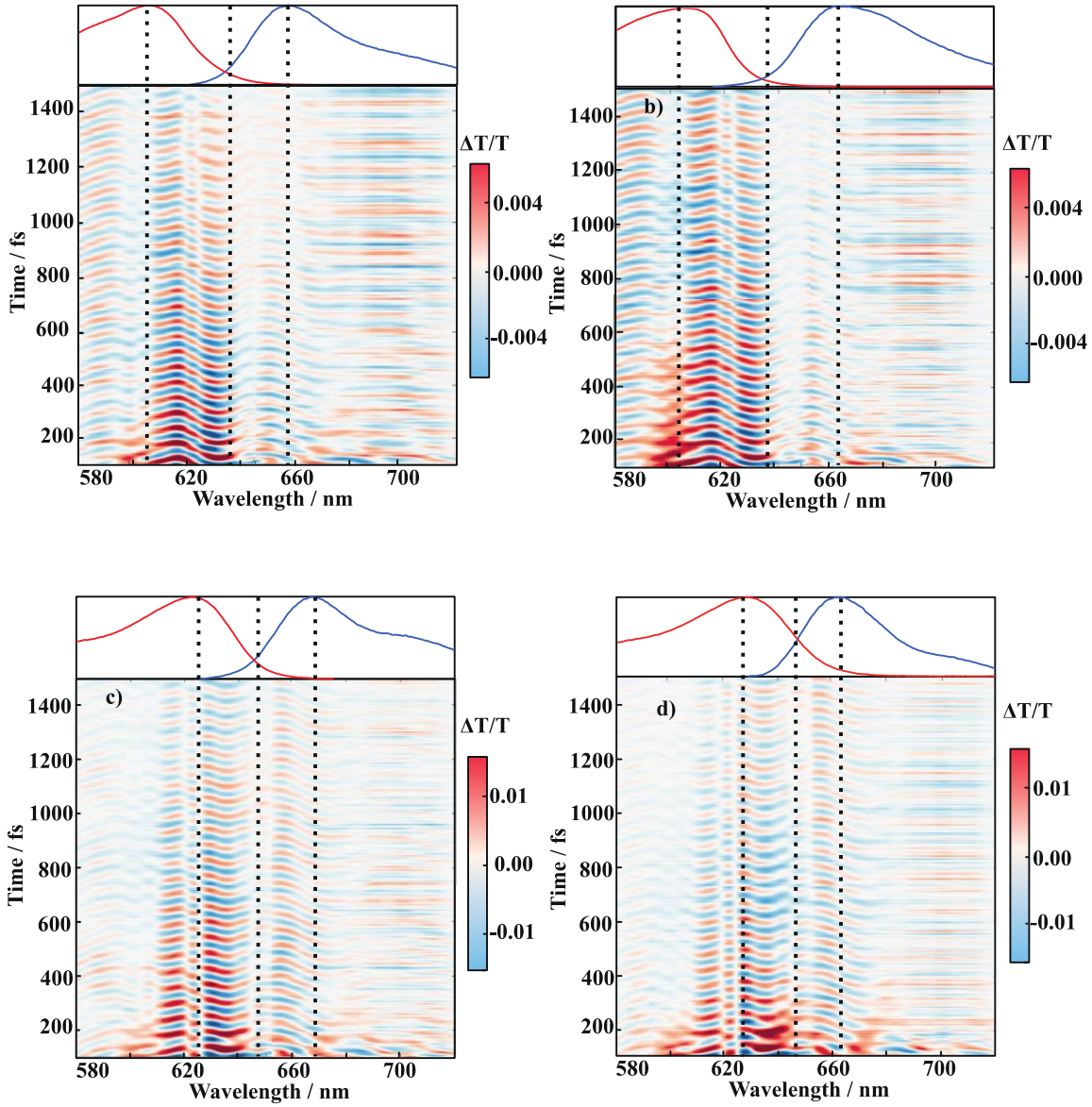

Figure 6.8 Purely vibrational coherent BBTA spectra of Ox 4 in (a) methanol, (b) acetonitrile, (c) DMSO, and (d) $[EMI]^{+}[SCN]^{-}$. In each spectrum, the dashed lines correspond to the maximum of the absorption spectra, overlap between absorption and fluorescence spectra and maximum of the fluorescence spectra.

Figure 6.8 shows the four purely vibrational coherent BBTA spectra where the most intense oscillations are found at ~ 620 nm in all the solvent studied. The purely coherent vibrational maps can show a zero-amplitude oscillation, known as a node, that can reveal information on the excited wave packet dynamics.[20,28,41–45] More precisely, an ultrafast pulse can launch

a vibrational wave packet on the displaced excited state potential energy surface (PES). Therefore, the nuclear wave packet is launched on one side of the PES, and its motion (that depends on the nuclear coordinate) is detected as a function of the probe frequency. During this motion, a phase shift of the wave packet is found at the minimum of the PES which manifests in the BBTA spectra as a node corresponding to the maximum of the fluorescence spectrum.[42]

A node is often found at the maximum of the fluorescence spectrum when the GSB and SE are well separated in the transient spectra.[42] Under such conditions, a second node corresponding to the maximum of the absorption spectrum might also be observed. In general, a node found at the maximum of the absorption spectrum gives information about ground state vibrational wave packets.[28,42] The maps shown in Figure 6.8 are very congested with multiple possible nodes found between 580 and 680 nm.

A first node that can be noticed is placed at the maximum of the absorption spectra, more evident for DMSO and $[EMI]^+$ $[SCN]^-$ and less pronounced in the case of methanol and acetonitrile. This node indicates the generation of vibrational wave packets in the ground state. A second node that is common to all the data presented is found between 638 and 650 nm (see dashed lines), these nodes separate signals with opposite phases which are depicted as blue and red in the coherent maps. Less evident is the node that should correspond to the maximum of the fluorescence spectra mainly because vibrational coherences at wavelengths > 660 nm are not very pronounced; therefore, establishing whether vibrational wave packets in the excited state are observed or not is unclear.[42]

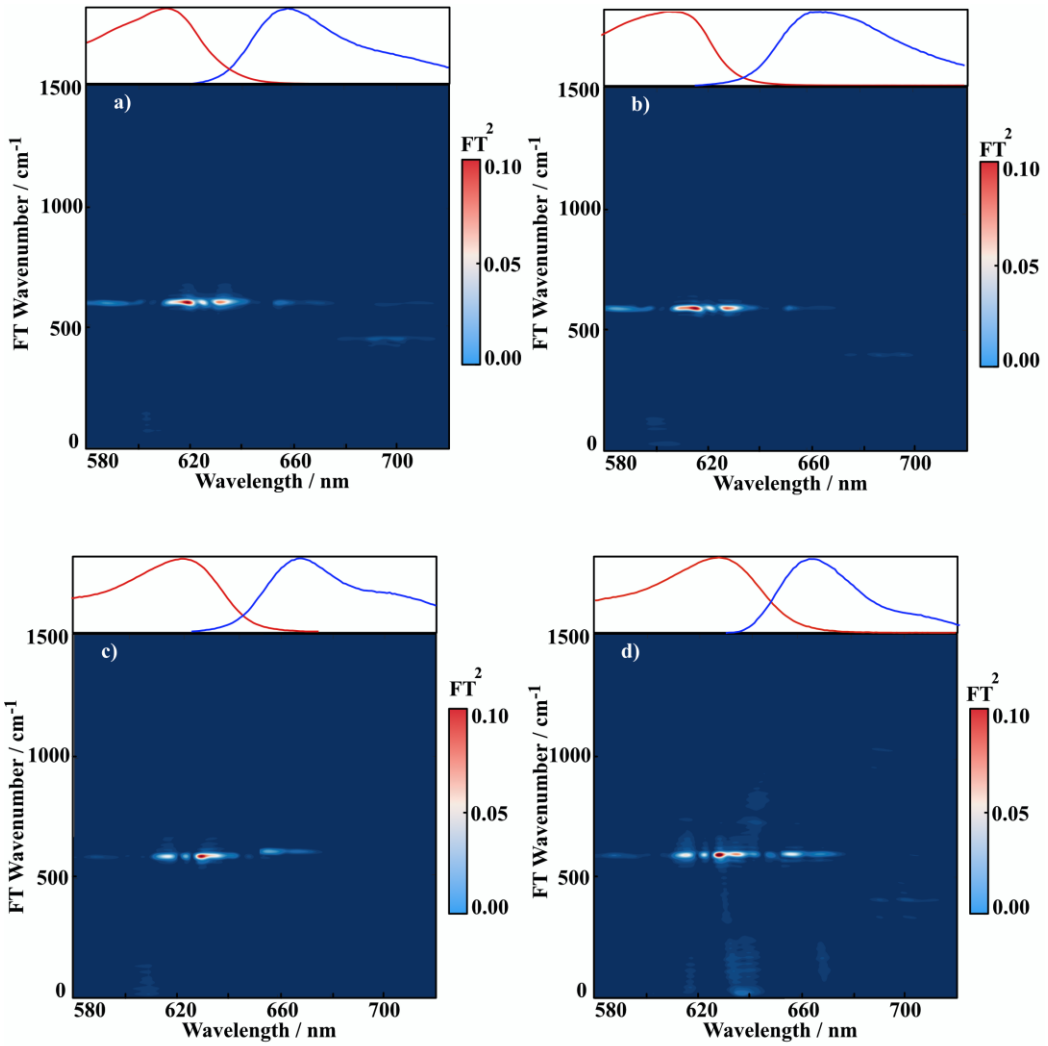

Figure 6.9 Fourier transform spectra of Oxazine 4 in (a) methanol, (b) acetonitrile, (c) DMSO, and (d) $[EMI]^+[SCN]^-$. The absorption (red) and fluorescence (blue) spectra of Ox 4 in the four solvents are given on the top of each panel.

Figure 6.9 shows the FT maps of the four coherent spectra depicted in Figure 6.8. All spectra display one peak centred at 586 cm^{-1} given by a predominant oscillation with a period of 57 fs. This observation is in good agreement with what has already been found for Oxazine 4 in methanol.[3] The FT maps also show a weaker FT amplitude found in all the spectra with the exception of DMSO at ~ 400 cm^{-1} which is red shifted in probe wavelength compared to the main one at 586 cm^{-1}. This second feature is seen only at long probe wavelengths when the contribution of the ground state vibrational coherence is not

as pronounced as at shorter wavelengths. Therefore, it is probably indicating a contribution from vibrational wave packets originated in the excite state.[42]

6.3.3 Damping Factors

To separate the ground and excited state vibrational wave packets that might be found in the vibrational coherent spectra is not always trivial, in particular when BBTA spectra show overlapping spectral features.[19,27,43,44,46] However, to address the nature of the observed oscillations the position of the node inferred in the coherent spectra and damping times can be used.[45–47] Therefore, in addition to the nodes in Figure 6.10, a nonlinear fitting was used to obtain the damping times of the oscillations in the purely coherent vibrational spectra. The kinetic traces were fitted with exponentially decaying cosine that reads:

$$I(t) = A \cos[\omega t - \phi]\, e^{-\gamma t} \qquad (6.2)$$

where A is a preexponential factor, ω is the angular frequency, t is the time delay, ϕ the phase and γ is the so-called damping factor that corresponds to $1/\tau$, with τ = damping time.

Figure 6.10 (a_n) shows the oscillations (blue) at 615 nm probe wavelength for each solution studied, and the dashed red line represents the best fitting obtained with equation 6.2. The best fitting was achieved by fixing ω (according to the FT of each spectrum), while ϕ was floated. The quality of the fit was then obtained by the analysis of the residual of the fit which is shown in green (see panels b_n). Moreover, a comparison between the FT spectrum at 615 nm probe wavelength and the FT of the fittings was carried out. The correlation between the experimental FT amplitude found and the calculated FT peak shows a good agreement between the two curves where the predominant amplitude at 586 cm^{-1} is almost perfectly reproduced in each data set (panels c_n).

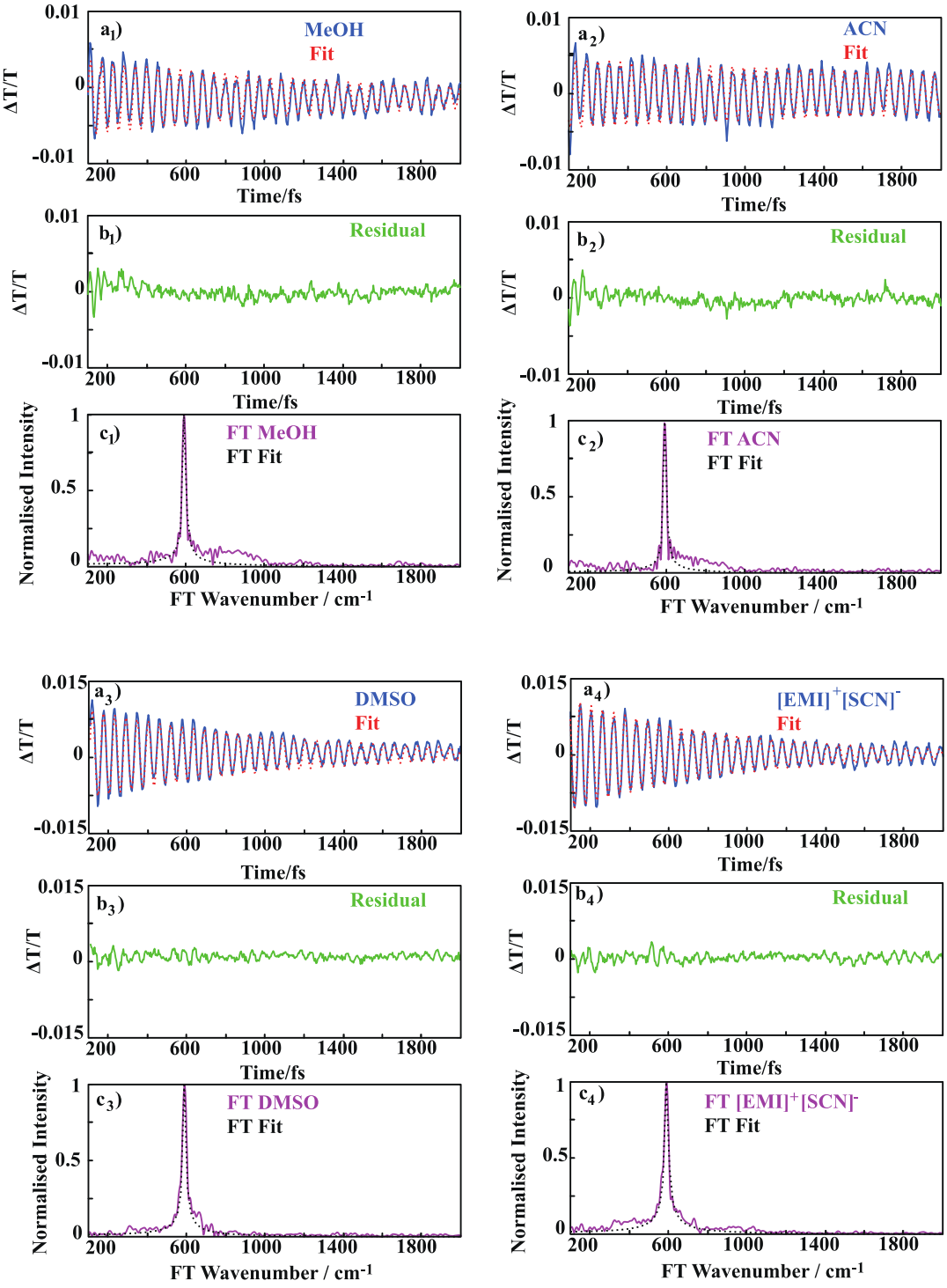

Figure 6.10 Ox 4 in methanol, acetonitrile, DMSO and $[EMI]^+$ $[SCN]^-$ coherent vibrational oscillations (in blue) at 615 nm shown in panels a_n and the best fitting shown as a dashed red line. The residual is given in panels b_n. The pink lines in panels c_n correspond to the experimental FT spectrum at 615 nm wavelength, while the black lines are the FT of the red dashed lines.

From the best fitting, four damping factors were extrapolated with the relative errors calculated as the standard deviation in ± 5 nm range from the central wavelength. For Ox 4 in methanol and acetonitrile, the damping times calculated are 1.5 and 3.4 ps which are longer than the damping times found for the dye in DMSO and the ionic liquid (~1 ps in both solvents).

The possibility to establish a trend that can relate a solvent property such as dielectric constant, polarity or viscosity with the different damping times turned out to be quite challenging. This lack of trend suggests, again, that the physical properties that are classically used to predict the interaction between the solvent and the solute are not sufficient to establish a strong correlation between protic, aprotic conventional solvents and ionic liquids.[10,13,35]

Moreover, to validate this hypothesis, the damping time of Ox 4 in a second ionic liquid, $[Et]^+[NO_3]^-$, was also calculated and reported in Table 6.3 (data given in the appendix, Ap. 6.1). The damping time extrapolated at 615 nm probe wavelength for the second IL studied is identical to $[EMI]^+$ $[SCN]^-$ and DMSO validating the hypothesis that the description of the ILs solvation dynamics with classical equations does not lead to a definitive understanding of the system.[10,11]

Table 6.3 Damping factors calculated at 615 nm probe wavelength for Ox 4 in conventional solvents and ionic liquids.

	Methanol	Acetonitrile	DMSO	$[EMI]^+[SCN]^-$	$[Et]^+[NO_3]^-$
Damping Time/ps	1.5 ± 0.1	3.4 ± 0.4	1.0 ± 0.3	0.8 ± 0.1	1.1 ± 0.1

It is well known that from the analysis of the oscillatory component of the BBTA spectra, it is possible to obtained information about the electronic state where the vibrational wave packets are originated. Bardeen *et al*. have already reported information about vibrational wave packet for Ox 4 in methanol suggesting that the use of ultrashort pulses with defined chirp may be used to selectively excite wave packets motion on the excited state.[36] Moreover, it has been found that the dye is characterised by level-dependent vibronic dephasing times which varies from > 10 to 1 ps in the case of the S_0 state and from 1 to 3 ps for the S_1 state.[36] At 610 nm the dephasing vibrational time found for Oxazine 4 in methanol is 1.3 ps[36] which is a typical dephasing time for the S_1 state. Therefore, the calculated dephasing times in the five solvents studied are not only in agreement with the published times for the dye in methanol, but they suggest that excited state oscillations are detected.

6.3.4 Fourier Transform Spectra Analysis

To further investigate the observation of possible excited state vibrational modes, the FT spectra obtained from the purely coherent maps were analysed, highlighting the FT peaks obtained when integrating over different probe wavelengths. Figure 6.11 shows the FT amplitudes obtained when the oscillatory signal is integrated over 580-620 nm (in red), 620-660 nm (in blue) and 660-720 nm (in green) probe wavelength. The first region corresponds to only the GSB signal found in the BBTA spectrum. The second interval is the GSB/SE, where the absorption and emission spectra overlap while the third region represents the ESA/GSB/SE signal where the spectral contributions partially come from the $S_1 \rightarrow S_n$ transitions. Each panel of Figure 6.11 also shows the FT peaks corresponding to the different solvent contributions (*) obtained from the comparison between the only solvent FT amplitude maps and the Raman spectra.[48–50] The FT amplitudes obtained when

integrating the oscillatory signal from 580 to 660 nm always show a predominant peak at 586 cm^{-1} which has been previously assigned to ground state ring breathing mode.[36,46] Weaker FT amplitudes can also be found in Figure 6.11 (a) such as FT amplitudes at 572 cm^{-1}, 733 cm^{-1} and 812 cm^{-1} that are attributed to Ox 4 ground state normal modes through Raman spectroscopy.[36]

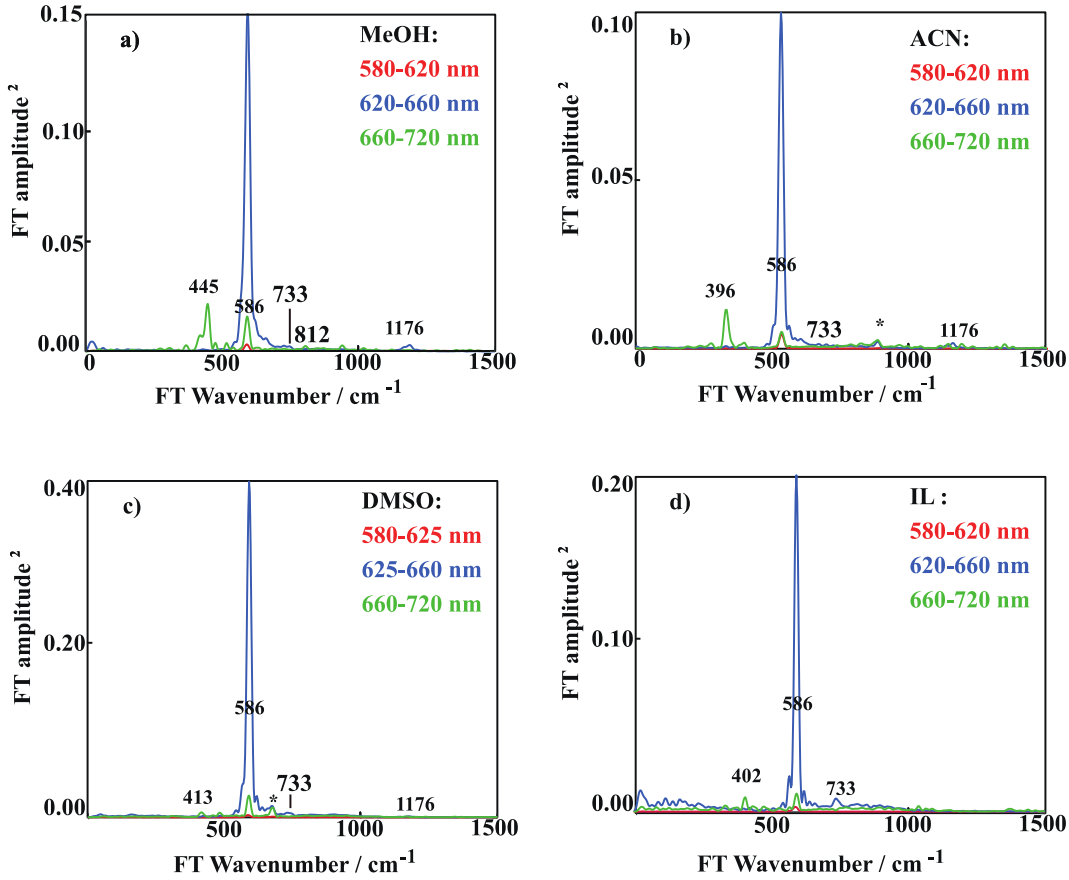

Figure 6.11 Relative FT^2 amplitude vs FT wavenumber for Ox 4 in (a) methanol, (b) acetonitrile, (c) DMSO, and (d) $[EMI]^+[SCN]^-$. The red traces correspond to the integrated FT spectra from 580 to 625 nm (only GSB region), the blue traces correspond to the 620-660 nm spectral region (GSB/SE) while the green traces are the 660 and 720 nm regions (ESA/GSB/SE).

A consistent peak ~ 400 cm^{-1} is inferred when integrating the red side of the spectra, and it appears to be particularly pronounced in methanol and acetonitrile. As already mentioned, isolating the contribution of the ground and excited state wave packet motions is not always

straightforward and it is very challenging in this case.[42] However, the presence of nodes in multiple regions of the purely coherent spectra, the extrapolation of damping times that indicate the observation of ground and excited state wave packets [28,41–43,45] and the FT amplitudes that are probe frequency-dependent suggest that the ~ 400 cm^{-1} might be assigned to an excited state FC active mode.[42,43]

6.3.5 Franck-Condon Analysis of Vibrational Coherences and Geometry Change

The vibrational coherences experimentally observed for Ox 4 in four different solvents were assigned through DFT and TDDFT calculations. In BBTA spectra only the Franck-Condon active modes can be observed.[20]

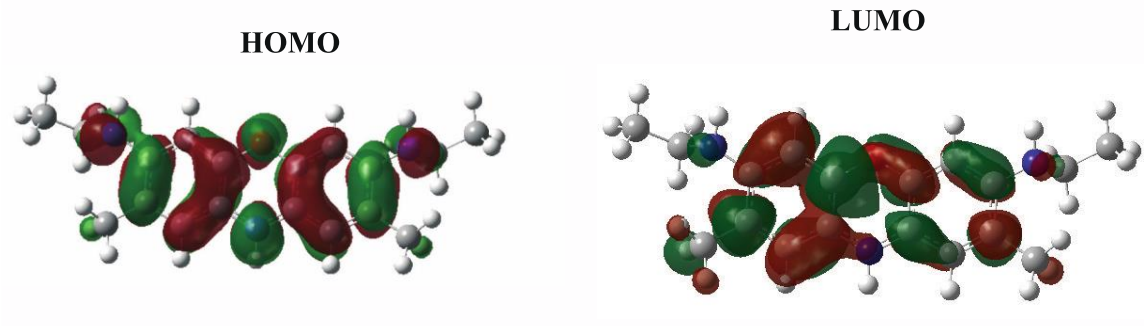

Figure 6.12 HOMO and LUMO orbitals for Oxazine 4 calculated with B3LYP/6-31 G+.

The principal normal modes were then assigned through comparison between DFT calculations and the literature.[36] DFT calculations confirm that the predominant mode at 586 cm^{-1} is a ring breathing mode of the Ox 4, and the mode at 1176 cm^{-1} is the second harmonic of the previous one. Furthermore, the FT peak at ~ 400 cm^{-1} can be assigned to a bending mode of the -CH belonging to the three rings. The other peaks found in the various solvents mainly correspond to ground states ring breathing mode of the Ox 4.

DFT calculations were also used to better understand the geometry change of the Ox 4 from S_0 to S_1. Theoretical investigation predicts that the main transition between the ground and the first excited state is the HOMO → LUMO (corresponding to a ππ* transition) which is characterised by an energy gap of 3.15 eV. This transition is calculated to be six times more probable than the HOMO → LUMO + 1 transition, which is the second most probable transition. Figure 6.12 shows the HOMO and LUMO molecular orbitals. Moreover, the comparison of the optimised S_0 and S_1 geometries shows that the main changes are related to the position of the oxygen in the central ring and the two ethyl groups. The comparison between the HOMO and LUMO shows that the MO change is mainly localised on the three rings validating the hypothesis that the vibrational coherences belong to both the ground and excited state.[20,51,52]

6.3.6 Two-Dimensional Electronic Spectroscopy

To characterise Ox 4 solvation dynamics, 2DES analysis has been carried out. It has been demonstrated that two-dimensional spectroscopy is a powerful technique to monitor the system-bath interaction through the frequency-frequency correlation function (FFCF).[33,53–60] Moreover, it is known that some parameters related to the lineshape of the 2D spectra such as the slope of the centre line (CLS), can be associated to the frequency-frequency correlation function for the electronic degrees of freedom.[60–62]

2DES data probed at a central wavelength of 640 nm at different t_2 are shown in Figure 6.13 for Ox 4 in methanol (see panels (a) and (b)), DMSO ((c), (d)), and $[EMI]^+[SCN]^-$ (see panels (e) and (f)). 2DES data showing the evolution of the line shape at increasing t_2 are also reported in the appendix, Ap. 6.2 and Ap. 6.3.

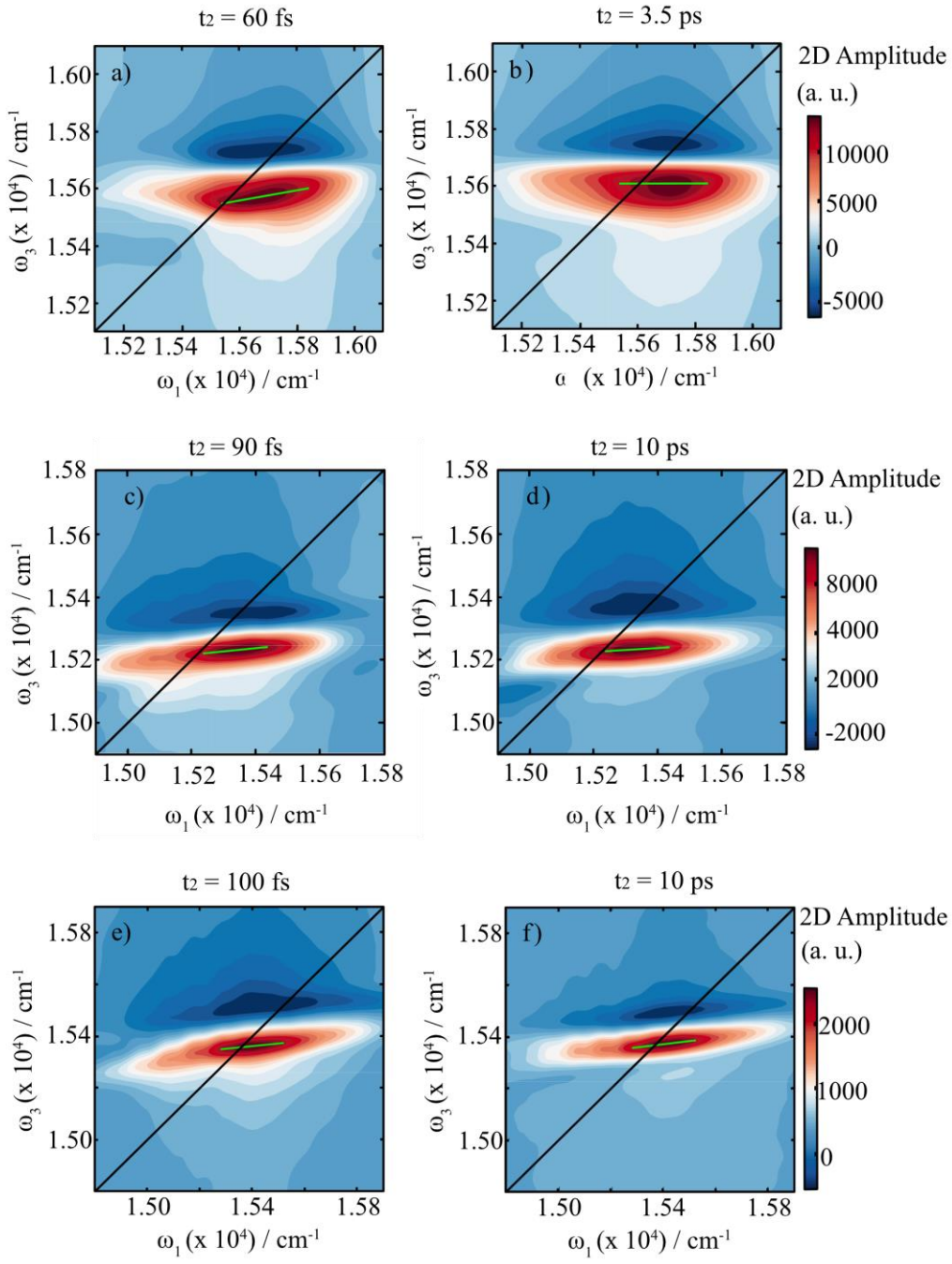

Figure 6.13 2DES data of Oxazine 4 in methanol at (a) t_2 = 60 fs and (b) t_2 = 3.5 ps, DMSO (c) t_2 = 60 fs and (d) 10 ps. Ox 4 in $[EMI]^+[SCN]^-$ at (e) t_2 = 100 fs and (f) t_2 = 10 ps. The absorption and emission spectra, on the top of each 2DES frequency-frequency map, are given in red and blue, respectively.

Of note, when studying the solute-solvent interaction is the slope of the centre lines that at early waiting time should show a positive slope due to the correlation between the

fluctuation of the electronic transitions. After a few ps, however, the slope is expected to decay to zero due to spectral diffusion. Figure 6.13 (a) shows an example data of Oxazine 4 in methanol, where an elliptical shape characterises the main positive peak at t_2 = 60 fs, with a positive centre line. This correlation is lost very rapidly in methanol, as indicated by the decay of the central line slope (CLS) in Figure 6.13 (b).

Figure 6.13 (c), and (d) show 2DES frequency-frequency correlation maps for Oxazine 4 in DMSO, where the correlation is not lost as fast as in methanol for the positive red feature. Moreover, figure 6.13 (e) and (f) show the data for Ox 4 in $[EMI]^+[SCN]^-$. When the dye is placed in such a viscous solvent, the central line slope of the positive feature associated with the excited state has a different behaviour compared to the methanol solution resulting to be more similar to the DMSO frequency-frequency correlation.

The CLS of Oxazine 4 in methanol, DMSO, and ionic liquid were found at subsequent waiting times to evaluate the loss of the correlation in the positive feature, while a change in the CLS was not investigated for the negative feature. Figure 6.14 (a) shows the recovery of the CLS for the dye in methanol, (b) in DMSO, and (c) is the ionic liquid.

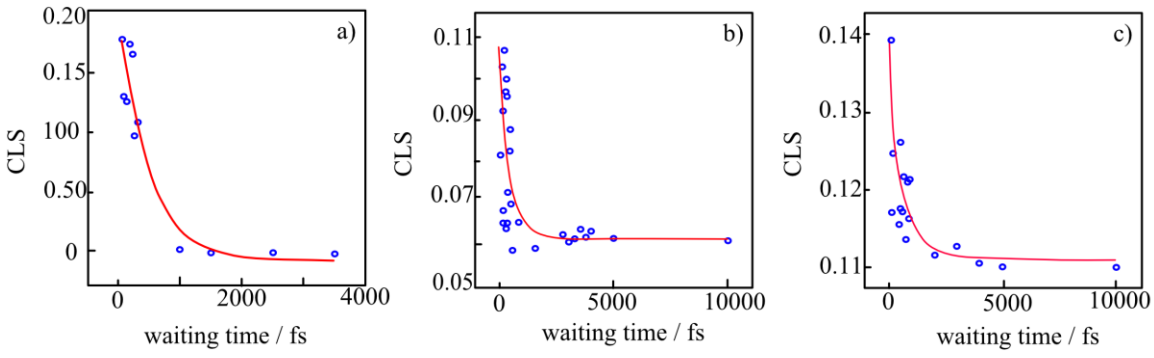

Figure 6.14 CLS vs t_2 for Oxazine 4 in (a) methanol, (b) DMSO, and (c) $[EMI]^+[SCN]^-$. The red line indicates the exponential fit.

For methanol the CLS decays to zero within 2 ps, and it can be fitted to a single exponential with a lifetime 400 ± 300 fs. On the contrary, Ox 4 in DMSO and ionic liquid do not decay to zero and have a long-time offset in the probed time delays. This behaviour indicates a longer lifetime when the Ox 4 is placed in the more viscous solvents, therefore, a slower spectral diffusion is observed indicating a weaker solute-solvent interaction. To convey a quantitative idea of the correlation between Ox 4 in DMSO and $[EMI]^+[SCN]^-$ I have also fit the CLS vs t_2 data in panels (b) and (c) with a monoexponential function which returns 500 ± 200 fs for DMSO and 700 ± 400 fs in the case of the IL. The lifetimes found for the Ox 4 in DMSO and IL give a good sense of the slower response of the solvents to the photoexcitation of the dye.

6.4 Conclusions

BBTA spectra characterised by congested signals and wave packet dynamics have been studied for Oxazine 4 in conventional solvents and ionic liquids. After population dynamics subtraction, the congested BBTA spectra are reduced to a few FC active modes that can be assigned through DFT calculations. The work explores the vibrational wave packet formed in the ground state and possibly excited state of the Oxazine 4. The purely vibrational coherent maps show intricate dynamics with multiple nodes, and from the fitting of the coherent oscillations and the FT of the coherent spectra, a possible formation of wave packets not only on the ground state but also in the excited state is found. It has been previously reported that a shift from 586 to 568 cm^{-1} is found under conditions that favour the excited state vibrational wave packet formation.[46] Thus, the shoulder observed at 570 wavenumbers, might be an additional symbol of excited state dynamics. Therefore, the FC mode around 400 cm^{-1} was assigned to an excited state FC active mode. 2DES was then implemented to investigate the excited-states solvation dynamics through the FFCF. From

the analysis, a clear trend showing a faster recovery of the CLS in methanol than in $[EMI]^+[SCN]^-$ is observed. From the BBTA and 2DES analysis reported in this chapter, the need of theoretical models that can predict and fully reproduce the 2D data as well as theoretical models that can provide information about the solvation dynamics are needed for a full understanding of the frequency-frequency correlation maps. Finally, the investigation of this rigid molecule in other ionic liquids could benefit a further understanding of the solvation dynamics of Oxazine 4.

6.5 Appendix

Ap. 6.1 Damping Factors of $[Et]^+[NO_3]^-$

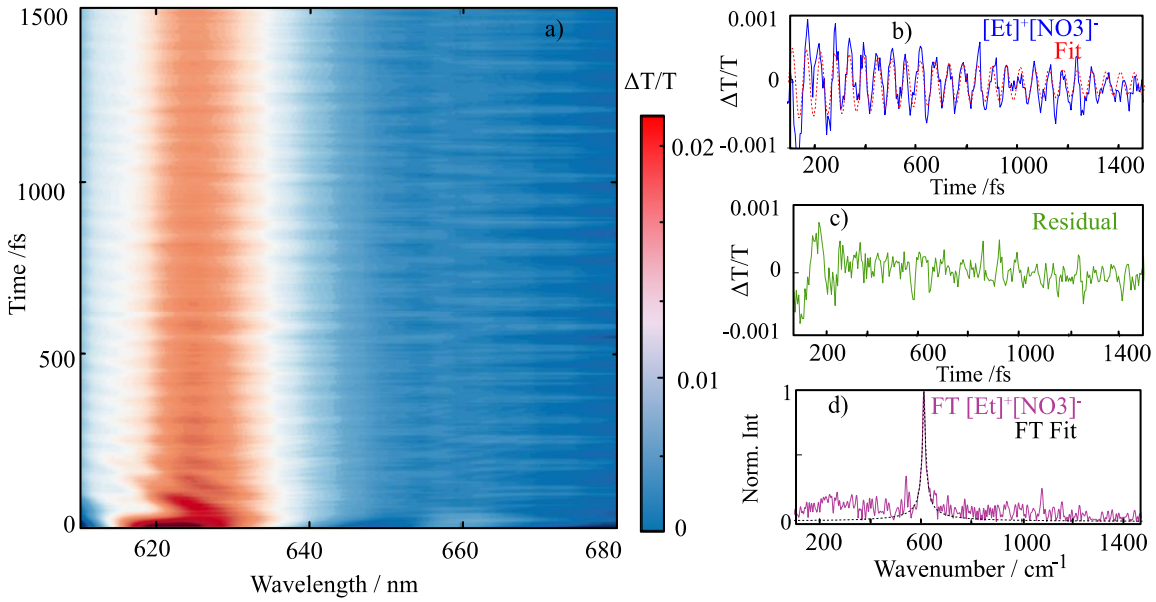

Figure Ap. 6.1 (a) BBTA spectrum of $[Et]^+[NO_3]^-$, (b) coherent vibrational oscillation (in blue) at 620 nm and the best fitting shown as a dashed red line. (c) The residual. (d) The pink line corresponds to the experimental FT spectrum at 615 nm wavelength, while the black line is the FT of the red dashed lines.

Ap. 6.2 2DES Oxazine 4 in Methanol

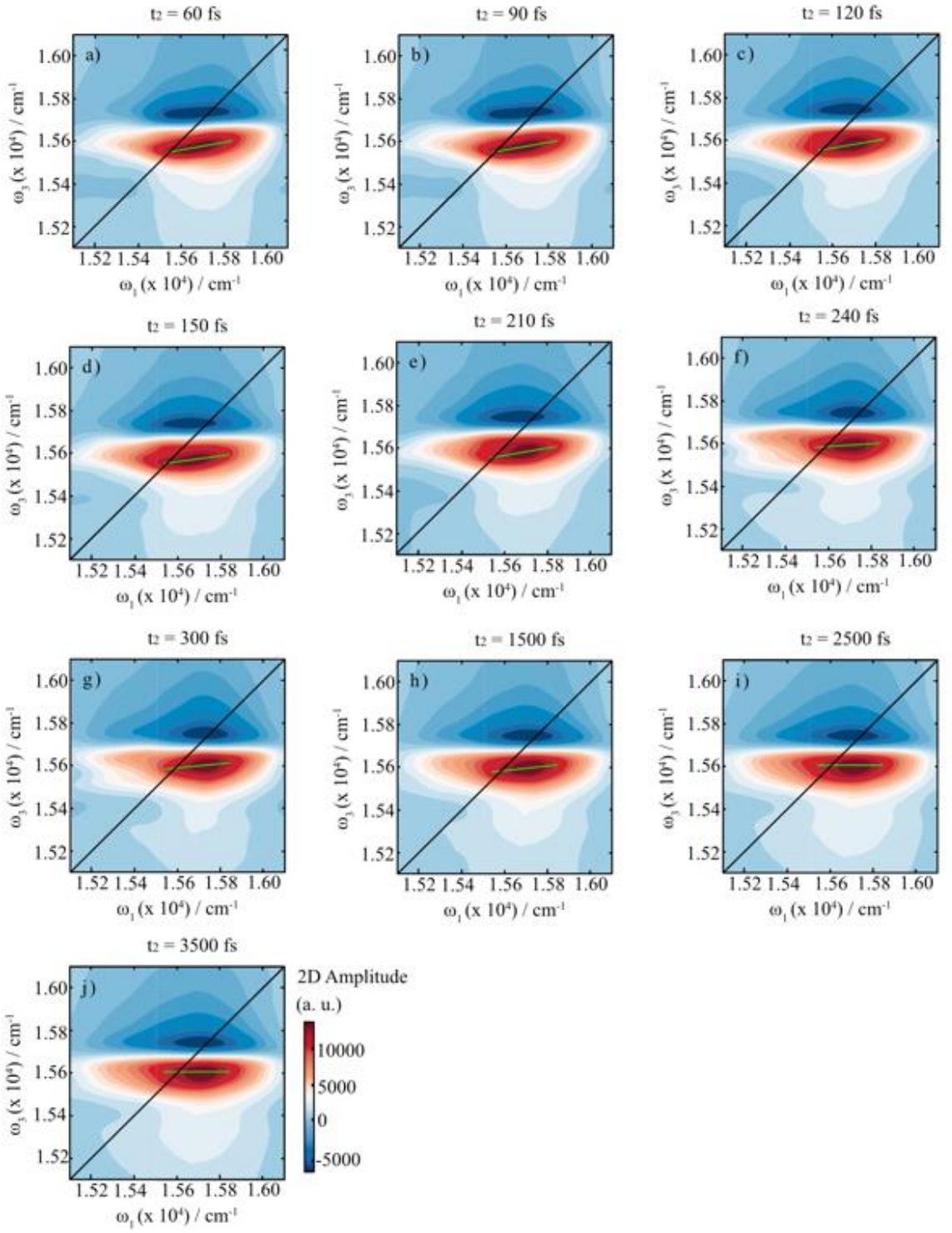

Figure Ap. 6.2 2DES data of Oxazine 4 in methanol at subsequent t_2 time delays.

Ap. 6.3 2DES Oxazine 4 in DMSO

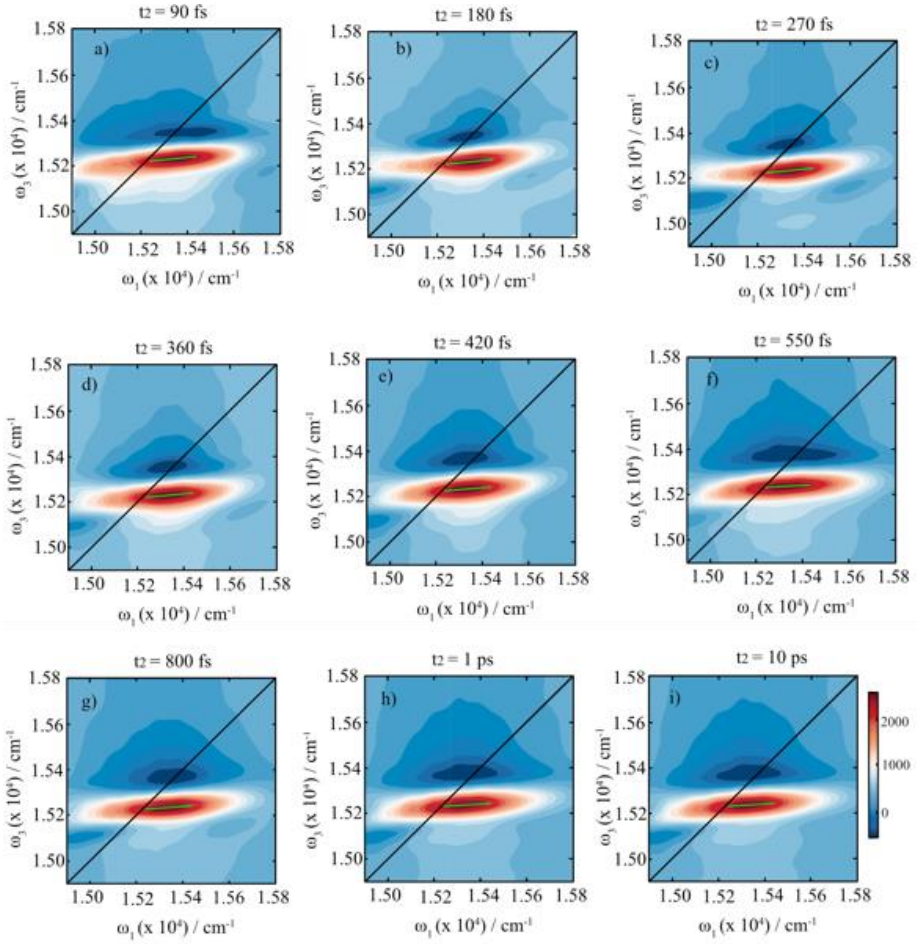

Figure Ap. 6.3 2DES data of Oxazine 4 in DMSO at subsequent t_2 time delays.

Ap. 6.4 2DES Oxazine 4 in $[EMI]^+[SCN]^-$

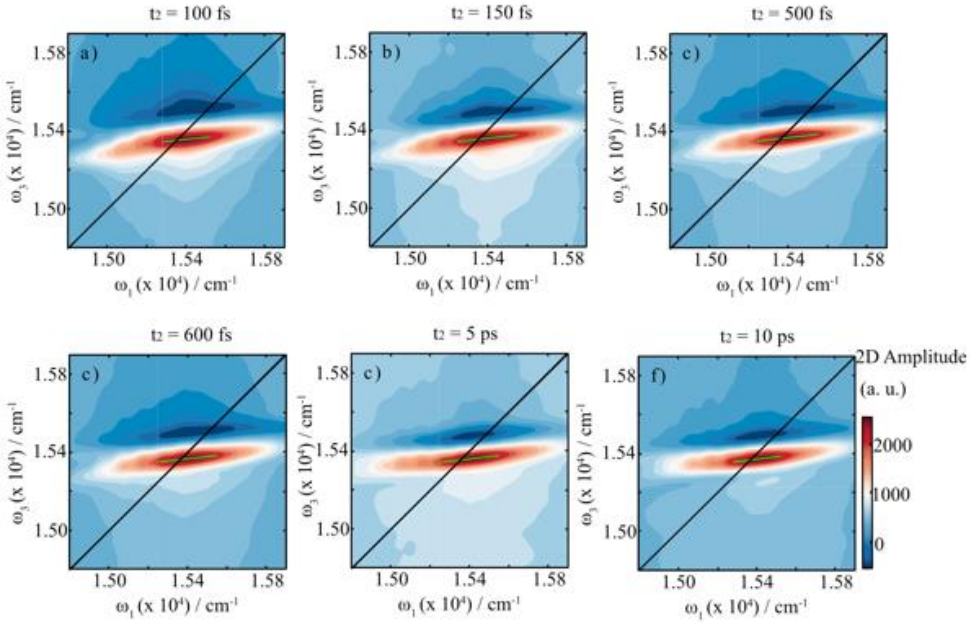

Figure Ap. 6.4 2DES data of Oxazine 4 in $[EMI]^+[SCN]^-$ at subsequent t_2 time delays.

References

1. Zinad, D. S., Mahal, A., Mohapatra, R. K., Sarangi, A. K. & Pratama, M. R. F. Medicinal chemistry of oxazines as promising agents in drug discovery. *Chem. Biol. Drug. Des.* **95**, 16–47 (2019).

2. Pal'chikov, V. A. Morpholines. Synthesis and biological activity. *Russ. J. Phys. Chem. A.* **49**, 787–814 (2013).

3. Bardeen, C. J. & Shank, C. V. Femtosecond electronic dephasing in large molecules in solution using mode suppression. *Chem. Phys. Lett.* **203**, 535–539 (1993).

4. Becker, P. C., Fragnito, H. L., Bigot, J. Y., Brito Cruz, C. H., Fork, R. L. & Shank, C. V. Femtosecond photon echoes from molecules in solution. *Phys. Rev. Lett.* **63**, 505–507 (1989).

5. Weiner, A. M., Silvestri, S. D. & Ippen, E. P. Three-pulse scattering for femtosecond dephasing studies: theory and experiment. *J. Opt. Soc. Am. B* **2**, 654-662 (1985).

6. Moshary, F., Arend, M., Friedberg, R. & Hartmann, S. R. Ultrafast relaxation and modulation in the oxazine dye nile blue. *Phys. Rev. A* **46**, R33–R36 (1992).

7. Cruz, C. H. B., Fork, R. L., Knox, W. H. & Shank, C. V. Spectral hole burning in large molecules probed with 10 fs optical pulses. *Chem. Phys. Lett.* **132**, 341–344 (1986).

8. Bardeen, C. J. & Shank, C. V. Ultrafast dynamics of the solvent-solute interaction measured by femtosecond four-wave mixing: LD690 in n-alcohols. *Chem. Phys. Lett.* **226**, 310–316 (1994).

9. Muramatsu, M., Nagasawa, Y. & Miyasaka, H. Ultrafast solvation dynamics in room temperature ionic liquids observed by three-pulse photon echo peak shift measurements. *J. Phys. Chem. A.* **115**, 3886–3894 (2011).

10. Jin, H., Baker, G. A., Arzhantsev, S., Dong, J. & Maroncelli, M. Solvation and rotational dynamics of coumarin 153 in ionic liquids: comparisons to conventional solvents. *J. Phys. Chem. B.* **111**, 7291–7302 (2007).

11. Ito, N., Arzhantsev, S., Heitz, and M. & Maroncelli, M. Solvation dynamics and rotation of coumarin 153 in alkylphosphonium ionic liquids. *J. Phys. Chem. B.* **108**, 5771–5777 (2004).

12. Gutowski, K. E. Green Chemistry in Industry. *Walter de Gruyter GmbH,* (2018).

13. Arzhantsev, S., Ito, N., Heitz, M. & Maroncelli, M. Solvation dynamics of coumarin 153 in several classes of ionic liquids: cation dependence of the ultrafast component. *Chem. Phys. Lett.* **381**, 278–286 (2003).

14. Karmakar, R. & Samanta, A. Solvation Dynamics of Coumarin-153 in a Room-Temperature Ionic Liquid. *J. Phys. Chem. A.* **106**, 4447–4452 (2002).

15. Ito, N., Arzhantsev, S. & Maroncelli, M. The probe dependence of solvation dynamics and rotation in the ionic liquid 1-butyl-3-methyl-imidazolium hexafluorophosphate. *Chem. Phys. Lett.* **396**, 83–91 (2004).

16. Mellein, B. R., Aki, S. N. V. K., Ladewski, R. L. & Brennecke, J. F. Solvatochromic Studies of Ionic Liquid/Organic Mixtures. *J. Phys. Chem. B* **111**, 131–138 (2007).

17. Abraham, M. H. & Jr, W. E. A. Comparative analysis of solvation and selectivity in room temperature ionic liquids using the Abraham linear free energy relationship. *Green Chem.* **8**, 906-915 (2006).

18. Crosthwaite, J. M., Muldoon, M. J., Aki, S. N. V. K., Maginn, E. J. & Brennecke, J. F. Liquid Phase Behavior of Ionic Liquids with Alcohols: Experimental Studies and Modeling. *J. Phys. Chem. B* **110**, 9354–9361 (2006).

19. Anderson, J. L., Ding, J., Welton, T. & Armstrong, D. W. *J. Am. Chem. Soc.* **124,** 14247-14254 (2002).

20. Dean, J. C., Refiq, S., Oblinsky, D. G., Casette, E., Jumper, C. C. Scholes, G. D. Broadband Transient Absorption and Two-Dimensional Electronic Spectroscopy of Methylene Blue. *J. Phys. Chem. A* **119**, 9098–9108 (2015).

21. Stratt, R. M. & Maroncelli, M. Nonreactive Dynamics in Solution: The Emerging Molecular View of Solvation Dynamics and Vibrational Relaxation. *J. Phys. Chem.* **100**, 12981–12996 (1996).

22. Heller, E. J. The semiclassical way to molecular spectroscopy. *Acc. Chem. Res.* **14**, 368–375 (1981).

23. Pollard, W. T., Dexheimer, S. L., Wang, Q., Peteanu, L. A., Shank, C. V. & Methies, R. A. Theory of dynamic absorption spectroscopy of nonstationary states. 4. Application to 12-fs resonant impulsive Raman spectroscopy of bacteriorhodopsin. *J. Phys. Chem.* **96**, 6147–6158 (1992).

24. Pollard, W. T., Lee, S. & Mathies, R. A. Wave packet theory of dynamic absorption spectra in femtosecond pump–probe experiments. *J. Chem. Phys.* **92**, 4012–4029 (1990).

25. Braun, M., Sobotta, C., Dürr, R., Pulvermacher, H. & Malkmus, S. Analysis of Wave Packet Motion in Frequency and Time Domain: Oxazine 1. *J. Phys. Chem. A.* **110**, 9793–9800 (2006).

26. Yang, T. S., Chang, R., Hayashi, M., & Lin, S. H. Femtosecond pump-probe study of molecular vibronic structures and dynamics of a cyanine dye in solution. *J. Chem. Phys.* **110**, 12070–12081 (1999).

27. Song, Y., Clafton, S. N., Pensack, R. D., Kee, T. W. & Scholes, G. D. Vibrational coherence probes the mechanism of ultrafast electron transfer in polymer–fullerene blends. *Nat. Commun.* **5**, 4933 (2014).

28. McClure, S. D., Turner, D. B., Arpin, P. C., Mirkovic, T. & Scholes, G. D. Coherent Oscillations in the PC577 Cryptophyte Antenna Occur in the Excited Electronic State. *J. Phys. Chem. B* **118**, 1296–1308 (2014).

29. Dantus, M., Rosker, M. J. & Zewail, A. H. Real-time femtosecond probing of ‘“transition states”’ in chemical reactions. *J. Chem. Phys.* **87**, 2395–2397 (1987).

30. Rose, T. S., Rosker, M. J. & Zewail, A. H. Femtosecond real-time observation of wave packet oscillations (resonance) in dissociation reactions. *J. Chem. Phys.* **88**, 6672–6673 (1988).

31. Dhar, L., Rogers, J. A. & Nelson, K. A. Time-resolved vibrational spectroscopy in the impulsive limit. *Chem. Rev.* **94**, 157–193 (1994).

32. Huang, M.-M., Jiang, Y., Sasisanker, P., Driver, G. W. & Weingärtner, H. Static Relative Dielectric Permittivities of Ionic Liquids at 25 °C. *J. Chem. Eng. Data* **56**, 1494–1499 (2011).

33. Hybl, J. D., Ferro, A. A., Chemical, D. J. T. J. of & 2001. Two-dimensional Fourier transform electronic spectroscopy. *J. Chem. Phys.* **115**, 6606-6622 (2001).

34. Khalil, M., Demirdöven, N. & Tokmakoff, A. Obtaining Absorptive Line Shapes in Two-Dimensional Infrared Vibrational Correlation Spectra. *Phys. Rev. Lett.* **90**, 047401 (2003).

35. Bardeen, C. J., Rosenthal, S. J. & Shank, C. V. Ultrafast Solvation Processes in Polar Liquids Probed with Large Organic Molecules. *J. Phys. Chem.* **103**, 10506–10516 (1999).

36. Bardeen, C. J., Wang, Q. & Shank, C. V. Femtosecond Chirped Pulse Excitation of Vibrational Wave Packets in LD690 and Bacteriorhodopsin. *J. Phys. Chem.***102**, 2759–2766 (1998).

37. Fleming, G. R. & Cho, M. Chromophore-solvent dynamics. *Annu. Rev. Phys. Chem.* **47**, 109–134 (1996).

38. Castner, E. W. & Maroncelli, M. Solvent dynamics derived from optical Kerr effect, dielectric dispersion, and time-resolved stokes shift measurements: an empirical comparison. *J. Mol. Liq.* **77**, 1–36 (1998).

39. Boeij, W. P. de, Pshenichnikov, M. S. & Wiersma, D. A. Ultrafast solvation dynamics explored by femtosecond photon echo spectroscopies. *Annu. Rev. Phys. Chem.* **49**, 99–123 (1998).

40. Bagchi, B. Dynamics of Solvation and Charge Transfer Reactions in Dipolar Liquids. *Annu. Rev. Phys. Chem.* **40**, 115–141 (1989).

41. Vos, M. H., Rappaport, F., Lambry, J.-C., Breton, J. & Martin, J.-L. Visualization of coherent nuclear motion in a membrane protein by femtosecond spectroscopy. *Nature* **363**, 320–325 (1993).

42. Rafiq, S. & Scholes, G. D. Slow intramolecular vibrational relaxation leads to long-lived excited-state wavepackets. *J. Phys. Chem. A.* **120**, 6792–6799 (2016).

43. Rafiq, S., Dean, J. C. & Scholes, G. D. Observing Vibrational Wavepackets during an Ultrafast Electron Transfer Reaction. *J. Phys. Chem. A.* **119**, 11837–46 (2015).

44. Yoneda, Y., Kudisch, B., Rafiq, S., Maiuri, M., Scholes, G. & Miyasaka, H. Vibrational coherence in ultrafast electron transfer reaction observed by broadband transient absorption spectroscopy. *Eur. Phys. J.* **205**, 09028 1-3 (2019).

45. Cina, J. A., Kovac, P. A., Jumper, C. C., Dean, J. C. & Scholes, G. D. Ultrafast transient absorption revisited: Phase-flips, spectral fingers, and other dynamical features. *J. Chem. Phys.* **144**, 175102 1-18 (2016).

46. Florean, A. C., Carroll, E. C., Spears, K. G., Sension, R. J. & Bucksbaum, P. H. Optical Control of Excited-State Vibrational Coherences of a Molecule in Solution: The Influence of the Excitation Pulse Spectrum and Phase in LD690. *J. Phys. Chem. B* **110**, 20023–20031 (2006).

47. van Stokkum, I. H. M., Jumper, C. C., Snellenburg, J. J., Scholes, G. D., van Grondelle, R. Maly, P. Estimation of damped oscillation associated spectra from ultrafast transient absorption spectra. *J. Chem. Phys.* **145**, 174201 1-12 (2016).

48. Neelakantan, P. Raman spectrum of acetonitrile. *Proc. Natl. Acad. Sci. India A.* **60**, 422–424 (1964).

49. Selvarajan, A. Raman spectrum of dimethyl sulfoxide (DMSO) and the influence of solvents. *Proc. Natl. Acad. Sci. India A.* **64**, 44–50 (1966).

50. Mammone, J. F., Sharma, S. K. & Nicol, M. Raman spectra of methanol and ethanol at pressures up to 100 kbar. *J. Phys. Chem.* **84**, 3130–3134 (1980).

51. Zewail, A. H. Femtochemistry: Atomic-Scale Dynamics of the Chemical Bond. *J. Phys. Chem. A.* **104**, 5660–5694 (2000).

52. Gruebele, M. & Zewail, A. H. Femtosecond wave packet spectroscopy: Coherences, the potential, and structural determination. *J. Chem. Phys.* **98**, 883–902 (1993).

53. Jonas, D. M. Two-dimensional femtosecond spectroscopy. *Annu. Rev. Phys. Chem.* **54**, 425–463 (2003).

54. Hybl, J. D., Albrecht, A. W., Faeder, S. M. G. & Jonas, D. M. Two-dimensional electronic spectroscopy. *Chem. Phys. Lett.* **297**, 307-313 (1998)

55. Roberts, S. T., Loparo, J. J. & Tokmakoff, A. Characterization of spectral diffusion from two-dimensional line shapes. *J. Chem. Phys.* **125**, 084502 1-8 (2006).

56. Nemeth, A., Sperling, J., Hauer, J., Kauffmann, H. F. & Milota, F. Compact phase-stable design for single- and double-quantum two-dimensional electronic spectroscopy. *Opt. Lett.* **34**, 3301-3301 (2009).

57. Brixner, T., Mančal, T., Stiopkin, I. V. & Fleming, G. R. Phase-stabilized two-dimensional electronic spectroscopy. *J. Chem. Phys.* **121**, 4221–4236 (2004).

58. Lee, Y., Das, S., Malamakal, R. M., Meloni, S., Chenoweth, D. M. & Anna, J. M. Ultrafast Solvation Dynamics and Vibrational Coherences of Halogenated Boron-

Dipyrromethene Derivatives Revealed through Two-Dimensional Electronic Spectroscopy. *J. Am. Chem. Soc.* **139**, 14733–14742 (2017).

59. Kwac, K. & Cho, M. Two-Color Pump−Probe Spectroscopies of Two- and Three-Level Systems: 2-Dimensional Line Shapes and Solvation Dynamics. *J. Phys. Chem. A.* **107**, 5903–5912 (2003).

60. Kwak, K., Park, S., Finkelstein, I. J. & Fayer, M. D. Frequency-frequency correlation functions and apodization in two-dimensional infrared vibrational echo spectroscopy: A new approach. *J. Chem. Phys.* **127**, 124503 1-17 (2007).

61. Lewis, N. H. C., Dong, H., Oliver, T. A. A. & Fleming, G. R. Measuring correlated electronic and vibrational spectral dynamics using line shapes in two-dimensional electronic-vibrational spectroscopy. *J. Chem. Phys.* **142**, 174202 1-10 (2015).

62. Kwak, K., Rosenfeld, D. E. & Fayer, M. D. Taking apart the two-dimensional infrared vibrational echo spectra: More information and elimination of distortions. *J. Chem. Phys.* **128**, 204505 1-10 (2008).

Chapter 7

Zinc Chlorin e6 and Zinc Chlorin e6 in a Maquette Protein

7.1 Introduction

Natural occurring photosynthetic organisms, such as plants, bacteria, and algae, can absorb sunlight and convert it into chemical energy. This process is known as photosynthesis.[1] These organisms contain light-absorbing molecules, commonly referred to as pigments embedded in a protein scaffold.[2] These pigments, mainly chlorophyll (Chl) and carotenoids can absorb specific regions of the electromagnetic spectrum.[1,3] Schematically, after light absorption, the energy migrates via electron energy transfer (EET) to the so-called reaction centre (RC) where a charge transfer reaction takes place as shown in Figure 7.1.[1,3]

The initial absorption event is facilitated by different arrangements that the pigments and the surrounding protein can manifest.[4] Thus, multiple pigment-protein architectures can be encountered in naturally occurring photorganisms where the existence of different arrangments depends on the natural light conditions of the photosynthetic organisms' habitat, and it is naturally optimised to give remarkably efficient light capture across a broad spectral range.[4]

Furthermore, it has been determined that the protein plays several roles during the EET. More specifically, depending on the disposition of each chromophore inside the protein binding pocket, the absorption spectrum can be tuned and modulated through the formation

of delocalised excited states over multiple Chls. These states have different transition energies compared to isolated chromophores.[4] Therefore, the pigment-protein interactions play a fundamental role in determining the absorption properties of the complex, particularly when the geometry between adjacent pigments (*i.e.*, the angles between two adjacent chlorophylls) is affected. Furthermore, the strength of inter-molecular dipole coupling can be modified.[4] The factor mentioned above determines the ground and excited state energy landscape of the pigment-protein complexes and the timescale associated with the EET process which has been observed to be very fast (from 100 fs to 1 ps).[4]

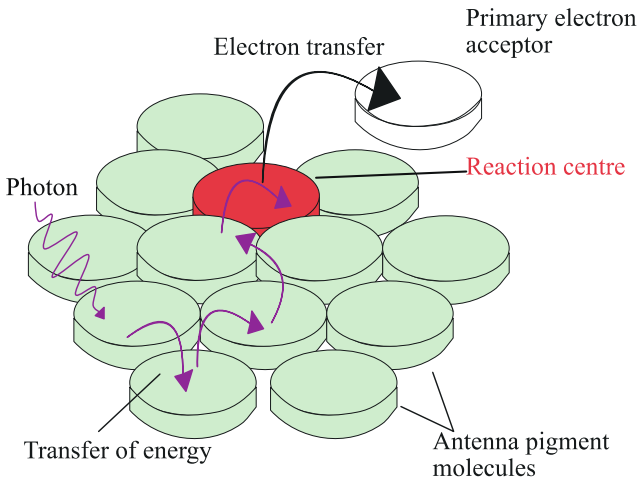

Figure 7.1 Representation of photosynthesis apparatus depicting photon absorption, energy transfer to a reaction centre, and electron transfer.

Therefore, the understanding of the electronic structure of these light-absorbing molecules is a crucial point for the study of EET processes occurring in photosynthetic organisms. Concerning this point, porphyrins and porphyrins derivatives (such as chlorophylls) electronic structures have been studied and well understood.[5] Their electronic spectra consist of two regions with the main band between 380 and 500 nm (Soret band or B band) and red-shifted weaker bands between 500-750 nm, known as Q-bands (Figure 7.2 (a)). The absorption spectra of porphyrins can be explained through the "four-orbital" model

proposed by Gouterman in 1961.[5] The model considers two occupied π and two unoccupied π^* orbitals, as illustrated in Figure 7.2 (b).[5,6] According to this theory, the absorption bands are given by electronic transitions from the two highest occupied molecular orbitals (HOMOs), which are labelled a_{1u} and a_{2u}, and to the two lowest unoccupied molecular orbitals (LUMOs) which are degenerate and labelled, e_g. The relative energies of the transitions depend on the number of substituents and the presence of a transition metal cation such as Zn^{2+}, Mg^{2+}, and Fe^{2+}, therefore, the electronic properties of the porphyrins and porphyrins derivatives are mainly determined by their symmetry.[5,7–10] According to theory, the Soret and Q bands derive from the linear combination of the four possible excitations (Figure 7.2 (c)) between the HOMOs and LUMOs. Thus, degenerate electronic transition along the x and y-axes (axes through opposing central nitrogen atoms, see Figure 7.2 (b)) results in allowed excitations at higher energies (Soret band) and formally forbidden at lower energies (Q-bands). The formally forbidden bands become weakly allowed with the symmetry breaking that occurs in many porphyrins.[11]

The number of Q-bands observed varies from metalloporphyrins (porphyrins containing a transition metal cation in the centre of the ring) to base-free porphyrins depending on their symmetry. Due to the N-H bond, the matal-free porphyrins have reduced symmetry compared to the metalloporphyrin, and the x- and y-axes along the opposite pyrrole nitrogen atoms are not equivalent (as they might be in metalloporphyrins without any substituents). The reduction in symmetry in the free-base porphyrins means that the transitions along the x and y-axis are not degenerate as in the metalloporphyrin. Therefore, their electronic spectra are characterised by four Q bands, two given by the vibronic transitions, 1-0 and the 0-0 which are further split into $Q_x(0,0)$, $Q_x(1,0)$, $Q_y(0,0)$ and $Q_y(1,0)$

where the x and y indicate the direction of the electronic transition whether it occurs along the x- or y-axes.[5,6,11]

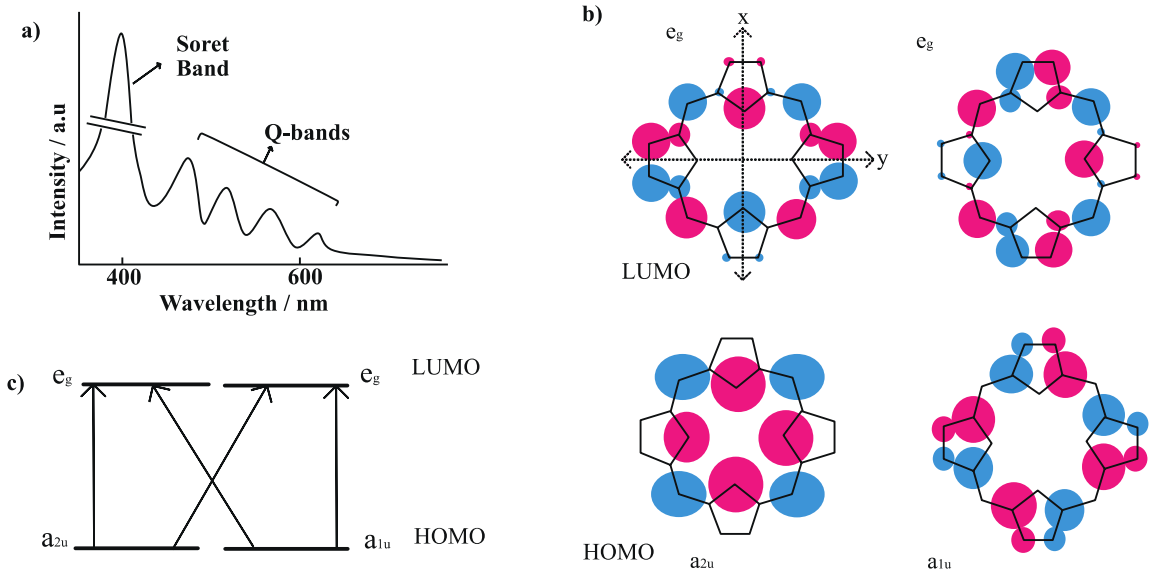

Figure 7.2 (a) Porphyrin spectrum showing Soret and Q-bands. (b) The four orbitals related to the "four orbitals" theory and (c) the simplified representation of the HOMOs to LUMOs electronic transitions.

To date, ultrafast spectroscopy, X-ray crystallography, and the theoretical studies of the so-called pigment-protein complexes have greatly improved the understanding of the excitation energy transfer and the excited state energy landscape.[1,3] However, given the high tunability of the systems, the protein dynamics is still unclear.[12] The uncertainties in the dynamical role of the protein (*i.e.*, how can the protein mediate the vibrational energy relaxation) have yet to be established. Moreover, the lack of clarity in the dynamics related to the protein response to the photoexcitation of chlorophyll (and similar pigments) turns these extremely efficient systems into one of the most interesting to study with ultrafast techniques including multidimensional spectroscopy. Therefore, the determination of the protein response and its "solvation" dynamics requires a deep understanding of the pigment-protein interactions.[4,13]

Despite the advance in technology and the increased interest in understanding the dynamical role of the protein in naturally occurring photosynthetic organisms,[4,14] the study of these phenomena is still challenging due to two main aspects. First, natural pigment-protein complexes usually contain many chromophores (> 12) that can generate additional EET contributions observed with ultrafast techniques. A second difficulty that can be encountered while studying pigment-protein complexes is that smaller natural proteins containing few pigments (*e.g.*, B820) are unstable under ambient conditions.[15] For these reasons finding a stable naturally occurring protein constituted of a few pigments is very challenging.

To overcome these issues, a de novo model tetra-helical maquettes containing zinc-chlorin e6 (ZnCe6) pigment is studied and the dynamics of both ZnCe6 and the ZnCe6 bonded to the protein (ZnCe6-m4d2) are presented in this chapter. The designer nature of the maquette protein allows facile editing where the binding residue can be substituted to explore dynamics in specific environments of the tetra-helical species. Broadband transient absorption (BBTA) data of ZnCe6 in methanol, buffer, and ZnCe6-m4d2 in buffer (pH = 9) are presented along with vibrational wave packets analysis. Density functional theory (DFT) calculations are used to assign the Fourier transform (FT) amplitudes observed.

7.2 Methods

7.2.1 Zn(II) Chlorin e6 and m4d2 Protein Samples

The maquette, m4d2, was synthesised in the Anderson laboratory, at the University of Bristol. The protein is the product of fully functional enzymes with a variety of applications.[16–18] X-ray crystallography reveals that the m4d2 protein binds one ZnCe6

moiety via a histidine residue, and the ZnCe6 and ZnCe6-m4d2 skeletal structures are shown in Figure 7.3 (a) and (b), respectively.

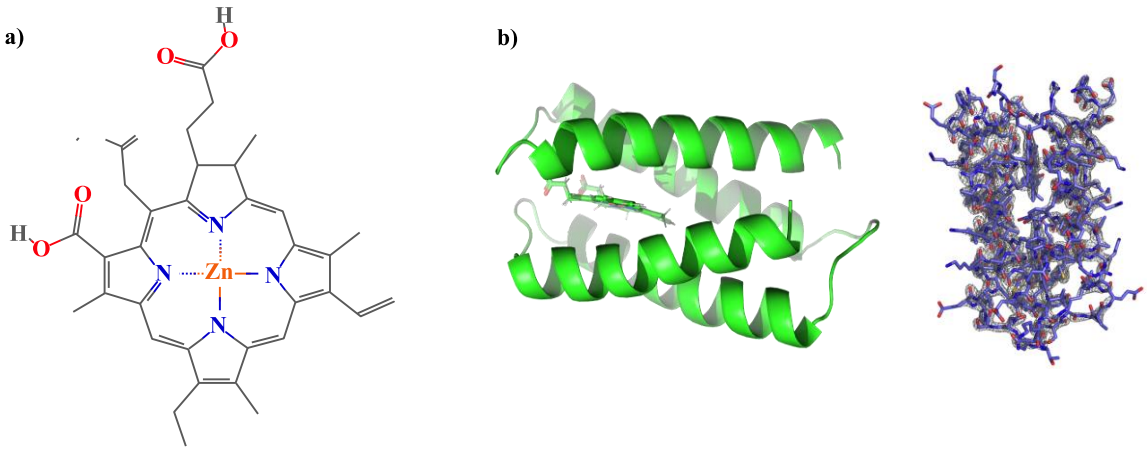

Figure 7.3 (a) Skeletal molecular structure of ZnCe6, and (b) structures of ZnCe6 bounds to m4d2 tetrahelical protein.

The ZnCe6-m4d2 complex was studied in buffer solution, pH = 9, at room temperature. The broadband transient absorption experiments were carried out in a short path length (1 mm) flow cell (Starna) and, all measurements were consistently carried out with samples having an optical density of 0.3 at 640 nm while the fluorescence spectra were taken in 1 cm cuvette.

Solutions of ZnCe6 were prepared by adding chlorin e6 (Frontier Scientific > 95 %) and zinc acetate ($Zn(OAc)_2$ dihydrate from Merck, 99.99%) to methanol (Sigma-Aldrich, anhydrous, 99.8 %) or to a phosphate buffer solution (pH = 9). The solutions were placed in a sonicator, at room temperature, for ~ 30 minutes. To follow the insertion of Zn^{2+} static visible absorption spectroscopy was used. Upon insertion into the chlorin moiety, a significant spectral red shift of the Q_y band from 633 to 640 nm was observed.[19] The

solutions were then filtered (Pall corporation acrodisc, syringe filter with nylon membrane, 0.2 μm), and 1 mm pathlength Starna cuvettes were used for visible absorption measurements while the fluorescence spectra were taken in 1 cm cuvette. The concentration of the ZnCe6 solutions was kept constant with an absorbance of 0.5 at ~ 640 nm. For consistency with the ZnCe6-m4d2 data, the broadband transient absorption experiments were carried out in a (1 mm) path length flow cell (Starna). The visible absorption spectra taken for both the ZnCe6 and ZnCe6-m4d2 samples before and after irradiation prove that long-living photoproducts were not produced during the experiments.

7.2.2 Ultrafast Experimental Details

Broadband transient absorption spectroscopy (BBTA) was used to investigate ZnCe6 in solution and ZnCe6-m4d2. A Ti: Sapphire laser (1 W, 800 nm, 1 kHz, Coherent Libra) was employed to pump a home-built non-linear parametric amplifier (NOPA) (see Chapter 5 for full details of the spectrometer) and to generate the broad visible spectrum that spans from 500 to 700 nm with a full-width-half maximum (FWHM) 100 nm and central wavelength at 600 nm. For the data shown in this chapter, the compression of the chirped pulses was carried out either with chirped mirrors or Dazzler ultrafast pulse shaper. The pulse duration was characterised with second-harmonic generation frequency-resolved optical gating (SHG FROG) when the pulse was compressed with chirped mirrors and transient gating FROG otherwise. Figure 7.4 (a) and (b) show the contour maps and (d) and (e) the profiles of the 15 and 28 fs pulses achieved with the chirped mirrors and Dazzler ultrafast pulse shaper, respectively. Both traces were analysed with the FROG software developed by Trebino's group.[20,21]

During BBTA measurements, two of the four beams that constitute the boxcar geometry were blocked, while the other two were focused on the sample with a spot size of ~90 μm at the focal point. The pulse energy at the sample, identical for both pump and probe beams, was attenuated to ~9 nJ for ZnCe6 solutions and 5 nJ for ZnCe6-m4d2.

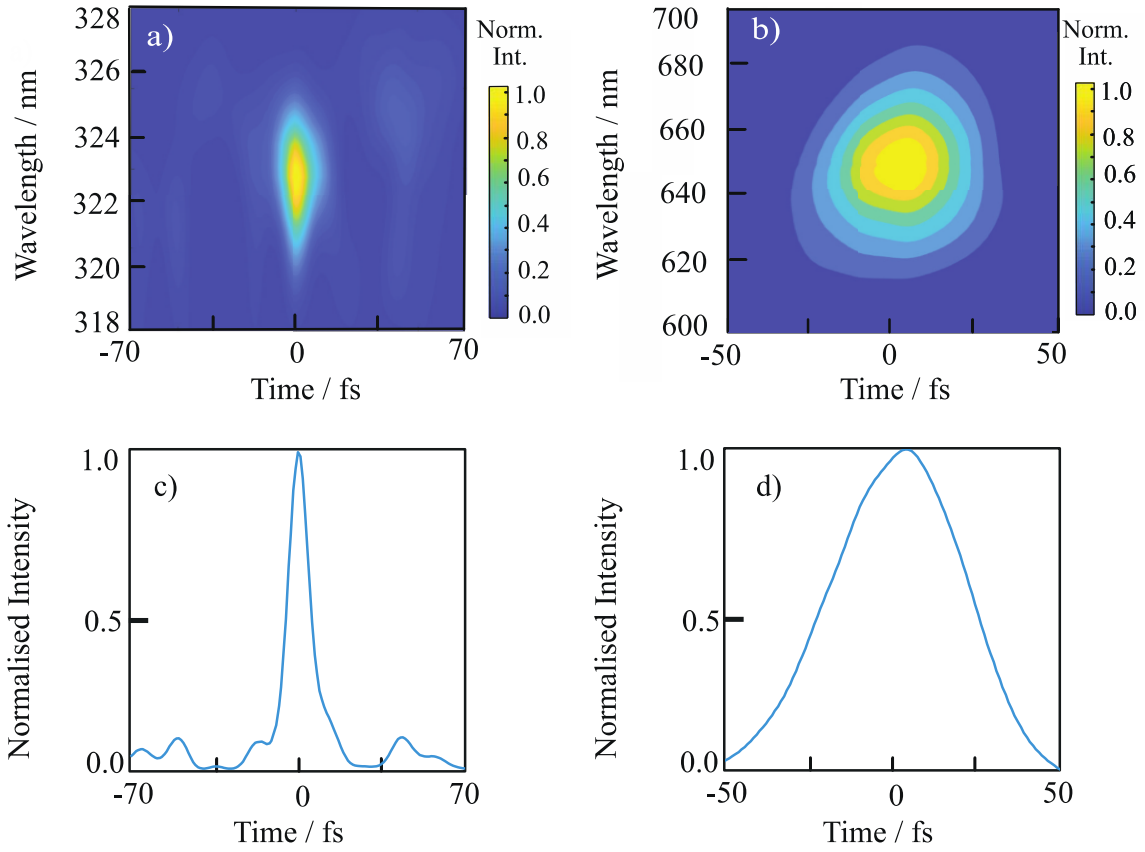

Figure 7.4 (a) Contour map and (c) pulse profile at 323 nm achieved with chirped mirrors compression. (b) Contour map and (d) pulse profile at 650 nm achieved with Dazzler ultrafast pulse shaper compression.

7.3 Results and Discussion

7.3.1 Static Spectra

The ZnCe6 and ZnCe6-m4d2 samples were characterised with both static fluorescence and visible absorption spectroscopy. Figure 7.5 shows the visible and fluorescence spectra

(taken at the excitation wavelength of 640 nm) for (a) ZnCe6 in methanol, (b) buffer, and (c) ZnCe6-m4d2. The chlorin e6 excitation involves $\pi^* \leftarrow \pi$ transitions that belong to chlorin core and give rise to the Q_y band,[5] shown as blue traces. A small shift of the Q_y band is observed in ZnCe6 spectra where the sample in methanol has a maximum at 640 nm, while for the metallochlorin in buffer, the absorption maximum is at 635 nm. When the ZnCe6 is bound to m4d2, the Q_y band absorption is shifted to 646 nm. Table 7.1 summarises the maxima of the absorption and fluorescence spectra alongside with the Stokes shift and the calculated reorganisation energies.

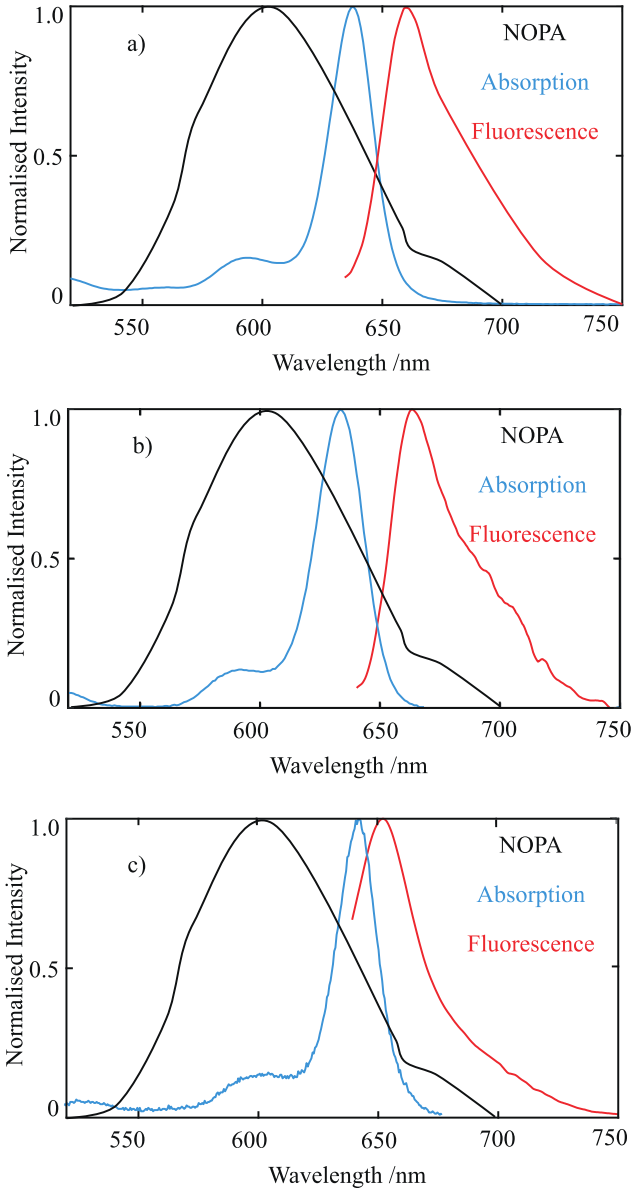

Figure 7.5 NOPA (black), absorption (blue) and fluorescence (red) spectra for ZnCe6 (a) in methanol, (b) buffer solution and (c) ZnCe6-m4d2 protein at room temperature. The fluorescence spectra were excited at 640 nm.

Traditionally, the Stokes shift is a tool for investigating the reorganisation energy (λ) which measures the strength of the interaction between the surrounding solvent and the solute to be half of it.[22–26] The λ values obtained for ZnCe6 in methanol and buffer are more significant than natural light-harvesting protein such as chlorophyll molecules in solution. It is known that the λ for chlorophyll a in methanol is 100 cm^{-1} while the λ for ZnCe6 in methanol and buffer are two and three times greater.[27] On the contrary, the λ calculated for the ZnCe6-m4d2 is quite similar to the λ observed for chlorophylls embedded in a protein scaffold (in photosystem I) where the calculated λ is 50-65 cm^{-1} (or between 6 and 11 nm).[28] To a first-order approximation, this discrepancy between the reorganisation energies of unbounded ZnCe6 and ZnCe6-m4d2 indicates that the protein's ability to "solvate" photoexcited ZeCe6 molecules is less effective than the methanol, and the protein may act as a less-strongly interacting bath.

Table 7.1 Absorption and fluorescence maxima, Stokes shift, and reorganisation energy for ZnCe6 in methanol, buffer, and ZnCe6-m4d2.

	ZnCe6, methanol	ZnCe6, buffer	ZnCe6-m4d2 buffer
λ_{abs} / nm	640	635	646
λ_{fluo} / nm	660	666	652
Stokes shift / nm / cm^{-1}	20 474	30 710	6 142
λ / cm^{-1}	236	355	71

7.3.2 Excited state Lifetime of ZnCe6 in Methanol

Zinc chlorin e6 was first studied in methanol, and the dynamics of its electronic excited state monitored with pump-probe spectroscopy up to 700 ps. The TA spectrum recorded is shown in Figure 7.6 (a) as a contour map. The data shows a broad positive feature spanning 620-690 nm with a maximum at 643 nm. This feature is composed of two signals: a ground state bleach (GSB) and stimulated emission (SE) deducible from the comparison with the static spectra given on the top of each panel (Figure 7.6). Slices of the TA spectrum for specific pump-probe delay times are given in Figure 7.6 (b) and show that the majority of the molecules recover to the ground state within 700 ps. Due to the reduction of the probe window obtained when the pulses are compressed with a Dazzler ultrafast pulse shaper, the excited state absorption that arises at ~560 nm (shown in the BBTA data in the following sections) could not be investigated for time delays longer than 1.5 ps.

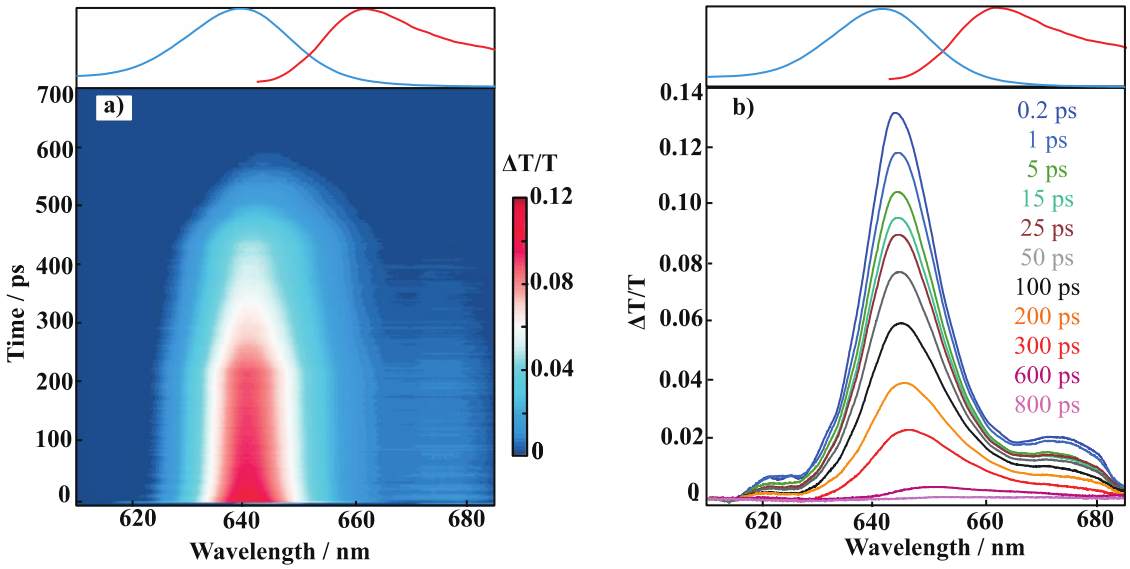

Figure 7.6 (a) Contour map of the ΔT/T ZnCe6 in methanol and (b) slices of the data given at subsequent time delays. ZnCe6 absorption (blue) and emission (red) spectra in methanol are shown on the top of each panel.

To follow the recovery of the molecule to the ground state, kinetics, at 640 and 680 nm probe wavelengths, were fitted with a multi-exponential function convolved with a Gaussian IRF and Heaviside step function, see Figure 7.7 (a) and (b). The lifetimes and amplitudes returned by the fits are given in Table 7.2 (R^2= 0.99).

Previous experiments carried out for porphyrin-like systems upon 647 nm photoirradiation report a short time constant (4.9 ± 0.5 ps) associated with vibrational cooling,[10,29] and a long lifetime (>> 100 ps) that had not been assigned. Therefore, in this study, the shortest lifetime observed, ~ 3 ps, can be associated with the vibrational relaxation while the longest time constant might be related to the S_0 repopulation through internal conversion but a final assignment of this lifetime is still challenging to achieve.[29]

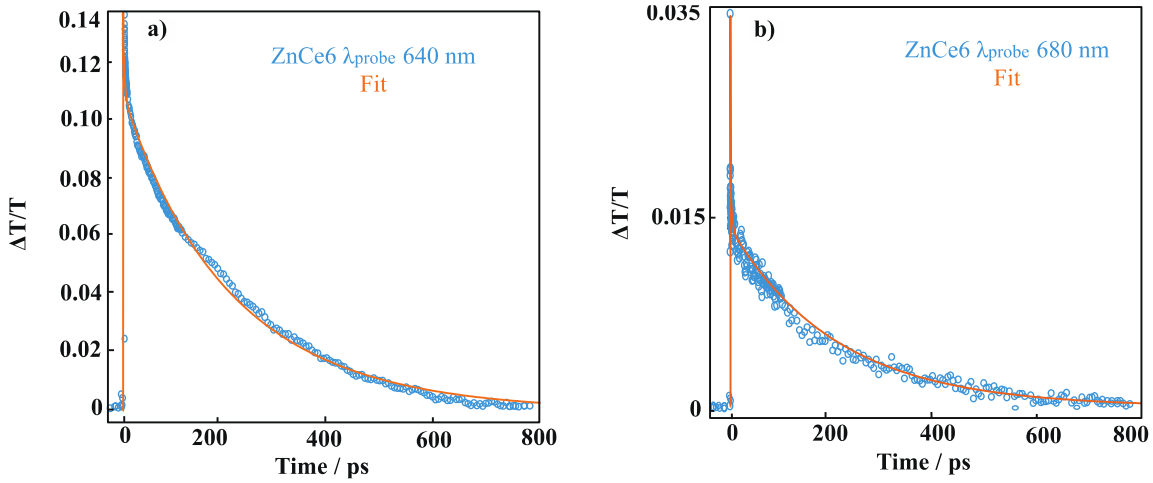

Figure 7.7 Kinetic traces at (a) 640 and (b) 680 nm given in blue and their fits in orange.

Table 7.2 Lifetime and percentage amplitudes obtained from TA fits.

	τ_1 / ps	A_1 / %	τ_2 / ps	A_2 / %
Pump-probe λ_{probe} = 640 nm	3.5 ± 0.2 ps	19	187 ± 1 ps	81
Pump-probe λ_{probe} = 680 nm	2.8 ± 0.5 ps	20	207± 5 ps	80

7.3.3 Broadband Transient Absorption Spectroscopy and Vibrational Wave packets

ZnCe6 BBTA spectra are given in Figure 7.8 (a) methanol and (b) buffer. The spectra show a positive feature centred at 643 nm attributed to a ground state bleach overlapping with stimulated emission and a weak negative feature centred at ~ 560 nm associated with the excited state absorption. The ZnCe6-m4d2 spectrum has similar spectral features compared to the pigment, a GSB + SE centred at ~647 nm, and an ESA on the blue edge of the spectrum as shown in Figure 7.8 (c).

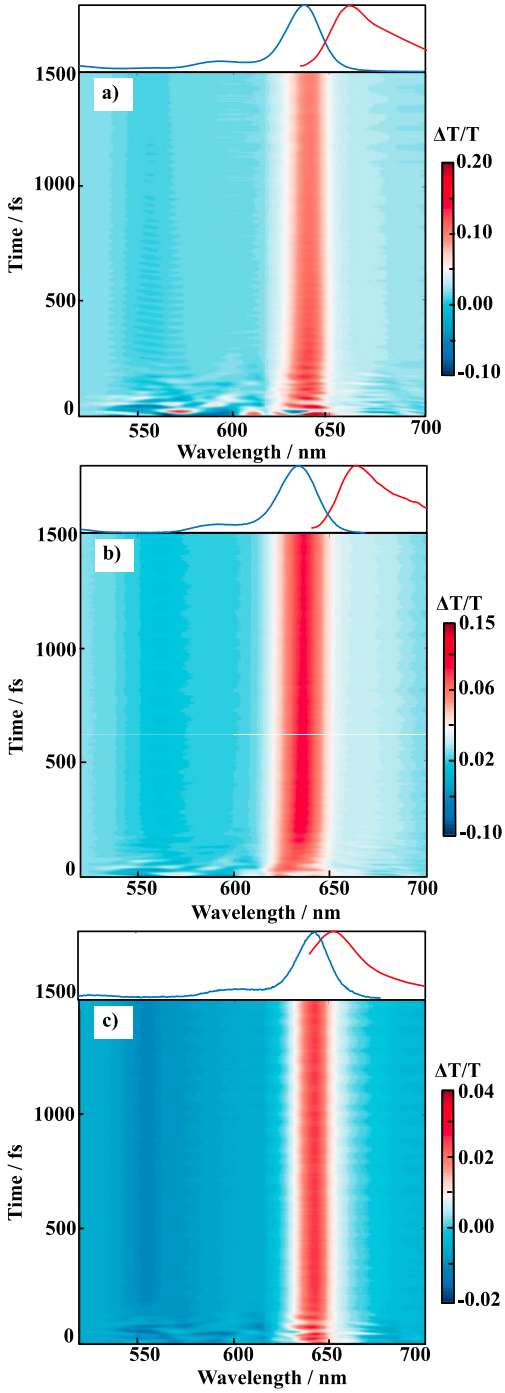

Figure 7.8 Broadband transient absorption spectrum of zinc chlorin e6 in (a) methanol, (b) buffer and (c) ZnCe6-m4d2. The linear absorption (blue) and fluorescence (red) spectra of each sample are displayed above the respective BBTA trace.

Figure 7.8 also shows that both the positive and negative components of the BBTA spectra are modulated by oscillations that arise from coherent vibrational wave packets, particularly evident in ZnCe6 in methanol. The wave packet dynamics can be isolated from

the underlying population relaxation dynamics by subtraction of the population dynamics.[30–32]

The following procedure was performed to isolate the oscillations: each probe wavelength of the BBTA spectrum (Figure 7.9 (a)) was fitted to a biexponential function, and the population dynamics were removed from the spectra. The purple trace in Figure 7.9 (b) corresponds to a slice of the raw data shown in Figure 7.9 (a) at 640 nm probe wavelength. After population dynamics removal, the purple trace taken as an example is converted into the orange trace shown in panel (b). Thus, the removal of the population dynamics at each probe wavelength leads to the purely vibrational coherent spectrum shown as a contour map in Figure 7.9 (c).

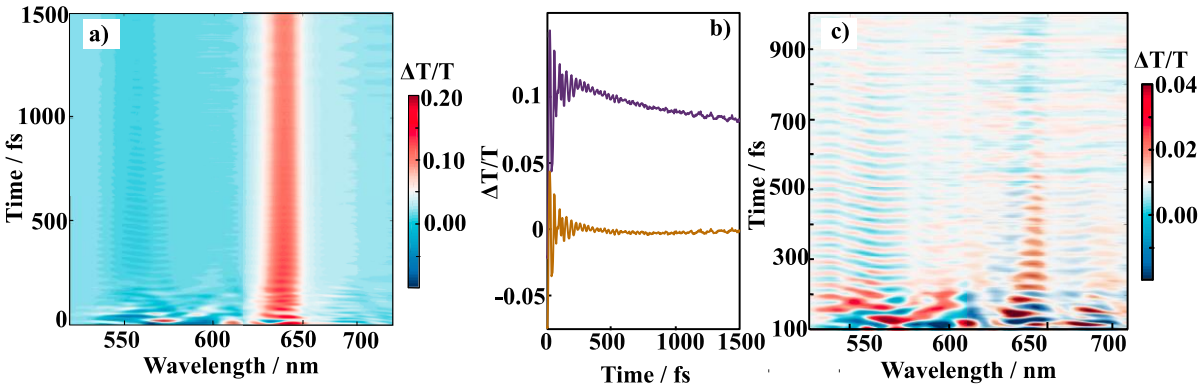

Figure 7.9 BBTA spectrum for ZnCe6 (a) in methanol, (b) comparison between a slice of the BBTA signal at 640 nm probe wavelength in purple and the same kinetics after subtracting the population dynamics; (c) the purely vibrational coherent spectrum.

This analysis was performed for the three datasets, returning oscillation maps, as shown in Figure 7.10 for ZnCe6 (a) in methanol, (b) buffer, and (c) ZnCe6-m4d2. The vibrational coherence amplitude for ZnCe6 in methanol is most pronounced at the blue edge of the spectrum (560 nm) and the maximum of the ground state bleach (640 nm).

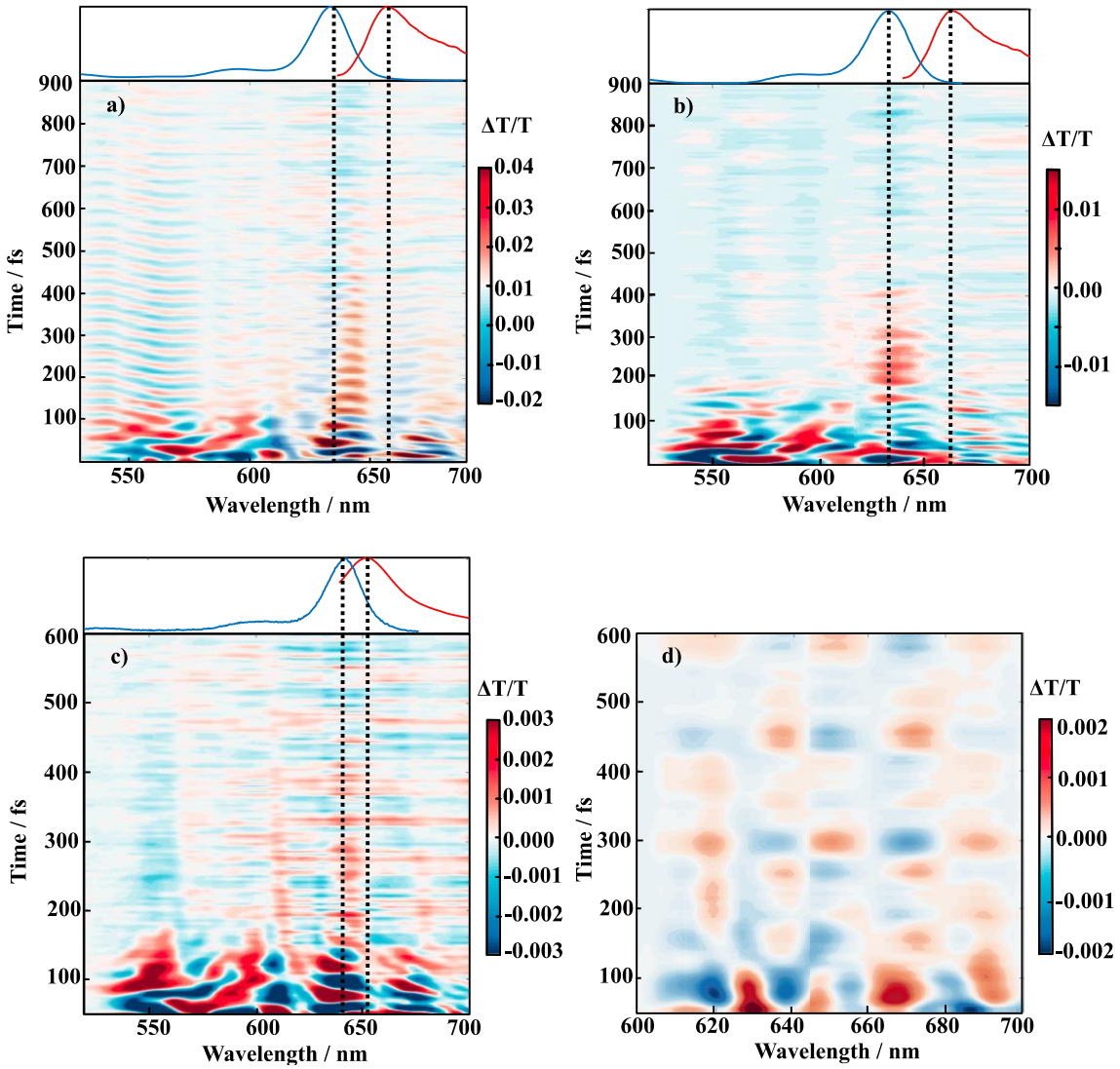

Figure 7.10 Coherent maps data for ZnCe6 (a) in methanol, (b) buffer, (c) ZnCe6-m4d2 in buffer and (d) only buffer (from 600 to 700 nm). The dashed black lines correspond to the maximum of the absorption (blue trace) and fluorescence (red trace) spectra.

The oscillations persist for ~900 fs at 560 nm and ~ 700 fs at 640 nm. The spectrum of the ZnCe6 in buffer at pH 9 shows oscillation centred at ~640 nm and weaker beating ~560 nm. The coherence centred at 640 nm persists for ~500 fs while the lower amplitude oscillation centred at ~560 nm extinguishes after ~300 fs. Very short-lived oscillations (< 200 fs) are observed in the ZnCe6-m4d2, which are more pronounced at ~ 643 nm. These

oscillations are weaker in the only buffer solution, and they persist for only 100 fs, as shown in Figure 7.10 (d) from 600 to 700 nm.

The coherent maps obtained and shown in Figure 7.10 are useful tools to investigate the ground and excited state wave packet dynamics, which can manifest in a BBTA spectrum through the presence of a node. The ability to recognise the node and its spectral position is helpful to assign whether the wave packet propagates in the ground or excited state.

An ultrafast pulse can launch wave packets in the displaced excited state. Once the wave packet motion is initiated, it starts moving back and forth in the PES and, it is detected as a function of the probe wavelength. During the motion of the wave packet, a node of zero amplitude is produced into the displaced PES because a phase-shift of the oscillation occurs under such conditions.[30,33–36] More precisely, a node should appear at the maximum of the absorption spectrum when the wave packet motion develops in the ground electronic state. Otherwise, it should coincide with the maximum of the fluorescence spectrum when the motion occurs in the excites state. However, when the Stokes shift is small as in this case, it has already been observed that the node can be slightly shifted compared to the maximum of the absorption or fluorescence spectra.[30,33,35,37]

Both the methanol and buffer solutions show a node at ~ 657 nm where the two sides of it are out of phase relative to each other denoting a minimum in the electronic potential energy surface in which the wave packets are propagating.[30,31,33,35–37] An example of out of phase oscillations is given in Figure 7.11, where panel (a) shows the vibrationally coherent spectrum of ZnCe6 in methanol with a dashed line indicating the position of the node, and panel (b) the out of phase oscillations around 657 nm.

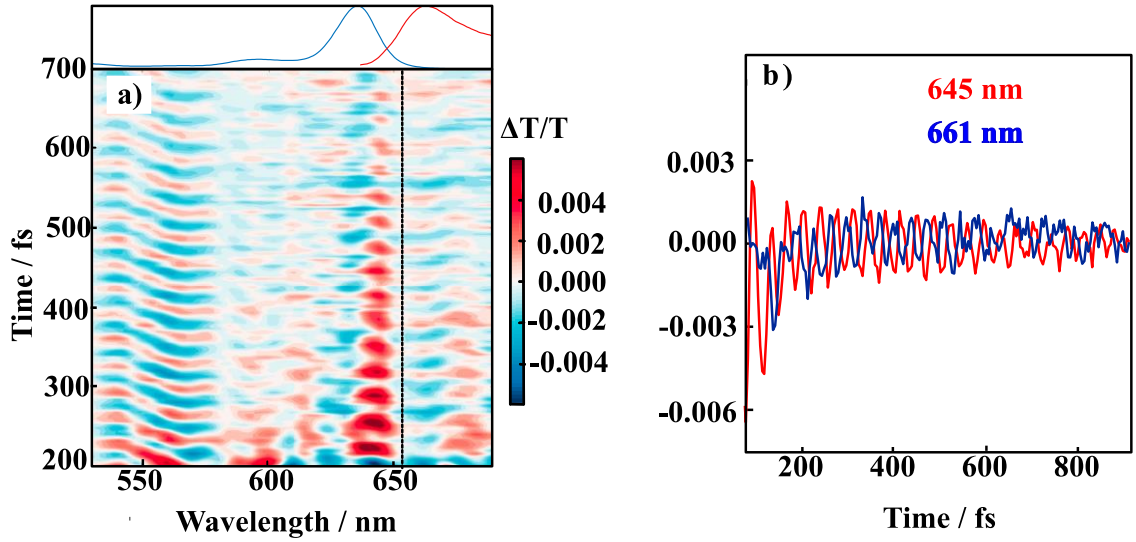

Figure 7.11 (a) ZnCe6 in methanol purely vibrational coherent spectrum from 200 to 700 fs, the dashed black line corresponds to the node at 657 nm probe wavelength. (b) Out of phase wave packet dynamics either side of the node.

Even though the node does not coincide with the maximum of the fluorescence spectrum, it may indicate vibrational wave packet generated in the excited state. In such a case, the shift of the node can be due to the destabilisation of the displaced excited state generating a blue shift of the node as already been observed.[32,35] Note that the main node centred at 657 nm might not be the only one in the coherence spectra of ZnCe6. However, the identification of other out-of-phase oscillations is still quite challenging due to the spectral congestion.

While in ZnCe6 solutions, the node at 657 nm is quite pronounced when the pigment is bound to the maquette protein; this node is not observed. The absence of the node can be due to (i) the different dynamics that characterise the pigment when it is bound to the protein environment or (ii) the possibility that the node is affected by the overlapping signals that have been observed in the BBTA. In other words, a possible generation of vibrational wave packets in both the excited state (SE) and ground state (GSB) leads to a

shift in the spectral position of the node (or to a non-evident presence of it) due to the relative amplitude of the two wave packets that interfere to generate it.[30]

7.3.4 Fourier Transform Maps

The Fourier Transform (FT) of the coherence spectra yields the frequencies associated with the wave packets. In the three samples studied, the FTs from 100 fs to 1.5 ps of the pure vibrational coherence spectra (shown in Figure 7.10) lead to maps of FT amplitudes displaying vibrational frequencies up to ~ 1400 cm^{-1} (Figure 7.12).

The FT spectrum of ZnCe6 in methanol (Figure 7.12 (a)) shows the main low-frequency amplitude with the maximum at ~ 400 cm^{-1} spanning the probe frequency from ~ 620 to ~ 700 nm and a higher FT amplitude positioned at ~1050 cm^{-1} with two relative maxima at ~ 550 and ~ 640 nm. Furthermore, the spectrum shows FT amplitudes at lower frequencies (< 400 cm^{-1}), which can explain the complexity of the vibrational wave packets observed in the time domain.

The FT amplitude map of ZnCe6 in buffer (Figure 7.12 (b)) displays a congested spectrum, especially up to 1000 cm^{-1} while the ZnCe6-m4d2 spectrum has the main FT frequency at 440 cm^{-1} for each probe wavelength studied, see Figure 7.12 (c). Two additional weaker peaks can be well distinguished, too, one at 640 and the second one 680 nm probe wavelengths. These peaks are centred at 330 and 500 cm^{-1} and belong to the ESA and GSB + SE regions observed in the BBTA spectrum.

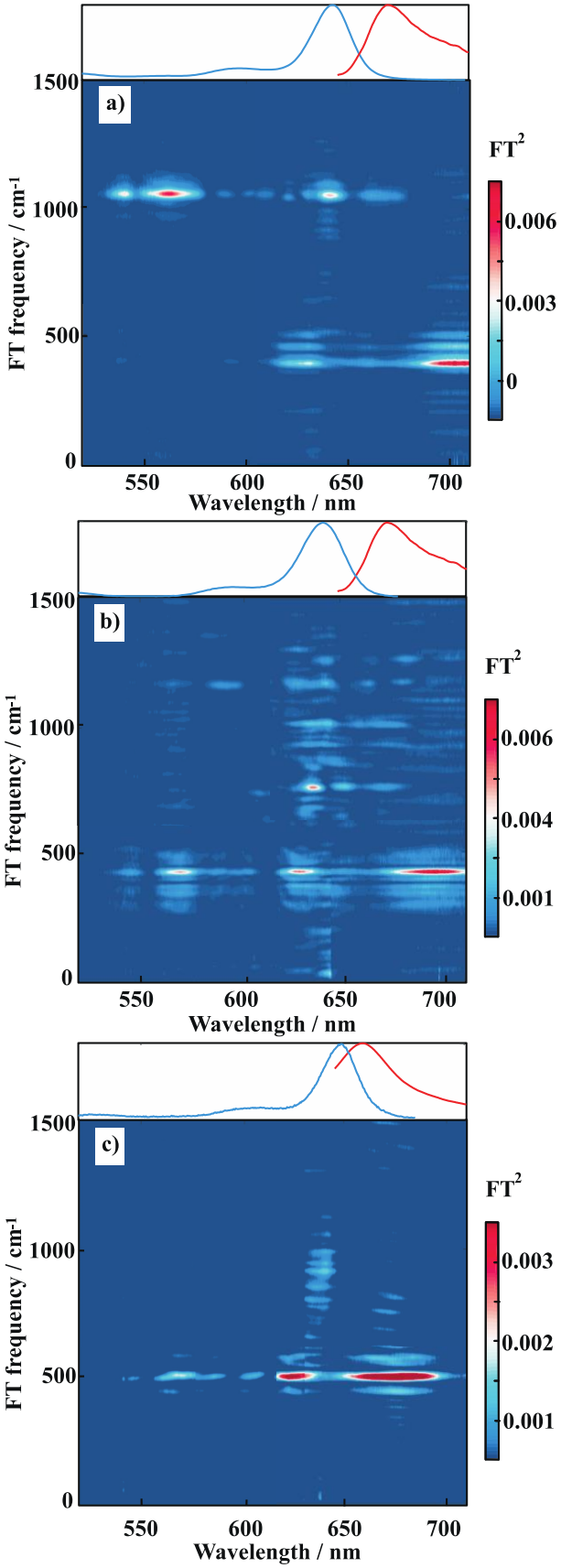

Figure 7.12 FT amplitudes spectra of ZnCe6 (a) in methanol, (b) buffer and (c) ZnCe6-m4d2 in buffer. Each spectrum is shown with the relative absorption (blue) and fluorescence (red) spectra.

7.3.5 Fourier Transform Amplitudes

For a better visualisation and understanding of the FT amplitudes, a summary is shown in Figure 7.13. To obtain the FT amplitudes shown in this figure, the BBTA spectrum was divided into three regions: ESA (535-600 nm), GSB+SE (600-660 nm), and 680 nm. Subsequently, the average FT amplitudes for each spectral region were calculated and shown in Figure 7.13 in panel (a), (c), and (e), in green, red and blue, as indicated in the graphs. The pump-probe spectra at t = 500 fs are also given for each solution studied (Figure 7.13 (b), (d), and (f)), and the three regions from which the FT amplitudes have been retrieved, highlighted in green, red and blue.

The FT spectrum of ZnCe6 in methanol (Figure 7.13 (a)), both for the ESA and GSB + SE, shows the main peak centred at 1054 cm^{-1} that appears to be less intense in the 680 nm FT amplitude map. Furthermore, the FT amplitudes obtained for the GSB + SE region and at 680 nm show a second intense peak at 385 and weaker amplitudes at ~460 and ~490 cm^{-1}.

Panel (c) corresponds to the FT amplitudes of the ZnCe6 in buffer showing the most intense feature at 423 cm^{-1} with satellite peaks, both in the ESA region and at 680 nm, while the GSB + SE region shows relatively intense peaks at 754, 1000, and 1156 cm^{-1} with weaker peaks between 780, 983, and 1156 cm^{-1}. The latter sets of peaks also coincide with very weak amplitudes observed in the ESA.

On the contrary, the ZnCe6-m4d2 complex does not show as many FT amplitudes as the only ZnCe6, with a predominant feature at 505 cm^{-1} and weak FT amplitudes between 1360 and 1450 cm^{-1} in the region corresponding to the ESA.

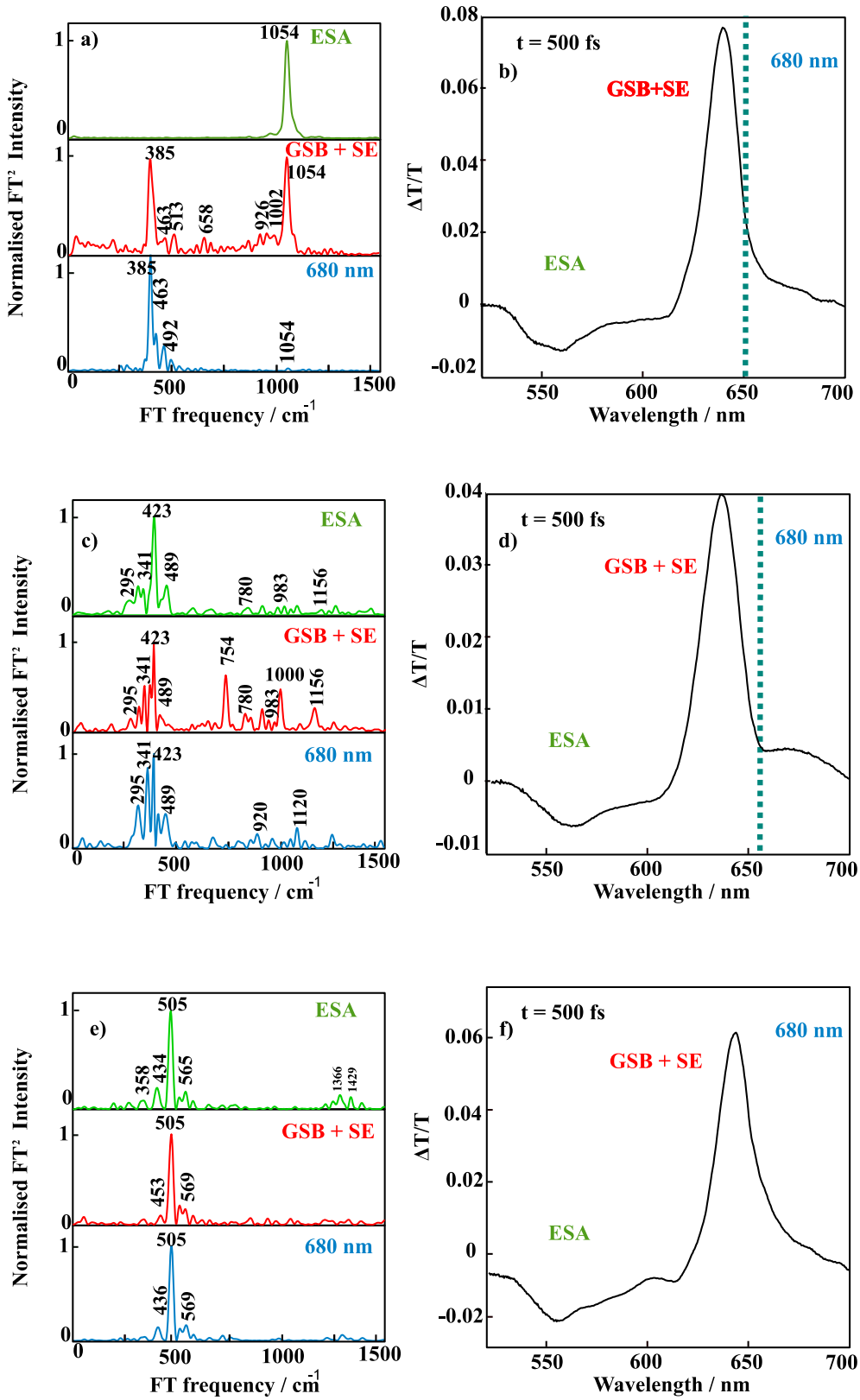

Figure 7.13 FT amplitudes and pump-probe spectra at the time delay t = 500 fs of ((a) and (b)) ZnCe6 in methanol, ((c) and (d)) buffer and ((e) and (f)) ZnCe6-m4d2. The FT amplitudes belong to the ESA (green), GSB + SE (red) and 680 nm (blue).

It is always very challenging to isolate the contribution of ground and excited state wave packets in congested spectra,[30,38] therefore, to assign the vibrational mode to the ground or excited state, I compared the FT amplitudes obtained integrating over the ESA (that conveys information only on the ground state) and the FT amplitudes obtained integrating over the GSB + SE where the signal derives from both the ground and the excited state. Figure 7.14 shows the two FT amplitudes obtained integrating over the ESA region (in green) and GSB + SE (in red) and the FT normalised spectra of the solvents for the entire probe frequencies (in blue). The FT maps of the methanol solution (Figure 7.14 (a), (d), and (g)) show the main peak at 1054 cm^{-1} that belongs to both the ESA and GSB + SE traces, therefore, it is associated with a ground state vibrational wave packet. Note that the observation of this mode in methanol and not in water might be due to a different interaction between the solute and the solvents, *i.e.*, a different coupling or solvation of this specific vibrational mode. On the contrary, the vibrational frequencies centred at 385 and 513 cm^{-1} are not observed for the only ground state signal or the only solvent spectrum. Thus, it can be supposed that they originate in the excited state.

The same procedure has been applied to ZnCe6 in buffer (Figure 7.14 (b), (e), and (h)) where the ground state vibrations observed at 780, 983, 1156 cm^{-1} have been previously assigned to ground state vibrational modes through Raman spectroscopy.[39] To assign the peaks between 0 and 600 cm^{-1} where Raman spectroscopy cannot provide information, I rely on the comparison between the traces obtained from the integration over the ESA and GSB + SE regions and the only solvent trace to eliminate its contribution. The modes between 260 and 700 cm^{-1} are common to the ESA, GSB + SE, and buffer traces; therefore, they either belong to the ground state or solvent while the peak at 754 cm^{-1} is unique to the GSB+SE trace and it can be associated with an excited state vibration. The same analysis

was done to identify the peak at 1000 cm^{-1} observed only for the red trace and associated with excited state vibrational mode.

Ultimately, the comparison between the FT amplitudes obtained for the ESA, GSB + SE and solvent, is shown for ZnCe6-m4d2, where all the peaks appear to belong either to the ground state or buffer. In this regard, note that the FT amplitudes observed for ZnCe6-m4d2 coincide with the main peaks obtained in the solvent spectrum which has been previously assigned to librational active modes of water.[40] Therefore, a neat separation between the ZnCe6-m4d2 and the buffer contribution to the FT frequency region that spans from 300 to 600 cm^{-1} remains very challenging.

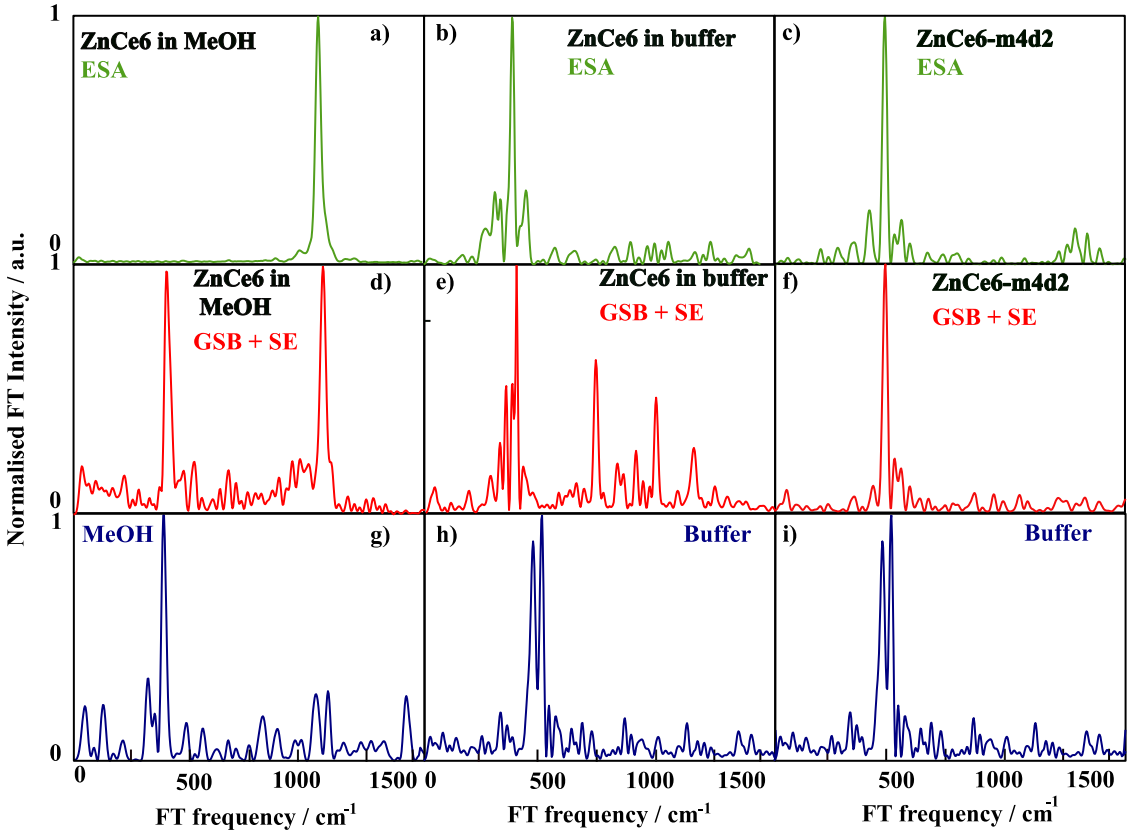

Figure 7.14 FT amplitudes obtained when integrating the ESA (green) and GSB + SE (red) region for ((a),(d)) ZnCe6 in methanol, ((b),(e)) ZnCe6 in buffer and ((c),(f)) ZnCe6-m4d2. Integrated FT amplitudes of (g) pure methanol and (b) buffer solution at pH=9.

7.3.6 Wave Packet Dephasing Analysis

To establish the dephasing rate of vibrational coherences, the data were fitted to a damped cosine function, and the analysis was focused on the highest amplitude oscillations in the purely coherent spectra at 640 nm. The oscillatory data used for the following analysis are unfiltered data population subtracted. At 640 nm one main FT frequency that varies from 450 to 500 cm^{-1} between the three samples is observed, therefore the data were fitted in the time domain to a damped cosine equation, like the one given below:[38]

$$I(t) = A \cos(\omega t + \phi)\, e^{-\gamma t} \qquad (7.1)$$

where A is the initial amplitude, γ is the decay constant or damping factor, ϕ is the phase, ω is the angular frequency associated with the vibration, and t is the pump-probe time delay. The quality of the fitting was monitored with the residual, and the ω was fixed during the analysis according to the observed main amplitude in the FT spectrum. The errors associated with each damping lifetimes were calculated as the standard deviation between the damping factor obtained at the central frequency of 640 nm and the damping factors calculated in ± 5 nm range.

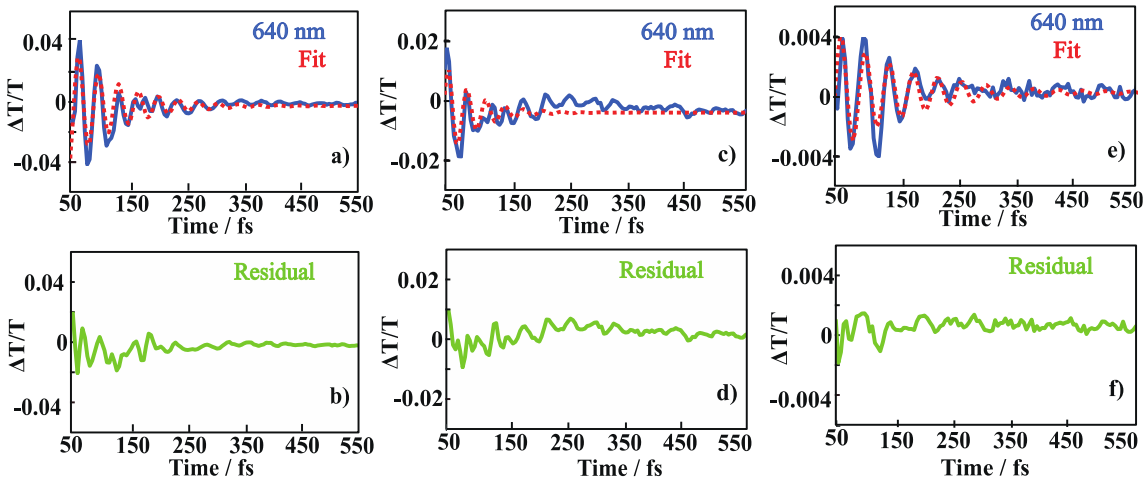

Figure 7.15 Oscillations (blue) and best fits (dashed-red) at 640 nm probe wavelength obtained for ZnCe6 (a) in methanol, (c) buffer, and (e) ZnCe6-m4d2. Panels (b), (d), and (f) show the residuals (green) of the fits.

Figure 7.15 shows the fits to vibrational wave packet and associated residual for 640 nm for ZnCe6 ((a), (b)) in methanol, ((c), (d)) in buffer and ((e), (f)) ZnCe6-m4d2. The values of the damping lifetimes obtained from the best-fittings as $1/\gamma$ (fs) are shown in Table 7.3.

Table 7.3 Damping lifetimes for the oscillations at 640 nm probe wavelength.

	Damping lifetime ($1/\gamma$) / fs
ZnCe6 in methanol	40 ± 10
ZnCe6 in buffer	30 ± 10
ZnCe6-m4d2	100 ± 20

The analysis carried out for ZnCe6 and ZnCe6-m4d2 in solution should be taken as an approximation to obtain a trend of values and not as an absolute determination of the dephasing times.[41] This fact occurs because the method applied in the fitting assumes that the data can be treated as a sum of damped cosine equations, which is not always precise if a single frequency comprises multiple relaxation times.[41,42] Moreover, the number of exponentially damped terms used in the fitting should be equal to the number of vibrational frequencies observed, quantum-mechanically the wave packets generated and detected are a superposition of vibrational states constituted by multiple vibrational modes.[30] In this specific case, where multiple vibrational modes, belonging to both the ground and excited state, are detected the isolation of the coherent portion of the data (particularly in ZnCe6 in buffer and ZnCe6-m4d2) is not trivial, and, the precise fitting routine would have been a difficult and time-consuming procedure.[33,42] Therefore, Table 7.3 shows that ZnCe6-m4d2 is characterised by a longer damping lifetime compared to ZnCe6 in methanol and buffer showing a different behaviour of the ZnCe6 when it is confined inside the protein compared to when a homogenous bath surrounds it.

The damping lifetimes indicate a weaker interaction between the ZnCe6 and the solvent, while in the ZnCe6-m4d2, this interaction is stronger. This observation is in agreement with the Stokes shift observed in the linear static spectra where the ZnCe6-m4d2 sample has a much smaller Stokes shift compared to the only metallochlorin in solution suggesting that, after excitation, the response of the two solvents, methanol, and water, to the electronic perturbation of the solute dipole moment is faster than the protein response. Thus, the protein is a less interacting bath compared to the other two solvents.

7.3.7 DFT Calculations and Vibrational Modes Assignment

To guide the assignment of the observed wave packets, DFT calculations were performed with Gaussian 09.[43] The S_0 and S_1 ZnCe6, polarizable continuum model (PCM) geometry optimisation, and harmonic frequencies were calculated with B3LYP functional and 6-31 G* basis set. The calculated spectra for S_0 and S_1 up to 1500 cm^{-1} are shown in Figure 7.16 where the frequencies were multiplied by 0.99 to account for the anharmonicity.[44]

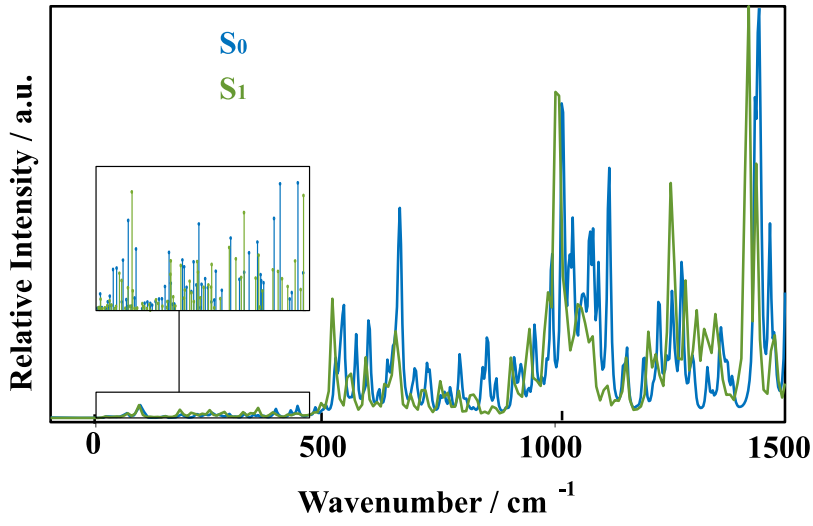

Figure 7.16 Calculated harmonic frequencies of ground (blue) and excited state (green) with B3LYP/6-31G and $\Delta\nu = 4$ cm^{-1}, the insert is a zoom-in of the region between 0 and 550 cm^{-1}.

From the S_0 and S_1 harmonic vibrations calculated, it can be observed that the ring breathing modes generate the experimental peaks obtained at low-frequencies, mainly bending and rocking of the chlorin substituents, for example, the ground state mode at 423 cm^{-1} is attributed to the bending of the -CH_2COOH, while the peak centred at 1054 cm^{-1}, very pronounced for ZnCe6 in methanol, has previously been observed in the FTIR spectrum and assigned to the (-CH_2CH_3COOH) bending.[44]

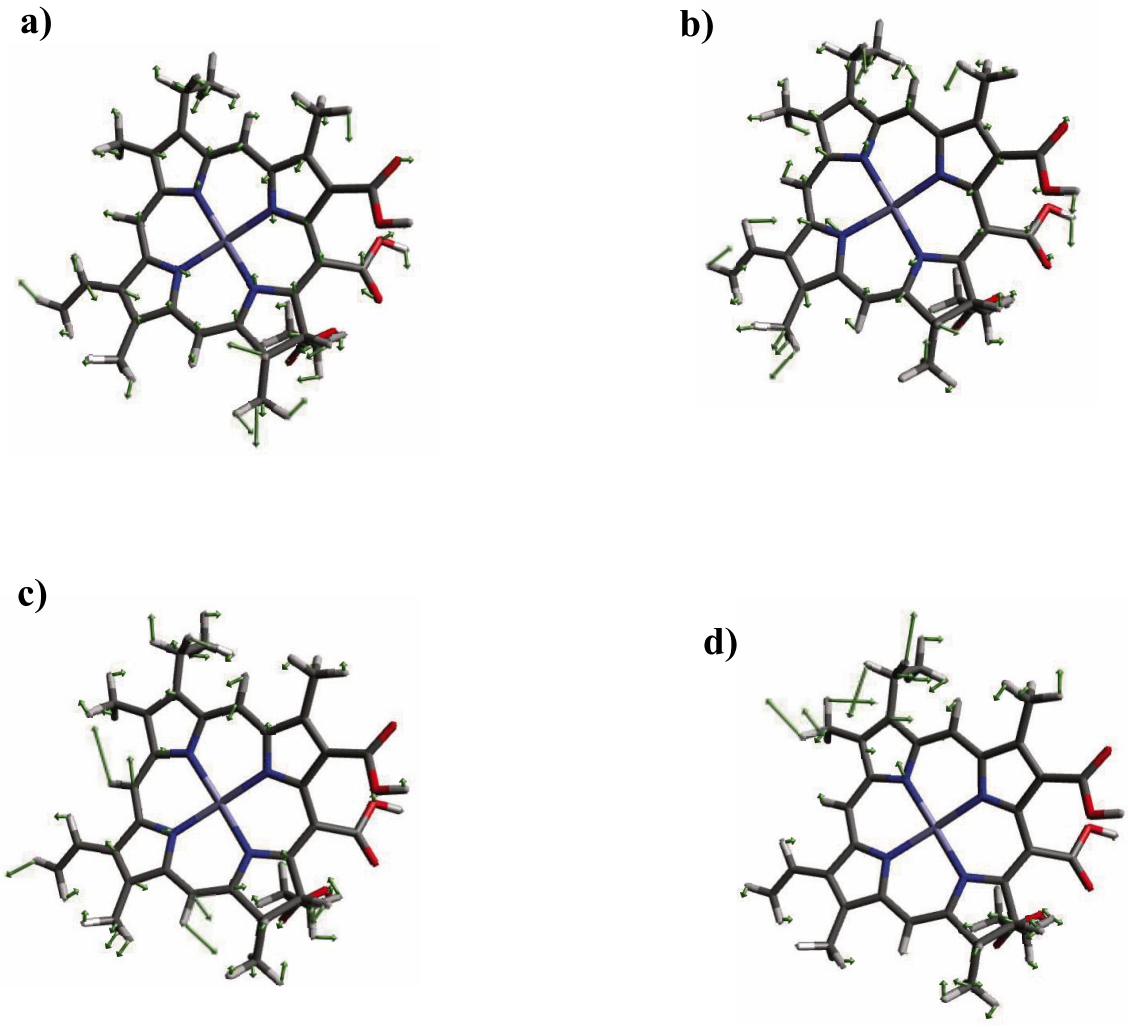

Figure 7.17 Nuclear displacement associated with S_1 normal vibrational modes and associated frequencies (a) 385, (b) 513, (c) 754, (d) 1000 cm^{-1}.

The FT amplitudes observed for ZnCe6 in methanol and buffer and assigned to excited state vibrational wave packets at 385, 513, 754, and 1000 cm^{-1} were compared to the S_1 calculated harmonic frequencies. The assignment is shown in Figure 7.17, where each figure represents the ZnCe6 S_1 optimised geometry, and the arrows display the position and intensity of the vibrations. Table 7.4 summarises the frequencies of the excited state FT amplitudes, the calculated harmonic frequencies multiplied by 0.99 for the S_1 state, and at which panel in Figure 7.17 each frequency corresponds to.

Table 7.4 Calculated harmonic frequencies for S_1 state and comparison with FT amplitudes assigned to the excited state.

Observed excited state FT amplitudes / cm^{-1}	Calculated harmonic frequencies x 0.99 / cm^{-1}	Corresponding normal mode in Figure 7.17
385	386	a)
513	515	b)
754	754	c)
1000	1000	d)

7.4 Conclusions

In this work, the BBTA spectra of ZnCe6 and ZnCe6-m4d2 reveal congested spectra characterised by vibrational wave packets. From the analysis of the wave packets, an insight into the ground and excited state dynamics can be obtained and, the purely coherent vibrational spectra for both ZnCe6 and ZnCe6-m4d2 can be reduced to few FC active modes. DFT calculations ran for ground, and excited state of ZnCe6 can be used to assign the observed normal modes. Thus, the congested BBTA spectrum can be simplified to a few active modes assigned through DFT. A second advantage encountered while using this

technique arises from the fact that the BBTA experiment can provide complementary information about the ground state active mode at low-frequencies (< 600 cm^{-1}), which are difficult to obtain from Raman spectroscopy.[31,34]

The main observation arising from this work comes from the different abilities that water and methanol have in stabilising the zinc chlorin e6 electronic excite state compared to m4d2. The stabilisation carried out by the two conventional solvents is more efficient compared to m4d2, meaning that the protein's ability to "solvate" the photoexcited ZnCe6 is less pronounced than the two pure solvents. It has been observed that the stabilisation of the ZnCe6 excited state induces a red shift of the fluorescence spectra, which is not observed in the data related to ZnCe6-m4d2 returning in a more significant Stokes shift for ZnCe6 in solution and smaller λ for the ZnCe6-m4d2 sample. The hypothesis of less efficient protein solvation is also supported by the damping lifetimes calculated that show a fast dephasing for zinc chlorin e6 in solution and a slower lifetime for ZnCe6-m4d2. This observation suggests that the protein acts as a less-strongly interacting bath.

Furthermore, it has been observed that the FT amplitude of ZnCe6 is strongly solvent dependent. For example, the active mode at 1054 cm^{-1}, which is isolated for ZnCe6 in methanol, is not observed when the chlorin is in a buffer solution. A second example that can be provided refers to the most intense low-frequency active mode at 385 that shifts to 423 cm^{-1} when going from methanol to water. A third example resides in the excited state active modes observed for ZnCe6 in the two conventional solvents that have also been assigned through DFT calculations. The differences observed between the FC active modes in methanol and buffer are likely due to the solvent ability to interact with each mode of the zinc chlorin e6.

Further insight into the solvation dynamics of ZnCe6 and ZnCe6 bonded to a maquette protein could be given by two-dimensional electronic spectroscopy (2DES).[31,45–50] The multidimensionality of the technique and the study of the frequency-frequency correlation function might convey information about the solvent reorganisation and, only through 2DES analysis, the ground state coherence and the excited state contribution could be isolated and individually analysed.[31,51] Finally, these observations may be used to model natural and artificial photosynthetic systems.[4]

References

1. Pandit, A., van Stokkum, I. H. M., van Amerongen, H. & Croce, R. Introduction: light-harvesting for photosynthesis. Photosynth Res **135**, 1–2 (2017).

2. Rivera, E., Montemayor, D., Masia, M. & Coker, D. F. Influence of site-dependent pigment-protein interactions on excitation energy transfer in photosynthetic light-harvestng. J. Phys. Chem. **117**, 5510-5521 (2013).

3. Voet, J. G. & Voet, D. Biochemistry. New ork, John Wiley & Son. (1995).

4. Fleming, G. R., Schlau-Cohen, G. S., Amarnath, K. & Zaks, J. Design principles of photosynthetic light-harvesting. Faraday Discuss **155**, 27–41 (2012).

5. Gouterman, M. Spectra of porphyrins. J. Mol. Spectrosc. **6**, 138–163 (1961).

6. Edwards, L., Dolphin, D., Gouterman, M. & Adler, A. Porphyrins XVII. Vapor absorption spectra and redox reactions: Tetraphenylporphins and porphin. J. Mol. Spectrosc. **38**, 16–32 (1971).

7. Huang, W.Y., van Riper, E. & Johnson, L. W. Single site electronic spectroscopy of free base chlorin in an n-octane crystal at 5 K. Spectrochim. Acta A Part Mol. Biomol. Spectrosc. **52**, 761–769 (1996).

8. Wójcik, J., Ratuszna, A., Peszke, J. & Wrzalik, R. Theoretical reproduction of the Q-band absorption spectrum of free-base chlorin. J. Chem. Phys. **142**, 034302 (2015).

9. Gurinovich, G., Sevchenko, A. & Solov'ev, K. N. The spectroscopy of porphyrins. Phys. Uspekhi **79**, 173-234 (1963).

10. Schalk, O., Brands, H., Balaban, T. S. & Unterreiner, A. N. Near-Infrared Excitation of the Q Band in Free Base and Zinc Tetratolyl-porphyrins. J. Phys. Chem. A **112**, 1719–1729 (2008).

11. Senge, O. M., Ryan, A. A., Letchford, K. A., MacGowan, S. A. & Mielke, T. Chlorophylls, Symmetry, Chirality, and Photosynthesis. Symmetry **6**, 781–843 (2014).

12. Röger, C., Miloslavina, Y., Brunner, D., Holzwarth, A. R. & Würthner, F. Self-Assembled Zinc Chlorin Rod Antennae Powered by Peripheral Light-Harvesting Chromophores. J. Am. Chem. Soc. **130**, 5929–5939 (2008).

13. Jesenko, S. & Znidaric, M. Optimal number of pigments in photosynthetic complexes. New J. Phys. **14**, 093017 (2012).

14. Scholes, G. D., Fleming, G. R., Olaya-Castro, A. & van Grondelle, R. Lessons from nature about solar light-harvestng. Nat. Chem. **3**, 763–774 (2011).

15. Murata, N. Research in Photosynthesis: Proceedings of the IXth International Congress on Photosynthesis (Volume III). Kluwer Academic Publishers (1992).

16. Anderson, R. J., Armstong, C. T., Kodali, G., Lichtestein, B. R., Watkins, D. W., Mancini, J. A., Boyle, A. L., Farid, T. A., Crump, M. P., Moser, C. C. & Dutton, P. L. Constructing a man-made c-type cytochrome maquette in vivo: electron transfer, oxygen

transport and conversion to a photoactive light-harvesting maquette. Chem. Sci. **5**, 507–514 (2014).

17. Farid, T. A., Kodali, G., Solomon, L. A., Lichtestein, B. R., Sheehan, M. M., Fry, B. A., Bialas, C., Ennist, N. M., Siedlecki, J. A., Zhao, Z., Stetz, M. A., Valentine, K. G., Anderson, J. L. R., Wand, A. J., Discher, B. M., Moser, C. C. & Dutton, L., Elementary tetrahelical protein design for diverse oxidoreductase functions. Nat. Chem. Biol. **9**, 826–833 (2013).

18. Armstrong, C. T., Watkins, D. W. & Anderson, R. J. Constructing manmade enzymes for oxygen activation. Dalton Trans. **42**, 3136–50 (2003).

19. Razeghifard, R. M. & Wydrzynski, T. Binding of Zn-chlorin to a synthetic four-helix bundle peptide through histidine ligation. Biochem. **42**, 1024–1030 (2003).

20. Trebino, R. Code for retrieving a pulse intensity and phase from its FROG trace. frog.gatech.edu.(2015)

21. Trebino, R. Frequency-Resolved Optical Gating: The Measurement of Ultrashort Laser Pulses. Springer Science and Business Media (2000).

22. Mertz, E. L., Tikhomirov, V. A. & Krishtalik, L. I. Stokes Shift as a Tool for Probing the Solvent Reorganization Energy. J. Phys. Chem. A **101**, 3433–3442 (1997).

23. Mukamel, S., Principle of Nonlinear Optics and Spectroscopy, Oxford Univ. Press (1995).

24. Reynolds, L., Gardecki, J., Frankland, S., Horng, M. & Maroncelli, M. Dipole Solvation in Nondipolar Solvents: Experimental Studies of Reorganization Energies and Solvation Dynamics. J. Phys. Chem. **100**, 10337–10354 (1996).

25. Jordanides, X. J., Lang, M. J., Song, X. & Fleming, G. R. Solvation Dynamics in Protein Environments Studied by Photon Echo Spectroscopy. J. Phys. Chem. B **103**, 7995–8005 (1999).

26. Jin, H., Baker, G. A., Arzhantsev, S., Dong, J. & Maroncelli, M. Solvation and rotational dynamics of coumarin 153 in ionic liquids: comparisons to conventional solvents. The J. Phys. Chem. B **111**, 7291–7302 (2007).

27. Szalay, L., Tombácz, E. & Singhal, G. Effect of solvent on the absorption spectra and Stokes' shift of absorption and fluorescence of chlorophylls. Acta Phys. Acad. Hung. **35**, 29–36 (1974).

28. Croce, R., Zucchelli, G., Garlaschi, F. M. & Jennings, R. C. A Thermal Broadening Study of the Antenna Chlorophylls in PSI-200, LHCI, and PSI Core. *Biochemistry* **37**, 17355–17360 (1998).

29. Baskin, S. J., Yu, H.-Z. & Zewail, A. H. Ultrafast Dynamics of Porphyrins in the Condensed Phase: I. Free Base Tetraphenylporphyrin. J. Phys. Chem. A **106**, 9837–9844 (2002).

30. Rafiq, S. & Scholes, G. D. Slow Intramolecular Vibrational Relaxation Leads to Long-Lived Excited state Wave packets. J. Phys. Chem. A **120**, 6792–6799 (2016).

31. Dean, J. C. Rafiq, S., Oblinsky, D. G., Cassette, E., Jumper, C. C, & Scholes, G. D., Broadband Transient Absorption and Two-Dimensional Electronic Spectroscopy of Methylene Blue. The J. Phys. Chem. A **119**, 9098–9108 (2015).

32. Rafiq, S., Dean, J. C. & Scholes, G. D. Observing Vibrational Wave packets during an Ultrafast Electron Transfer Reaction. J. Phys. Chem. A **119**, 11837–46 (2015).

33. McClure, S. D., Turner, D. B., Arpin, P. C., Mirkovic, T. & Scholes, G. D. Coherent Oscillations in the PC577 Cryptophyte Antenna Occur in the Excited Electronic State. J. Phys. Chem. B **118**, 1296–1308 (2014).

34. Vos, M. H., Rappaport, F., Lambry, J.-C., Breton, J. & Martin, J.-L. Visualization of coherent nuclear motion in a membrane protein by femtosecond spectroscopy. Nature **363**, 320–325 (1993).

35. Cina, J. A., Kovac, P. A., Jumper, C. C., Dean, J. C. & Scholes, G. D. Ultrafast transient absorption revisited: Phase-flips, spectral fingers, and other dynamical features. J. Chem. Phys. **144**, 175102 (2016).

36. Yang, T. S., Chang, M. S., Cheng, R., Hayashi, M. & Lin, S. H. Femtosecond pump-probe study of molecular vibronic structures and dynamics of a cyanine dye in solution. J. Chem. Phys. **110**, 12070, (1999).

37. 36. Arpin, P. C., Turner, D. B., McClure, S. D., Jumper, C. C., Mirkovic, T., Challa, J. R., Lee, J., Teng, C. Y., Green, B. R., Wilk, K. E., Curmi, P. M. G., Hoef_emden, K.,

McCamant, D. W. & Scholes, G. D.,. Spectroscopic Studies of Cryptophyte Light Harvesting Proteins: Vibrations and Coherent Oscillations. J. Phys. Chem. B **119**, 10025–10034 (2015).

38. Giancoli, D. C. Physics for scientists and engineers: with modern physics (4th edition). *Pearson* (2000).

39. van Stokkum, I. H. Jumper, C. C., Snellenburg, J. J., Scholes, G. D., van Grondelle R. & Maly, P. Estimation of damped oscillation associated spectra from ultrafast transient absorption spectra. J. Chem. Phys. **145**, 174201 (2016).

40. Carey, D. M. & Korenowski, G. M. Measurement of the Raman spectrum of liquid water. *J. Chem. Phys.* **108**, 2669–2675 (1998).

41. Bardeen, C., Wang, Q. & Shank, C. Femtosecond Chirped Pulse Excitation of Vibrational Wave Packets in LD690 and Bacteriorhodopsin. J. Phys. Chem. A **102**, 2759–2766 (1998).

42. Wise, F., Rosker, M., Millhauser, G. & Tang, C. Application of linear prediction least-squares fitting to time-resolved optical spectroscopy. IEEE J. Quantum. Elect. **23**, 1116–1121 (1987).

43. M. J. Frisch, G. W. Trucks, H. B. Schlegel, G. E. Scuseria, M. A. Robb, J. R. Cheeseman, G. Scalmani, V. Barone, G. A. Petersson, H. Nakatsuji, X. Li, M. Caricato, A. Marenich, J. Bloino, B. G. Janesko, R. Gomperts, B. Mennucci, H. P. Hratchian, J. V. Ortiz, A. F. Izmaylov, J. L. Sonnenberg, D. Williams-Young, F. Ding, F. Lipparini, F.

Egidi, J. Goings, B. Peng, A. Petrone, T. Henderson, D. Ranasinghe, V. G. Zakrzewski, J. Gao, N. Rega, G. Zheng, W. Liang, M. Hada, M. Ehara, K. Toyota, R. Fukuda, J. Hasegawa, M. Ishida, T. Nakajima, Y. Honda, O. Kitao, H. Nakai, T. Vreven, K. Throssell, J. A. Montgomery, Jr., J. E. Peralta, F. Ogliaro, M. Bearpark, J. J. Heyd, E. Brothers, K. N. Kudin, V. N. Staroverov, T. Keith, R. Kobayashi, J. Normand, K. Raghavachari, A. Rendell, J. C. Burant, S. S. Iyengar, J. Tomasi, M. Cossi, J. M. Millam, M. Klene, C. Adamo, R. Cammi, J. W. Ochterski, R. L. Martin, K. Morokuma, O. Farkas, J. B. Foresman, and D. J. Fox, Gaussian, Inc., Wallingford CT, (2016).

44. Gladkova, O., Parkhats, M., Gorbachova, A. & Terekhov, S. FTIR spectra and normal-mode analysis of chlorin e(6) and its degradation-induced impurities. Spectroch. Acta Part A. **76**, 388–94 (2010).

45. Jonas, D. M. Two-dimensional femtosecond spectroscopy. Ann. Rev. Phys. Chem. **54**, 425–463 (2003).

46. Brixner, T., Stenger, J., Vaswanu, H. M., Cho, M., Blankenship, R. E. & Fleming, G. R., Two-dimensional spectroscopy of electronic couplings in photosynthesis. Nature **434**, 625–628 (2005).

47. Turner, D. B., Dinshaw, R., Lee, K. K., Belsley, M., S., Wilk, K. E., Curmi, P. m: G. & Scholes, G. D. Quantitative investigations of quantum coherence for a light-harvesting protein at conditions simulating photosynthesis. Phys. Chem. Chem. Phys. **14**, 4857–4874 (2012).

48. Ostroumov, E. E., Mulvaney, R. M., Cogdell, R. J. & Scholes, G. D. Broadband 2D Electronic Spectroscopy Reveals a Carotenoid Dark State in Purple Bacteria. Science **340**, 52–56 (2013).

49. Fuller, F. D., Pan, J., Gelzinis, A., Butkus, V., Senlik, S. S., Wilcox, D. E., Yocum, C. F., Valkunas,L., Abramavicius, D. & Ogilvie, J. P. Vibronic coherence in oxygenic photosynthesis. Nat. Chem. **6**, 706–711 (2014).

50. Butkus, V. Gelzinis, A., Augulis, R., Gall, A., Buchel, C., Robert, B., Zigmantas, D., Valkunas, L. & Abramavicius, D. Coherence and population dynamics of chlorophyll excitations in FCP complex: Two-dimensional spectroscopy study. J. Chem. Phys. **142**, 212414 (2015).

51. Kwak, K., Park, S., Finkelstein, I. J. & Fayer. M. D. Frequency-frequency correlation functions and apodization in two-dimensional infrared vibrational echo spectroscopy: A new approach. J. Chem. Phys. **127**, 124503 (2007).

Chapter 8

Conclusions and Future Work

8.1 Conclusions and Future Work

In this thesis, I have explored a range of photophysical phenomena in light-absorbing molecules using ultrafast time-resolved techniques. The ultrafast dynamics of three chemical systems have been studied: a dinucleotide of guanine and thymine, Oxazine 4 in different solvents, and zinc chlorin e6 in free solution and bound in a protein maquette. Further, I constructed and characterised a phase stabilised spectrometer characterised by boxcar geometry that I used to collect broadband transient absorption and two-dimensional electronic spectroscopy data.

In Chapter 4, a model for a part of DNA composed of guanine and thymine moieties was studied with transient absorption and time-resolved infrared spectroscopies. From analysis of the TA data, an additional lifetime component of ~ 10 ps was observed for the dinucleotide that was absent in the constituent monomers. TRIR measurements elucidated the origin of the additional ps lifetime, corresponding to charge transfer between guanine and thymine to form $d(G^{+}pT^{-})$, via a vibrational signature of the guanine cation. Moreover, analysis of d(GpT) TRIR spectra at different excitation wavelengths revealed delocalised FC states across guanine and thymine moieties. Theoretical calculations also predict that the vertical excited states are characterised by a mixture of delocalised, localised, and charge transfer states which strongly depend on the specific geometry of the dinucleotide, and critically whether it was open or π-stacked. Therefore, the study of this nucleotide comprised from naturally abundant nucleobases were characterised by short-lived charge transfer products ($dG^{+}pT^{-}$) which decay back to ground state neutral molecules in few ps.

This process might have a crucial role in guaranteeing the photostability of DNA upon UV irradiation.

In Chapter 5, I reported the successful implementation and characterisation of a phase-stable two-dimensional electronic spectrometer that was used to carry out to separate experiments: broadband transient absorption spectroscopy and 2DES. The apparatus was used to investigate Oxazine 4 in different solvents, as shown in Chapter 6. Through the population removal from the BBTA spectra, the purely vibrational coherent spectra were obtained. The FT of these spectra reveal FC active modes in each sample studied. The BBTA data display a strong vibrationally active frequency at 586 cm^{-1} in both conventional solvents and 1-ethyl-3-methylimidazolium thiocyanate. The vibrational active mode was previously assigned through DFT calculations and Raman spectroscopy to a ground state ring breathing mode. The purely coherent maps reveal nodes in each solution studied which offer an insight into the dynamics of the ground and excited state. The fitting of the oscillation in the purely vibrational coherent maps corroborated the hypothesis of excited state vibrational wave packets detection, probably observed at ~ 400 cm^{-1}. Moreover, two-dimensional electronic spectroscopy was used to investigate the strength of solute-solvent interactions for Oxazine 4 in methanol, DMSO and 1-ethyl-3-methylimidazolium thiocyanate. Analysis of the 2DES central line slope returned a very fast solvent reorganization in the case of the less viscous solvent while a longer-lived frequency-frequency correlation for DMSO and 1-ethyl-3-methylimidazolium thiocyanate.

In Chapter 7, broadband transient absorption spectroscopy was used to investigate the excited state dynamics of zinc chlorin e6 in methanol, buffered water, and bound to a protein maquette. FC active modes were obtained for both ground and excited states, which

were assigned using DFT calculations and/or prior Raman spectroscopy studies. The comparison between the ZnCe6 and ZnCe6-m4d2 analysis revealed two key aspects. The first finding was related to the protein ability to "solvate" the chlorin molecule, which via analysis of the data I have observed to be less effective than methanol and buffered water. The second aspect refers to the FC active vibrational modes which were observed to differ for the solutions of ZnCe6 in methanol and buffer. For example, a predominant FT frequency at 1054 cm^{-1} belonging to the ZnCe6 in methanol it was not found when the same compound was in water buffered solution. This evidence shows a distinct interaction between the solute and the two solvent and a change in the chlorin electronic structure going from methanol to water.

For a better assignment of the FC active vibrational frequencies observed in both Oxazine 4 and ZnCe6 samples, Franck-Condon calculations beyond the harmonic approximation would be very useful. However, due to the large displacement between the ground and first excited state in the two molecules investigated, these calculations cannot be carried out with conventional software such as Gaussian09. Therefore, the investigation of these active vibrational frequencies will require more sophisticated approaches.

To reduce the noise generated by the laser fluctuations in time, a shot-to-shot referencing for NOPA normalisation would be required. Moreover, the 2DES spectrometer could be improved by modifying the compression stage in such a way that it would be possible to achieve the transform-limited pulse (~10 fs for Gaussian beam with FWHM 100 nm). For example, by using the Dazzler pulse shaper in combination with the Wizzler (Fastlite) an optimum pulse compression can be achieved. The Dazzler-Wizzler loop has the ability to

re-optimize the pulse compression with a high level of control within few minutes; therefore, it guarantees the compression maximum efficiency and stability.

As future work in terms of samples, my inclinations would be the systematic study of Oxazine 4 in a larger variety of ionic liquids, and the investigation of the solvation dynamics of chlorin e6 in different protein maquettes with the possibility to extend the study to a two (and hopefully one day a multiple) chromophores containing protein. Moreover, the solvation dynamics of the protein maquette could be explored with multidimensional spectroscopy to disentangle the congested BBTA spectra, as shown for Oxazine 4.

In summary, in this thesis, I have applied ultrafast spectroscopy to study charge transfer and vibrational coherent states alongside with the development of a state-of-the-art two-dimensional spectrometer. The studies carried out in this thesis, and the implementation of the 2DES setup are presented with the hope that they will contribute to the development of the physical-chemistry field with particular attention to the investigation of the plethora of questions that can be addressed with multidimensional spectroscopies.